UNIVERSITY OF CALGARY

# Viscous Fingering and Static/Dynamic Heterogeneity Induced Instabilities in Porous Media

by

Mozhdeh Sajjadi

A THESIS

SUBMITTED TO THE FACULTY OF GRADUATE STUDIES

IN PARTIAL FULFILLMENT OF THE REQUIREMENTS FOR THE

DEGREE OF DOCTOR OF PHILOSOPHY

GRADUATE PROGRAM IN CHEMICAL AND PETROLEUM ENGINEERING

CALGARY, ALBERTA

SEPTEMBER, 2015

# Abstract

This dissertation addresses different aspects of flow instability in non-isothermal miscible displacements through media with static and dynamic permeability distributions. The research is conducted in three steps. In the first step non-isothermal flows in homogeneous media are studied by numerical simulation of the displacement process in a Hele-Shaw cell. The results show that the stability of the process highly depends on the strength of interactions between the two fronts determined by the thermal lag coefficient. The relative rate of diffusion of heat in the medium can magnify the effect of lag between the two fronts or compensate for it depending on the considered scenario.

Miscible displacements with adverse mobility ratios are analyzed in the second part of this study for layered heterogeneous media. The effects of the flow parameters and the heterogeneity characteristics of the domain are examined. Qualitative and quantitative analysis of the results lead to characterization and unification of four distinct regimes that govern the flow displacement for different parameters. The unification allows to distinguish between the flows in which the instability is dominated by heterogeneity and those with viscous fingering dominant instability.

Finally in the last two chapters of this dissertation, the changes in the porosity and permeability in melting porous media are modeled. The effects of the melting parameters on the amount of melted material and the rate of melting are analyzed. In addition, the heat transfer mechanisms in presence of the bypassing flow around frozen blocks of different geometries are analyzed and their melting rates are unified based on the shape factor and initial porosity of the block. In study of the flow displacements prone to instability, the dominant mechanisms that affect the growth and patterns of instability for different melting parameter values are recognized and their contribution to enhancement or attenuation of

fingers are determined analytically. The study shows that instabilities in general enhance melting but the enhancement is limited for displacements with small melting potentials.

# Acknowledgements

My years of study and work towards the PhD degree have been full of memorable moments and valuable experiences and for that I would like to sincerely thank my supervisor Dr. Jalel Azaiez whose support and guidance has always encouraged me to go forward. But above that to me Dr. Azaiez has been a symbol of sincerity and responsibility in scientific and professional careers and an understanding and honorable person. My respect and gratitude to him is endless.

I also would like to thank my thesis committee members Dr. Farouq Ali, Dr. Chen, and Dr. Maini for their valuable input on my PhD dissertation.

I have been fortunate to take courses with excellent professors at the Chemical and Petroleum Engineering Department and my gratitude goes to them for leading me through my graduate studies. I am also grateful to all office and technical staff of the department of Chemical and Petroleum Engineering especially Arthur de Verra for their help during last years. My sincere appreciation goes to the support team of West Grid especially Dr. Doug Philips for their constantly provided help.

I should give my special gratitude to all my colleagues in flow simulation lab especially Dr. Hossein Hejazi and Dr. Qingwang Yuan who provided me with precious support and ideas over the last years.

Lastly and most importantly I have to thank my parents for their endless support, encouragement and inspiration.

The financial support of this work has been provided through funds and scholarships by the following organizations: Natural Sciences and Engineering Research Council of Canada (NSERC), Alberta Innovates Technology Future (AITF), University of Calgary's Board of Governors, and Ursula and Herbert Zandmer.

To my husband and my son,
to whom I owe the most

# Table of Contents


**Abstract** . . . i
**Acknowledgements** . . . iii
Table of Contents . . . v
List of Tables . . . vii
List of Figures . . . viii
List of Symbols . . . xiii
1 Introduction . . . 1
2 Review of the Background . . . 6
2.1 Thermo-Viscous Fingering in Homogeneous Porous Media . . . 6
2.1.1 Instabilities in Isothermal Displacements . . . 7
2.1.2 Instabilities in Non-Isothermal Displacements . . . 9
2.2 Coupling of Heterogeneity and Viscous Fingering . . . 17
2.3 Melting and Flow Dynamics in Media with Changing Porosity . . . 25
2.3.1 Melting of Ice in Porous Media . . . 26
2.3.2 Flow of Magma and Precipitation-Dissolution Problems . . . 30
2.3.3 Heavy Oil Recovery Processes . . . 34
2.4 Goals and Objectives . . . 37
3 Dynamics of Fluid Flow and Heat Transfer in Homogeneous Porous Media . 39
3.1 INTRODUCTION . . . 40
3.2 Physical Problem and Mathematical Model . . . 42
3.3 Numerical Method . . . 45
3.4 Results . . . 46
3.4.1 Validation of Results . . . 46
3.4.2 Reference Cases . . . 47
3.4.3 Effects of the Thermal Lag Coefficient . . . 47
3.4.4 Transversely Averaged Properties . . . 52
3.4.5 Breakthrough Time and Sweep Efficiency . . . 54
3.4.6 Effects of the Lewis Number . . . 57
3.5 Conclusion . . . 61
4 Scaling and Unified Characterization of Flow Instabilities in Layered Heterogeneous Porous Media . . . 64
4.1 Introduction . . . 65
4.2 Physical Model and Numerical Method . . . 68
4.3 Results and Discussion . . . 72
4.3.1 Flow Structures . . . 73
4.3.2 Mixing Length . . . 75
4.3.3 Time Dependent Dominance of Flow Regimes . . . 86
4.3.4 Breakthrough Time . . . 88
4.3.5 Effects of Dispersion . . . 89
4.4 Summary and Conclusion . . . 91

5 Heat and Mass Transfer in Melting Porous Media: Stable Miscible Displacements 94
5.1 Introduction . . . 95
5.2 Modeling . . . 97
5.2.1 Main Model Equations . . . 100
5.2.2 Constitutive Correlations . . . 102
5.2.3 Initial and Boundary Conditions . . . 107
5.2.4 Dimensionless Equations . . . 108
5.3 Numerical Method . . . 111
5.3.1 Validation . . . 113
5.4 Results and Discussion . . . 114
5.4.1 Reference Scenarios . . . 116
5.4.2 Effect of $H_T$ . . . 121
5.4.3 Effect of Ste . . . 124
5.4.4 Effect of $\phi_{min}$ . . . 125
5.4.5 Effect of Le . . . 127
5.4.6 Time trends of melting . . . 129
5.4.7 Frozen Blocks . . . 133
5.5 Conclusion . . . 147
6 Hydrodynamic Instabilities of Flows Involving Melting in Under-Saturated Porous Media . . . 150
6.1 Introduction . . . 151
6.2 Modeling . . . 152
6.2.1 Initial and Boundary Conditions . . . 157
6.3 Numerical Method . . . 157
6.4 Results and Discussions . . . 158
6.4.1 Simulation Results for Unstable Scenarios . . . 159
6.4.2 Mechanisms Affecting the Development and Growth of Instabilities . . . 166
6.4.3 Melting Trends in Unstable Scenarios . . . 176
6.4.4 Quantitative Study of Enhancement of Melting due to Instabilities . . . 178
6.4.5 Effect of Le, Pe, and $\lambda$ on Melting . . . 181
6.5 Summary and Conclusion . . . 182
7 Summary and Conclusion . . . 184
A Improvement of Sweep Efficiency of Miscible Displacement Processes in Heterogeneous Porous Media . . . 193
B Generalization of the Melting Curves for Different $H_T$ . . . 198
Bibliography . . . 200

# List of Tables

5.1 List of values for the thermal properties of the fluid, rock and solid phases, and the flow in formation corresponding to the displacement of bitumen in Cold Lake formation in northern Alberta, Canada. . . . . 104
5.2 List of values for the the thermal properties of the fluid, rock, and solid phases corresponding to flow of water in frozen ground. . . . . 105

A.1 Flow conditions for the described displacement scenarios and the corresponding breakthrough time, weep efficiency at breakthrough and optimum well spacing for each scenario. . . . . 197

# List of Figures and Illustrations


2.1 Stability criteria defined by Mishra et al. [23]; $R_s$ and $R_f$ are the log mobility ratios corresponding to the effect of slow and fast diffusing properties respectively; The lines $L_n$ ($n = 1\ ,2\ ,3$) are defined through $R_f = -\delta^{n/2} R_s$, $\delta$ is the diffusion ratio. . . . . 16

2.2 Critical ranges: (a) M = 1, line separates channeling and dispersive regions, and (b) at M = 10, lines separate channeling and dispersive regions and dispersive and fingering regions [67]. . . . . 22

2.3 Antarctic sea ice melting between September 2008 and February 2009; Courtesy of the National Snow and Ice Data Center, University of Colorado, Boulder, Colorado. . . . . 27

2.4 (A) Microscopic photographs depicting brine pores of laboratory-grown, organic-free sea ice, (B) ice grown in the presence of organic materials that sculpt the brine pores [83]. . . . . 28

2.5 Configurations of a single pipe frozen ground;[90]. . . . . 29

2.6 Viscous fingering during replenishment of felsic magma [101]. . . . . 31

2.7 Formation of worm holes in homogeneous porous media due to infiltration of fluids in carbonate rocks [109]. . . . . 32

2.8 Schematic of SAGD steam chamber a) whole chamber with exaggerated view of steam fingers [119] b) Pore scale near interface events [128]. . . . . 37

3.1 Schematic of a horizontal double diffusive flow. . . . . 42

3.2 Concentration contours comparing an isothermal flow with a non-isothermal flow: $\beta_C = 2$, $\lambda = 1$, a) $\beta_T = 0$, b) $\beta_T = 1$. . . . . 48

3.3 Concentration contours at: $\beta_C = -2$, $\beta_T = 3$, a) $\lambda = 1$ b) $\lambda = 0.4$ . . . . . 49

3.4 Temperature contours at: $\beta_C = -2$, $\beta_T = 3$, a)$\lambda = 1$ b) $\lambda = 0.4$ . . . . . 49

3.5 Concentration and temperature contours at: $\beta_C = -2$, $\beta_T = 3$, $\lambda = 0.8$, a) Concentration b) Temperature . . . . . 50

3.6 Concentration contours at: $\beta_C = 2$, $\beta_T = -3$, a)$\lambda = 1$ b) $\lambda = 0.5$ . . . . . 51

3.7 Temperature contours at: $\beta_C = 2$, $\beta_T = -3$, a)$\lambda = 1$ b) $\lambda = 0.5$ . . . . . 51

3.8 Concentration and Temperature Contours at: $\beta_C = 2$, $\beta_T = -3$, $\lambda = 0.8$, a) Concentration b) Temperature . . . . . 51

3.9 Transversely averaged concentration and temperature distributions for the cases discussed in Figures 3.3-3.5 at t=1400: a) average concentration for different lag coefficients, b)average concentration and temperature for $\lambda = 0.8$, c)average concentration and temperature for $\lambda = 0.4$ . . . . . 53

3.10 Transversely averaged concentration and temperature distributions for the cases discussed in Figures 3.6-3.8 at t=2000, $\beta_C = 2$, $\beta_T = -3$: a) average concentration for different thermal lag coefficients, b) average concentration and temperature for $\lambda = 0.8$, c) average concentration and temperature for $\lambda = 0.5$. . . . . 53

3.11 The breakthrough time and sweep efficiency of solvent and heat flooding at breakthrough for $\beta_C = -2$, and $\beta_T = 2,\ 3,\ 4$: a) Breakthrough time, b) Concentration Sweep Efficiency, c) Heat Sweep Efficiency. . . . . 55

3.12 The breakthrough time and sweep efficiency of solvent and heat flooding at breakthrough for $\beta_C = 2$, and $\beta_T = -1,\ -2,\ -3$: a) Breakthrough time, b) Concentration Sweep Efficiency, c) Heat Sweep Efficiency. . . . . 56

3.13 The breakthrough time and sweep efficiency of solvent and heat flooding at breakthrough for $\beta_C = 2$, and $\beta_T = 0,\ 1,\ 2$: a) Breakthrough time, b) Concentration Sweep Efficiency, c) Heat Sweep Efficiency. . . . . 57

3.14 Concentration contours at: $\beta_C = -2$, $\beta_T = 3$, Le $= 10$, a) $\lambda = 1$ b) $\lambda = 0.4$ . 58

3.15 Concentration contours at: $\beta_C = 2$, $\beta_T = -3$, Le $= 10$, a)$\lambda = 1$ b) $\lambda = 0.5$ . . 58

3.16 The breakthrough time and sweep efficiency of solvent and heat flooding at breakthrough for $\beta_C = -2$, $\beta_T = 2,\ 3,\ 4$, and Le $= 10$: a) Breakthrough time, b) Concentration Sweep Efficiency, c) Heat Sweep Efficiency. . . . . 59

3.17 The breakthrough time and sweep efficiency of solvent and heat flooding at breakthrough for $\beta_C = 2$, $\beta_T = -1,\ -2,\ -3$, and Le $= 10$: a) Breakthrough time, b) Concentration Sweep Efficiency, c) Heat Sweep Efficiency. . . . . 60

3.18 The breakthrough time and sweep efficiency of solvent and heat flooding at breakthrough for $\beta_C = 2$, $\beta_T = 0,\ 1,\ 2$, and Le $= 10$: a) Breakthrough time, b) Concentration Sweep Efficiency, c) Heat Sweep Efficiency. . . . . 61

4.1 Schematic of the flow, . . . . . 68

4.2 Periodic permeability models with permeability varying between $\kappa = 0.7$ and $\kappa = 1.6$ for $s = 0.5$; a) $q = 1$ and b) $q = 9$ . . . . . 70

4.3 Concentration contours for a viscously unstable flow with $\beta_C = 3$, Pe $= 1024$, and $A = 2$ in a) a homogeneous medium, b) a double-layer heterogeneous medium, and c) a nine-layer heterogeneous medium. In each frame the red color (left) represents $c = 1$ and the blue color (right) represents $c = 0$. . . . 75

4.4 Mixing zone length versus time for stable and unstable flows in homogeneous medium and in a nine-layer heterogeneous medium; Pe $= 1024$, $A = 2$, $s = 0.1$, a) throughout the process in logarithmic scales, b) at early times. . . . . 76

4.5 Mixing zone length versus time for heterogeneous media with different number of layers for $\beta_C = 3$, Pe $= 1024$, $A = 2$ and $s = 0.1$; a) throughout the process, b) at the initial times (fewer graphs are shown for better distinction between the lines). . . . . 78

4.6 Generalized MZL versus generalized time for $\beta_C = 3$ and $s = 0.1$; a) for $w^* =$ 25.6, 51.2, 56.9, 64, 73.1, 102.4, 113.8, 128, 146.3, 170.7, 204.8, 256, 241.3, and 512, b) for $w^* = 51.2$ in log-log scale indicating the flow regimes. . . . . 80

4.7 Weak effect of heterogeneity in media with small dimensionless width of layers for $\beta_C = 3$, $s = 0.1$, Pe $= 200$, and $A = 2$ . . . . . 81

4.8 Concentration contours for $\beta_C = 3$, Pe $= 200$, $A = 2$, a) homogeneous porous medium and b) 9-layer heterogeneity, $w^* = 11.1$, c) 3-layer heterogeneity, $w^* = 33.3$. In each frame the red color (left) represents $c = 1$ and the blue color (right) represents $c = 0$. . . . . 82
4.9 Generalized MZL for different combinations of mobility ratio and variance of permeability distribution $(\beta_C, s)$ . . . . . 83
4.10 Re-normalization of MZL to account for variance of permeability distribution $s$; The flow parameters are: Pe $= 2048$, $A = 4$, $q = 7$, a) $\beta_C = 3$, b) $s = 0.1$, different log mobility ratios. . . . . 84
4.11 Fitting of $M\tilde{Z}L_s$ curves of different displacement scenarios with Pe $= 2048$, $A = 4$, $q = 7$, $s = 0.1$, and for different mobility ratios as noted on the plot. . 85
4.12 Effect of viscosity model on MZL for an unstable flow with mobility ratio of $M = 20$ corresponding to $\beta_C = 3$, with Pe $= 2048$, $A = 4$, and $s = 0.1$ in a 5-layer and a 7-layer medium corresponding to $w^* = 102.4$ and $w^* = 73.1$ respectively. . . . . 86
4.13 Average slope of MZL $(\dot{L}_d)$ at different time windows for $\beta_C = 3$, Pe $= 2048$, $A = 2$ and $s = 0.01$ . . . . . 87
4.14 Breakthrough time of the flow with $\beta_C = 3$, $s = 0.1$, at the total dimensionless length of $L_{total} = 2700$; a) breakthrough time versus number of layers for different Pe and $A$, b) breakthrough time versus $1/w^* = q.A/\text{Pe}$. . . . . 89
4.15 Effect of dispersion on MZL for $s = 0.1, q = 9, \beta_C = 2$, Pe $= 512$, $A = 2$, for a) $L = 0.7$ and different $\alpha_D$, b) $\alpha_D = 0.5$ and different $L$ . . . . . 91

5.1 Schematic of the phases present in the domain and the melting process: a) initial stage with rock, frozen material, and melted fluid present; b) volume flooded by heated fluid; c) melting of the remainders of frozen material. . . . 98
5.2 Diagram of the modeled domain with the solvent concentration, fluid temperature, and porosity distribution profiles at $t_0$ and $t > t_0$ . . . . . 100
5.3 The average Concentration, Temperature, and porosity profiles for reference scenarios with $\phi_{min} = 0.7$ and Le $= 1$: a) no heat transfer to melting (HT0) scenario ($H_T = 1e-7$, Ste $= 0.54$), b) instantaneous thermal equilibrium scenario ($H_T = 100$, Ste $= 0.54$), c) non-melting scenario ($H_T = 10$, Ste $= 1e-5$) and d) instantaneous melting scenario ($H_T = 10$, Ste $= 100$) with numerical solutions and the corresponding approximations. . . . . 116
5.4 Effect of $H_T$ on temperature, porosity, and concentration profiles for Le $= 1$, $\phi_{min} = 0.7$, Ste $= 0.5$, and $H_T = 1e-7$ to 100 at $t = 500$. . . . . 123
5.5 Effect of Ste on temperature, porosity, and concentration profiles for Le $= 1$, $H_T = 10$ and $\phi_{min} = 0.7$, and Ste $= 0.04$ to 100 at $t = 500$. . . . . 124
5.6 Effect of $\phi_{min}$ on temperature, porosity, and concentration profiles for stable scenarios with Le $= 1$, Ste $= 0.5$, $H_T = 10$ and $\phi_{min} = 0.6$, 0.7, 0.8, and 0.9 at $t = 500$ . . . . . 126

5.7 Effect of Le on temperature, porosity, and concentration profiles for stable scenarios with $\phi_{min} = 0.7$, $H_T = 10$ and Ste = 0.5 and 3.2 and Le = 1 and 10 at $t = 500$. . . . . 129
5.8 Effect of heat transfer coefficient on the amount of melt produced for different scenarios with Le = 1, $\phi_{min} = 0.7$, Ste = 15, and $H_T = 1e-4$ to 100. . . . . 130
5.9 Effect of Ste, Le, and $\phi_{min}$ on melting rate at ITE conditions, for $H_T$ = 10,Le = 1 and 10, $\phi_{min} = 0.7$ and 0.9, and Ste = 0.04 to 100. . . . . 131
5.10 Effect of Ste, Le, and $\phi_{min}$ on the advance rate of the melting front at ITE conditions, for $H_T$ = 10,Le = 1 and 10, $\phi_{min} = 0.7$ and 0.9, and Ste = 0.04 to 100. . . . . 132
5.11 Melting of a square shaped frozen block of size $l = Pe/3$ for Pe = 128, Le = 1, $\lambda = 0.8$, Ste = 1.2. a) Initial porosity distribution for $\phi_{min} = 0.2$, b) Change in porosity and differential velocity contours at $t = 30$, and c) Temperature contours at $t = 30$. . . . . 134
5.12 Melting of a square frozen block with $\phi_{min} = 0.8$ at $t = 30$ a) Change in porosity and differential velocity and b) Temperature contours. The other parameters are similar to those in Figure 5.11. . . . . 135
5.13 Melting of a long rectangle shaped frozen block of length $l = Pe/3$ and width $w = Pe/12$ for Pe = 128, Le = 1, $\lambda = 0.8$, Ste = 1.2. a) Initial porosity distribution for $\phi_{min} = 0.2$, b) Change in porosity and differential velocity contours at $t = 30$, and c) Temperature contours at $t = 30$. . . . . 137
5.14 Melting of a wide rectangle shaped frozen block of length $l = Pe/12$ and width $w = Pe/3$ for Pe = 128, Le = 1, $\lambda = 0.8$, Ste = 1.2. a) Initial porosity distribution for $\phi_{min} = 0.2$, b) Change in porosity and differential velocity contours at $t = 30$, and c) Temperature contours at $t = 30$. . . . . 137
5.15 Fractional flux of heat entering the frozen region ($u_f \nu$) for different block geometries and the one dimensional scenario. The data points represent cumulative melt ratio (i.e. cumulative melt of the frozen block over the cumulative melt of the 1D scenario at each time step) for the corresponding frozen block geometry at $t = 5$ (triangles) and $t = 30$ (asterisks). Other parameters are set as $H_T = 0.1$, Pe = 128, Le = 1, $\lambda = 0.8$, Ste = 1.2. . . . . 140
5.16 Cumulative melt production for the wide rectangle frozen block with dimensions similar to Figure 5.14an for Pe = 128, Le = 1, $\lambda = 0.8$, Ste = 1.2. . . . . 142
5.17 Effect of the block geometry on cumulative melt production; Parameters set as Pe = 128, Le = 1, $\lambda = 0.8$, Ste = 1.2 and $\phi_{min} = 0.8$. . . . . 143
5.18 Effect of the block geometry and initial porosity of the frozen block on Melt % production for Pe = 128, Le = 1, $\lambda = 0.8$, Ste = 1.2. . . . . 145
5.19 Unification of cumulative melt curves for different geometries and different initial porosity values for the scaled cumulative melt $melt/((1-\phi_{min}) \times w_{FB})$ versus scaled time as $t/(1-\phi_{min})^{1/3}$. Other parameters are Pe = 128, Le = 1, $\lambda = 0.8$, Ste = 1.2. . . . . 146

5.20 Scaling of cumulative melt production for circular obstacles with different initial porosity values matched with that of a long rectangle with $\phi_{min} = 0.2$. Other parameters are Pe = 128, Le = 1, $\lambda = 0.8$, Ste = 1.2. . . . . 147

6.1 Diagram of the modeled domain at $t_0$ and $t > t_0$ . . . . . 153
6.2 The effect of the thermal log mobility ratio ($\beta_T$) on development of instabilities; Ste = 3.2, $t = 250$. . . . . 161
6.3 The effect of $\beta_C$ and $\beta_T$ on instabilities of non-melting scenarios; $H_T = 1e-7$, Ste = 0.04, $\phi_{min} = 0.7$, $t = 250$. . . . . 161
6.4 The effect of the solutal log mobility ratio ($\beta_C$) on development of instabilities; Ste = 3.2, $t = 250$. . . . . 161
6.5 The effect of the heat transfer coefficient ($H_T$) on development of instabilities; Ste = 1.2, $t = 250$. . . . . 163
6.6 The effect of the melting potential of the fluid (Ste) on development of instabilities; $t = 250$. . . . . 165
6.7 The effect of the initial saturation of the frozen material ($\phi_{min}$) on development of the instabilities; Ste = 0.2, $t = 250$. . . . . 166
6.8 Approximation of $\lambda'$ in stable scenarios; solid lines correspond to analytical approximations and the scattered data points present the obtained values from non-linear numerical simulations. . . . . 168
6.9 The effect of Ste and $\phi_{min}$ on the gradient magnitudes for stable scenarios; $(\beta_C, \beta_T) = (0, 0)$, $t = 250$. a) Concentration gradient, b) Temperature gradient 170
6.10 The contour lines of constant porosity $\phi_{min} = 0.85$ and the matching contours of constant temperature for different Ste values; $t = 250$ . . . . . 172
6.11 The effect of Ste and $\phi_{min}$ on the Melting Zone Length ($MZL_\phi$); $t = 250$. . . 174
6.12 The effects of $\beta_C$ and $\beta_T$ on the melt production for a) Ste = 0.2 and 3.2 and $H_T = 1$, and b) $H_T = 0.01$ and 1 and Ste = 3.2. . . . . 177
6.13 The Effects of $\phi_{min}$ and Ste on melt production a) $\phi_{min} = 0.7$ and 0.9, and Ste = 0.2 and 20 , and b) $\phi_{min} = 0.7$ and Ste $= 0.04 - 100$. . . . . 178
6.14 Relative Increase of Melting (RMI) in unstable scenarios for different Ste values and $\phi_{min} = 0.7$ (solid lines) and $\phi_{min} = 0.9$ (dashed lines) a) versus time, b) versus the increase in relative contact area RCA$-1$. . . . . 179
6.15 Temperature contour lines $\theta_\phi = 0.5$ and $\theta_\phi = 1e-3$ representing the melting front's profiles for different scenarios with small and large melting potentials. 181

A.1 Quantitative description of the displacement front behavior through analysis of time variation of a) MZL, b) EP position, c) Sweep Efficiency; breakthrough of each case is marked as a solid circle on its curve . . . . . 195
A.2 Unified curves after scaling the length and time using the diffusive scaling for a) MZL, b) EP position and c) sweep efficiency with respect to scaled time. . 197

B.1 Melt % in the new dimensionless system scaling the diffusion rate with respect to $H_T$. . . . . 199

# List of Symbols, Abbreviations and Nomenclature

| Abbreviation | Definition |
|---|---|
| 2D | Two Dimensional |
| 3D | Three Dimensional |
| AB-AM | Adams-Bashforth - Adams-Moulton Method |
| AGF | Artificial Ground Freezing |
| CSS | Cyclic Steam Stimulation |
| FE | Finite Element |
| HT0 | No Heat Transfer Condition |
| ITE | Instantaneous Thermal Equilibrium |
| IVC | Initial Value Calculation |
| LSA | Linear Stability Analysis |
| QSSA | Quasi-Steady-State Approximation |
| RK4 | Fourth Order Runge-Kutta Method |
| SA-SAGD | Solvent Assisted SAGD |
| SAGD | Steam Assisted Gravity Drainage |
| TVF | Thermo-Viscous Fingering |
| U of C | University of Calgary |
| VAPEX | Vapor Extraction |
| VF | Viscous Fingering |

| Symbol | Definition |
|---|---|
| $A$ | Geometric Aspect Ratio |
| $A_{Potential}$ | Potential Area to Be Swept by a Stable Front |
| $A_{\phi}$ | Swept Area by Melting Front |
| $C$ | Mass Concentration of Solvent |
| $C_1$ | Solvent Concentration at Inlet |
| $C_2$ | Solvent Concentration at Outlet |
| $C_{drop}$ | Solvent Concentration After Dilution |
| $D_{FB}$ | Diameter of the Frozen Block |
| $D_C$ | Mass Diffusion Coefficient |
| $D_T$ | Heat Diffusion Coefficient |
| EP | Location of the End Point of the Fluid Front |
| $H_T$ | Dimensionless Group for Heat Transfer Coefficient |
| $H_{\phi}$ | Melting Rate Coefficient |
| $HI$ | Heterogeneity Index |
| $L$ | Relative Strength of Longitudinal Dispersion |
| $L_{total}$ | Total Injection - Production Distance |
| $L_x$ | Length of the Domain (Hele Shaw cell or porous medium) |
| $L_y$ | Width of the Domain (Hele Shaw cell or porous medium) |
| $\dot{L}_d$ | Average Slope of the $MZL$ versus Time Curve |
| Le | Lewis Number |
| $\hat{\text{Le}}$ | Effective Lewis Number ahead of Melting Front |
| $M$ | Mobility Ratio |
| $Melt\%$ | Relative Cumulative Melt |
| $MZL$ | Mixing Zone Length |

| | |
|---|---|
| $MZL_{Master}$ | Master Mixing Zone Length |
| $MZL_{\phi}$ | Melting Zone Length |
| $\tilde{MZL}$ | Generalized Mixing Zone Length |
| $\tilde{MZL}_s$ | $\tilde{MZL}$ Scaled with Respect to Permeability Variation |
| $P$ | Pressure |
| Pe | Péclet Number |
| $\mathrm{Pe}_C$ | Solutal Péclet Number |
| $\mathrm{Pe}_T$ | Thermal Péclet Number |
| $\mathrm{Pe}_p$ | Pore Level Péclet Number |
| Pr | Prandtl Number |
| $RCA$ | Relative Contact Area |
| $RMI$ | Relative Melt Increase |
| $\mathrm{Re}_p$ | Pore Level Reynold's Number |
| $S_s$ | Saturation of Frozen Material |
| Ste | Modified Stefan Number |
| $\mathrm{Ste}'$ | Stefan Number |
| $\mathrm{Ste}_c$ | Critical Stefan Number |
| $T$ | Temperature |
| $T_1$ | Temperature at Inlet |
| $T_2$ | Temperature at Outlet |
| $T_m$ | Melting Temperature |
| $U$ | Injection Darcy Velocity |
| $U_T$ | Advance Rate of the Thermal Front |

| | |
|---|---|
| $c, c^*$ | Dimensionless Concentration |
| $c_0$ | Initial Concentration (Dimensionless) |
| $c_{av}$ | transversely Averaged Concentration |
| $c_k$ | Kozeny's Constant |
| $c_s$ | Specific Heat Capacity of Frozen Phase (Solid) |
| $c_R$ | Specific Heat Capacity of Rock (Porous Matrix)) |
| $c_{pf}$ | Specific Heat Capacity of Fluid |
| $\bar{c}$ | Base State Concentration |
| $\bar{c}_{\phi_{min}}$ | Estimated Concentration of ITE Scenarios |
| $c'$ | Concentration Disturbance |
| $dy$ | Grid Size in $-y$ direction |
| $dt$ | Time Step Size |
| $d_p$ | Grain Size of the Porous Medium |
| $e$ | Thickness of the Hele Shaw cell |
| $f$ | Natural Log of Permeability |
| $h$ | Heat Transfer Coefficient |
| $\mathbf{i}$ | Unit Vector along the Flow Direction |
| $k_f$ | Thermal Conductivity of Fluid |
| $k_{rel}$ | Relative Thermal Conductivity of Fluid |
| $k_R$ | Thermal Conductivity of Rock |
| $l_{FB}$ | Length of the Frozen Block |
| $l_D$ | Correlation Length of Permeability |
| $l_y$ | Dimensionless Width of the Domain |
| $q$ | Number of Heterogeneity Layers |
| $q_{optM}$ | $q$ Resulting in Maximum $t_{BT}$ |

| | |
|---|---|
| $q_{optm}$ | $q$ Resulting in Minimum $t_{BT}$ |
| $s$ | Range of Variation of Log-Permeability |
| $\bar{s}$ | Specific Surface Area of the Porous Medium |
| $\bar{s}_0$ | Reference Specific Surface Area |
| $\bar{s}_s$ | Specific Surface Area of the Frozen Phase |
| $\bar{s}_{s,0}$ | Reference Specific Surface Area of the Frozen Phase |
| $t$ | Time |
| $t_0$ | Initial Time |
| $t_{BT}$ | Breakthrough Time |
| $t_{Master}$ | Master Time |
| $t_c$ | Characteristic Diffusion Time |
| $t_s$ | $\tilde{t}$ Scaled with Respect to Permeability Variation |
| $\tilde{t}$ | Generalized Time |
| $\tilde{t}_{CD}$ | $\tilde{t}$ of Channeling - Lateral Dispersion Transition |
| $\tilde{t}_{dC}$ | $\tilde{t}$ of Initial Diffusion - Channeling Transition |
| $\hat{t}$ | Scaled Time for Flow Ahead of Melting Front |
| $u, v$ | Components of Velocity in $(x, y)$ Directions |
| $\mathbf{u}$ | Interstitial Velocity Vector |
| $\hat{u}$ | Dimensionless Velocity in Fixed reference Frame |
| $\vec{u}_D$ | Darcy Velocity Vector |
| $\bar{u}, \bar{v}$ | Components of Base State Velocity in $(x, y)$ Directions |
| $u_D, v_D$ | Components of Darcy Velocity in $(x, y)$ Directions |
| $u_F$ | Equivalent Velocity Inside the Frozen Region |
| $u_O$ | Equivalent Velocity Around the Frozen Region |
| $w$ | Width of the Layers |

| | |
|---|---|
| $w_{FB}$ | Width of the Frozen Block |
| $w^*_{c-H}$ | $w^*$ Boarder of Heterogeneity Domination |
| $w^*_{c-h}$ | $w^*$ Boarder of Homogeneous Behavior |
| $w^*_{optM}$ | $w^*$ Resulting in Maximum $t_{BT}$ |
| $w^*_{optm}$ | $w^*$ Resulting in Minimum $t_{BT}$ |
| $x, y$ | Coordinates Along and Transverse to the Flow |
| $\hat{x}$ | Dimensionless Length in Fixed Reference Frame |
| $x_0$ | Location of the Fronts at $t_0$ |
| $x_c$ | Characteristic Length |
| $x_\phi$ | Location of the Melting Front |
| $\tilde{x}$ | Generalized Length |
| | |
| $\Delta h_f$ | Latent Heat of Infusion |
| $\alpha$ | Dimensionless Concentration After Dilution |
| $\alpha_D$ | Transverse/Longitudinal Dispersion Ratio |
| $\beta_C$ | Solutal Log-Mobility (Viscosity) Ratio |
| $\beta_T$ | Thermal Log-Mobility (Viscosity) Ratio |
| $\delta$ | Amplitude of Perturbations |
| $\theta, \theta^*$ | Dimensionless Temperature |
| $\bar{\theta}$ | Base State Temperature |
| $\zeta$ | Auxiliary Variable |
| $\zeta_\nabla$ | $\zeta$ with Maximum $\lvert\nabla\theta\rvert$ |
| $\theta'$ | Temperature Disturbance |
| $\theta_\nabla$ | $\theta$ with Maximum $\lvert\nabla\theta\rvert$ |
| $\theta_0$ | Initial Temperature (Dimensionless) |

| | |
|---|---|
| $\kappa$ | Permeability |
| $\kappa_R$ | Permeability of the Rock |
| $\kappa_{min}$ | Initial Permeability of the Frozen Region |
| $\lambda$ | Thermal Lag Coefficient |
| $\lambda'$ | Advance Rate of the Melting Front |
| $\mu$ | Viscosity of the Fluid |
| $\mu_1$ | Viscosity of the Injected Fluid |
| $\mu_{1T}$ | Viscosity of Injected Fluid in Thermal Flooding |
| $\mu_2$ | Viscosity of Inhabitant Fluid |
| $\mu_{2T}$ | Viscosity of Inhabitant Fluid in Thermal Flooding |
| $\nu$ | relative Width of the Frozen Block |
| $\rho_R$ | Density of the Rock (Porous Matrix) |
| $\rho_f$ | Density of Fluid |
| $\rho_{rel}$ | Relative Density of Solid to Fluid |
| $\rho_s$ | Density of Frozen Phase (Solid) |
| $\sigma$ | Penetration Scale of Perturbation |
| $\phi$ | Porosity |
| $\phi_{min}$ | Initial Porosity at the Frozen Region |
| $\phi_R$ | Porosity of the Rock |
| $\phi_0$ | Reference Porosity |
| $\psi$ | Stream Function |
| $\omega$ | Vorticity |

# Chapter 1

# Introduction

---

In this thesis, miscible displacements in porous media are studied in terms of the development of hydrodynamic instabilities on the diffusing fronts. In this context the viscosity ratio between the injected fluid and the displaced one is set to unfavorable values to induce viscous fingering. Consideration of heat transfer mechanisms and non-uniform distribution of permeability in the medium extend the applicability of the study to non-isothermal displacements in heterogeneous media. The coupling between the viscosity driven instability due to thermal or solutal adverse mobility ratios, and the heterogeneity guided channeling is investigated thoroughly. Furthermore a dynamic model of heterogeneity whose formation and pattern depend on the other instability mechanisms are introduced and modeled in the final parts of the study.

The problem of miscible viscous fingering (VF) is encountered in various natural phenomena and industrial and environmental applications including but not limited to secondary and tertiary oil recovery, filtration, polymer processing, pollution spreading in soils, fixed bed regeneration and engineering separation techniques [1, 2]. Viscous fingering, that classically happens when a fluid of a smaller viscosity displaces another miscible more viscous fluid, has been identified as one of the most important phenomena in miscible displacement processes for decades [3, 4]. The inherent instability leads to a deformation of the interface into finger like patterns called viscous fingers [5, 6, 7]. Until 1990s, the simplest form of viscous fingering in miscible displacements was deemed to be too difficult for numerical simulation. Enhance-

ment of the computing capability facilitated the investigation of multivarious forms of the problem. Since then numerous works have been devoted to studying this type of instability in miscible displacements through experimental, analytical, and numerical studies looking at the characteristics and mechanisms of instability. Different aspects of the problem have been explored in these works such as the geometry of the model (e.g. rectilinear [7, 8, 9], radial, or five-spot geometry) in two and three dimensions [10, 11], the fluid properties (Newtonian, non-Newtonian [12], visco-elastic), the dispersion model (anisotropic and velocity dependent dispersion [11, 13]), for reactive [14, 15, 16, 17] and nonreactive displacements, in systems with constant and variable injection rates [18], and considering the additional inertial effects in the momentum equation[19, 20]. Such a vast amount of work on this subject reflects the complexity and importance of the problem.

In the current work the viscous fingering in non-isothermal displacement processes is investigated. So it is assumed that in addition to the injected fluid's concentration, its temperature can also contribute to the adverse mobility ratio and thus affect the instability. Such instability is often referred to as thermo-viscous fingering (TVF). Thermo-viscous fingering is mainly observed in thermal oil recovery processes but is also encountered in geothermal reservoir recharge [21], injection molding, and some polymer processing processes [22]. Due to the instantaneous thermal equilibrium between the fluids and the porous matrix the heat, that is shared with the porous medium, is convected in a slower rate than the mass and thus two fronts are formed in such systems. These fronts may have different viscosity gradients and diffusion rates and thus show different tendencies towards or against the development of instabilities controlling the growth rate and the preferred scale of fingers. The problem can be generalized to miscible displacements with two components of the fluid affecting the viscosity being diffused and convected at different rates (known as double diffusive-double convective displacements) [23, 24]. The dynamics of the two fronts are coupled [25] and

may show stability criteria that are not conventionally expected [23]. The early studies on the instability of non-isothermal displacement processes did not start until 2000 [4]. In 2007 Islam and Azaiez developed a model for thermo-viscous fingering in rectilinear geometry and studied the linear stability and nonlinear behavior of the process [26, 22, 27]. In Chapter 3 an extension to the previous studies is presented analyzing the effect of different stability properties of the thermal and solutal fronts through numerical solution of the nonlinear equations. A larger variety of thermal and solutal log mobility ratios are examined for different relative diffusion rates and the results are analysed based on their sweep efficiency and breakthrough times.

In addition to viscous forces the effect of the permeability distribution in the porous medium on the stability of the displacement is also studied in this work. In real porous media the permeability distributes in a random manner and the heterogeneity affects the validity of the results obtained for homogeneous media. The interactions between viscous instabilities (including TVF) and heterogeneity driven instability (also called channeling) have been an interesting subject for researchers for many years due to the extensive application of these studies in industrial displacement processes. But the vast study on this problem is not only due to its applicability and rather stems from the complexity of the mechanisms affecting the dynamics of the flow and the front patterns. Different flow regimes have been observed for different parameter values and attempts to derive a single descriptive parameter that can categorize different scenarios in the dominant flow regimes have only been partially successful using empirical correlations. In Chapter 4 a systematic examination of the flow instability in viscously unstable displacements in layered porous media is presented that leads to unification of the trends with the use of a new dimensionless group. The application of the unifying group in up-scaling and design of displacement processes in oil and gas recovery is presented in Appendix A.

Although in most of the named applications the porous medium is static, there are natural phenomena and some industrial applications that deal with a form of heterogeneity that evolves through the progress of the displacement process. This form of heterogeneity can be called dynamic heterogeneity. There are different mechanisms that can lead to dynamic heterogeneity like precipitation/dissolution of the minerals or melting/freezing inside the pores of the medium. Examples of natural and industrial phenomena that experience such an evolving heterogeneity include melting of sea ice, melting of the ice in artificially or naturally frozen ground, melting of the rocks due to flow of magma, precipitation of minerals in geothermal processes, and melting of bitumen at the advancing edge of the steam chamber in processes such as SAGD, VAPEX, SA-SAGD and so on. The system that is modeled in Chapters 5 and 6 consists of a porous medium being partially saturated with a frozen material that is distributed homogeneously in the medium. The rest of the pores are saturated with the melt or a fluid fully miscible with the melted form of the frozen material. Injection of a hot fluid miscible with the inhabitant one starts the displacement process which is prone to viscous instability on both thermal and solutal fronts. The heat of the fluid melts down the frozen material in the regions flooded by hot fluid and the melting introduces new mechanisms to the flow dynamics. First, spending the heat on melting defines a new profile for the thermal front that is mostly controlled by the melting parameters rather than the convection-diffusion equations. Secondly, the melt that joins the flow dilutes the fluid and reduces the concentration at the melting region resulting in formation of two concentration fronts: one at the melting region and the second ahead of the melting front in the frozen region where the injected fluid is being convected and diffused into the inhabitant fluid. The third new mechanism is the increase of permeability of the medium in the regions experiencing melting (hence the dynamic heterogeneity) that results in increase of the flow through those regions and further enhancement of melting. The dynamic heterogeneity

that is produced by viscous fingers and yet like in static heterogeneous media guides the instabilities and contributes to the flow instability is a new concept that has been explored in this work. The defined problem considering the flow of hot fluid through the frozen region and the development of instabilities in this system have not been studied in any other works before and therefore Chapter 5 deals with the fundamental aspects of the problem in the absence of the destabilizing mechanisms. At the end of the chapter the frozen region is introduced to the medium as frozen blocks confined within the simulated domain that allow the bypass of the frozen region. This new configuration is similar to the studies that assume the flow to happen around an unpermeable frozen block. In Chapter 6 the instability of the flow in melting media is investigated.

Before closing this chapter, it needs to be mentioned that this is a paper based dissertation consisting of published or under review journal manuscripts. So, parts of the introduction, the reviewed articles, and the mathematical models are repeated throughout the chapters. In particular, the sections of Chapter 6 describing the model and the numerical methods (Sections 6.2 and 6.3) can be skipped due to close similarity to the corresponding sections in Chapter 5. At the first page of each chapter the corresponding article is referred to in the footnotes. Appendix A is a conference paper presented in SPE conference on the application of the ideas in Chapter 4 in oil industry. Appendix B describes the scaling that unifies melting processes with different heat transfer coefficients, amended to Chapter 6.

# Chapter 2

# Review of the Background

---

The review of the studies related to the research work presented in this dissertation consists of three main sections. The first section corresponds to the studies on viscous fingering (VF) and thermo-viscous fingering (TVF). The second section elaborates on the studies on the flow instabilities in heterogeneous porous media. The final section of this survey is dedicated to the studies dealing with the melting and dynamic porosity in porous media.

## 2.1 Thermo-Viscous Fingering in Homogeneous Porous Media

Flow displacements in porous media have been the subject of numerous studies due to their importance in many processes such as enhanced oil recovery, solute transport in aquifers, filtration, carbon dioxide sequestration, determination of pore size distribution of catalysts for reactors, and packed bed regeneration. In practice, the viscous fingering instability which occurs when a high-viscosity fluid is displaced by a low-viscosity one, results in early breakthrough and reduction of efficiency of the displacement process. This instability appears in the form of finger-shaped penetrations of the displacing fluid into the displaced one, commonly referred to as fingering or Saffman-Taylor instability [5, 6, 28]. Although this form of instability is named after Taylor and Saffman, the first study on viscous fingering was carried by Hill [5]. The paper by Hill in 1952, regarded as the pioneering work on viscous fingering, included linear stability analysis and experimental work on the coupling of density

fingering and viscous fingering. It was only in the late 1950's that Saffman and Taylor [6, 29] and Chuoke et al. [30] performed linear stability analyses on one-dimensional displacements. Saffman and Taylor also carried out some immiscible displacement tests in a rectangular Hele-Shaw cell and published their now-classical papers. Since then, viscous fingering has been extensively investigated through linear stability analysis, nonlinear simulations, and experimental measurements.

Due to the large amount of work on viscous fingering, a brief overview of the studies in this field is brought in this introductory section and more detailed review of the literature is devoted to the main focus of this section, namely thermo viscous fingering (TVF). Also because the literature on viscous fingering is very diverse with respect to the geometry and assumptions applied to the models and experiments, this survey will not cover some of the works concerned with other aspects of instabilities observed in displacement processes. Research studies dealing with non-Newtonian fluids, or other mechanisms of instability such as gravity fingering or reaction driven systems will not be covered in the present review. For extensive reviews on fingering instability, one may consult the seminal work of Homsy (1987) [1] which has covered most of the early literature on isothermal miscible and immiscible viscous fingering as well as that of McCloud and Maher (1995) [2] who has focused on experimental studies for isothermal flows.

### 2.1.1 Instabilities in Isothermal Displacements

The early studies dealing with viscous fingering considered immiscible displacements in which surface tension results in a sharp interface between the injected and the displaced fluids. The first nonlinear simulation involving miscible displacements was carried out by Peaceman and Rachford in 1962 [31] who used the finite difference method for the computation of instabilities in a heterogeneous porous medium with rectilinear geometry. In 1969 Wooding [32]

carried out experimental studies by visualizing fingering patterns in a Hele-Shaw cell through X-ray absorption technique. By comparing the finger patterns with the results of similar experiments in porous media reported by Slobod and Thomas (1963) [33], Wooding justified the use of the Hele-Shaw geometry for analysing viscous fingering instabilities. According to these findings, the Hele-Shaw cell geometry was able to mimic the fingering phenomenon in porous media. This simplification of the geometry made the experiments easier to carry out and facilitated focusing of the experiments on the effect of isolated parameters. More advancement in numerical simulation was achieved by using spectral methods in modeling the instability. Tan and Homsy [8] proposed a spectral method based on the Fourier transform to model viscous fingering of a miscible flow in a rectilinear Hele-Shaw cell. These simulations were able to capture the mechanisms of instability such as *shielding, spreading*, and *tip splitting*, observed by Wooding and Morel-Seytoux [34] through miscible displacement experiments in porous media. Later in 1992 Zimmerman and Homsy using the spectral methods, showed the consistency of the results of $3D$ simulation with those of $2D$ simulations [35]. These findings justified simulation of the $3D$ phenomenon of viscous fingering in porous media using a $2D$ displacement model of the flow in a Hele-Shaw cell.

Although in this research we focus on nonlinear simulations of TVF, a brief review on stability analyses of miscible displacement processes will be also presented to illuminate the characteristics of these instabilities. Linear stability analysis allows to determine the growth rate of each disturbance wavelength through linearization of the governing equations. Tan and Homsy [7, 36] were the first to present a thorough and detailed study of the linear stability of viscous fingering in isothermal miscible displacements. These authors adopted the quasi-steady-state approximation (QSSA) where the growth rate of the perturbations is assumed to be asymptotically larger than the rate of changes in the base state. This assumption allowed them to determine the most dangerous wavelength at each time step,

and was justified by the authors through initial value calculations. However, QSSA method has recently been questioned by Ben et al. [37] for sharp base state profiles at the onset of the flow. Also recently the stability studies of different displacement scenarios by Kim and Choi [38, 39] have shown that the validity of QSSA is questionable for small values of $t_0$ and that the results from QSSA method are identical to those of the eigenanalysis. Nevertheless there have been many subsequent stability analyses that have adopted QSSA. These include but are not limited to studying the characteristics of instabilities in displacements with non-monotonic viscosity profiles (Manickam and Homsy [40]), and studying the effects of non-Newtonian behavior in the involved fluids (Azaiez and Singh [12]). In general the linear stability analyses on miscible displacements have lead to the following conclusions:

- If the mobility ratio is unfavorable, perturbations with long wave lengths grow faster;
- Shallow gradient of viscosity mitigates the viscous instability;
- Disturbances with a wave number higher than a cut-off value vanish due to transverse dispersion.

As mentioned earlier, there has been a growing interest in the viscous fingering instability when it is coupled with heat transfer. This interest which has been mainly motivated by its application in thermal recovery in oil industry, has resulted in a great wealth of information. In the following section a brief review of these investigations is presented.

### 2.1.2 Instabilities in Non-Isothermal Displacements

In non-isothermal displacement processes the viscosity of the fluids may vary with the concentration of the solvent as well as the temperature of the fluids. This results in a nonlinear instability that has been referred to as thermo-viscous fingering [25, 41]. Due to differences in the rates of transport of heat and mass, thermo-viscous fingering involves two fronts, the

first being the concentration front and the second the thermal front [22, 27]. It has been observed that fingering on each of these fronts can contribute to the instability of the flow and the rate of growth of the fingers depends on both effects [25].

As mentioned before, thermal displacements are encountered in many oil recovery applications such as hot water flooding, steam flooding, cyclic steam stimulation (CSS), and steam assisted gravity drainage (SAGD), most of which are based on the injection of steam. Therefore existing experimental studies on thermo- viscous fingering have mostly focused on steam flooding due to its wide applications in oil recovery. In steam-based recovery processes, the steam -fluid interface shows different instability mechanisms than those observed in hot water flooding [42] or solvent flooding. In steam based processes, heat loss to the surroundings is enhanced in the steam fingers due to extended contact area, and phase change occurs inside the fingers. As a result the steam becomes liquid and its viscosity increases drastically resulting in the attenuation or disappearance of the finger. Hence, although steam flooding experiments fall under non-isothermal displacements, they will not be included in the present literature review due to the irrelevance of the mechanisms of instabilities in such processes to the problem of interest.

In what follows, studies dealing with miscible and immiscible non-isothermal displacements are discussed. The review will first examine briefly the case of pure thermal displacements where only one single fluid is involved and then extends to displacements involving two fluids. Though important, the studies on thermal recovery processes using commercial simulators, carried out for a large number of projects dealing with heavy oil and bitumen recovery [43, 44, 45] are not included in the present literature review as they have not focused on the flow instability per se, and are not directly relevant to the proposed research.

Special cases of thermo-viscous fingering in which the injected and the displaced fluids have similar compositions but different temperatures can be observed in phenomena such as

flow of magma through dikes and fissures in eruption of fissures [46] and the flow of injected melt in injection molding processes. Few studies dealing with TVF have focused exclusively on pure thermal displacements. One example would be the experimental measurements conducted by Kuang and Maxworthy [47] in which a fluid at a high temperature was injected in a cylindrical capillary tube to displace the same fluid at a lower temperature. The study allowed to identify three front stability regimes based on the injection flow rate. For lower injection rates the flow was diffusion dominated whereas for high injection rates the flow was viscously dominated. These two regimes were separated by a medium injection-rates regime that allowed for a transition between diffusion and viscous regimes. Although in these experiments the stability was studied as a function of the flow rate, the analytical studies and numerical simulations have shown that changing the injection rate does not affect the intrinsic stability conditions of the flow and affects only the growth rate of fingers [22, 23]. Holloway and deBruyn [48, 49] also examined the 3D instability of a displacement involving hot glycerin injected to displace cold glycerin in a radial Hele- Shaw cell. Their studies involved both experiments and numerical simulations using FLUENT$^{TM}$. The authors found that the fingering instability required a minimum initial viscosity ratio and a minimum injection rate to develop in radial geometry. The wavelength of these instabilities had a slight dependence on the width of the cell but none on the injection rate or the viscosity contrast.

The vast majority of TVF studies involved displacements in which both mass and heat were transported. These works are discussed next in chronological order. The first numerical study to model non-isothermal miscible displacements with consideration of double diffusive convection in the system was the finite element based work of Saghir et al. [4]. The vertical displacement of glycerin with water at constant flow rate and evolution of thermo-viscous fingers were analyzed through numerical simulations and experiments. Despite the adverse mobility ratio 1485, the model actually failed to reproduce the expected complex instabilities

in the system. Inaccuracy of the numerical scheme and inclusion of many different factors influencing the instabilities such as, thermal effects, solutal effects, and gravity may have contributed to the failure of the simulations to reveal the finger structures.

In another study, Sheorey et al. [50] conducted numerical experiments on simulation of *immiscible* displacements in isothermal and non-isothermal conditions using a finite difference scheme and operator-splitting algorithm. Although their numerical simulations encountered oscillations in laterally averaged saturation profiles due to a number of inaccuracies in the calculation process, in a subsequent experimental study still involving immiscible fluids Sheorey et al. [51] were able to obtain conclusive and interesting results in regards to non-isothermal displacements. The study revealed the stabilizing effects of heat transfer in the displacing processes that allowed for high recovery during non-isothermal injections of water in a 5 spot pattern geometry.

In 2004, the first linear stability analysis for non-isothermal *miscible* displacements was conducted by Pritchard [25] for a displacement in a homogeneous porous medium with radial geometry. The author considered two moving fronts and found that viscous fingering instability on any of the two fronts can induce perturbations on the other one and affect the dynamics of its instability. The stability analysis in this work followed the approach of Ben et al. [37] and was based on an expansion of perturbations in terms of eigenfunctions. Pritchard pointed out that the fluid front controlled the instability i.e. growth rate of fingers and their wavelengths when both solutal and thermal log mobility ratios were positive. The reason that the solutal front lead the instability was attributed to the higher Péclet number for solute diffusion compared to thermal diffusion. For a flow with small lag between the fronts and high thermal mobility ratio, the thermal front had more influence on fingers' characteristics. In 2009 Pritchard [52] performed another study on stability of double diffusive miscible displacements in a rectilinear Hele-Shaw cell still adopting the method by Ben et al. [37]

based on a spectral approach to obtain asymptotic response to long wave perturbations. In a Hele-Shaw cell the flow does not experience heat exchange with the medium like what happens in porous media and both of the two fronts travel at the same advancement rate. For such a case, the only parameter that makes a double diffusive displacement different from a simple isothermal displacement is the higher diffusion rate of heat compared to concentration. Pritchard determined the growth rate and boundaries of instability at different times scales and different diffusion ratios. The main conclusion of this work was that the stability of double-diffusive miscible displacements cannot be simply predicted using viscosity gradient analysis and not even using the stability analysis methods based on early time behavior of the system. The author also commented on the the stability properties of the defined system to be distinct from those of non-monotonic single species displacements.

The first successful nonlinear simulation of thermo-viscous fingering through which the known mechanisms of fingering instabilities were observed and analysed was conducted by Islam et al. [41]. Non-isothermal miscible displacements were modeled in a two dimensional homogeneous rectilinear porous medium and in a Hele-Shaw geometry where the fluids and solids were assumed to be in thermal equilibrium. The work adopted a spectral method through semi-implicit predictor corrector time stepping scheme along with operator splitting technique. The study accounted for heat loss to the porous medium and was able to capture the gap between the two fronts. For higher diffusion rates of heat and low porosity values (i.e. more heat transferred to the porous medium) the authors observed that the instability was dominated by the solutal front. This result was in agreement with Pritchard's linear stability analysis. Following their previous work, Islam and Azaiez in 2010 [27] performed more detailed analysis of the results of nonlinear simulations. The interface area between the displacing and the displaced fluid was used to quantify the complexity of the fingers as a measure of the scale of instability. In their analyses the isothermal displacement showed more

instability compared to the same solutal front being accompanied by an unstable thermal front with high diffusion rate. However the sweep efficiency for all isothermal and non-isothermal cases showed similar results which was probably due to the definition of efficiency with respect to a moving reference frame adopted in their study. The authors also examined the instability in quarter five-spot miscible displacements in 2011 [53]. The results they found for enhanced instability of the front at high diffusion ratios when both log mobility ratios were positive was in contrast with what was reported in the rectilinear geometry where increases in thermal diffusion rate resulted in a decrease of instability with respect to the reference isothermal case. Other conclusions of this work were in qualitative agreements with their findings in the rectilinear geometry.

For linear stability analysis of the non-isothermal miscible displacement in homogeneous porous media, Islam and Azaiez [22] used quasi-steady-state approximation (QSSA) and initial value calculation (IVC) approaches. The step -profile approximation method borrowed from [7, 9] was used as an alternative for the numerical method in QSSA approach. In IVC method the initial set of linearized equations were solved for the growth rate of individual perturbations. It was found that IVC method could distinguish between instabilities caused by velocity, temperature or composition perturbations and the instability criteria was set based on the highest growth rate of any of these quantities. The short time stability analysis led to the conclusion that for large Lewis numbers, the flow experiences an instability dominated by the concentration variations. Although for the QSSA method the dimensions of the domain needed to be defined, the results revealed to be insensitive to the width of the domain as long as it was wide enough to accommodate all the eigenfunctions. The stability curves plotted based on the QSSA method were qualitatively similar to those found using the step profile approximation but showed the effect of thermal log mobility ratio less significantly. The results of IVC method on the other hand were similar to QSSA method

for unit diffusion ratio (i.e. when rate of diffusion of both parameters were assumed to be the same) but showed different trends with increase of thermal log mobility ratio for higher diffusion ratios (i.e. higher thermal diffusion rates). This implied that the assumption in the QSSA approach based on a slow rate of diffusion compared to the growth rate of disturbances, is not valid for higher rates of diffusion. The IVC analysis revealed that for flows with high thermal diffusion rate, the instability was attenuated with an increase of thermal log mobility ratio. Islam and Azaiez [22] mentioned that the nonlinear simulations confirm the results of IVC compared to the QSSA method which showed that IVC method was a better approach to capture the characteristics of thermo-viscous fingering instabilities. The work mainly focused on the effect of positive thermal log mobility ratios and did not spend much effort to examine the effect of negative log mobility ratios for any of the fronts.

Stability analysis of double diffusive viscous fingering performed by Mishra et al. [23] for miscible flooding in rectilinear Hele-Shaw geometry looked at the effects of log mobility ratios of the two parameters changing viscosity with different diffusion rates. In terms of the problem configuration and modeling equations, this analysis was similar to that of [52] and can be regarded as a special case of the work of [27] with no gap between the two fronts. However it took a different approach and resulted in a broader stability analysis and more general conclusions. The slow and fast diffusing properties discussed in the mentioned work, can represent concentration and temperature of the fluids and the analysis can be applied to studying thermo-viscous fingering instabilities. The effect of porosity was not included in the study and hence the lag between the two fronts was not actually considered. The viscosity gradient analysis along with linear stability analysis (LSA), formed a stability chart which showed the stability conditions for different values of log mobility ratios and diffusion ratios. It was reported that aside from the zones with increasing viscosity in the flow direction for which instability was trivially expected, the non-monotonically and even

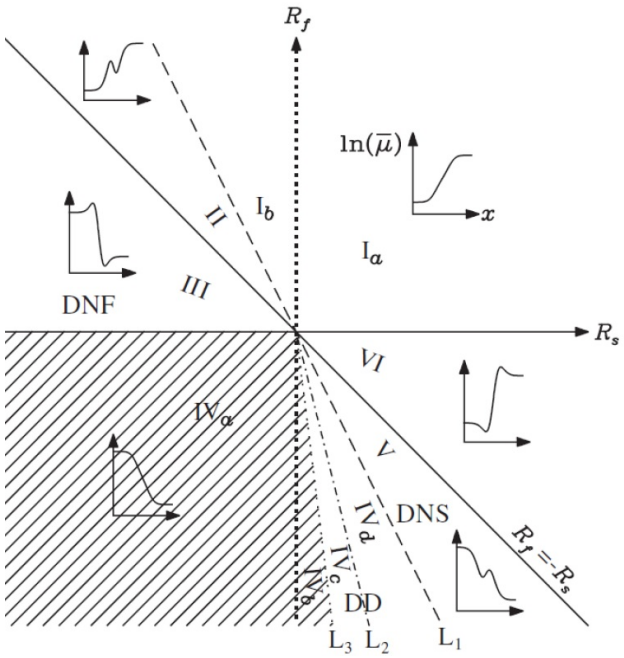


Figure 2.1: Stability criteria defined by Mishra et al. [23]; $R_s$ and $R_f$ are the log mobility ratios corresponding to the effect of slow and fast diffusing properties respectively; The lines $L_n$ $(n = 1\ ,2\ ,3)$ are defined through $R_f = -\delta^{n/2} R_s$, $\delta$ is the diffusion ratio.

monotonically decreasing viscosity profile zones also may experience instability. These zones are shown in Figure 2.1. In their work Mishra et al. showed that negative log mobility ratio did not necessarily correspond to a stable displacement as conventionally expected. For example in the zone with monotonic decrease of viscosity the instability was due to a pure diffusive effect. The authors were able to confirm their findings by capturing the developed instabilities in nonlinear simulations results.

In 2012 Azaiez and Sajjadi [24] relaxed the assumption adopted by Islam and Azaiez that required the thermal and solutal fronts be initially coincident and travel at the same speed and performed a stability analysis on general flow displacements involving two components with different diffusion and convection rates. The stability analysis by Azaiez and Sajjadi [24] using the step-profile approximation and QSSA method accompanied by numerical simulation of the nonlinear problem, could be regarded as a generalization of the previous works

and they recovered the results by Islam and Azaiez [22] and Mishra et al. [23] as special cases of the more general problem.

## 2.2 Coupling of Heterogeneity and Viscous Fingering

The vast majority of studies dealing with the viscous fingering instability, whether thermal or isothermal, have focused on homogeneous porous media. However, in practical applications porous media are actually heterogeneous and the variations in the microstructure of the medium change the permeability at different points. The displacement in a heterogeneous medium involves two mechanisms leading to instability: adverse mobility ratio leading to viscous fingering, and variation of permeability leading to channeling or heterogeneous fingering. In this section a review of the literature studying the coupling between viscous instability and channeling in heterogeneous media is presented.

The first experimental study of miscible displacement in heterogeneous porous media which later became the main reference of many subsequent numerical works was performed by Blackwell et al. in 1959 [54]. In these experiments, the effects of the mobility ratio, and heterogeneity of the medium on the recovery were investigated in stratified porous media. Oil recovery was measured with respect to solvent injection before and after the breakthrough of solvent. The authors noticed that the oil recovery before breakthrough depended primarily on the mobility ratio. It was noted in the paper that this conclusion is not supported by real field applications where the heterogeneity of the reservoir was observed to reduce the recovery compared to homogeneous fields. By injecting a dyed solvent in the channel and recording the solvent/oil interface pattern at different time steps, Blackwell et al. were able to detect early formation of viscous fingers and shielding and coalescence of fingers at later times.

Although such qualitative studies of the flow in heterogeneous media were useful in

comprehending the process, because of its direct application in oil and gas industry, the quantification of the heterogeneity with a single parameter has been an interesting subject for researchers for many years. The Dykstra-Parson's coefficient $V_{DP}$ (proposed in 1950) and Lorenz coefficient $L_C$ (proposed in 1905 [55] and modified for use in petroleum engineering in 1950 [56]) in stratified reservoirs are among the most famous parameters of this type, that mainly consider the range of variations of permeability and the frequency of these variations to describe the severity of the heterogeneity [57]. Though still efficiently used to describe the heterogeneity of the medium, these single factors had shortcomings in representing the whole medium and had to be used in combination with other factors. For example in 1988, Jensen and Lake [58] examined the values of $V_{DP}$ and $L_C$ for different models of permeability distribution and showed that these parameters that were defined for log-normal random permeability distributions, were not sufficient to describe the severity of heterogeneity in media better described by other distribution models. Due to such limitations different forms and modified versions of these factors have been proposed over the years for different heterogeneous media such as non-normal random heterogeneity [58], layered composite reservoirs [59], inclined stratified reservoirs [60], and so on.

The relative importance of heterogeneity (measured by one of these factors) to that of viscous forces (traditionally measured through mobility ratio), has been mostly performed *qualitatively* for constant mobility ratios. Therefore the quantitative measurements that were later proposed by Koval [3], Todd and Longstaff [61], and Fayers [62] became very popular. These 1D methods were based on Buckley-Leverett's theory for miscible displacements, only differing in the definition of the fractional flow functional. Koval's method, in particular, has been successful in calculating the efficiency of the displacement process at and after the breakthrough of solvent at the effluent and has been extensively used for predicting the performance of immiscible and miscible displacements in different unstable oil recovery pro-

cesses. In Koval's method the factor representing viscosity ratio was empirically calculated by matching the experimental data of Blackwell et al. [54] and the heterogeneity factor was defined based on the recovery obtained from injection of one pore volume of solvent in different reservoir rock samples. Although such empirical methods provided reasonably good predictions using simple graphical methods for industrial purposes, they did not investigate the mechanisms of any of the viscous fingering or the channeling phenomena.

In an effort to better understand the mechanisms and other details of the flow in heterogeneous media, two dimensional simulations were developed. The first 2D simulation of displacements in heterogeneous porous media dates back to 1962 when Peaceman and Rachford performed numerical simulations of unidirectional displacements using finite difference method [31]. They validated their simulation results with the previously discussed experiments of Blackwell et al. [54]. Due to low order numerical algorithm and coarse spatial resolution ($4 \times 20$ grid) this work was unable to capture the early growth of fingers and the instability had to be triggered by random variation of permeability in the domain. The delay in initiation and growth of fingers in the simulations compared to the experiments by Blackwell et al., could be attributed to the coarse grid size used by Peaceman and Rachford which did not allow for proper implementation of the adverse mobility ratio responsible for initiation of the instabilities in the model. In 1987 Christie and Bond [63] attempted to improve the finite difference method of Peaceman et al. [31] by refining the grids to $130 \times 130$ meshes. Finer grid size allowed for the incorporation of higher Péclet number and achieving a better agreement with the experimental results of Blackwell et al. [54].

In 1988 Araktingi and Orr [64] employed particle-tracking method to simulate viscous fingering in fully miscible displacements in homogeneous and heterogeneous porous media. The simulation results for the homogeneous media were validated by comparing the recovery rate of the simulated processes with experimental results of Blackwell et al. [54]. Also

the mechanisms observed for viscous fingering were compared to those reported by Homsy [1]. The fingering patterns did not exactly resemble the predictions and the width of the fingers obtained from the model were about 35% larger than that of the corresponding fingers in LSA. These differences were attributed to the non-inclusion of dispersion in LSA which made it applicable only to initial growth of fingers. Araktingi and Orr also compared their simulation results for homogeneous media with Koval's results [3] by taking the transverse average of concentration at different time steps and determining their locations along the flow direction. They found that due to the complexity of the front patterns, different locations may have the same average concentration which makes the assumption of a single characteristic velocity for each concentration value inexact. The deviation from Koval's assumption was less critical for concentration values near the edges of the concentration range (i.e. $C = 0.1$ and $C = 0.9$) which showed that Koval's technique might be useful for predicting breakthrough time and recovery using the velocities of the ends of the mixing zone.

In the analysis of the effect of heterogeneity on instability, the authors used the correlation length and variance of permeability distribution, which was constructed as a random variable with log-normal distribution, to define the characteristics of the heterogeneity of the porous medium. Araktingi and Orr categorized the instability behavior based on the value of a heterogeneity index (HI) (first introduced by Gelhar and Axness [65]) to show the dominance of heterogeneity or viscosity. They found that in porous media with high $HI$ the finger patterns were led by the permeability variations and did not change with changes in the mobility ratio. Whereas for small $HI$ corresponding to little variation of permeability or small correlation between high permeable zones, the fingering patterns were similar to those in homogeneous media. One of the shortcomings of this analysis was that the effects of the mobility ratio and the flow rate were not considered in the definition of $HI$ and as Chen and

Meiburg [66] later showed, the proposed index did not represent all of the characteristics of the porous medium affecting the instability. In a similar but more systematic analysis towards the characterization of different heterogeneous media based on the dominant flow regimes, Waggoner et al. [67] examined miscible displacements in stratified media by performing numerical simulations for different mobility ratios. The heterogeneous media were generated with different values of Dykstra-Parson's coefficient $V_{DP}$ and correlation lengths of permeability $l_D$. Visual study of the instability patterns and the growth rate of the mixing zone revealed three flow regimes described as fingering, dispersive, and channeling. The fingering and channeling regimes were similarly observed by Araktingi and Orr for small and large $HI$ values respectively but the dispersive flow which showed no significant form of instability was first introduced by Waggoner et al. [67]. According to their results for correlation lengths smaller than a critical value, the heterogeneity of the medium worked towards increasing the effective dispersion coefficient rather than creating bypassing fingers. Media with larger $V_{DP}$ tolerated less dispersivity and would show channeling behavior for smaller $l_D$ values. Larger mobility ratios enhanced the development of fingers even in the channeling regime and reduced the extension of the dispersive regime. The simulated scenarios were categorized by their dominating flow regimes and the results were presented on $l_D$ versus $V_{DP}$ plots for different mobility ratios (Figure 2.2). The authors showed that the lines separating the flow regimes for a constant mobility ratio could be described by constant $HI$ values and thus found the parameter suited for categorization of the flow regimes in heterogeneous media.

Following their earlier works and using the same method of simulation, Tchelepi and Orr [68] examined the correlation between dispersion and permeability heterogeneity in miscible displacements and compared their simulation results with 3D experimental flow instabilities. An analysis of the dispersivity at small mobility ratios showed that although for stable

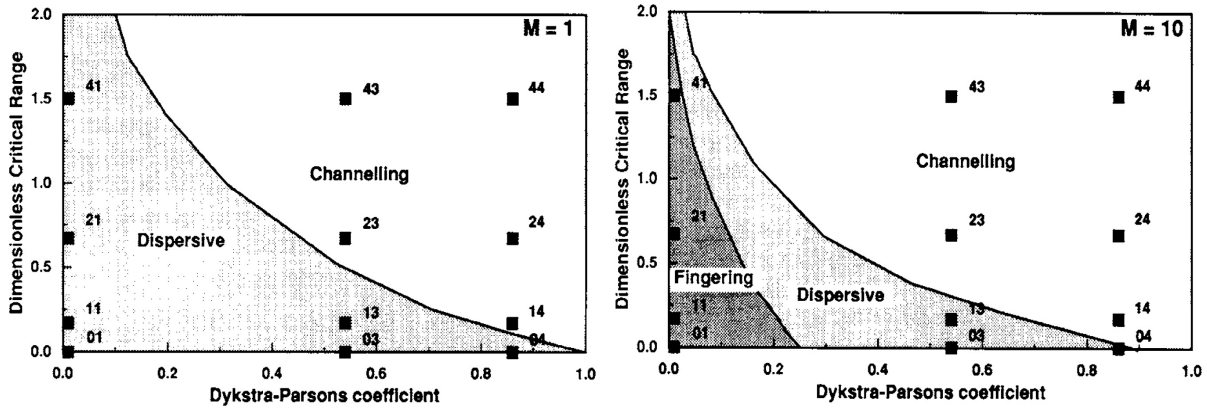


Figure 2.2: Critical ranges: (a) M = 1, line separates channeling and dispersive regions, and (b) at M = 10, lines separate channeling and dispersive regions and dispersive and fingering regions [67].

flow in homogeneous media the length of the mixing zone was independent of the value of the mobility ratio (as long as it was smaller than unity), in heterogeneous media a smaller mobility ratio could suppress the influence of heterogeneity. Although in that sense the dispersive flow regime was recognized, all the analyzed cases were limited to favorable mobility ratios and did not necessarily show the contribution of heterogeneity to the appearance of the dispersive regime. Their numerical experiments on a highly correlated heterogeneous medium showing that the medium would not allow dispersive flow even for small mobility ratios as low as 0.04 was qualitatively in agreement with the results of Waggoner et al. [67]. They also found that the two dimensional simulations were able to represent unstable three dimensional flow in homogeneous and randomly distributed heterogeneous porous media as long as the heterogeneity in the third dimension was not significant.

Viscous fingering in porous media with random permeability distribution was further studied by Tan and Homsy in 1992 [69] through nonlinear simulation of the flow using spectral method. Shinozuka's analytical scheme [70] for realization of a random permeability field with Gaussian log distribution was incorporated in their model. Again the correlation length and variance of the distribution were used to characterize the permeability field. For a

fixed correlation length, their conclusions were in agreement with Araktingi and Orr's results showing that larger variance of permeability resulted in dominated heterogeneous channeling and increased instability. However variation of the length of the mixing zone with the correlation length was shown to be non-monotonic. The optimum correlation length which resulted in enhanced propagation of fingers was of the same scale as viscous fingers growing in homogeneous media in a flow with the same Péclet number. This suggested a resonance between viscous fingering and heterogeneity instability with commensurate intrinsic length scales. Furthermore, the nonlinear simulations of the flow in a randomly distributed permeability model at fixed Péclet number and variable log mobility ratios showed that the path the fingers chose to grow in, was dictated by the high permeable regions of the field whereas nonlinear dynamics and therefore the growth rate of the fingers were dominated and governed by the pressure fields due to mobility variations [69]. This description applies to displacements with unfavorable mobility ratios showing channeling flow regime (e.g. cases 23,24,43 and 44 in Figure 2.2b).

Tan and Homsy's theory of resonance between intrinsic wavelengths of the system and those of the heterogeneity were in agreement with the experiments of Fernandez et al. [71]. Using magnetic resonance imaging, Fernandez et al. were successful in obtaining 3D visualization of viscous fingers and providing some qualitative analysis of the effects of heterogeneity in chromatographic columns. Their qualitative analysis also confirmed the findings of Tan and Homsy showing that for lower mobility ratios the patterns of the instability were mainly defined by permeability variations but the growth of the fingers depended on the mobility ratio and other parameters affecting the dynamics of viscous fingering. The uncontrolled heterogeneity and the small size of the samples in the experiments by Fernandez et al. did not allow for a thorough analysis of the effect of heterogeneity and the observation of typical mechanisms of viscous fingering.

In two related studies, De Wit and Homsy [72, 73] performed nonlinear simulations and linear stability analysis of miscible displacements in media with spatially periodic heterogeneity. The linear stability analysis showed that the growth rate of viscous fingers change by a correction factor, a function of the mobility ratio and the permeability field's axial wave number, due to the resonance between wave numbers of the permeability field and those of the intrinsic viscous fingers. The dominance of viscous fingering or channeling in different processes was determined by studying the mixing zone length, with a linear growth for viscously unstable flows in homogeneous media and a growth rate of $\sqrt{t}$ for viscously stable ones in heterogeneous media [69, 72]. It was found that for a layered system, the flow in more permeable layers had a quasi-homogeneous trend. The resonance theory proposed by Tan and Homsy was again tested in layered media and was found to comply with the results of the linear stability analysis.

The method used by Tan and Homsy for the realization of a random permeability field set the base for further investigations by other researchers. Chen and Meiburg in 1998 [66] adopted the same correlation to generate a random permeability field in their extensive investigation of miscible displacements in the quarter five-spot configuration. In their work the relative contribution of viscosity and permeability to vorticity were considered as the indicator of the preponderance of any of these mechanisms. The resonance between the heterogeneity and mobility driven instabilities was elaborated on by comparing the variations of the front thickness with the correlation length of the porous medium and was shown to lead to lower recovery at the breakthrough. The investigations by Chen and Meiburg confirmed the previous results regarding the effect of the variance of permeability distribution on instability, but the effect was found to be more pronounced for some parameter regimes than others. It was also found that small correlation lengths and high diffusion rates, result in the heterogeneity to be weakened and the medium to appear homogeneous to the flow.

The same could apply to the flow in media with very large correlation scales which would have the same recovery as a homogeneous medium. Chen and Meiburg also examined the applicability of the heterogeneity index defined by Araktingi and Orr [64] in reducing the number of independent parameters when defining the regime of instability. They found that this parameter was not well suited for this purpose and there were other parameters (such as the mobility ratio or the diffusion rate) involved in this characterization.

Some of the studies on viscous fingering in heterogeneous porous media were based on the fractal nature of viscous fingering. In these studies, the porous medium was defined as a combination of pores and throats where pores had a constant size while the radii of the throats were randomly distributed in the medium. The flow in the designed network was calculated by solving Darcy's equation for flow in throats and material balance in pores. Ferer and his coworkers used this method to analyze the effect of heterogeneity of the medium on flow stability by characterizing the heterogeneity through the coefficient of variation (the square root of variance over the mean throat area) [74, 75, 76]. Qualitative observations of these studies agreed with the findings of other methods showing that viscous fingering was more independent of the heterogeneity for flows with higher mobility ratio. Although such studies shed light on some aspects of viscous fingering, the studies were limited to non-correlated porous media and therefore the interaction between channeling and viscous instability was actually not considered.

## 2.3 Melting and Flow Dynamics in Media with Changing Porosity

The model that will be analyzed in Chapters 4 and 5 deals with a dynamic change of the porosity and the permeability of the porous medium with the advancement of the fluid. The change occurs due to melting of the solid material (frozen phase) clogging parts of the matrix. So both thermo-viscous fingering and heterogeneity induced instability are expected to

be involved in this process but with some differences from the previously discussed systems. The heterogeneity in this model develops as a result of the formation of thermal fingers that melt the frozen material on their way and form high permeability regions. Therefore the interactions are expected to be more complex than the discussed thermo-viscous fingering in heterogeneous porous media. This phenomenon (i.e. dynamic variation of permeability with fluid flow) that couples different sources of instability in a dynamic manner is observed in different natural and industrial displacement processes from flow of magma, flow of underground water through frozen soil, and melting of sea ice, to effluent disposal [77] and oil reservoir extraction [78]. Despite the diverse applicability of the proposed model in different fields, there is a lack of directly related articles with the same scope, and the review of literature is inevitably dedicated to the mentioned applications. The similarities and differences between the model we have adopted and these studies are stressed whenever possible for a better understanding of the model used in our work.

### 2.3.1 Melting of Ice in Porous Media

Melting of ice in porous media has been the subject of many studies in different fields from hydro-mechanics to thermodynamics and geological studies. One of the applications of this model is in the study of the melting of sea ice as a porous medium. Sea ice forms on the surface of cold waters (especially in Arctic and Antarctic oceans) and reduces the heating of the oceans through solar radiations (see Figure 2.3). Sea ice is a habitat for microbial communities and is even deemed to be able to filter open waters by entraining oil and other buoyant pollutants in its pores [79]. The one year old sea ice has around 10 to 15% porosity with an average thickness of 1.5 m [79, 80] (Figure 2.4). During warm seasons water absorbs orders of magnitude more heat than ice from solar heating due to albedo effect (more radiation absorbency) and the heated sea water plays an important role in the

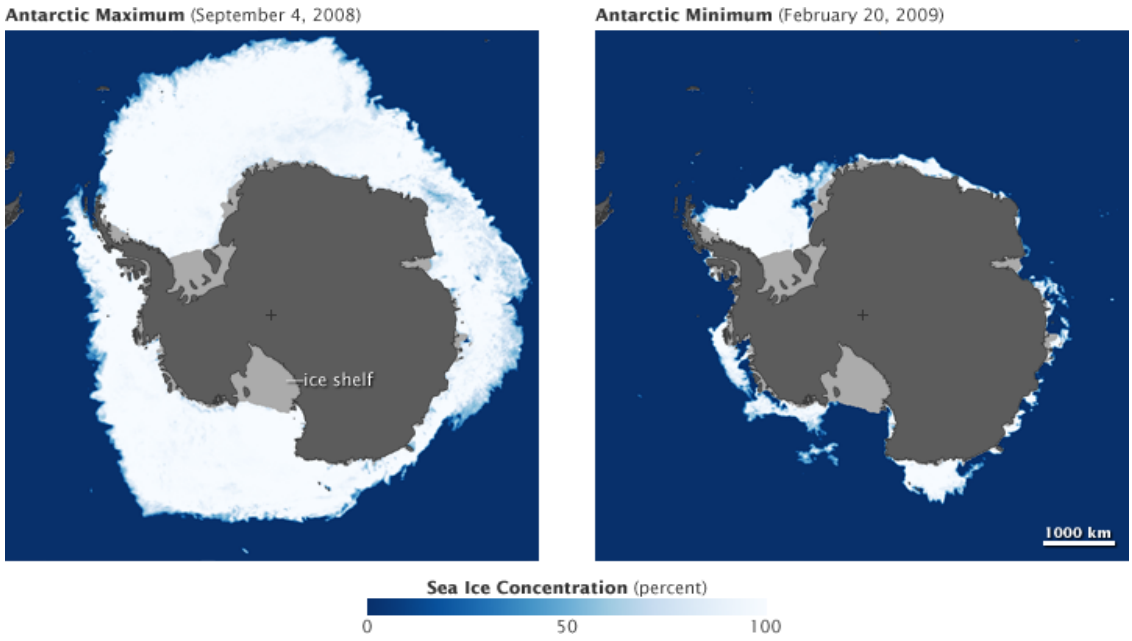


Figure 2.3: Antarctic sea ice melting between September 2008 and February 2009; Courtesy of the National Snow and Ice Data Center, University of Colorado, Boulder, Colorado.

melting of sea ice [81, 82]. According to the described physics of this phenomenon, the flow of water through porous ice may have a comparable contribution to the heat transfer and the melting process as the flow of water around the ice plate does. However, the dynamics of sea ice melting considering the effect of its porosity on the rate of melting have not been modeled and the attributed studies consider the heat exchange to happen only at the ice plates' boundaries.

In sea ice, the porous medium is built with ice and there are only two phases involved. But in some other ice-melting problems such as artificial ground freezing (AGF) extensively used in tunneling, landslide stabilization, mining, and containment of hazardous waste [84] and also in natural permafrost degradation that affects the performance of structures in these regions [85], a third phase building the structure of the porous medium is present (Figure 2.5). The soil (the third phase) is involved in the distribution of energy, fluid, and the frozen material. Conceptually the water in the under-saturated soil occupies the volume

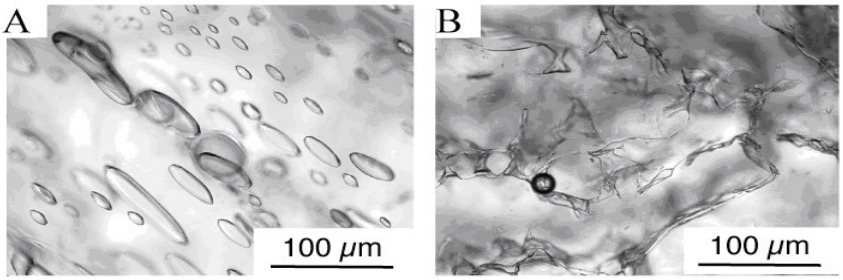


Figure 2.4: (A) Microscopic photographs depicting brine pores of laboratory-grown, organic-free sea ice, (B) ice grown in the presence of organic materials that sculpt the brine pores [83].

between the particles and the water network is interconnected by thin liquid films on particle surfaces [86]. Liquid transfer in the soil takes place through these films. Yet the process of water movement is altered considerably by the presence of the ice phase as freezing (and thawing) results in heat and mass transfer from warm regions to cold regions [87]. With the progress of freezing, the salinity of the liquid films increases, and thus their freezing temperature decreases. The electrical and thermal gradients in the soil provide the driving force for transport of water in the soil [88]. So in general the flow of fluid in between the soil and ice particles happens through different mechanisms than the forced convection discussed in our model. Yet there are natural situations in which the convective heat transfer to the flowing water cannot be neglected. For example in water saturated layers of ground with large porosity, the convective heat transfer by the flow of groundwater plays an important role in melting of frozen jackets during AGF [89]. But even the studies dealing with such cases assume the water flow to happen in the unfrozen region and use Stefan's boundary conditions for the interface between the frozen zone and the melted region [90, 89]. The definition of the problem and the impermeability of the frozen region except for the narrow melting zone, along with the prominent role of density variation in such natural convection problems, make them inherently different from the proposed problem in the present work and the results cannot be interpreted or be compared between these models. The lack of

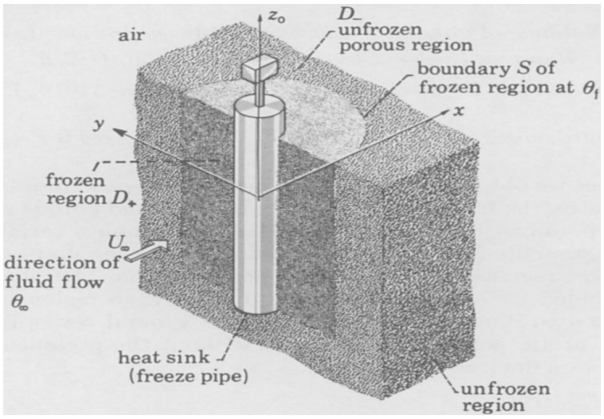


Figure 2.5: Configurations of a single pipe frozen ground;[90].

interest in complication of the problem of melting with the inclusion of convection through the frozen region may be understandable for field size models. But even in most of the classic thermodynamic works studying melting of ice in a porous medium, the fluid is only in contact with ice on its walls [91, 92, 93] and the flow is caused by natural convection in the fluid filled region. For example in 1986 Kazmierczak et al. [94] considered the melting of a phase change material in a confined porous medium heated at one end by the application of a constant temperature boundary condition. Their analytical work was one of the many similar studies in this area. The study found a similarity solution for the natural convection in the boundary layer near the solid-fluid interface and showed the profound effect of Stefan number on the rates of melting and heat transfer. In 1988 Jany and Bejan [95] looked at the same problem in the limit of vanishing Stefan numbers and relying on numerical experiments and scale analysis, they found a sequence of these characteristic regimes for the melting process: *(i)* conduction, *(ii)* mixed conduction and convection, and *(iii)* convection. In 1989 Bejan [92] proposed a purely analytical treatment of the problem that could describe the three-regime sequence of the transient heating and melting phenomena. The rate of melting and the distribution of temperature inside the fluid were found as functions of the Stefan number.

In an experimental and numerical study in 1990, Chellaiah and Viskanta examined the

melting process and temperature distribution in a glass bead porous medium saturated with a frozen material [93]. The modeling of this work which was done by Beckermann and Viskanta in 1988 [96] was among the rare models that considered a melting region in which there was no thermal equilibrium between the liquid and the frozen phase, by adopting a mean temperature within a small interval around the fusion temperature. In other words the liquid and frozen phases were allowed to coexist in a volume element. The volume fraction of liquid in the element was assumed to vary linearly with the element's temperature difference from the fusion temperature. Chellaiah and Viskanta came to the same conclusion as [95] that the melting at first was dominated by conduction and as times passed, the effect of natural convection became more important. Although the energy equations of Beckermann and Viskanta's model are very close to our model, the range of temperature at the melting zone and the correlation between the porosity and temperature were imposed independently of the specific physical situation. These assumptions were shown not to have any significant effects on the distribution of temperature and the location of the melting wall. Yet the small range of Stefan numbers used in the simulations and experiments (Ste $= 0.05 - 0.4$) may have affected the insensitivity of the results to the chosen functionals.

### 2.3.2 Flow of Magma and Precipitation-Dissolution Problems

Viscous fingering and variation of the porous medium have also been observed and studied in flow of magma and problems related to geothermal energy [97, 98, 99, 100, 101] (Figure 2.6). The porous medium in these models is deformable and expands or compacts in response to variations of the fluid flux. Even in the models describing flow of magma that do not consider the medium's response to pressure variations, a velocity vector is assigned to the solid particles of the medium [99]. The elasticity of the porous medium which interacts with the dependence of fluid flux on porosity and produces porosity waves in the medium

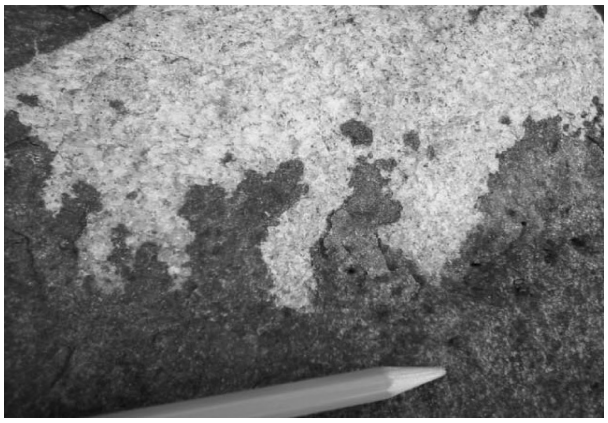

Figure 2.6: Viscous fingering during replenishment of felsic magma [101].

[100], the possibility for different physical phenomena such as fluidization to happen during the process, the involvement of different minerals in the solid and fluid phases due to their different origins, and inadequate knowledge of the mechanical and thermal properties of rocks at such high temperatures make these problems complicated and hard to analyze without simplifying assumptions [98]. Similar to other geological problems, the gravitational force is an important factor in defining the pressure field. The proposed model in chapters 4 and 5 lacks many of the details involved in the problem of flow of magma and only general qualitative results may be applicable in explaining some of the behaviors. Although the melting process in the magma flow is not very close to our problem, the other aspect which is the variation of porosity with precipitation/dissolution of a solid phase in the porous medium does consider the interactions between the flow dynamics and the changes in the permeability of the medium. Precipitation/dissolution of the solid phase that occurs in magma flows is also encountered in other geological settings [102, 103]. Infilling or infiltration of pore spaces, resulting in porosity reduction or formation of worm holes respectively, produce pockets of high porosity and induce a heterogeneity in the domain (Figure 2.7). The flow dynamics in addition to the chemical kinetics of precipitation/dissolution are important factors in determining the patterns of porosity and mineral distribution [104]. In addition

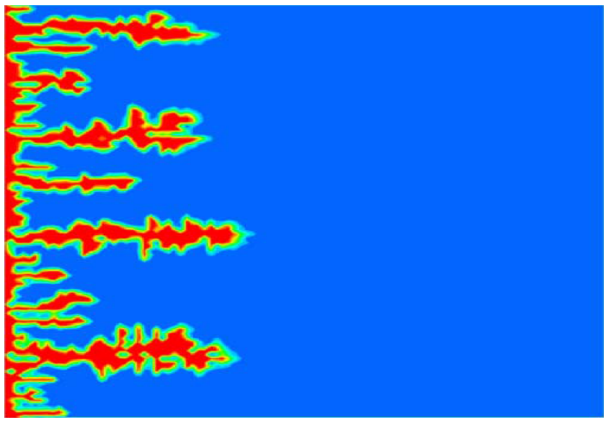

Figure 2.7: Formation of worm holes in homogeneous porous media due to infiltration of fluids in carbonate rocks [109].

to changes of porosity and permeability in the medium during reactive transport processes, the structure of the pore and consequently the porosity-permeability relationship was shown to be changed [105]. Accounting for such variations required pore scale modeling of crystal growth and accurate description of precipitation in porous media. While attempts have been made to verify the geometrical models proposed for the variations of porosity, permeability and the specific surface area of particular rock types [106, 107, 108], data concerning a wide range of rocks and reactions remain very limited. Mineral deposition takes place as the fluid becomes supersaturated with a specific component. Supersaturation may occur through changes in the fluid pressure and temperature, dissolution of a mineral in the fluid that results in supersaturation with respect to another mineral, and mixing of two saturated or under-saturated fluids. The dissolution/precipitation caused by temperature gradients have been modeled by Olivella et al. [110] who have examined the sealing effect in radioactive waste disposal in salt rock. The temperature gradients at the unsaturated medium described induced water fluxes from cold regions to hot regions (and vapor flux from hot regions to cold regions) a phenomenon known as *convection by phase change* [110]. This results in the deposition of salt and a reduction of the porosity at the evaporation zone and its

dissolution at the condensation zone. The solid phase was assumed to be mobile in the form of inclusions. The characteristic times corresponding to the transport of different components (dissolved salt, water vapor, and thermal energy) through diffusion/dispersion, advection, and convection were defined. The FE simulation results confirmed the proposed sealing phenomenon at the vicinity of hot regions that shifted the liquid saturated region away from the hot boundary.

The interplay between the chemical and physical aspects of mineral precipitation has been also analyzed for fractured porous media by Emmnuel and Berkowitz [103]. The authors examined the experimental findings of Lee and Morse [111] and Hilgers and Urai [112] that showed the mineral depositions to occur at the inlet of the fractures instead of being distributed along the length of the fractures by the modeling of mixing induced precipitation. Emmanuel and Berkowitz stressed the important role of specific surface area on the deposition patterns and incorporated two different models for this parameter assuming that the porous medium is built of spherical grains [113] or spherical pores [106]. The simulations results showed that even in initially homogeneous systems, the choice of the surface area-porosity function is important and affects the porosity patterns and chemical reactions.

1D analytical solution for the problem of precipitation/dissolution reactions and the resulting changes of porosity in a diffusion process were recently sought by Hayek et al. [102]. The solutions were obtained as traveling waves. The choice of the form of solutions made the admissible boundary conditions limited. The concentration of one of the reactants was fixed in space and time, and the values of the parameters were set at unrealistic ranges. Even in the results, the concentrations at the boundary reached such large values that the porosity could exceed unity. The analytical solutions provided by Hayek et al. had therefore limited applicability in natural systems and the main application was meant for bench marking numerical codes. Comparing the analytical solutions with numerical simulation results for

an explicit and an implicit scheme showed that for reactive transport problems with moderate porosity changes, only implicit schemes produced accurate solutions and explicit schemes did not necessarily converge to the analytical solution [102, 114].

In the described systems the change in porosity and species concentration are correlated in the same manner as in our study except that the effect of convection was mostly neglected in favor of diffusion. In our model, the change in porosity is governed by heat front and although it affects the concentration profile, the porosity does not depend on the concentration. So although melting acts like a dissolution process, it is independent of the concentration value and mass transfer parameters.

### 2.3.3 Heavy Oil Recovery Processes

Another example of melting of frozen material in porous media would be melting of bitumen in heavy oil reservoirs where the inhabitant fluid is immobile and could be deemed frozen at the initial temperature. One of the most successful processes in recovery of bitumen is steam assisted gravity drainage (SAGD) during which the steam is injected in a preheated reservoir through a horizontal well positioned above another horizontal well which produces the water and oil draining from the formed chamber. The growth of the steam chamber is crucial to the success of SAGD processes so much that the process is terminated if the chamber does not reach the expected height at an expected time [115]. So a realistic estimation of the rise rate of the steam chamber is very important in the design of the process. Due to the viscosity and density contrast between the steam and the mobilized bitumen, viscous and gravity fingering is a common phenomenon at the interfaces. The instabilities forming on the walls and the rising front of the chamber are believed to enhance the heat exchange rate between the injected fluid and bitumen and to improve the thermal efficiency of the process. The early models of SAGD process over emphasized the role of fingers in the heat

transfer process which not only resulted in over-estimation of the fingers' lengths but also predicted rise rates much smaller that those obtained from field thermocouple data (Figure 2.8a). For example the model proposed by Butler [116] predicted steam fingers of 3 m length for Athabasca bitumen reservoirs while experimental results (though mostly estimations) did not support such predictions[117, 118]. Later findings focused more on the conductive heat transfer and showed more moderate results for the finger sizes. In 2005 Ito and Ipek [115] discussed the steam fingering in SAGD process based on the numerical history matches of the real field data. The formation of the fingers in this work was mostly attributed to local geomechanical changes of the formation (such as shear failure and dilation) rather than the density difference or the mobility contrast. The authors assumed that the majority of the condensate fell within the wall of the steam fingers while the oil fell at the perimeter of the fingers and then at the lower part of the fingers it flew through the steam fingers. Such a counter current flow of oil and steam weakened the steam fingering phenomenon. The size of the fingers estimated in this work based on the temperature distribution above the steam chamber were around 2 m long. This estimation was later questioned by Gotawala and Gates [119] based on the length scale of heat diffusion in Athabasca oil sand that reached $1-3$ m and could suggest that the temperature contours had reached the thermocouples and not the steam fingers. Referring to the work by Ito and Ipek [115] Gotawala and Gates [119] also questioned the significance of steam fingering in growth of steam chambers by putting more weight on the role of the overall dilation of the medium and conductive heating. They also commented on some details of Butler's model like the maximum rise of the fingers happening off the centerline and predicting a zero rise rate at the center of the finger, to be counter-intuitive and not supported by experimental results [120]. Gotawala and Gates proposed a modified version of Butler's theory which included the effect of the steam density and also used a more accurate approximation for the temperature profile in the oil sand with keeping

seven terms of the Maclaurin series [121] instead of the single term used by Butler. These modifications resulted in improved estimation of the rise rate of the chamber and corrected the asymmetry of the results of Butler with respect to the finger's centerline.

The intense energy consumption of the SAGD process led to attempts to modify this process through the co-injection of non-condensable gas to form a gas cap and reduce the heat loss to the over burden [122], low pressure SAGD [123], VAPEX [124], and solvent aided SAGD (SA-SAGD) [125]. The latter benefits from the combined advantages of solvent dilution in VAPEX and steam heating in SAGD. But as a brief review of modeling of SAGD revealed, a clear understanding of the pore scale phenomena is missing which becomes even less promising when more physical complications such as temperature dependent solubility and concentration dependent viscosity are added. In a series of interesting studies, Mohammadzadeh and Chatzis investigated the microscale phenomena happening during SAGD family processes using visualization techniques [126, 127, 128] (Figure 2.8b). The qualitative study of the flow visualizations using glass-etched micromodels with characterized pore structures confirmed that the steam chamber propagation owed to randomly distributed fingers on the invading steam front. The steam fingering was observed both on top of the steam chamber and at the proximity of its side wings although the buoyant front on top of the chamber produced larger vertically growing fingers. Mohammadzadeh and Chatzis were also able to characterize the flow regions for steam, and the draining oil-condensate emulsion under the action of gravity and capillary forces. The approximate thickness of the flow zones and the flow regimes in these zones provided the required insight for the development of more realistic analytical models of the process. The visualizations of SA-SAGD in a following work revealed an enhancement of the recovery due to the temperature gradient near the interface of the mobilized oil and the steam-solvent chamber that promoted mass convection from solvent condensate to bitumen. Despite the fact that in these works the roles

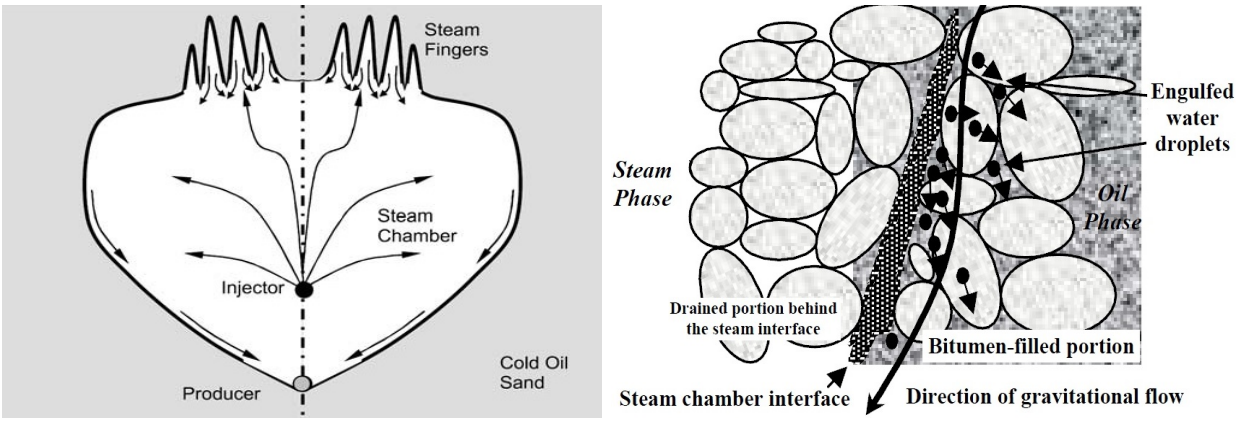


Figure 2.8: Schematic of SAGD steam chamber a) whole chamber with exaggerated view of steam fingers [119] b) Pore scale near interface events [128].

of both conductive and convective heat transfer mechanisms were recognized, their relative importance and the effect of the size of the fingers on the heat transfer process were not discussed and hence cannot be compared with the theoretical models mentioned earlier. In SAGD and other similar solvent assisted processes, the phase change in the heating agent (steam) is an important factor that defines the correlation between the injection pressure and the latent heat available for melting of bitumen. In addition, the main mechanisms of flow and instability which are based on the gravitational force and the density contrast are not included in our model. Yet we strongly believe (and have shown in the results sections of chapters 4 and 5) that the qualitative understanding of the effect of different parameters on the melting process gained from the present study are beneficial for these applications as well.

## 2.4 Goals and Objectives

Despite the extensive amount of studies on thermo-viscous fingering both on the analytical stability and nonlinear simulations, some aspects of this problem require further exploration. One of these aspects is the effect of different combinations of log mobility ratios on the

stability and the efficiency of non-isothermal displacements. Furthermore, considering the moving reference frame the instabilities are modeled in, a new measure of the sweep efficiency of the process that is closer to the definition used in real applications helps in translating the results to industrial applications.

The review of the literature on heterogeneity induced instability reveals that although many of the earlier works were devoted to characterization of the porous medium and the flow regimes in heterogeneous media, the recent stability analyses and numerical simulations have overlooked this concept. Also the range of parameters used in these studies does not allow for a conclusive categorization of the flow characteristics. So a more general description of the flow behavior under different conditions is sought for using a thorough analysis of the flow regimes for different parameters values.

Finally in research works dealing with melting in porous media despite the importance of convective heat transfer in melting this mechanism has been ignored in most of the studies. The effect of convective heat transfer on the melting process and the relative importance of this mechanism with respect to outer boundary convection (i.e. the convection happening at the boundaries of the frozen region) are examined in this work. Another objective of this study is to determine the role of instability in the melting process. Specifically in the heavy oil recovery processes, the contribution of instabilities on the efficiency and enhancement of heat transfer is not fully understood. With the knowledge gained from the previous studies on TVF and flow in heterogeneous media, the new form of instability which involves an interaction between different instability mechanisms and phase change during the displacement process is going to be explored. Through a systematic analysis, the details of the melting process in unstable scenarios are identified.

# Chapter 3

# Dynamics of Fluid Flow and Heat Transfer in Homogeneous Porous Media

---

[1] Non-isothermal miscible viscous flows in homogeneous porous media is studied by modelling the process in a Hele-Shaw cell. The main focus is on the effect of heat exchange between the displacing fluid and the solid matrix on the resulting viscous fingering instability. The nature of the instability is examined by considering two flow scenarios involving the displacement of a cold fluid by a hot one and vice-versa. The effects of the heat exchanges with the surrounding medium and the ratio of the diffusion rates are analyzed both qualitatively and quantitatively. Simulation results show that accounting for the heat exchanges is crucial for the identification of the process stability; although depending on the initial characteristics of the fluids, the effects may differ significantly. In particular it is found that the heat exchanges with the porous medium decrease the influence of temperature difference between the two fluids on the viscosity gradient. Furthermore the diffusion rate of heat in the fluids can magnify the effect of thermal lag coefficient or compensate for it depending on the considered scenario As a general rule, for a cold fluid displacing a hot fluid, higher heat exchange rate and larger diffusion ratio result in flow instability while for a hot fluid displacing a cold one, an increase in heat exchange rate and diffusion ratio tends to suppress the growth of the instability.

[1]This chapter is the exact reproduction of the following journal article:
M. Sajjadi and J. Azaiez, "Dynamics of Fluid Flow and Heat Transfer in Homogeneous Porous Media", *Canadian Journal of chemical Engineering*, vol. 91, no. 4, pp. 687-697, 2013.

## 3.1 INTRODUCTION

Flow displacements in porous media have been the subject of numerous studies due to their importance in many processes such as enhanced oil recovery, solute transport in aquifers, filtration and packed bed regeneration [40]. In practice, the viscous fingering instability which occurs when a high-viscosity fluid is displaced by a low-viscosity one, results in early breakthrough and a reduction of the efficiency of the displacement process [40]. This instability appears in the form of finger-shaped penetrations of the displacing fluid into the displaced one [5, 29, 28]. For extensive reviews on the viscous fingering instability see Homsy (1987) [1] and McCloud and Maher (1995) [2].

In non-isothermal displacement processes such as hot water flooding, steam flooding, Steam-Assisted Gravity Drainage (SAGD), hot solvent injection and some polymer processing techniques, the viscosity of the fluids may vary with the concentration of the solvent as well as the temperature of the fluids. This results in a nonlinear instability that has been referred to as thermo-viscous fingering [25, 41]. Due to differences in the rate of transport of heat and mass, thermo-viscous fingering involves two fronts, the first being the concentration front and the second the thermal front [22, 27]. It has been observed that fingering of each of these fronts can contribute to the instability of the flow and the rate of growth of the fingers depends on both effects [25, 52].

Heat exchange between the fluids in thermal processes is believed to reduce the viscosity contrast at the concentration front and these processes are expected to be less unstable than their isothermal counterparts [22, 27]. In particular, in an experimental study of immiscible displacements, Sheorey et al. [51] reached a higher recovery during non-isothermal injections and reported stabilizing effects of the thermal transfer.

Stability analysis of non-isothermal miscible displacements has been studied in different

research works. Islam et al. [41, 22, 27] performed both nonlinear simulations and linear stability analysis of thermo-viscous fingering in rectilinear porous media. They found that at large values of the Lewis number and small values of porosity, thermo-viscous fingering is mainly influenced by changes of concentration and is less sensible to the thermal front [41]. The effect of the porosity which determines the lag between thermal and concentration fronts, has been presented in the work by Islam et al. The conditions of stability regarding fluid properties are however missing from their works. Other stability analyses of double diffusive viscous fingering [52, 23] consider the displacement to take place in a Hele-Shaw cell and therefore do not encounter different advance rates for the two diffusing fronts.

The most recent stability analysis was performed by Mishra et al. [23] who looked at the influence of the log mobility ratios of two parameters S and F affecting viscosity with different diffusivity rates. The slow and fast diffusing parameters, S and F, can represent concentration and temperature of the fluids. In their work Mishra et al. [23] have shown that a negative log mobility ratio does not necessarily correspond to a stable displacement as conventionally expected. As mentioned before the effect of porosity was not included in their study and hence possible heat exchange with the porous medium was ignored. As is shown in the present work, these heat exchanges can actually play a major role in the flow.

In this chapter, the viscous fingering of miscible non-isothermal flow displacements are studied in terms of the fluid characteristics that may affect the instability. The breakthrough time and the sweep efficiency at the time of breakthrough are used as quantitative measures of the instability. Considering the porosity of the medium, the effects of thermal lag coefficient and diffusion ratio on the mechanism of fingering have been studied through an examination of concentration, temperature and viscosity gradient fields.

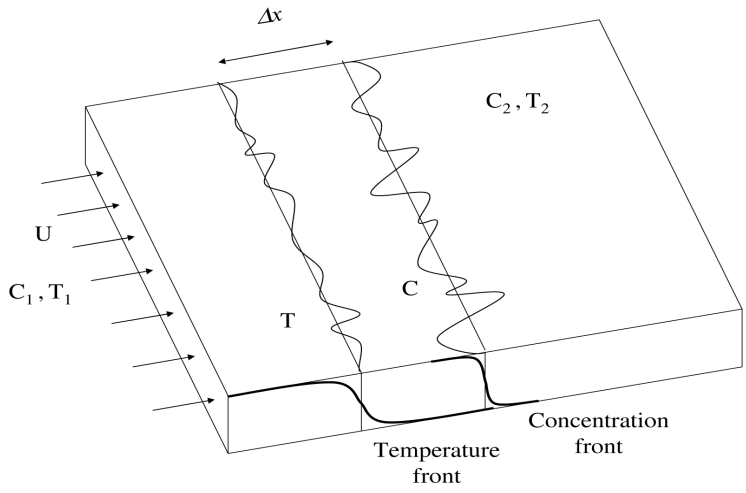


Figure 3.1: Schematic of a horizontal double diffusive flow.

## 3.2 Physical Problem and Mathematical Model

To analyze the instability, a two-dimensional miscible displacement in a horizontal rectilinear homogeneous medium of constant porosity $\phi$ and permeability $\kappa$ is considered. The displacing fluid with viscosity $\mu_1$ and uniform temperature $T_1$ is injected at a uniform velocity $U$ along the $x$ axis to displace a second fluid of viscosity $\mu_2$ and uniform temperature $T_2$ (Fig.3.1). The length, width, and thickness of the medium are $L_x$, $L_y$, and $e$, respectively. Both displacing and displaced fluids are considered to be Newtonian and incompressible.

The mathematical model consists of the conservation of mass and momentum and mass-energy balance equations:

$$\frac{\partial u}{\partial x} + \frac{\partial \nu}{\partial y} = 0 \tag{3.1}$$

$$\begin{aligned} \frac{\partial P}{\partial x} &= -\frac{\mu u}{\kappa} \\ \frac{\partial P}{\partial y} &= -\frac{\mu \nu}{\kappa} \end{aligned} \tag{3.2}$$

$$\phi\frac{\partial C}{\partial t} + (\mathbf{u}.\nabla)C = \phi D_C \nabla^2 C \tag{3.3}$$

$$\phi\frac{\partial T}{\partial t} + \lambda(\mathbf{u}.\nabla)T = \phi D_T \nabla^2 T \tag{3.4}$$

In the above equations $\mathbf{u}$(u,v) is the velocity vector, $P$ the local pressure, $\phi$ the porosity, $\kappa$ the permeability, and $\mu$ the viscosity. Furthermore, the concentration and temperature are denoted by $C$ and $T$ respectively, with corresponding mass and thermal diffusion coefficients $D_C$ and $D_T$. Under the assumption of thermal equilibrium between the solid and fluid, the thermal front travels slower than the fluid front, as heat gets shared between the solid porous matrix and the fluids. Such effect of redistribution of heat is incorporated in the model in the form of a *thermal lag* coefficient $\lambda$ which represents the ratio of the speed of the thermal front to that of the solutal front [129, 25]:

$$\lambda = 1 - U_T = \frac{\phi\rho_f c_{pf}}{\phi\rho_f c_{pf} + (1-\phi)\rho_R c_R} \tag{3.5}$$

Where $\rho_R$, $c_R$, $\rho_f$, and $c_{pf}$ are the density and heat capacities of the solid phase and fluid phase respectively. Note that $\lambda \leq 1$ with higher values corresponding to smaller difference between the velocities of concentration and temperature fronts and lower values corresponding to higher rates of dissipation of $T$. Therefore, two fronts associated with the propagation of temperature and mass can be identified. As a result of heat losses to the surrounding medium, the thermal front in general will lag behind the solutal one associated with mass.

The flow will be analyzed in a Lagrangian reference frame moving at the velocity $U/\phi$ and the model equations are made dimensionless using diffusive scaling:

$$\begin{aligned} (x^*, y^*) &= \frac{x, y}{D_C\phi/U} \qquad t^* = \frac{t}{D_C\phi^2/U^2} \qquad (u^*, v^*) = \frac{(u, v)}{U/\phi} \\ \mu^* &= \frac{\mu}{\mu_1} \qquad p^* = \frac{P}{\mu_1/\kappa D_C} \qquad c^* = \frac{C}{C_1} \qquad \theta^* = \frac{T - T_2}{T_1 - T_2} \end{aligned} \tag{3.6}$$

This results in the following dimensionless equations:

$$\begin{aligned}
&\frac{\partial u^*}{\partial x^*} + \frac{\partial v^*}{\partial y^*} = 0 \\
&\frac{\partial p^*}{\partial x^*} = -\mu^*(u^* + 1), \quad \frac{\partial p^*}{\partial y^*} = -\mu^* v^* \\
&\frac{\partial c^*}{\partial t^*} + u^*\frac{\partial c^*}{\partial x^*} + v^*\frac{\partial c^*}{\partial y^*} = \left(\frac{\partial^2 c^*}{\partial x^{*2}} + \frac{\partial^2 c^*}{\partial y^{*2}}\right) \\
&\frac{\partial \theta^*}{\partial t^*} + \lambda\left(u^*\frac{\partial \theta^*}{\partial x^*} + v^*\frac{\partial \theta^*}{\partial y^*}\right) + (\lambda - 1)\frac{\partial \theta^*}{\partial x^*} = \mathrm{Le}\left(\frac{\partial^2 \theta^*}{\partial x^{*2}} + \frac{\partial^2 \theta^*}{\partial y^{*2}}\right)
\end{aligned} \tag{3.7}$$

In the above equations Le is the Lewis number:

$$\mathrm{Le} = \frac{D_T}{D_C} = \frac{\mathrm{Pe}_C}{\mathrm{Pe}_T} \tag{3.8}$$

where $\mathrm{Pe}_C = UL_x/D_C$ and $\mathrm{Pe}_T = UL_x/D_T$ are the solutal and thermal Péclet numbers, respectively. For convenience of notation, the stars are dropped from the equations. The dependence of the viscosity on temperature and concentration of the fluid is defined as an exponential function ([25, 27, 23]):

$$\mu(c, \theta) = \exp\left(\beta_C(1 - c) + \beta_T(1 - \theta)\right) \tag{3.9}$$

In this equation $\beta_C$ is the natural logarithm of the viscosity ratio $\mu_1/\mu_2$ in an isothermal miscible displacement and $\beta_T$ is the natural logarithm of the ratio of the viscosity $\mu_{1T}/\mu_{2T}$ in a single fluid flow with two different temperatures. The equations are expressed using a stream function-vorticity formulation. The curl of the pressure gradient results in a relation between viscosity and vorticity:

$$\begin{aligned}
&\nabla P = -(\mathbf{u} + \mathbf{i}).\mu \\
\Rightarrow \quad &(\nabla \times \nabla)\, P = -\nabla \times (\mathbf{u} + \mathbf{i})\mu - \nabla\mu \times (\mathbf{u} + \mathbf{i}) = 0 \\
&\nabla \times \mathbf{u} = -\frac{1}{\mu}\nabla\mu \times (\mathbf{u} + \mathbf{i}) \\
&\omega = -\frac{1}{\mu}\frac{\partial \mu}{\partial c}\nabla c \times (\mathbf{u} + \mathbf{i}) - \frac{1}{\mu}\frac{\partial \mu}{\partial \theta}\nabla\theta \times (\mathbf{u} + \mathbf{i})
\end{aligned} \tag{3.10}$$

$$\omega = \beta_C\{v\frac{\partial c}{\partial x} - (u+1)\frac{\partial c}{\partial y}\} + \beta_T\{v\frac{\partial \theta}{\partial x} - (u+1)\frac{\partial \theta}{\partial y}\} \tag{3.11}$$

Equation 3.11 provides the relation between concentration and temperature gradients and vorticity $\omega$. This equation and the relation between stream function and vorticity ($\omega = \frac{\partial v}{\partial x} - \frac{\partial u}{\partial y} = -\nabla^2\psi$) are used to develop the model used in the nonlinear simulations.

$$\frac{\partial c}{\partial t} + \frac{\partial \psi}{\partial y}\frac{\partial c}{\partial x} - \frac{\partial \psi}{\partial x}\frac{\partial c}{\partial y} = \nabla^2 c \tag{3.12}$$

$$\frac{\partial \theta}{\partial t} + \lambda\left(\frac{\partial \psi}{\partial y}\frac{\partial \theta}{\partial x} - \frac{\partial \psi}{\partial x}\frac{\partial \theta}{\partial y}\right) + (\lambda - 1)\frac{\partial \theta}{\partial x} = \mathrm{Le}\nabla^2\theta \tag{3.13}$$

$$\omega = -\beta_C\left(\frac{\partial \psi}{\partial x}\frac{\partial c}{\partial x} + (\frac{\partial \psi}{\partial y} + 1)\frac{\partial c}{\partial y}\right) - \beta_T\left(\frac{\partial \psi}{\partial x}\frac{\partial \theta}{\partial x} + (\frac{\partial \psi}{\partial y} + 1)\frac{\partial \theta}{\partial y}\right) \tag{3.14}$$

## 3.3 Numerical Method

The above system of equations has the following one-dimensional fundamental solution corresponding to a zero velocity in the Lagrangian frame:

$$\begin{aligned} \bar{c} &= \frac{1}{2} erfc\left(\frac{x}{2\sqrt{t}}\right) \\ \bar{\theta} &= \frac{1}{2} erfc\left(\frac{x - (\lambda - 1)t}{2\sqrt{\mathrm{Le}.t}}\right) \\ \bar{u}(x, y, t) &= \bar{v}(x, y, t) = 0 \end{aligned} \tag{3.15}$$

Following Islam and Azaiez (2010), the problem is formulated such that $c$ and $\theta$ are expressed as the sum of the fundamental solutions $\bar{c}$ and $\bar{\theta}$ and disturbances $c'$ and $\theta'$. The initial and boundary conditions are similar to those adopted by Islam and Azaiez [2010].

$$\begin{aligned} c_0(x, y, t_0) &= \bar{c}(x, t_0) + \delta \times rand(y) \times \exp(-x^2/\sigma^2) \\ \theta_0(x, y, t_0) &= \bar{\theta}(x, t_0) + \delta \times rand(y) \end{aligned} \tag{3.16}$$

$$
\begin{aligned}
(\omega, c, \theta)(-\mathrm{Pe}_C/2 - t, y, t) &= (0, 1, 1) \\
(\omega, c, \theta)(\mathrm{Pe}_C/2 - t, y, t) &= (0, 0, 0) \\
(\omega, c, \theta)(x, \mathrm{Pe}_C/A, t) &= (\omega, c, \theta)(x, 0, t)
\end{aligned}
\tag{3.17}
$$

where $A = L_x/L_y$ is the cell's aspect ratio and $\delta$ and $\sigma$ determine the amplitude of perturbations and their penetration on the concentration front. $t_0$ is the initial time given to base state to get diffused. The set of nonlinear partial differential equations is solved using a pseudo-spectral method based on the Hartley transform. This results in a set of ordinary differential equations in time, that are solved using an Adams-Bashforth semi-implicit two-step scheme. According to the expression of the viscosity (Equation 3.9), both concentration $C$ and temperature $T$ can influence the instability interactively. The interaction between the two fronts will depend strongly on the thermal lag coefficient which determines the rate of lagging between the thermal front and the flood front. Hence the thermal lag coefficient will have a significant importance in predicting the development of the fingers in the process.

## 3.4 Results

The nonlinear simulations of non-isothermal viscous fingering have been performed by solving the afore-mentioned system of equations (Equation 3.7). Unless specified otherwise, all results are presented for $\mathrm{Pe}_C = 2000, A = 2$, and $t_0 = 1$. The main focus of this study is on the influence of the thermal lag coefficient $\lambda$ and the diffusion ratio Le on the instability and the fingers development. The first analysis will focus on variations of $\lambda$ for a fixed Le.

### 3.4.1 Validation of Results

Concentration contours for an isothermal case with $\beta_C = 3$, $\beta_T = 0$, $\mathrm{Pe}_C = 500$ and $A = 2$ were obtained and matched those reported by Tan and Homsy [8]. For a non-isothermal

case; $\beta_C = 3$, $\beta_T = 2$, Le $= 1$, $\lambda = 0.75$, and $\mathrm{Pe}_C = 1000$, the results were similar to those obtained by Islam and Azaiez [27].

### 3.4.2 Reference Cases

As the first case, viscous fingering in an isothermal flow ($\beta_T = 0$) is compared with a non-isothermal flow ($\beta_T = 1$) for $\beta_C = 2$. Figure 3.2 shows the concentration contours of both flows at the break-through time of the non-isothermal case as the fingers reach the downstream boundary. The thermal and solutal diffusion rates are considered to be the same (Le $= 1$) and it assumed that there is no heat exchange between the fluids and the solid matrix ($\lambda = 1$). Therefore both temperature and concentration have the same contribution to instability and the non-isothermal flow can be thought of as an isothermal flow with effective $\beta_C = 3$. Higher log-mobility ratio of the non-isothermal flow results in enhancement of instability and the growth of more complex fingers in Figure 3.2b compared to those of Figure 3.2a. It should be noted that in the case of Figure 3.2b, concentration and temperature contours are identical. The two cases depicted in Figure 3.2 are taken as references in the subsequent analysis and will be referred to in the discussion.

In general for cases with unit thermal lag coefficient and unit diffusion ratio; both solutal and thermal fronts are convected and diffuse at the same rates, and the flow dynamics are equivalent to those of an isothermal displacement with an effective mobility ratio $\beta_C + \beta_T$. However, whenever either or both parameters are different from one, the dynamics can be substantially different. The effects of these two parameters are analyzed in the following sections.

### 3.4.3 Effects of the Thermal Lag Coefficient

The role of the thermal lag coefficient is more crucial in some cases as the redistribution of the heat between the fluids and the solid matrix can de-stabilize an otherwise stable flow or

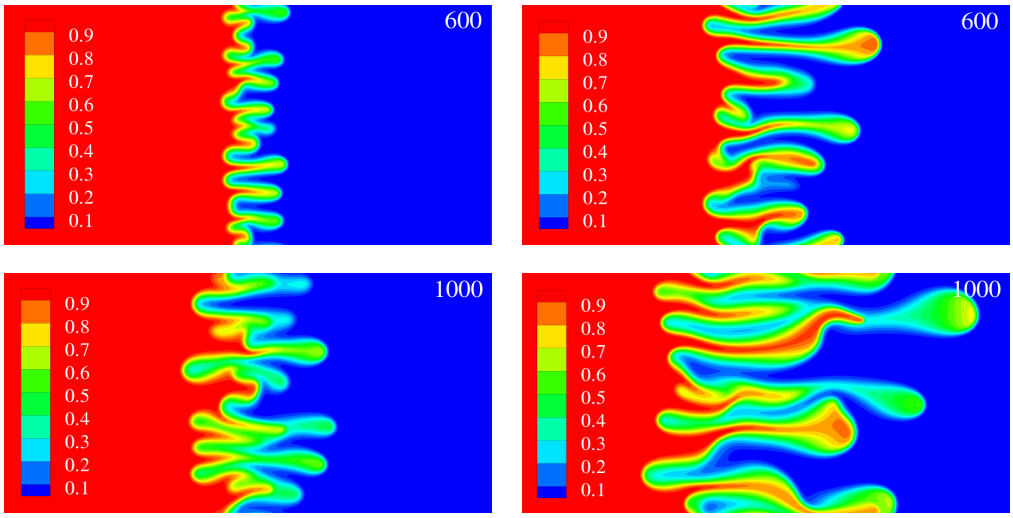


a) $\beta_T = 0$ b) $\beta_T = 1$

Figure 3.2: Concentration contours comparing an isothermal flow with a non-isothermal flow: $\beta_C = 2$, $\lambda = 1$, a) $\beta_T = 0$, b) $\beta_T = 1$.

vice-versa. In what follows the cases corresponding to the displacement of a cold less viscous fluid by a hot more viscous one ($\beta_C < 0, \beta_T > 0$) and that of a hot more viscous fluid by a cold less viscous one ($\beta_C > 0, \beta_T < 0$) are examined for a fixed Le $= 1$. In such cases $\lambda$ affects the strength of $\beta_C$ or $\beta_T$ acting against the other to change the instability conditions.

**A Hot More Viscous Fluid Displacing A Cold Less Viscous Fluid:** Figure 3.3 illustrates the importance of the thermal lag coefficient and of accounting for heat losses to the surrounding medium. The concentration contours for the case $\beta_C = -2$ and $\beta_T = 3$ reveal radically different results in the case where heat losses are accounted for $\lambda = 0.4$ versus that when they are ignored $\lambda = 1$. In this particular case, concentration gradients act in favour of the stability while the temperature gradients have a destabilizing effect. Since in this case $\beta_C + \beta_T > 0$, the flow is unstable for $\lambda = 1$. However, as a result of heat exchange with the porous medium, the flood front is actually stable for $\lambda = 0.4$. For this flow scenario, lower $\lambda$ or in other words stronger heat losses to the porous medium acts in favour of stability in two ways; first by reducing the destabilizing effects of the thermal front

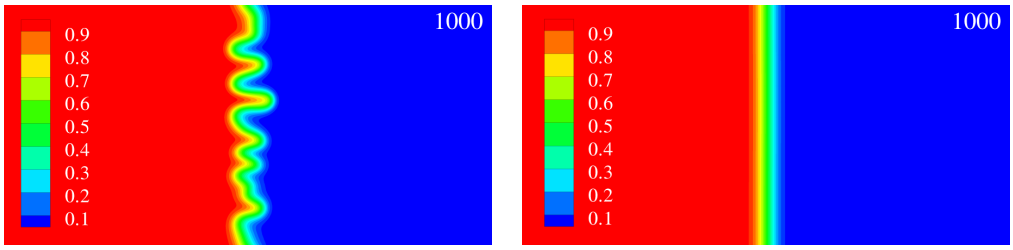


(a) $\lambda = 1$ (b) $\lambda = 0.4$

Figure 3.3: Concentration contours at: $\beta_C = -2$, $\beta_T = 3$, a) $\lambda = 1$ b) $\lambda = 0.4$

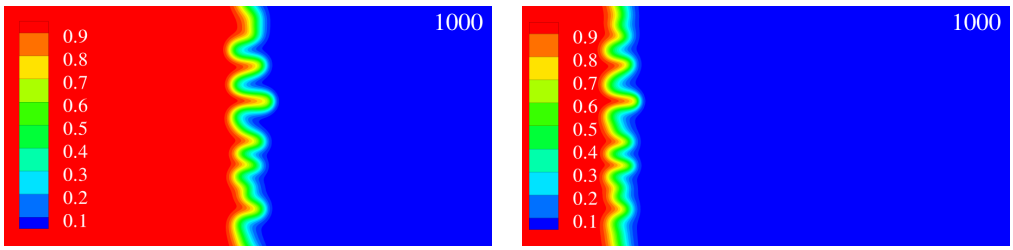


(a) $\lambda = 1$ (b) $\lambda = 0.4$

Figure 3.4: Temperature contours at: $\beta_C = -2$, $\beta_T = 3$, a)$\lambda = 1$ b) $\lambda = 0.4$

on the solutal one due to the larger lag between the two fronts, and second by attenuating the instability at the thermal front due to its lower velocity $\lambda U$.

The temperature contours for the same displacement process shown in Figure 3.4b with $\beta_T = 3$ can be compared to the reference case in Figure 3.2b with the effective log mobility ratio of $\beta_C + \beta_T = 3$. Both fronts have the same mobility ratio and it could be expected to have the same rate of growth of instability fingers if they were traveling at the same velocity. It is apparent that the fingers on the thermal front are less developed even at $t = 1400$ compared to the fingers in the reference case at $t = 1000$. Another reference case with $\beta_C = 3$ and $\text{Pe} = 0.4 \times 2000$ which is the same as the effective $\text{Pe}_T$ for the non-isothermal displacement has been studied to isolate the effect of lower heat flow rate from the effect of the interaction. It has been observed that slower growth of thermal fingers is mainly due to a smaller rate of heat transport; $U_T = \lambda U$ or in this case $U_T = 0.4U$.

Figure 3.5 shows concentration and temperature fields for a similar displacement process

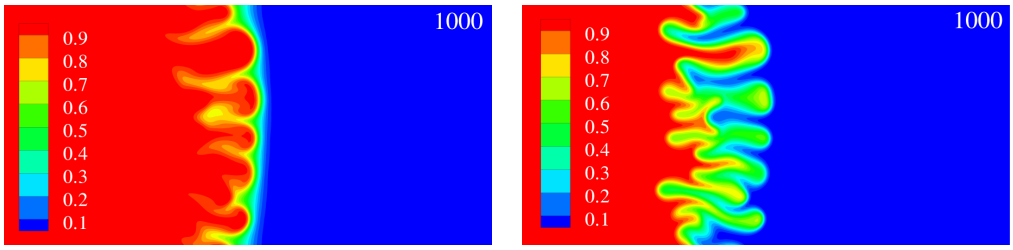


(a) Concentration (b) Temperature

Figure 3.5: Concentration and temperature contours at: $\beta_C = -2$, $\beta_T = 3$, $\lambda = 0.8$, a) Concentration b) Temperature

as in Figure 3.3 but for $\lambda = 0.8$. In this case the lag between the two fronts is smaller and the interaction between temperature and concentration is more significant since the thermal front has a higher flow rate and remains in the vicinity of the solutal front for a longer time. Unlike the case with $\lambda = 0.4$, the thermal fingers now affect the solutal front and disturb the flow resulting in backward fingers to form on the solutal front.

**A Cold Less Viscous Fluid Displacing A Hot More Viscous Fluid:** In the previous case it was found that heat exchange with the medium attenuates or even suppresses the instability. An opposite trend is reported in this scenario involving the displacement of a hot more viscous fluid by a cold less viscous one, ($\beta_C > 0$, $\beta_T < 0$). Figures 3.6 to 3.8 depict results for a flow where $\beta_C = 2$ and $\beta_T = -3$. In this case heat exchange with the surrounding medium enhances the instability and can actually destabilize an otherwise stable flow (Figure 3.6). In such a scenario, the flow is stable in the absence of heat exchanges ($\lambda = 1$), but becomes unstable when the stabilizing thermal front starts to lag behind the unstable solutal front ($\lambda = 0.5$). The corresponding temperature contours are shown in Figure 3.7. In one case they are coincident with the concentration contours ($\lambda = 1$) while in the other they are disconnected and have moved far in the upstream direction as a result of the heat exchanges with the porous medium.

To further see the effects of the thermal lag coefficient, $\lambda$ is set to 0.8 and the correspond-

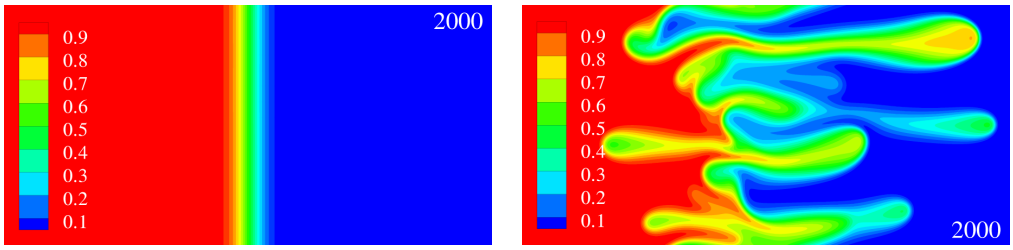


(a) $\lambda = 1$ (b) $\lambda = 0.5$

Figure 3.6: Concentration contours at: $\beta_C = 2$, $\beta_T = -3$, a)$\lambda = 1$ b) $\lambda = 0.5$

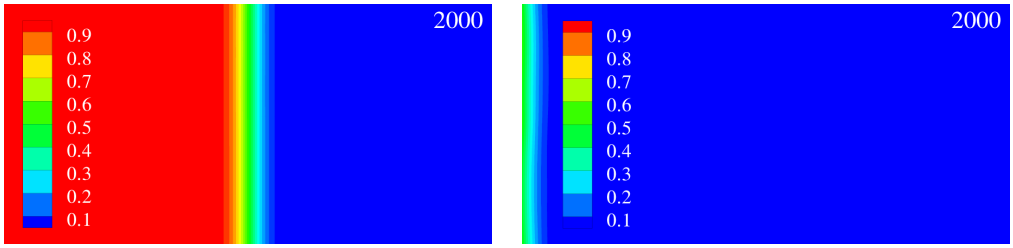


(a) $\lambda = 1$ (b) $\lambda = 0.5$

Figure 3.7: Temperature contours at: $\beta_C = 2$, $\beta_T = -3$, a)$\lambda = 1$ b) $\lambda = 0.5$

ing concentration and temperature contours are shown in Figure 3.8. Due to slower lagging of the thermal front in this case, there are more interactions between the two fronts acting towards the growth of some instabilities at the thermal front and a delay in the advancement of fingers on the solutal front compared to those observed in the case with $\lambda = 0.5$ as depicted in Figure 3.6.

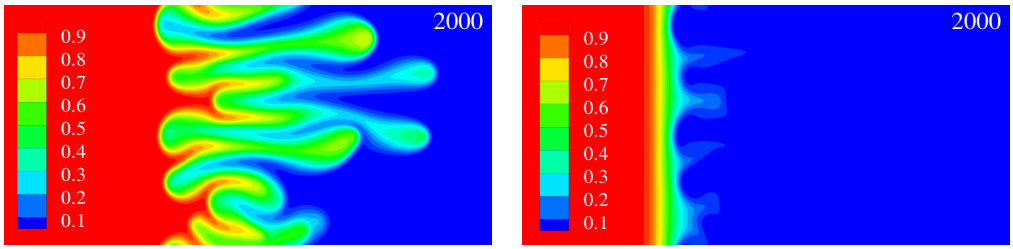


(a) Concentration (b) Temperature

Figure 3.8: Concentration and Temperature Contours at: $\beta_C = 2$, $\beta_T = -3$, $\lambda = 0.8$, a) Concentration b) Temperature

### 3.4.4 Transversely Averaged Properties

Averages of the concentration and temperature fields over the width of the medium are obtained to determine the distribution of these properties and observe the overlap between the concentration and temperature mixing zones.

Figure 3.9 depicts results for the case of a hot more viscous fluid displacing a cold less viscous one that was discussed earlier. Figure 3.9a shows transversely averaged concentration profiles for three values of $\lambda$, while concentration and temperature averages for $\lambda = 0.8$ and $\lambda = 0.4$ are depicted in Figures 3.9b and c, respectively. In this scenario, the thermal front is unstable and the solutal one is stable. It is clear from Figure 3.9a that at $\lambda = 0.4$, the solutal front is essentially stable and is the same as that of the base state. Comparing the other two curves in this figure with the base state profile, it can be noted that for $\lambda = 1$, the deviations from the base state develop both in the downstream and upstream directions while for $\lambda = 0.8$ they develop towards the upstream of the front. These two profiles correspond to the standard fingering and backward fingering instabilities discussed earlier. Looking at Figures 3.9b and c it is observed that the coupling between the two fronts observed for $\lambda = 0.8$ which results in backward fingering has essentially disappeared for $\lambda = 0.4$, and even though the thermal front is unstable it does not affect the solutal one which remains undisturbed (Figure 3.9c).

Figure 3.10 shows similar graphs but for the case where a cold less viscous fluid displaces a hot more viscous one. Here the curve of $\lambda = 1$ presents a stable flood, and as $\lambda$ is decreased the instability becomes stronger. Furthermore in this scenario, the thermal front is stable and the less it interacts with the solutal front, the more unstable the latter front is. In Figure 3.10b corresponding to $\lambda = 0.8$, the stable thermal front interacts with the concentration front and does not allow backward fingers to develop leading to a better sweep efficiency at the flooded zone. On the other hand when $\lambda = 0.5$, there is essentially no overlap between

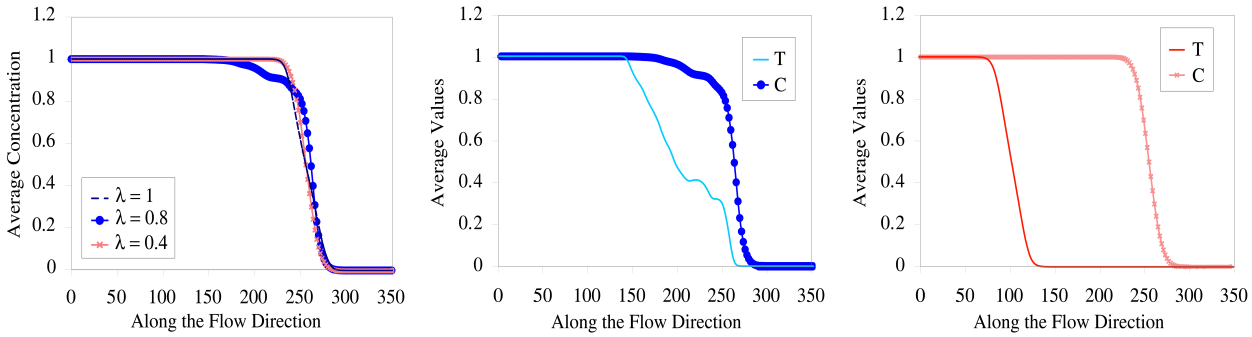


(a) Average Concentration (b) Average C and T for $\lambda = 0.8$ (c) Average C and T for $\lambda = 0.4$

Figure 3.9: Transversely averaged concentration and temperature distributions for the cases discussed in Figures 3.3-3.5 at t=1400: a) average concentration for different lag coefficients, b)average concentration and temperature for $\lambda = 0.8$, c)average concentration and temperature for $\lambda = 0.4$

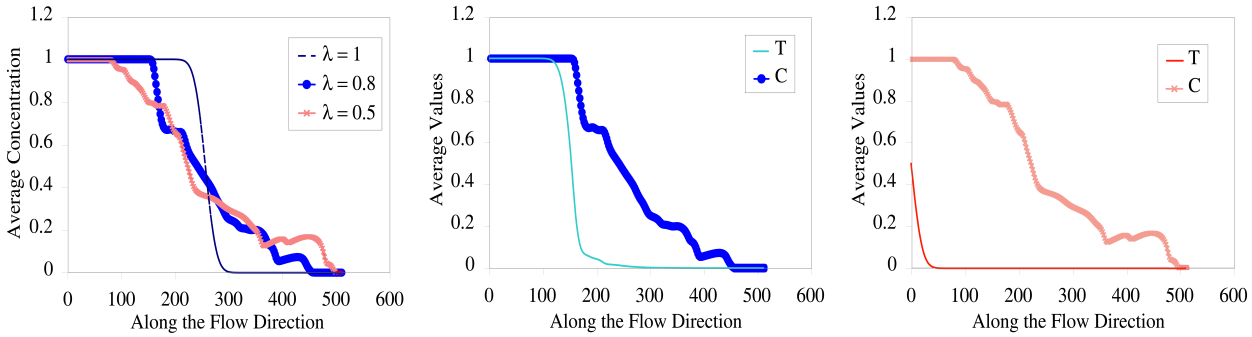


(a) Average Concentration (b) Average C and T for $\lambda = 0.8$ (c) Average C and T for $\lambda = 0.5$

Figure 3.10: Transversely averaged concentration and temperature distributions for the cases discussed in Figures 3.6-3.8 at t=2000, $\beta_C = 2$, $\beta_T = -3$: a) average concentration for different thermal lag coefficients, b) average concentration and temperature for $\lambda = 0.8$, c) average concentration and temperature for $\lambda = 0.5$.

the two fronts and as a result the concentration front extends both upstream and downstream (Figure 3.10c).

### 3.4.5 Breakthrough Time and Sweep Efficiency

One of the parameters that can represent the effect of fingering instability to industrial purposes is the sweep efficiency of the flooding process at the breakthrough time. After breakthrough, the solvent is produced at the production end and the efficiency of the flooding process does not change significantly. Here the breakthrough time is measured by tracking the mixing zone end and measuring the time it reaches a fixed channel length. The length of the channel is chosen small enough so that breakthrough occurs in all cases. The breakthrough sweep efficiency is the area swept by the solvent concentration of $c = 0.5$ over the total area of the channel.

In a hot more viscous fluid displacing a cold less viscous fluid process, the flow becomes more unstable when the destabilizing thermal front moves close to the solutal front such that both the breakthrough time and solutal sweep efficiency decrease with increasing thermal lag coefficient. Figure 3.11 shows variations of the breakthrough time, concentration and heat sweep efficiency with the thermal lag coefficient $\lambda$ and for different thermal log mobility ratios. For small $\lambda$ the concentration sweep efficiency is virtually constant and close to one. The breakthrough time is also constant and equal to 1400. These trends are expected from a stable front. For larger $\lambda$ the sweep efficiency and breakthrough time decrease due to enhanced fingering. Larger $\beta_T$ which result in stronger instability on the thermal front results in induced instability at solutal front and consequently a lower sweep efficiency and smaller breakthrough times.

In a thermal process, the efficiency of heating is also of interest and is depicted in Figure 3.11c. The efficiency of the heating process depends strongly on $\lambda$ and varies also with the

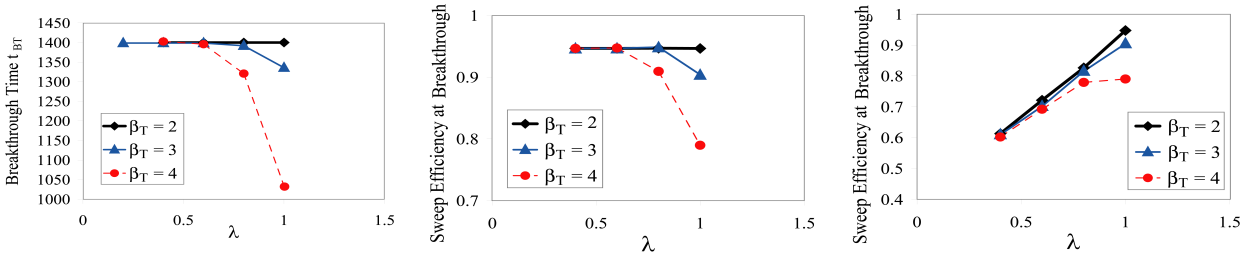


(a) Breakthrough time (b) Concentration Sweep Efficiency (c) Heat Sweep Efficiency

Figure 3.11: The breakthrough time and sweep efficiency of solvent and heat flooding at breakthrough for $\beta_C = -2$, and $\beta_T = 2,\ 3,\ 4$: a) Breakthrough time, b) Concentration Sweep Efficiency, c) Heat Sweep Efficiency.

breakthrough time. The potential area that can be swept by stable thermal front can be estimated as $A_{Potential} = L_y \lambda U t_{BT}$. Although the real area swept by thermal front depends on its stability, the roles of $\lambda$ and $t_{BT}$ are more dominant in defining the efficiency of thermal flooding. The breakthrough time defines the distance the thermal front can travel during the process before breakthrough. The dependence of heat sweep efficiency on the breakthrough time becomes more significant for higher $\lambda$ as the solutal front becomes more unstable and the breakthrough time decreases significantly. Thermal sweep efficiency increases with increasing $\lambda$ and is maximum when there is no heat loss to the surrounding porous medium. If the breakthrough time remains constant with $\lambda$, the only parameter changing the heating efficiency is the velocity of the thermal front and therefore the thermal sweep efficiency follows a linear trend with $\lambda$. Any reduction in breakthrough time reduces the sweep efficiency of heat, and it can be claimed that any deviation from a linear dependence of heat sweep efficiency on $\lambda$ is the result of changes in the breakthrough time. For larger $\lambda$, the slope of the thermal sweep efficiency graph is reduced as a result of close interactions between the fronts.

Opposite trends for the breakthrough time are obtained in the case involving a cold less viscous fluid displacing a hot more viscous fluid in Figure 3.12a. Here the breakthrough time overall increases with $\lambda$ as a result of the attenuation of the instability with increase

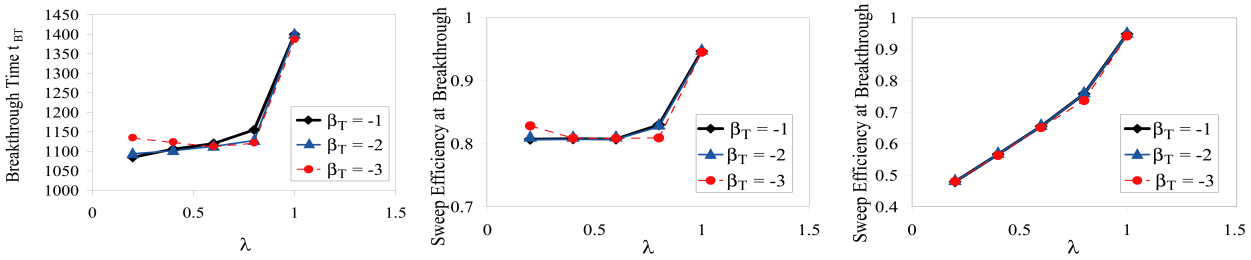


(a) Breakthrough time (b) Concentration Sweep Efficiency (c) Heat Sweep Efficiency

Figure 3.12: The breakthrough time and sweep efficiency of solvent and heat flooding at breakthrough for $\beta_C = 2$, and $\beta_T = -1,\ -2,\ -3$: a) Breakthrough time, b) Concentration Sweep Efficiency, c) Heat Sweep Efficiency.

of thermal lag coefficient. Actually in this case, a gradual change is observed up to $\lambda = 0.8$ followed by a rapid increase thereafter. It is worth noting that for $\beta_T = -2$ and $\beta_T = -3$ there is an increasing trend, while for $\beta_T = -1$ the breakthrough time actually decreases as $\lambda$ increases from 0.2 to 0.6. Similar trends for increase with $\lambda$ are obtained for the concentration sweep efficiency which reaches its maximum corresponding to a stable displacement process at $\lambda = 1$ for $\beta_T = -2$ and $\beta_T = -3$ (Figure 3.12b). In this scenario the thermal front is stable if not influenced by instabilities at the solutal front and the thermal sweep efficiency curves follow the linear trend more closely. The slope of the thermal sweep efficiency increases for large $\lambda = 1$ as a result of the stronger interactions with the unstable solutal front and later breakthrough of the solvent (Figure 3.12c).

Now that we are looking at the efficiency of different displacement processes, it is worth examining the efficiency and breakthrough time of non-isothermal displacements with composition and temperature properties acting in favour of the instability. Although such processes are encountered more in oil recovery, the values of the diffusion ratio and thermal lag coefficient (Le and $\lambda$) have actually no effect on the nature of the instability for processes with $\beta_C > 0$ and $\beta_T > 0$ so they have not been included in the previous analysis. Figure 3.13 shows how the breakthrough time and sweep efficiency are affected by $\lambda$ and illustrate the severity of the instability when both $\beta_C$ and $\beta_T$ are positive. The trends are in general

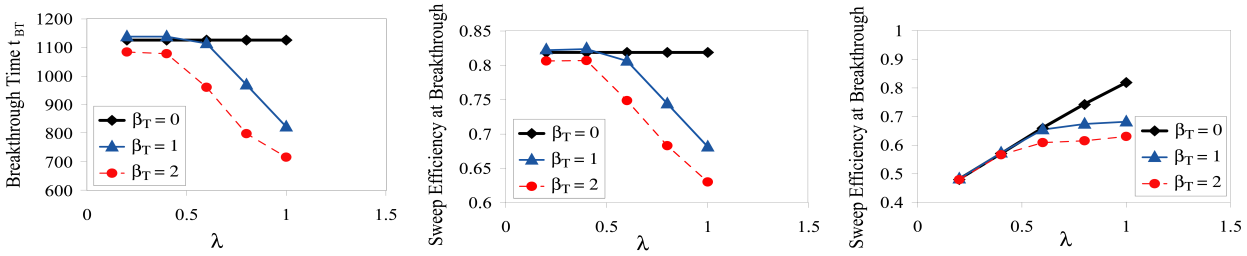


(a) Breakthrough time (b) Concentration Sweep Efficiency (c) Heat Sweep Efficiency

Figure 3.13: The breakthrough time and sweep efficiency of solvent and heat flooding at breakthrough for $\beta_C = 2$, and $\beta_T = 0,\ 1,\ 2$: a) Breakthrough time, b) Concentration Sweep Efficiency, c) Heat Sweep Efficiency.

similar to those shown in Figure 3.11 except that in none of the cases shown here the process is stable, hence the graphs do not converge at any point to stable conditions. Despite the experimental observations of Sheorey et al. [51] which indicate higher recovery rates using non-isothermal displacements, the efficiency of non-isothermal displacements actually show lower heat and solutal sweep efficiency as $\beta_T$ is increased. This implies that the heating of a reservoir should be performed to mobilize the oil in place and not to increase the stability of the displacement process.

### 3.4.6 Effects of the Lewis Number

At higher heat diffusion rates, the temperature profile has a shallower slope and the thermal front is more stable on its own. For $\lambda = 1$, as Le increases the heat diffuses faster and the two fluids reach thermal equilibrium faster. Although for $\lambda < 1$ higher Le results in slower separation between the fronts, at the same time it weakens the effect of thermal front on stability of the solutal front. In this section, the cases discussed so far are going to be re-examined for a higher diffusion ratio to study the effect of diffusion ratio on stability.

Starting with the cases where a hot more viscous fluid displaces a cold less viscous fluid, Figure 3.14 shows the flow at the same conditions as in Figure 3.3 but for Le = 10. Higher Le in this case acts in favour of stability by transferring the heat of displacing fluid to the

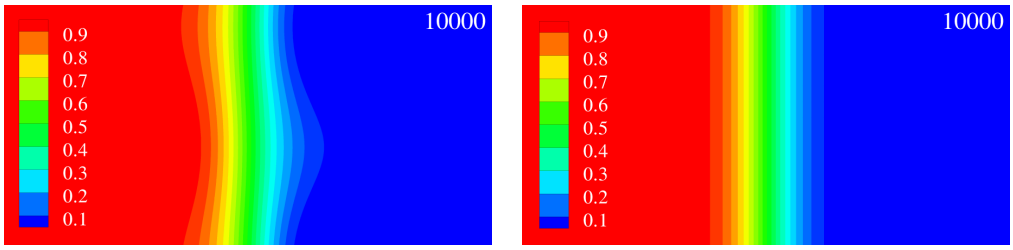


(a) $\lambda = 1$ (b) $\lambda = 0.4$

Figure 3.14: Concentration contours at: $\beta_C = -2$, $\beta_T = 3$, Le $= 10$, a) $\lambda = 1$ b) $\lambda = 0.4$

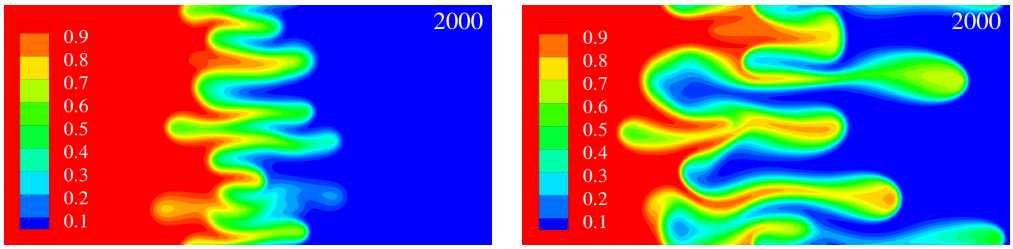


(a) $\lambda = 1$ (b) $\lambda = 0.5$

Figure 3.15: Concentration contours at: $\beta_C = 2$, $\beta_T = -3$, Le $= 10$, a)$\lambda = 1$ b) $\lambda = 0.5$

displaced fluid and making the displaced fluid less viscous. So the mobility ratio becomes more favourable and attenuates the instability (Figure 3.14a). In this case where thermal front is the cause of instability, higher Le and lower $\lambda$ stabilize the unstable flow so the displacement is more stable for $\lambda < 1$. This is also true for the case of Figure 3.5 with $\lambda = 0.8$ which shows stability until the thermal front reaches upstream boundaries.

If the case of Figure 3.6 in which a cold less viscous fluid displaces a hot more viscous fluid, is considered to have a higher heat diffusion rate (higher Le), then low temperature of displacing fluid cools the displaced fluid faster and makes it more viscous and the displacing fluid becomes less viscous. Therefore the advantage of having high viscosity due to low temperature in the displacing fluid vanishes and the flow instability increases. At $\lambda = 1$ the stable flow of Figure 3.6a becomes unstable in Figure 3.15a due to diffusion of heat in between the fluids. The effect of higher Le becomes less important as the thermal front lags and moves away from the solutal front so at $\lambda = 0.5$ the fingers are similar at both Le values.

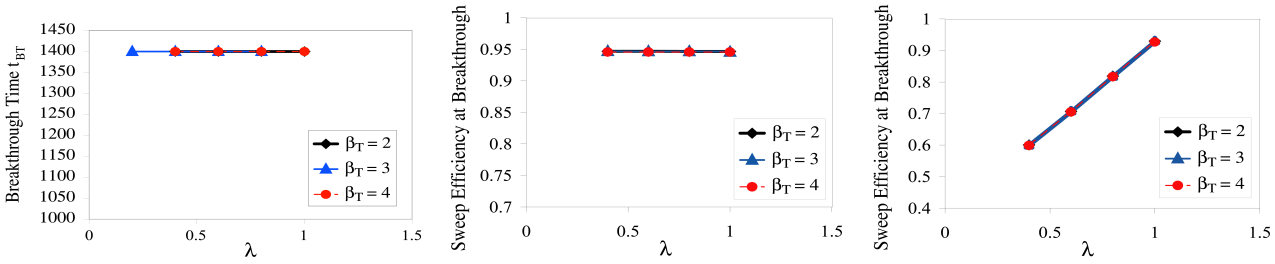


(a) Breakthrough time (b) Concentration Sweep Efficiency (c) Heat Sweep Efficiency

Figure 3.16: The breakthrough time and sweep efficiency of solvent and heat flooding at breakthrough for $\beta_C = -2$, $\beta_T = 2,\ 3,\ 4$, and Le = 10: a) Breakthrough time, b) Concentration Sweep Efficiency, c) Heat Sweep Efficiency.

The effect of the diffusion ratio on the sweep efficiency and the breakthrough time are shown in Figures 3.16 to 3.18. For the first case of a hot more viscous fluid displacing a cold less viscous one, as mentioned before, a lower lag coefficient and a higher diffusion ratio result in reduced instability. This leads to a breakthrough time $t_{BT} = 1400$ corresponding to stable conditions for all $\lambda$ values when the diffusion ratio is increased to Le = 10. Even for $\beta_C = -2$ and $\beta_T = 4$ which should result in more instability than the case of Figure 3.14a, the results of efficiency and breakthrough time are similar to the stable cases. The instability for these scenarios arises in later times (like in Figure 3.14a) and to be able to see its effects on the efficiency, a larger length for the reservoir should be considered. The same applies to the sweep efficiency of the solutal front which remains relatively constant close to the efficiency of a stable flow process for the defined parameters and the assigned length of the reservoir. The sweep efficiency of the thermal front follows a linear behaviour with $\lambda$ corresponding to stable conditions as well.

The efficiency and breakthrough time of cases with cold less viscous fluid displacing hot more viscous fluid for Le = 10 are examined in Figure 3.17. The breakthrough time graph shows the same trends as those reported for lower Le in Figure 3.12a but with less sensitivity to $\lambda$ (which has been elaborated on before). For Le = 10 at $\lambda = 1$ the breakthrough time varies more significantly with the thermal log mobility ratio $\beta_T$ than for Le = 1. This is

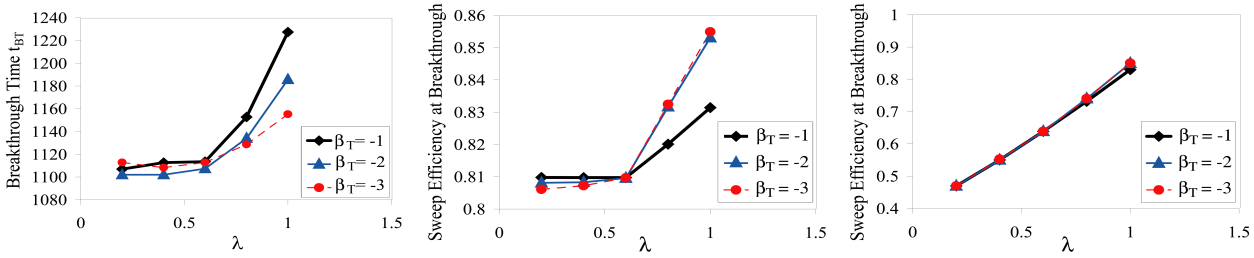


(a) Breakthrough time (b) Concentration Sweep Efficiency (c) Heat Sweep Efficiency

Figure 3.17: The breakthrough time and sweep efficiency of solvent and heat flooding at breakthrough for $\beta_C = 2$, $\beta_T = -1$, $-2$, $-3$, and Le $= 10$: a) Breakthrough time, b) Concentration Sweep Efficiency, c) Heat Sweep Efficiency.

due to the fact that the case Le $= 1$ $\beta_T = -2$ and $\beta_T = -3$ basically corresponds to stable flow conditions and even for $\beta_T = -1$ the instability is not very severe. The change in the efficiency and breakthrough time for flows with slow growing fingers and higher stability is less pronounced and requires longer simulation times to be observed. While for unstable flow conditions, the breakthrough time is smaller and due to fast growth of fingers, the efficiency of the process is more sensitive to the value of the log mobility ratios which define the scale of the instability.

Like in the previous cases, the case of positive $\beta_C$ and $\beta_T$ with higher diffusion ratio is less sensitive to the changes in the thermal lag coefficient (Figure 3.18). Still the highest sensitivity to $\beta_T$ or strongest instability of the thermal front is observed at $\lambda = 1$ when the interaction between the two fronts is maximum and the thermal front has its highest strength due to higher flow rate. At lower thermal flow rates (smaller $\lambda$ values) the heat of the injected fluid does not affect the process significantly and the flow has similar efficiency and breakthrough time as the isothermal flow.

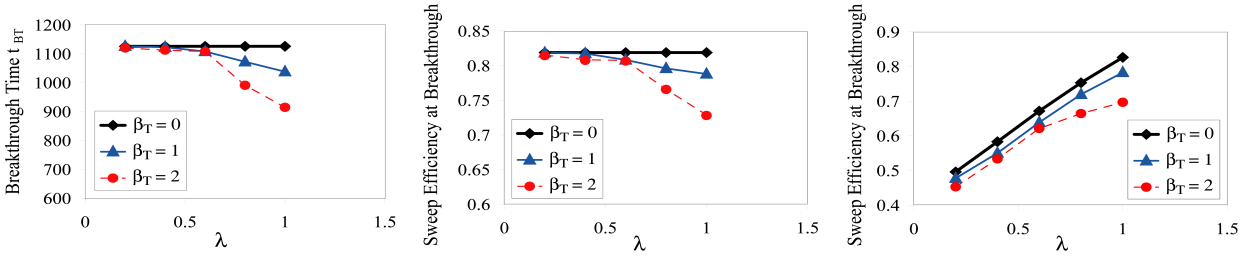


(a) Breakthrough time (b) Concentration Sweep Efficiency (c) Heat Sweep Efficiency

Figure 3.18: The breakthrough time and sweep efficiency of solvent and heat flooding at breakthrough for $\beta_C = 2$, $\beta_T = 0,\ 1,\ 2$, and Le $= 10$: a) Breakthrough time, b) Concentration Sweep Efficiency, c) Heat Sweep Efficiency.

## 3.5 Conclusion

In this chapter the influence of thermal lag coefficient and diffusion ratio on thermo-viscous fingering has been investigated. Nonlinear simulations based on a pseudo-spectral method have been used to examine the stability of displacement flow at different conditions. To recognize the physical behavior of the flow the temperature profile of each displacement process has been analyzed. The average concentration and temperature curves have been used to study the interaction between thermal and concentration fronts. As a quantitative measure of instability, breakthrough of mixing zone defined as the distance between dimensionless concentration (or temperature) values of 0.01 and 0.99 at a defined production end has been examined for different thermal lag coefficients and different diffusion ratios. The effect of thermal log mobility ratio has been studied on the efficiency of the displacement and heating processes and the breakthrough time.

It has been shown that the rate of heat exchange with the medium is a significant factor in prediction of stability of the displacement process. Two different scenarios have been discussed the first being a hot more viscous fluid injected to displace a cold less viscous fluid and the second being a cold less viscous fluid injected to displace a hot more viscous fluid. The flow in the first scenario with Le $= 1$ has been shown to be stable at very low thermal

lag coefficients due to weaker instability on thermal front and less interaction between the two fronts. At higher $\lambda$ values the interaction between the two fronts resulted in backward fingering in concentration front which could affect the sweep efficiency of the process. The flow showed most enhanced instability at $\lambda = 0.8$. The second scenario showed instability for all levels of heat exchange with the medium except for the case where no heat exchange was considered to take place in the system. The effect of thermal front on solutal front vanished when the lag between the two fronts became larger and therefore the effect of $\lambda$ was limited to delaying or reducing instability and the criteria of stability did not change with changing $\lambda$ except for $\lambda = 1$ for which the flow was stable. The discussions about enhancement of instability at different conditions have been examined by looking at the breakthrough time and the efficiency of the process which confirm the previous results.

For higher diffusion ratio of Le = 10 in the first scenario ($\beta_C < 0$, $\beta_T > 0$) it was observed that viscous fingering instability driven by temperature gradient is not as powerful as for lower Le values and the stability of the flow mainly depends on concentration gradient. In the second scenario with $\beta_C > 0$ and $\beta_T < 0$ higher diffusion ratio weakened the stabilizing effect of negative temperature gradient at all $\lambda$ values and hence destabilized the flow at $\lambda = 1$. In general the sensitivity of stability to $\lambda$ decreased as Le was increased and the stability was mainly led by concentration front.

The effect of the thermal log mobility ratio on the stability and sweep efficiency of the process have been examined for another case of displacement where both temperature and concentration profiles contribute to the instability. Although none of the parameters discussed in this study affect the nature of the instability of such processes, variations of the efficiency of the process is of particular interest for industrial purposes. The efficiency analyses reveal that higher temperature of the injected fluid for an already unstable displacement results in enhanced instability and lower sweep efficiency and breakthrough time. This effect

is weakened for higher diffusion rate of heat and faster heat exchange with the reservoir rocks, but for moderate values of $\lambda$ can decrease the efficiency significantly. As a result, it can be concluded that when heating of the reservoir is the main purpose of the hot fluid injection (which is the main reason in oil recovery processes), heat sweep efficiency becomes important which depends highly on the thermal lag coefficient or the heat capacity of the reservoir and the injected fluid.

# Chapter 4

# Scaling and Unified Characterization of Flow Instabilities in Layered Heterogeneous Porous Media

---

[1] The physics of miscible flow displacements with unfavorable mobility ratios through layered heterogeneous media are analyzed and the interactions between the instability mechanisms are investigated. The flow model is solved numerically using a pseudo-spectral method and the effects of various physical parameters such the injection velocity, diffusion, viscosity and the heterogeneity length scale and variance are examined. The flow instability is characterized qualitatively through concentration contours as well as quantitatively through the mixing zone length and the breakthrough time. This characterization allowed to identify four distinct regimes that govern the flow displacement. Furthermore, generalized curves of the mixing zone length have been generated for any flow scenario in which the first three regimes of diffusion, channeling and lateral dispersion superpose into a single unifying generalized curve and allowed to clearly identify the start of the fourth regime of fingering. A critical effective Péclet number $w_c^*$ based on the layers width is proposed to distinguish flow regimes where heterogeneity effects are expected to be important from those where the flow can be safely treated as homogeneous. A similar scaling of the breakthrough time was obtained and allowed to identify two optimal effective Péclet numbers $w_{opt}^*$ that result in the longest and

[1]This chapter is the exact reproduction of the following journal article:
M. Sajjadi and J. Azaiez, "Scaling and Unified Characterization of Flow Instabilities in Layered Heterogeneous Porous Media", *Physical Review E (Statistical, Nonlinear and Soft Matter Physics)*, vol. 88, no. 3, pp. 033017 (12 pp.), 2013.

shortest breakthrough time for any flow displacement.

## 4.1 Introduction

The problem of instability in miscible displacements is encountered in a variety of applications such as polymer processing, fixed bed regeneration, chromatographic separations [72], as well as in oil recovery processes where phase behavior acts in favor of local efficiency of the displacement through miscible flooding. Yet, in many applications, a lower viscosity of the injected solvent results in reduced sweep efficiency of the process due to *viscous instabilities*. Viscous instabilities have been the subject of numerous studies since 1952 when Hill conducted a linear stability analysis along with experiments to examine the coupling between gravity driven and viscous driven instabilities [5]. Interested readers are referred to the reviews of Homsy [1] and McCloud and Maher [2] on viscous fingering in porous media. Other forms of this problem considering non-monotonic viscosity profile [40], non-Newtonian fluids [12], heat transfer in the system [22, 27, 23, 24, 130], and chemical reaction [14, 16, 15] can be found in the literature.

In field applications, the reservoir rocks have variable permeability and are rarely homogeneous. The non-uniform distribution of the permeability changes the preferred path of the flow and becomes the source of another instability mechanism known as *channeling*. Viscous and heterogeneity induced instabilities appear in the form of extended tails of the injected fluid, called fingers. The faster these fingers grow, the faster the injected fluid reaches the production end, and the flow is characterized as more unstable.

Due to its numerous applications, this problem has been studied extensively by researchers working in different fields varying from geology to chemical and petroleum industries. A large number of the investigations have attempted to determine the criteria for the dominance of any of the viscous or heterogeneity mechanisms in the flow. Such

attempts started with quantification of the heterogeneity with a single parameter such as the Dykstra-Parson's coefficient $V_{DP}$ or Lorenz coefficient $L_C$ in stratified reservoirs [58] or through geometric parameters for artificially built heterogeneous systems [76, 131]. These parameters have mainly considered the range of variations of permeability and the frequency of these variations to describe the severity of the heterogeneity [57]. In these works, the relative importance of heterogeneity to that of viscous forces traditionally measured through mobility ratio, has been *qualitatively* determined for constant mobility ratios.

Koval's method in proposing a single factor $K = HE$ that combined the effects of heterogeneity $H$ and viscous forces $E$ was among the rare quantitative analyses in this regard [3]. Although Koval's factors have been useful in the determination of the loss of efficiency due to both instability mechanisms, it was limited to 1D studies and did not analyze the mechanisms of instability and finger structures. Another quantitative analysis was conducted by Sorbie et al. [132] where the $V_{DP}$ and the correlation length $l_D$ of random heterogeneity were used as measures of the severity of the heterogeneity. The effects of the ratio of the transverse ($k_z$) to longitudinal ($k_x$) permeability on the flow regimes were investigated using an effective aspect ratio $R_L = A\sqrt{k_z/k_x}$, where $A$ is the geometric aspect ratio. It was found that large values of $R_L$ corresponding to transverse (vertical) equilibrium (TE) conditions result in dispersive flow while scenarios far from the TE conditions, namely in Dykstra-Parson's regimes (DP) result in isolated channeled fingers. However the effect of $R_L$ was shown to be important only for very small correlation lengths and became negligible even for $l_D = 0.1$. The authors commented that for layered media, transverse permeability may not have significant effects on the flow except for neutral mobility ratio. In a subsequent study, Yang et al. [133] used asymptotic analysis to analyze flows with no dispersion in spatially uncorrelated heterogeneous media for limiting values of the parameter $R_L$. The asymptotic analysis was compared with predictions from full numerical simulations and allowed to separate and

characterize the flow in the limiting regimes.

The first experimental study on miscible flows through heterogeneous porous media was performed by Balckwell et al. in 1959 [54] and has been a reference for many subsequent analytical and numerical studies. Among these, one should cite the study of Araktingi and Orr [64] who have used the particle-tracking method to successfully model miscible flows through heterogeneous porous media and have reported results that are in agreement with the experimental ones by Blackwell et al. [54].

The pseudo-spectral method was also used by Tan and Homsy [69] to study the effects of random permeability variations with Gaussian log distribution on viscous fingering. In both studies, the effects of variance and correlation length of the permeability distribution on the growth rate of the instabilities were analyzed. In particular, Araktingi and Orr [64] observed a monotonic increase of the instability with both the correlation length and the variance of the heterogeneity. Tan and Homsy [69] observed a maximum growth rate at a certain correlation length of heterogeneity and discussed the resonance between the mechanisms of instabilities at an optimum correlation length, commensurate with the intrinsic scale of viscous fingers. These two studies were later followed by linear stability analysis and nonlinear simulation studies [72, 73, 66, 134]. In particular, the study by De Wit and Homsy [72, 73] who focused on media with harmonically varying permeability, showed that the wave number at which resonance is observed depends on the log mobility ratio and the Péclet number.

In this chapter, a thorough examination of the effects of different parameters on the development of the instability in heterogeneous media is presented. The study will analyze the different regimes of the flows and will propose a unified picture of the flow that incorporates the effects of all pertinent parameters, including the injection velocity, diffusion rate, the mobility ratio as well as the characteristics of the heterogeneous medium such as variance and length scale of permeability.

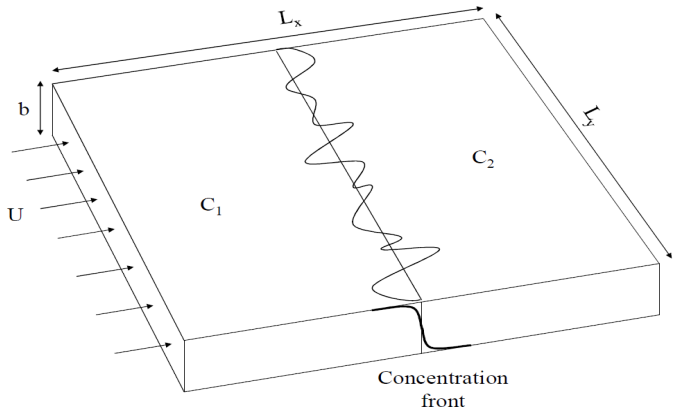


Figure 4.1: Schematic of the flow,

## 4.2 Physical Model and Numerical Method

Figure 4.1 shows a schematic of the simplified model used in this work. A fluid (fluid 1) with uniform concentration $C_1$ is injected in the heterogeneous porous medium with an average velocity $U$ to displace the resident fluid (fluid 2) of uniform concentration $C_2$. The flow is assumed to be incompressible, Newtonian and isothermal, and is governed by the equations for the conservation of mass and momentum and the mass convection-diffusion [22].

$$\frac{\partial u}{\partial x} + \frac{\partial \nu}{\partial y} = 0 \tag{4.1}$$

$$\begin{aligned} \frac{\partial P}{\partial x} &= -\frac{\mu \phi u}{\kappa} \\ \frac{\partial P}{\partial y} &= -\frac{\mu \phi \nu}{\kappa} \end{aligned} \tag{4.2}$$

$$\frac{\partial C}{\partial t} + (\mathbf{u}.\nabla)C = D_C \nabla^2 C \tag{4.3}$$

In the above equations $\mathbf{u}$(u,v) is the interstitial velocity vector, $P$ the local pressure, $\kappa$ local permeability, $\phi$ the porosity and $\mu$ the viscosity. Furthermore, the concentration

is denoted by $C$ and the mass diffusion coefficient by $D_C$. Following Tan and Homsy [8], diffusive scaling is used to make the equations dimensionless:

$$
\begin{aligned}
&(\hat{x}, y^*) = \frac{x, y}{D_C\phi/U} \qquad t^* = \frac{t}{D_C\phi^2/U^2} \qquad (\hat{u}, v^*) = \frac{(u, v)}{U/\phi} \qquad p^* = \frac{P}{D_C\mu_1\phi/\kappa_1} \\
&\mu^* = \frac{\mu}{\mu_1} \qquad \kappa^* = \frac{\kappa}{\kappa_1} \qquad c^* = \frac{C}{C_1}
\end{aligned}
\tag{4.4}
$$

The permeability is scaled by the average permeability of the medium; $\kappa_1$ . A Lagrangian reference frame moving with the average injection velocity, $U/\phi$, is used so $x^* = \hat{x} - t^*$ and $u^* = \hat{u} - 1$, and the resulting dimensionless equations are:

$$
\begin{aligned}
&\frac{\partial u^*}{\partial x^*} + \frac{\partial v^*}{\partial y^*} = 0 \\
&\frac{\partial p^*}{\partial x^*} = -\frac{\mu^*}{\kappa^*}(u^* + 1), \quad \frac{\partial p^*}{\partial y^*} = -\frac{\mu^*}{\kappa^*}v^* \\
&\frac{\partial c^*}{\partial t^*} + u^*\frac{\partial c^*}{\partial x^*} + v^*\frac{\partial c^*}{\partial y^*} = \left(\frac{\partial^2 c^*}{\partial x^{*2}} + \frac{\partial^2 c^*}{\partial y^{*2}}\right)
\end{aligned}
\tag{4.5}
$$

Henceforth, the stars are dropped for simplicity. In the above equations, two variables need to be specified to close the formulation of the problem. First, the nature of dependence of the viscosity on concentration must be specified. In this study, an exponential dependence of the viscosity on concentration [25, 41, 23] is adopted unless indicated otherwise. Such a dependence closely characterizes the "quarter power mixing rule" widely used in petroleum industry to describe viscosity of non associating mixtures and also mixtures of diluted aqueous solutions [135, 136, 137]:

$$
\mu(c) = \exp[\beta_C(1 - c)] \tag{4.6}
$$

In the above equation $\beta_C$ is the natural logarithm of the viscosity ratio $\mu_2/\mu_1$ and is related to the mobility ratio $M$ as $\beta_C = \ln(M)$. Furthermore, the form of the permeability used to characterize the heterogeneity of the medium needs to be defined. At the pore scale, the variability of the permeability should be negligible for Darcy's description of the flow to be applicable. But it should be sensed by the flow in larger scale for the medium to be called

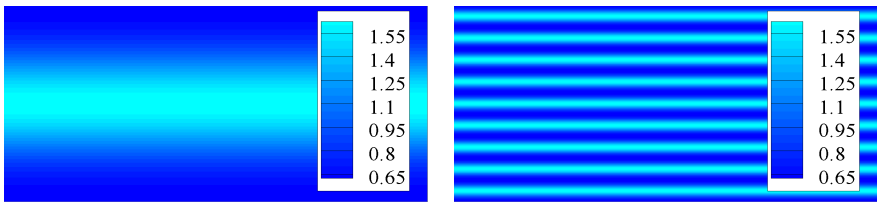


(a) (b)

Figure 4.2: Periodic permeability models with permeability varying between $\kappa = 0.7$ and $\kappa = 1.6$ for $s = 0.5$; a) $q = 1$ and b) $q = 9$

heterogeneous. In the present study the permeability of the medium is assumed to vary only in the transverse ($y$) direction. As it shall be seen later, the gradient of the natural log of the permeability $f = \ln(k)$ appears in the definition of the vorticity and therefore the heterogeneity will be characterized using the natural log of the permeability; $f$. For a layered heterogeneous medium, $f$ is defined as [72]:

$$f = \ln[\kappa(x, y)] = s\cos(\frac{2\pi}{l_y}qy) \tag{4.7}$$

where $s$ is the range of variation of $f$ while $q$ is the frequency of layers across the flow channel in the $y$ direction and $l_y$ is the dimensionless width of the domain. Two examples of heterogeneity models for different values of $q$ are shown in Figure 4.2. Although this adopted periodic permeability is a simple model of heterogeneity, it still allows to reveal some of the mechanisms that can occur in more stochastic permeability models that are difficult to characterize due to the complexity of such models.

Using the definition of vorticity ($\omega$) and the stream function ($\psi$) where $\nabla^2\psi = -\omega$, and adopting the correlations for the viscosity and natural log of the permeability, the set of equations 4.5 lead to:

$$\frac{\partial c}{\partial t} + \frac{\partial \psi}{\partial y}\frac{\partial c}{\partial x} - \frac{\partial \psi}{\partial x}\frac{\partial c}{\partial y} = \nabla^2 c \tag{4.8}$$

$$\begin{aligned}\omega &= (\nabla\psi + \mathbf{j}).(\frac{\partial(\ln(\mu))}{\partial c}.\nabla c - \nabla \ln \kappa) \\ &= -(\nabla\psi + \mathbf{j}).\,(\beta_C \nabla c + \nabla f)\end{aligned} \tag{4.9}$$

These dimensionless equations admit a base-state solution $\bar{c}$ corresponding to a uniform injection velocity (in the moving reference frame; $\bar{u} = \bar{v} = 0$):

$$\bar{c} = \frac{1}{2}\,\mathrm{erfc}\left(\frac{x}{2\sqrt{t}}\right) \tag{4.10}$$

The equations are transformed in Hartley space using the Hartley transform [138]. This method has the advantage of increasing the accuracy of differentiations in space but requires periodic boundary conditions. Therefore, the solution is sought as the sum of the base state profile $\bar{c}$ and perturbations ($c'$) that decay far upstream and downstream [139]. This leads to a nonlinear ordinary differential equation for the concentration perturbation coupled with algebraic equations for the vorticity, all expressed in the Hartley transform space [139]. Since the non-periodic part of the solution is calculated analytically through base state Equation 4.10, periodic boundary and initial conditions can be set for the perturbed concentration and for vorticity as:

$$\begin{aligned}&(\omega', c')(-\mathrm{Pe}/2, y, t) = (0, 0) \\ &(\omega', c')(\mathrm{Pe}/2, y, t) = (0, 0) \\ &(\omega', c')(x, \mathrm{Pe}/A, t) = (\omega', c')(x, 0, t) \\ &(\omega', c')(x, y, 0) = (\delta\ \mathrm{rand}(y) e^{-x^2/\sigma^2}, 0)\end{aligned} \tag{4.11}$$

In the above equations, $\mathrm{Pe} = \frac{UL_x}{D_C}$ is the Péclet number and $A = L_x/L_y$ is the aspect ratio of the domain. In dimensionless form $l_x = \mathrm{Pe}$ and $l_y = \mathrm{Pe}/A$ are the length and the width of the medium respectively.

The differential equation for the transform of the concentration perturbation is stepped in time using a fourth-order Adams-Bashforth/Adams-Moulton scheme with operator splitting.

Furthermore, under-relaxation was used in the iterative process relating the vorticity to the stream-function. This algorithm was shown to be numerically stable and highly accurate for Péclet numbers as high as Pe = 1750 for log-mobility ratio $\beta_C = 5$ and for $\beta_C$ as large as $\beta_C = 7$ when Pe = 500. More details about the numerical algorithm are found in [139, 140]

The numerical method was validated by comparing the time evolution and the related viscous fingers interactions for the homogeneous case where $\beta_C = 3$, Pe = 500, and $A = 2$ with those of Tan and Homsy [8]. Furthermore, the convergence of the numerical solution was examined by considering cases with different spatial resolutions varying from $256 \times 256$ to $1024 \times 1024$ while changing the time step accordingly. In particular, for the largest mobility ratio examined, $\beta_C = 5$, the convergence was confirmed by checking that the concentration contours based on grids of $512 \times 512$ and $1024 \times 1024$ were actually identical.

## 4.3 Results and Discussion

As mentioned before, a heterogeneous medium is characterized by the length scale and variance of the permeability distribution. In the periodic permeability field defined by Equation 4.7, the width of the channels which varies like the inverse of the number of layers can be regarded as the length scale of heterogeneity while $s$ gives a reasonable estimation of the variance of the permeability distribution. In a first stage, the focus will be on the effects of the permeability length scale (number of layers $q$) on the flow structures and growth of the mixing zone. The analysis will be then expanded to analyze the effects of other parameters and examine the flow breakthrough time. Unless specified otherwise, the mobility ratio, permeability variance, Péclet number and cell aspect ratio are fixed as $\beta_C = 3$, $s = 0.1$, Pe = 1024, and $A = 2$.

### 4.3.1 Flow Structures

In this section, the results are presented in the form of time sequences of concentration contours which vary between zero and one. For brevity, the time sequences are presented not necessarily at the same time intervals, and only the frames that help characterize and understand the development of the flow are shown.

In Figure 4.3 two flow displacements through layered media with $q = 2$ and $q = 9$ are compared with that in a homogeneous medium. It is clear that the flow structures differ from one case to the other, with the fingers extending faster in the flow direction in the case of the 2-layers and slower in the nine-layer medium. The number of initial fingers in the heterogeneous cases is determined solely by the number of layers while it depends on the flow properties $(\mathrm{Pe}, \beta_C)$ in the homogeneous medium. In the latter case, the number of fingers decreases through a number of interaction mechanisms that have already been discussed in the literature. Focusing on the heterogeneous scenarios, the fingers in the two-layered medium remain constrained within the high permeable channels which is to be contrasted with the nine-layer medium where from the initial nine fingers, only two end up dominating the flow at later times.

The smaller length scale of heterogeneity in the nine-layer medium results in larger $\nabla f$ and a rapid growth of instabilities at early times ($t = 100$). However the fingers in the wider channels of the double-layer medium end up surpassing those in the nine-layer medium. This can be explained by the fact that the instability in the double layer medium is driven by the so-called channeling mechanism in which the dynamics are governed by the viscous forces and the paths of the flow are dictated by the heterogeneity of the medium [69]. In this case, viscous and heterogeneity driven forces keep acting with two distinct sharp fingers extending and developing independently until the flow reaches the downstream boundary. In the nine-layer medium however, due to the smaller channels width, after a while the

fingers get so close to each other that further development and growth is stalled in favor of lateral dispersion across the channels. This dispersion causes the channeled fingers to fade into a thick wavy front. Since the growth of fingers during this dispersive stage is slow, the thickness of the dispersed front is virtually the same as the length of the fingers at the start of the dispersion. It is anticipated that an even smaller width of the layers will result in earlier start of dispersion and a thinner dispersed front. Later, instabilities develop at the front as a result of viscous forces as shown in Figure 4.3c and lead to two dominant fingers. These instabilities are not dictated by the heterogeneity of the nine-layer medium but the thickness of the front (influenced by the thickness of the layers) is expected to affect the number of emerging fingers as well as their growth rates.

The differences between the two heterogeneous displacements and the homogeneous one help explain different phenomena observed in experimental and numerical studies of flow through heterogeneous porous media. In particular, the dispersion of fingers across the channels in the nine-layer medium results in stronger mixing of the fluids which explains the increase in macroscopic dispersion in heterogeneous media reported in different simulation and experimental studies [141, 142]. Furthermore, the fact that the effects of heterogeneity in the nine-layer medium pales as the dispersion of fingers across the channels occurs and that the later fingers are not determined by the channels (see Figure 4.3c) confirms the results of [64] where it was reported that for smaller correlation length of heterogeneity, fingers do not follow high permeable channels.

In what follows, the flow instability in heterogeneous media is characterized through a quantitative analysis. *In specie*, the length of the mixing zone along the flow direction [7] and the breakthrough time [66] are used to quantify and characterize the instability.

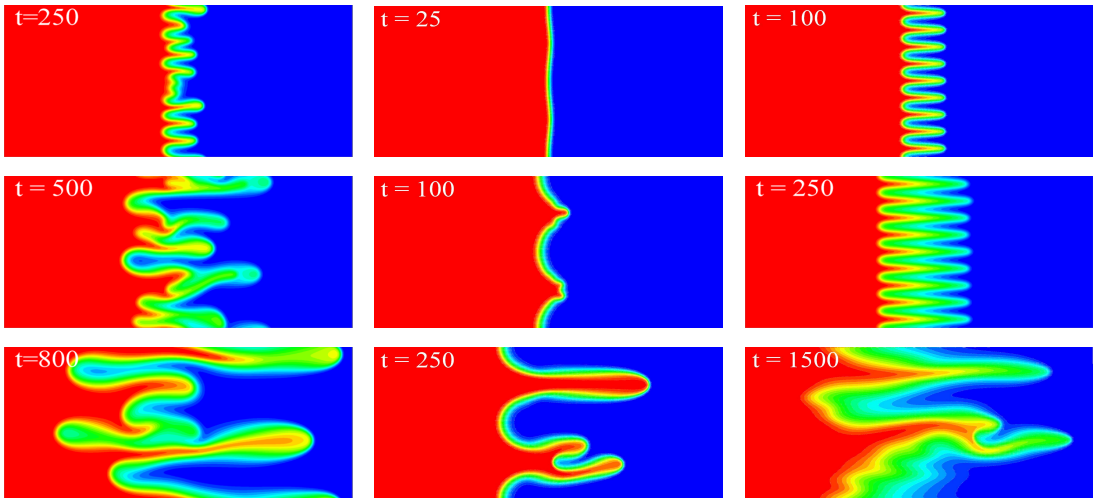


(a) Homogeneous medium (b) Double layer medium (c) Nine layer medium

Figure 4.3: Concentration contours for a viscously unstable flow with $\beta_C = 3$, Pe $= 1024$, and $A = 2$ in a) a homogeneous medium, b) a double-layer heterogeneous medium, and c) a nine-layer heterogeneous medium. In each frame the red color (left) represents $c = 1$ and the blue color (right) represents $c = 0$.

### 4.3.2 Mixing Length

By averaging the values of concentration across the flow channel *Mixing Zone length* (MZL) is determined. The mixing zone is defined as the zone with average concentration values between 0.01 and 0.99 [8].

$$c_{av}(x) = \frac{1}{l_y}\int_0^{l_y} c(x,y)dy$$
$$MZL = x_{c_{av}=0.01} - x_{c_{av}=0.99} \tag{4.12}$$

To elaborate more on the behavior of the flow with time, the variation of the MZL with time is depicted in Figure 4.4 for the nine-layer case discussed above. For comparison purposes, the MZL of the viscously unstable flow in a homogeneous medium as well as those of neutral flow ($\beta_C = 0$) in the nine layer medium and in a homogeneous medium are also presented. Figure 4.4a illustrates the whole curves in log-log scales to elucidate the trend of growth of mixing zone while Figure 4.4b focuses on the initial stages of the flow in linear scales.

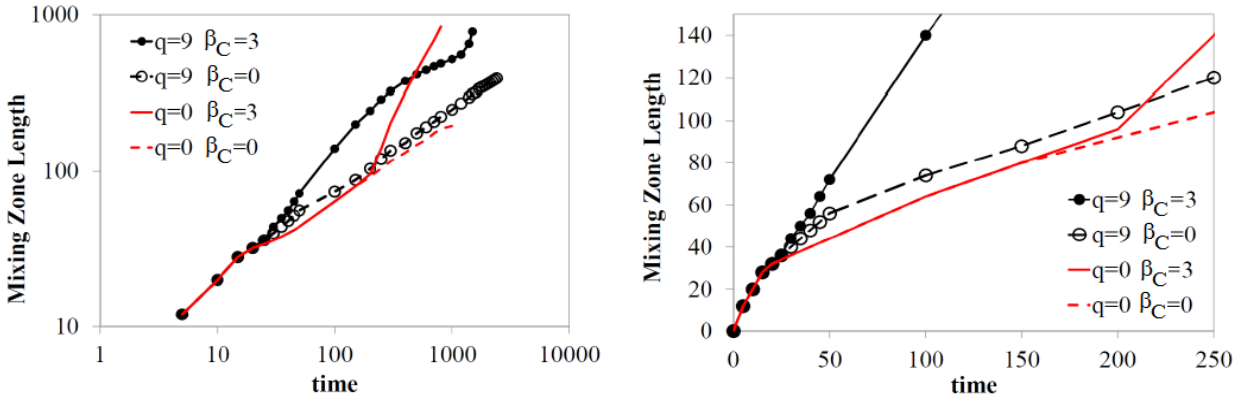


(a) (b)

Figure 4.4: Mixing zone length versus time for stable and unstable flows in homogeneous medium and in a nine-layer heterogeneous medium; Pe = 1024, $A = 2$, $s = 0.1$, a) throughout the process in logarithmic scales, b) at early times.

It can be seen from Figure 4.4 that the viscously stable flow ($\beta_C = 0$) shows dispersive behavior in both the homogeneous medium and the nine-layer medium with its MZL growing as $\sqrt{t}$. In a homogeneous porous medium, the unstable flow ($\beta_C = 3$) goes first through a dispersive regime similar to that observed in the stable flow. This first regime which lasts up to $t \simeq 200$ is followed by the development of viscous instability where MZL grows almost linearly with time (see Figure 4.4b). In the nine-layer medium, the unstable flow also goes through initial dispersion but the MZL graph follows that of the viscously stable flow in the heterogeneous medium which has a slightly higher dispersion rate than that in the homogeneous medium. Around $t \simeq 25$, viscous forces help channeled fingers grow faster than the viscously stable scenario. At this stage, even though the fingers follow the path dictated by the heterogeneity, their growth rate depends on both viscous forces and heterogeneity. Later, the growth rate of the MZL decreases as the fingers start to disperse across the channels. Lateral dispersion continues until the gradient of concentration across the channels becomes negligible. Subsequently, viscous instabilities develop on the dispersed front at around $t \simeq 1400$ and viscous fingering becomes the dominant regime resulting in a sudden increase of the MZL.

We will now investigate the effect of the length scale of the heterogeneity (width of the channels) on the flow behavior. To this end, more numerical simulations were conducted for various numbers of layers and the corresponding MZL were determined. Figure 4.5 depicts the variations of the MZL for the homogeneous medium and for heterogeneous media with $q = 2, 5, 7, 9$, and 15. This figure reveals that regardless of the number of layers, the heterogeneous flows go through the same regimes identified earlier in the special case of the nine-layer medium. However, the extent and strength of these regimes vary from one case to the other, and in some cases such as the two-layer medium, the channeled fingers reach the domain boundary before lateral dispersion of fingers can be actually observed. As can be seen in Figure 4.3, the growth rate of the mixing zone is larger at the initial stages of the flow for media for larger number of layers because of larger $\nabla f$. Therefore, at early times the growth rate of MZL increases monotonically with increasing $q$ as shown in Figure 4.5b. At later times however, a larger number of layers reduces the width of the channels and as a result speeds up lateral dispersion. Therefore the front becomes uniform across the medium faster and the last stage of viscous fingering develops earlier. As can be seen, the two regimes of channeling and dispersion that precede the viscous fingering are shortened as the number of layers is increased. As we shall see later, for a large enough number of layers, the MZL of the layered heterogeneous medium will actually asymptotically approach that of the homogeneous medium where only the initial diffusive regime and viscous fingering are observed.

Hydrodynamic Scaling

The close similarity in the curves for different numbers of layers raises the question of whether it is possible to obtain a single curve that can describe the variations of the MZL for any arbitrary number of layers. In order to explore this idea, it is proposed to analyze the main parameters that govern the flows in the different regimes identified earlier. First one

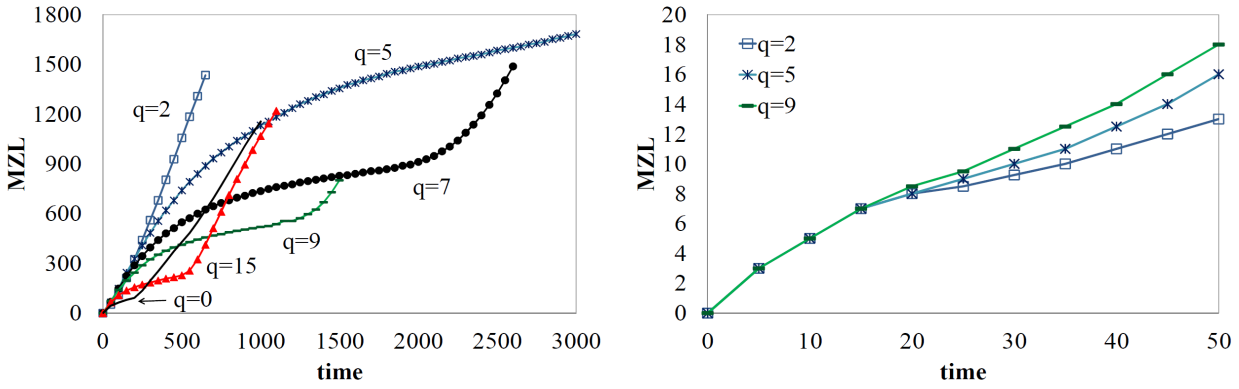


(a) (b)

Figure 4.5: Mixing zone length versus time for heterogeneous media with different number of layers for $\beta_C = 3$, Pe $= 1024$, $A = 2$ and $s = 0.1$; a) throughout the process, b) at the initial times (fewer graphs are shown for better distinction between the lines).

can note that the first stages of the instability are mainly governed by the flow within the high permeability layers. This suggest to characterize the instability at this scale. Hence, a characteristic time for lateral dispersion across a layer of width $w = L_y/q$ and a characteristic length in the streamwise direction are defined as $t_c = w^2/D_C$ and $x_c = Uw^2/(D_C\phi)$, respectively. In dimensionless form these characteristic parameters become:

$$\begin{aligned} t_c^* &= \frac{t_c}{D_C\phi^2/U^2} = \frac{(w^* \times D_C\phi/U)^2/D_C}{D_C\phi^2/U^2} = w^{*2} \\ x_c^* &= \frac{x_c}{D_C\phi/U} = \frac{U(w^* \times D_C\phi/U)^2/(D_C\phi)}{D_C\phi/U} = w^{*2} \end{aligned} \tag{4.13}$$

The stars on the dimensionless parameters were retained to distinguish them from the dimensional ones. The width of the domain in dimensionless form is $l_y = \text{Pe}/A$ and the dimensionless width of each layer can be determined as $w^* = \text{Pe}/(q.A)$. A generalized time $\tilde{t}$ and length $\tilde{x}$ are then defined as:

$$\begin{aligned} \tilde{t} &= \frac{t}{t_c} = \frac{t^*}{t_c^*} = \frac{t^*}{(\frac{\text{Pe}}{q.A})^2} \\ \tilde{x} &= \frac{x}{x_c} = \frac{x^*}{x_c^*} = \frac{x^*}{(\frac{\text{Pe}}{q.A})^2} \end{aligned} \tag{4.14}$$

A large number of simulations were conducted for many combinations of a wide range of parameters with Pe = 512, 1024, 2048, $A = 2, 4, 8$, and $q = 1$ *to* 20, and the mixing lengths were determined. The corresponding generalized mixing zone lengths ($\tilde{MZL} = MZL/x_c$) are plotted versus the generalized time and are shown in Figure 4.6a. It is clear that the scaling does indeed result in a single curve for different displacement scenarios. Even for cases where the simulations stopped due to the fingers reaching the boundaries, $\tilde{MZL}$ still follows the unifying generalized curve. However, it should be stressed that the different curves do superpose only up to the time where the viscous fingering regime starts. At this convective regime, the growth rate of the MZL depends on the Péclet number and cannot be predicted based only on this dispersive scaling. The results of this scaling imply that the quantitative behavior of the displacement can be predicted for any given scenario and length scale of permeability variations.

The proposed generalization allows identifying and defining the different dominant flow regimes and the transition times in between these regimes. Figure 4.6b shows a log-log plot of the $\tilde{MZL}$ versus $\tilde{t}$ with trend lines fit to each segment categorizing a particular flow regime. These regimes can be identified as *initial diffusion, channeling, lateral dispersion,* and *viscous fingering.* In the initial diffusion regime, $\tilde{MZL}$ grows almost as $\sqrt{\tilde{t}}$. The coupling between viscous forces and heterogeneity increases the growth rate of $\tilde{MZL}$ to almost a linear function of time; $\tilde{t}^{1.01}$ and leads to the channeling regime. In the third regime, lateral dispersion causes the growth rate to decrease to less than the initial diffusion regime and $\tilde{MZL} \equiv \tilde{t}^{0.32}$. Ultimately viscous fingering leads to $\tilde{MZL}$ growing faster than in previous regimes. The transition from initial diffusion to channeling occurs at $\tilde{t}_{dC} \approx 0.01$ while that from channeling to lateral dispersion is at $\tilde{t}_{CD} \approx 0.07$. Finally lateral dispersion leads to viscous fingering which develops at different times depending on the value of Pe.

The scaling group $w^* = \mathrm{Pe}/(q.A) = Uw/D_C$ suggests that larger velocity, weaker dif-

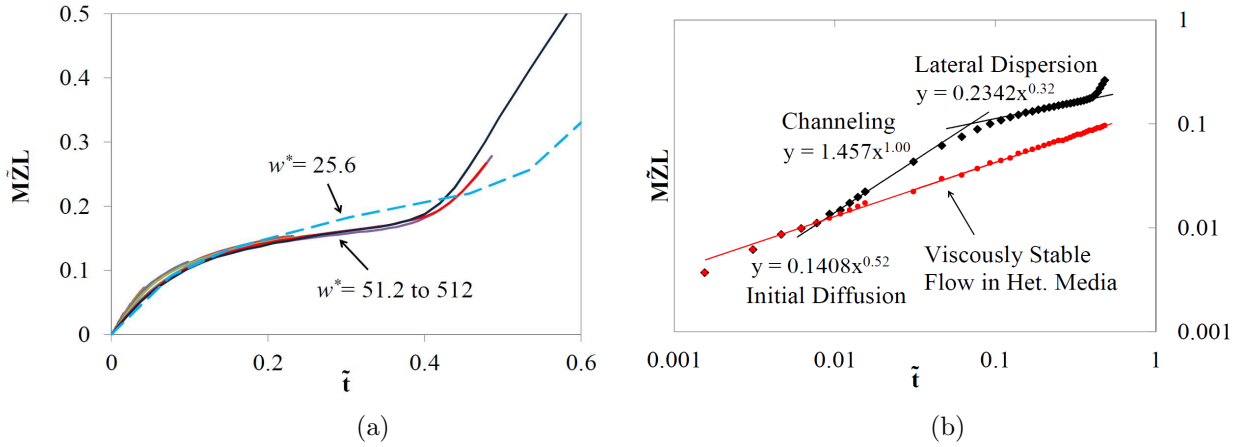


Figure 4.6: Generalized MZL versus generalized time for $\beta_C = 3$ and $s = 0.1$; a) for $w^* = 25.6,\ 51.2,\ 56.9,\ 64,\ 73.1,\ 102.4,\ 113.8,\ 128,\ 146.3,\ 170.7,\ 204.8,\ 256,\ 241.3$, and 512, b) for $w^* = 51.2$ in log-log scale indicating the flow regimes.

fusion rate or larger channels width result in a slower transition from channeling to lateral dispersion and further to viscous fingering. In all these cases, fingers develop individually in the channels and grow longer with minimum interactions. Such fingers require more time to get transversely dispersed and the flow stays in the lateral dispersion regime for longer time before viscous fingering starts.

Small values of $w^*$ however, result in stronger dispersion compared to the rate of advancement of instabilities and hinders the development of channeling. In such cases, emerging channeling fingers if any, will fade rapidly into a dispersed front in the early stages of the flow, allowing viscous fingering to develop across that front. In an extreme case, a layered system with a large enough number of layers will not experience channeling or lateral dispersion and will go directly through viscous fingering as in a homogeneous porous medium. Therefore as $w^*$ decreases, $M\tilde{Z}L$ deviates from the unifying generalized curve characterizing the flow in a heterogeneous medium, and as we shall see later, MZL will approach that of a homogeneous case. One can therefore select a critical value of the effective Péclet number $w_c^*$ to separate flows in which heterogeneity is dominant from those in which it can be ignored. The value of this critical Péclet number can be determined on the basis of the extent of

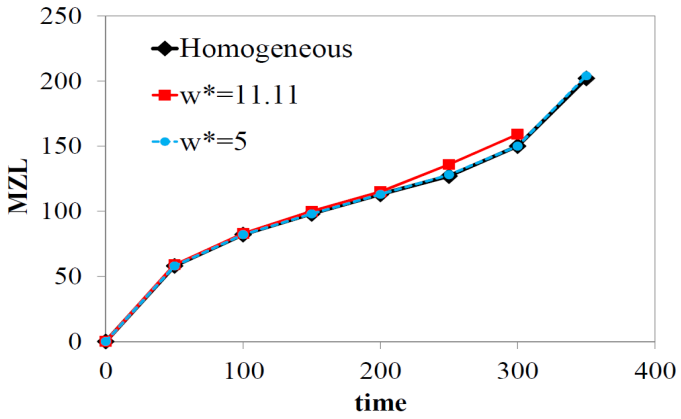


Figure 4.7: Weak effect of heterogeneity in media with small dimensionless width of layers for $\beta_C = 3$, $s = 0.1$, Pe $= 200$, and $A = 2$

the lateral dispersion regime and specifically the slope of the $M\tilde{Z}L$ in that region. Hence a displacement flow with $M\tilde{Z}L$ slope in the lateral dispersion region of more than about $t^{0.4}$ (the slope of the lateral dispersion regime on the curve corresponding to $w^* = 25.6$) leans towards a homogeneous system and the effects of heterogeneity can be deemed negligible.

To further illustrate these conclusions, the MZL for Pe$/(q.A) = 11.11$ and for Pe$/(q.A) = 5$ as well as for the homogeneous medium are depicted in Figure 4.7. The results are presented in terms of MZL since $M\tilde{Z}L$ is not defined for a homogeneous medium. It is clear that the curves are virtually indistinguishable, indicating that flows in such heterogeneous media essentially behave like in a homogeneous medium, at least in terms of their MZL.

The close similarity between heterogeneous flows with small effective Péclet number $w^*$ and those in homogeneous medium was actually found to be not limited to quantitative properties such as the MZL, but is also observed in the actual flow structures. Figure 4.8 shows concentration contours for the homogeneous medium and heterogeneous media with $w^* = 11.11$ and $w^* = 33.3$ at $t = 300$. It is clear that the flow structures in the homogeneous medium and the heterogeneous one with $w^* = 11.11$ are virtually identical while the effects of heterogeneity manifested in the form of fingers developing in the high

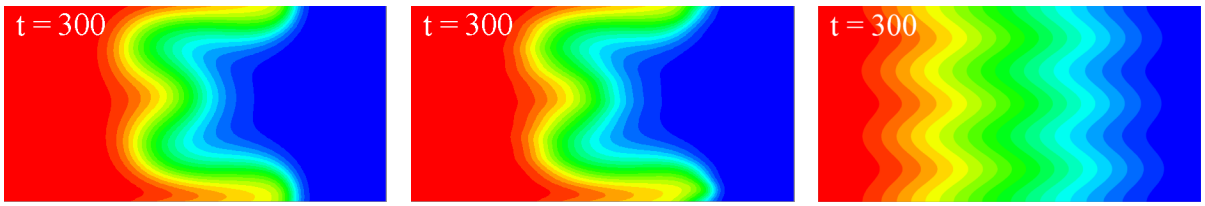


(a) Homogeneous (b) $q = 9$ (c) $q = 3$

Figure 4.8: Concentration contours for $\beta_C = 3$, Pe $= 200$, $A = 2$, a) homogeneous porous medium and b) 9-layer heterogeneity, $w^* = 11.1$, c) 3-layer heterogeneity, $w^* = 33.3$. In each frame the red color (left) represents $c = 1$ and the blue color (right) represents $c = 0$.

permeability channels are dominant in the medium with $w^* = 33.3$. This further confirms the criteria based on the parameter $w^*$ to define a limit for a permeability length scale below which the effects of heterogeneity are so small that they do not play any significant role in driving the instabilities, and the medium can be treated as homogeneous in terms of the flow dynamics. As a general guideline, one may treat flow displacements in heterogeneous media as effectively homogeneous flows for $w^* < w^*_{c-h} = 15$ and as heterogeneous flows for $w^* > w^*_{c-H} = 30$.

It is important at this stage to note that the generalized curve in Figure 4.6b was generated for given values of the log mobility ratio ($\beta_C = 3$) and permeability variance ($s = 0.1$). It would therefore be interesting to determine how the previous conclusions may change for other values of $\beta_C$ and $s$.

Figure 4.9 depicts generalized curves for different combinations of $(\beta_C, s)$. Regardless of the values of $\beta_C$ or $s$, all curves follow the same trends and go through the different regimes that have been identified earlier. It is worth noting that increasing $s$ has the same effect on $\tilde{MZL}$ as decreasing $q$ had on $MZL$ in Figure 4.5. Higher permeability variance leads to stronger growth rate of fingers inside the channels during the channeling regime, while it delays the transition to viscous fingering. This is different from the effect of the viscosity ratio which shortens the transition regime as it increases the growth rate of instabilities in all regimes.

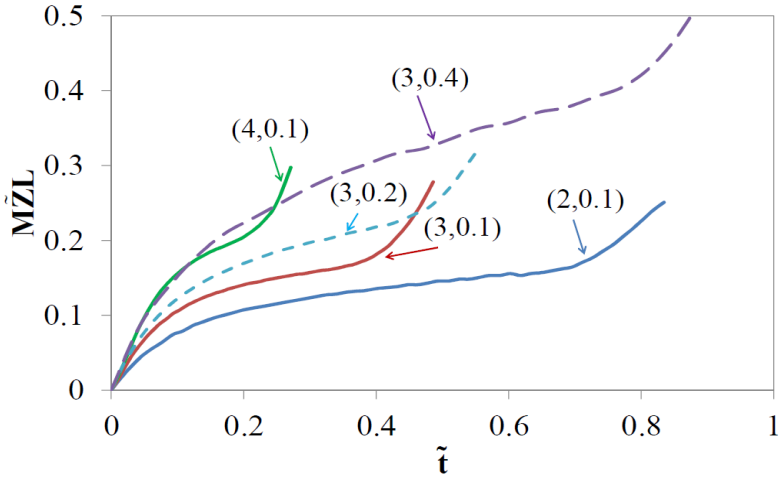


Figure 4.9: Generalized MZL for different combinations of mobility ratio and variance of permeability distribution $(\beta_C, s)$

Based on the results in Figure 4.9 one may wonder if the scaling developed so far can be further extended to include the effects of the heterogeneity variance and viscosity. These two aspects are examined in the following sections.

Heterogeneity Scaling

A proper scaling of MZL to account for the effects of changes in the permeability variance can be accomplished by dividing both the generalized length and time by $\kappa_c = exp(2 \times s)$, which is the ratio between the maximum and minimum permeability values. This scaling can be justified by noting from Darcy's equation that the effects of permeability $\kappa$ are commensurate with those of velocity $u$, ceteris paribus:

$$u = -\frac{\kappa}{\mu}\frac{\partial p}{\partial x} \tag{4.15}$$

One may therefore posit that variations of $\kappa \equiv e^s$ affect MZL in the same way as velocity does, or equivalently as $\text{Pe} = UL_x/D_C \equiv w^*$. This and the fact that we have seen that the appropriate hydrodynamic scaling is based on $w^{*2}$ leads to the proposed heterogeneity scaling of $e^{2s}$ commensurate with $w^{*2}$. The results of scaling the generalized $MZL$ to account

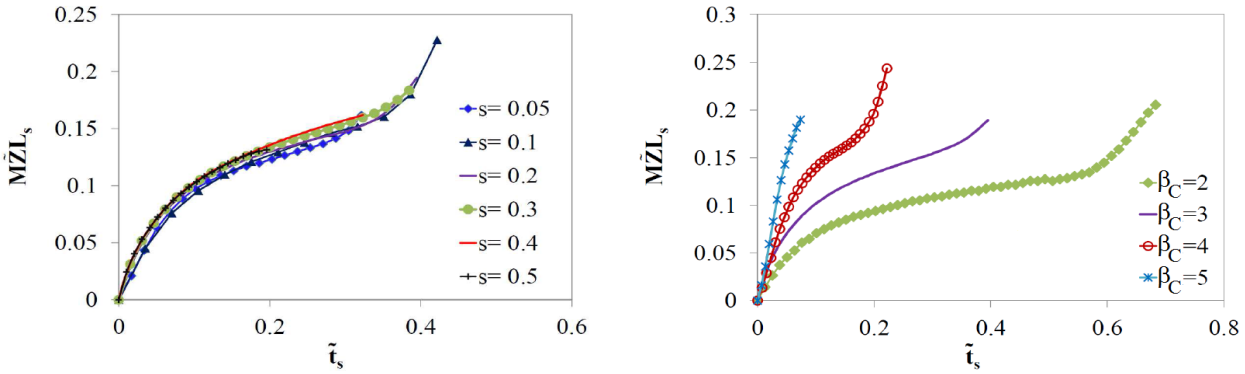


(a) (b)

Figure 4.10: Re-normalization of MZL to account for variance of permeability distribution $s$; The flow parameters are: Pe $= 2048$, $A = 4$, $q = 7$, a) $\beta_C = 3$, b) $s = 0.1$, different log mobility ratios.

for the effect of the strength of heterogeneity as $\tilde{t}_s = \tilde{t}/e^{2s}$ and $M\tilde{Z}L_s = M\tilde{Z}L/e^{2s}$ are shown in Figure 4.10. It is clear that the proposed scaling does allow to collapse the various curves into a single unifying curve that allows to characterize MZL regardless of the values of the heterogeneity variance. Figure 4.10b shows the re-normalized curves for different log-viscosity ratios, and here again qualitative similarity between the different curves indicates that it may be possible to also scale the effects of viscosity.

Viscosity Scaling

As mentioned before, the effect of log mobility ratio is to enhance the instabilities in all regimes and it is different from the effect of other properties discussed so far which are mainly related to the heterogeneity of the medium. The graphs of $M\tilde{Z}L_s$ for different values of $\beta_C$ shown in Figure 4.10b can be reduced to a master curve by scaling only the length by $e^{\beta_C/3.1}$. Hence the proposed scaling is as follows:

$$MZL_{master} = \frac{M\tilde{Z}L_s}{e^{(\beta_C/3.1)}}$$
$$t_{master} = \tilde{t}_s \tag{4.16}$$

This normalization was obtained through an estimation of the calculated factors for

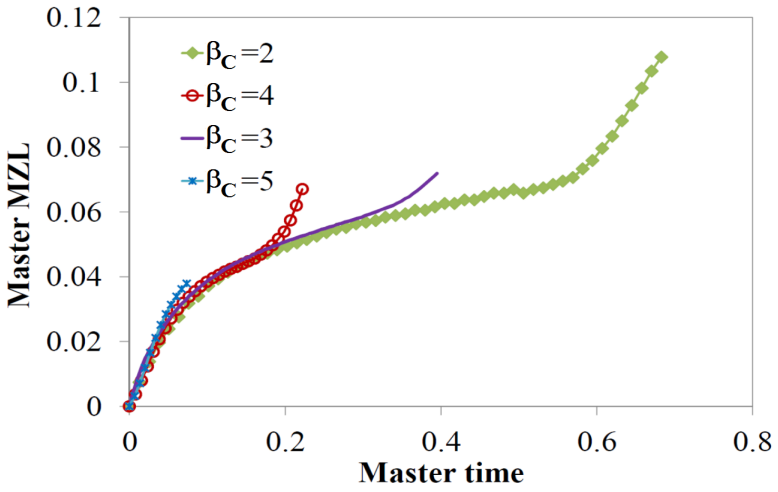


Figure 4.11: Fitting of $M\tilde{Z}L_s$ curves of different displacement scenarios with Pe = 2048, $A = 4$, $q = 7$, $s = 0.1$, and for different mobility ratios as noted on the plot.

matching the curves and is not based on any actual physical arguments. Still, as can be seen from Figure 4.11, it allowed to build a general unifying curve that characterizes the first flow regimes for any values of the fluid properties or the medium heterogeneity. Note that despite the superposition of the curves in the channeling and lateral dispersion regimes, earlier transition from lateral dispersion to viscous fingering is observed for higher log mobility ratios.

Before closing this section, the dependence of the previous conclusions on the type of viscosity model will be examined. Different models are used in the literature [143, 144] but for the sake of brevity, the discussion will be based on the quarter power mixing rule defined as [144]:

$$\left(\frac{1}{\mu}\right)^{1/4} = \left(\frac{C_1}{\mu_1}\right)^{1/4} + \left(\frac{C_2}{\mu_2}\right)^{1/4} \tag{4.17}$$

Generalized MZL plots generated with the quarter power mixing rule are shown in Figure 4.12 for viscosity ratio of $M = 20$ equivalent to $\beta_C = 3$ in the exponential viscosity correlation for $q = 5$ and $q = 7$. For comparison purposes, the corresponding $M\tilde{Z}L$ curves for the exponential viscosity model are also plotted. It can be seen that the variations of $M\tilde{Z}L$ of

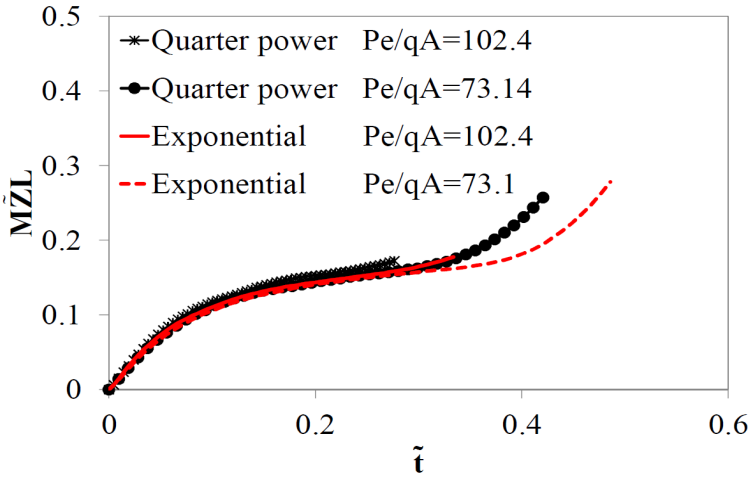


Figure 4.12: Effect of viscosity model on MZL for an unstable flow with mobility ratio of $M = 20$ corresponding to $\beta_C = 3$, with Pe $= 2048$, $A = 4$, and $s = 0.1$ in a 5-layer and a 7-layer medium corresponding to $w^* = 102.4$ and $w^* = 73.1$ respectively.

both viscosity models are qualitatively similar and the different regimes discussed earlier can be identified in both cases. This implies that the same conclusions can be drawn for both models, and indicates that it may actually be valid for any viscosity model.

### 4.3.3 Time Dependent Dominance of Flow Regimes

The present study shows that flows in heterogeneous porous media go through the same flow regimes at different heterogeneity length scales and with different flow properties. Therefore, the dominance of any instability mechanism depends on the time window at which it is considered, and this allows to explain and predict the flow behavior. In particular, the dominance of heterogeneity induced instabilities in large length scale of heterogeneity reported by [64, 145] is due to the fact that the effective Péclet number Pe$/(q.A)$ in such cases is large and as a result the flow will be mainly in the channeling regime on the generalized graph. Furthermore, in the work of Tan and Homsy [69] followed by that of DeWit and Homsy [73], the average slope of MZL between $t = 200$ and $t = 400$; $\dot{L}_d$, was used to characterize the instability. Their simulations showed that $\dot{L}_d$ has a maximum at a particular heterogeneity

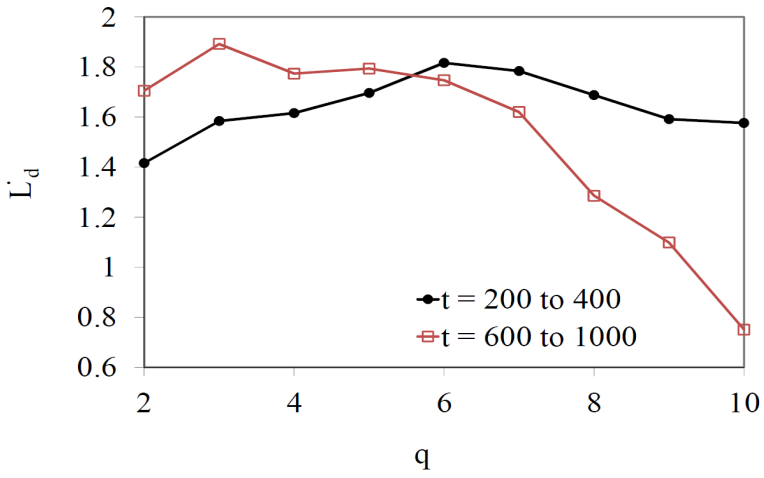


Figure 4.13: Average slope of MZL ($\dot{L}_d$) at different time windows for $\beta_C = 3$, Pe $= 2048$, $A = 2$ and $s = 0.01$

length scale, which was attributed to a resonance between viscous and heterogeneity driven instabilities at commensurate length scales. The results of the present study and the identified general flow behavior, shows that such a maximum can be attributed to the fact that in a heterogeneous medium, $\dot{L}_d$ increases with $q$ because of higher $\nabla f$ for larger $q$, hence the initial increase. However for even larger $q$, the flow goes through lateral-dispersion therefore leading to smaller average $\dot{L}_d$, for a fixed time period. Figure 4.13 depicts $\dot{L}_d$ determined between $t = 200$ and $t = 400$ versus the number of layers for the same conditions used by [73] ($\beta_C = 3$, Pe $= 2048$, $A = 2$). If the same displacement process is considered at later times (e.g. between $t = 600$ and $t = 1000$ as shown in Figure 4.13), heterogeneity models with larger length scales get the chance to go through lateral dispersion and one observes a rapid decrease in the average slope of MZL. The slope of MZL increases with time in the channeling regime, hence for media in which the flow is still in the channeling regime an increase in $\dot{L}_d$ is expected at $t = 600$ to $t = 1000$ time window. Due to these changes, it is not surprising that the maximum $\dot{L}_d$ shifts from $q = 6$ to smaller value of $q$ as the time window is changed from $[t = 200, t = 400]$, to $[t = 600, t = 1000]$.

### 4.3.4 Breakthrough Time

Beside the mixing zone length, there are other parameters for quantifying the instability that are easier to measure in field applications. One of these parameters is the breakthrough time of the injected solvent at the production end. The breakthrough time $t_{BT}$ is defined as the time when the leading edge of the mixing zone ($c = 0.01$) reaches the downstream end of the porous medium with the total length $L_{total} = t_{BT} + x_{c=0.01}@BT$. In this section the effect of the length scale of the permeability on the breakthrough time is analyzed and applicability of the discussed generalization to such measurements is sought.

Figure 4.14a depicts the variation of the $t_{BT}$ with the number of layers $q$ for the sets $(\mathrm{Pe}, A) = (3072, 8), (2048, 4), (2048, 2)$, and $(1024, 2)$. All results were obtained for $\beta_C = 3$ and $s = 0.1$ and the point $q = 0$ corresponds to the homogeneous case. It is clear that the variation of $t_{BT}$ with $q$ is non-monotonic and actually exhibits a minimum and a maximum for all considered cases. For wide channels (small but non-zero $q$), the flow is more unstable since its is dominated by channeling where fingers develop early in particular in comparison with the homogeneous case ($q = 0$) (c.f. Figure 4.3), hence a smaller breakthrough time. This minimum breakthrough time corresponds to the largest number of layers for which the flow remains in the channeling regime throughout the displacement process. For intermediate values of $q$, the flow spends most of its traveling time in the lateral dispersion regime resulting in longer breakthrough times, while for narrow channels (large $q$) fast transition to viscous fingering causes early breakthrough of the injected fluid. Clearly there are two optimum number of layers $q_{optM}$ and $q_{optm}$ that result in a maximum and minimum breakthrough time. These optimum numbers of channels depend on the Péclet number and the cell aspect ratio and seem to decrease with increasing $A$ and decreasing Pe.

Following the scaling strategy adopted for characterizing the flow through MZL, the $t_{BT}$ is plotted versus $1/w^*$ and the results are shown in Figure 4.14b. The scaling clearly

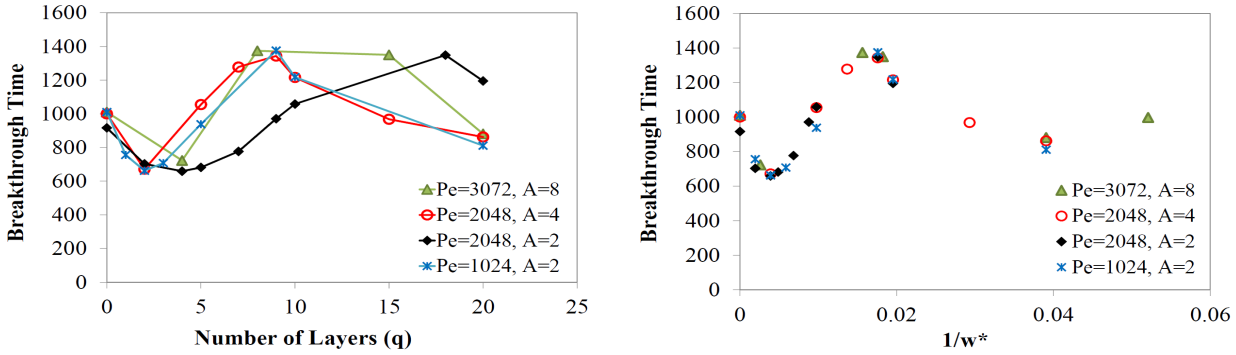


(a) (b)

Figure 4.14: Breakthrough time of the flow with $\beta_C = 3$, $s = 0.1$, at the total dimensionless length of $L_{total} = 2700$; a) breakthrough time versus number of layers for different Pe and $A$, b) breakthrough time versus $1/w^* = q.A/\text{Pe}$.

allows to superpose all curves into a single one regardless of the combinations of Pe and $A$, and to distinguish the extrema of $t_{BT}$. In particular, it is found that the minimum of the breakthrough time is reached for $w^* = w^*_{optm} \approx 250$ while the maximum is attained for $w^* = w^*_{optM} \approx 60$. It can be concluded that for any displacement scenario (a given mobility ratio and a diffusion rate) in a porous medium with determined permeability distribution, the injection rate of the solvent can be adjusted to the distance between injection and production locations to meet the optimum characteristics $\frac{\text{Pe}}{q.A}$. This will ensure that the process remains in the lateral dispersion regime for most of the time and promotes high sweep efficiency of the process.

### 4.3.5 Effects of Dispersion

The previous scaling and flow analysis were based on constant isotropic diffusion in the flow. Questions may however arise about the extent and validity of the present study for general dispersive flows. In the case of homogeneous media, a number of numerical studies have examined the effects of dispersion on the dynamics of viscous fingering [11, 69, 146, 13]. It was found that *isotropic* velocity-dependent dispersion has no significant effects on the

finger structures and quantitative properties such as the mixing length, while anisotropy can result in important differences in the finger structures. For heterogeneous media, the picture becomes more complicated as a result of the competition between different mechanisms [147]. The present study revealed that all flows dominated by the medium heterogeneity ($w^* > w^*_{c-H}$) can be characterized by a single generalized curve. For such flows, it is reasonable to expect that the effects of dispersion will be negligible in comparison with those arising from the medium heterogeneity, and actually most relevant studies have ignored dispersive effects [132, 133]. In order to ascertain this and check the generality of the proposed scaling, simulations that account for dispersion were carried out for layered heterogenous media using a velocity-dependent anisotropic dispersion model [148, 13]. Two dimensionless groups are adopted; $\alpha_D = \frac{a_T}{a_L}$ representing the ratio of the strength of dispersion in the transverse and longitudinal directions, and $L = \frac{a_L U}{a_L U + D_C}$ measuring the relative strength of the longitudinal dispersion [13].

A series of simulations were conducted to determine the effects of the two parameters $\alpha_D$ and $L$. It was found that for flows dominated by heterogeneity, velocity-dependent anisotropic dispersion has very small effects on the finger structures and quantitative properties such as the mixing length. Actually, the only noticeable effects were in the fourth regimes where some minor differences in the fingers' shapes were observed though the overall structure and number of fingers were unaffected by dispersion.

Figure 4.15 depicts the variation of the MZL with time for different values of the dispersivity ratio $\alpha_D$ and strength $L$ and for $A = 2, s = 0.1, q = 9, \mathrm{Pe} = 512$ and $\beta_C = 2$. Clearly the mixing zone length is not affected by dispersion over the wide range of the parameters $\alpha_D$ and $L$ that have been explored. Results were also obtained for other values of $A, s, \mathrm{Pe}$ and $\beta_C$, and it was found that in all cases, the MZL does not change as a result of dispersion, at least in the first three regimes, while some differences may be observed during the

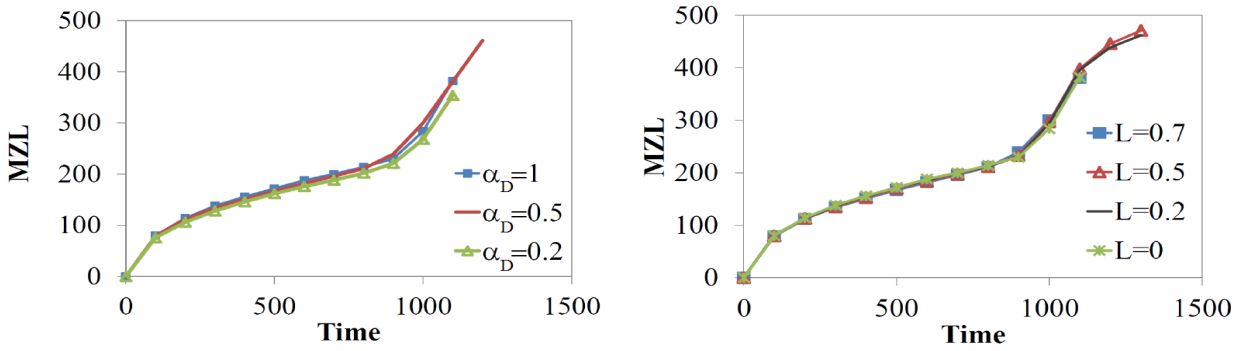


(a) (b)

Figure 4.15: Effect of dispersion on MZL for $s = 0.1, q = 9, \beta_C = 2$, Pe $= 512$, $A = 2$, for a) $L = 0.7$ and different $\alpha_D$, b) $\alpha_D = 0.5$ and different $L$

last fingering regime. These results indicate that the proposed scaling actually extends to dispersive flows and the previous conclusions are valid for general dispersive flows in layered heterogeneous media.

## 4.4 Summary and Conclusion

The coupling between viscous fingering and heterogeneity induced instability has been investigated through a qualitative analysis of concentration contours as well as quantitative characterizations through the mixing zone length (MZL) and the breakthrough time ($t_{BT}$). The study considered a wide range of parameters such as the Péclet number, cell aspect ratio, fluids mobility ratio and heterogeneity length scale and variance, and revealed that in all the scenarios examined, flow displacements in layered heterogeneous media go through similar flow regimes, though not necessarily at the same extent and with the same intensity. Generalized curves have been obtained for different combinations of the mobility ratio and variance of permeability distribution, by scaling time and MZL using characteristic time and characteristic length based on the channels width. The slopes of the generalized curve have been used to identify four regimes that the flow goes through; namely an initial diffusive

regime followed by a channeling regime, then lateral dispersion and finally viscous fingering. Such characterization of the flow regimes helps to explain dominance of viscous fingering or channeling regimes reported in earlier studies for different length scales of permeability and for different Péclet numbers . Furthermore, this scaling allowed identifying the transition from flows where heterogeneous effects are dominant to those where these effects can be neglected and the flow can be treated as homogeneous. Such a transition is governed by a critical effective Péclet number based on the channels width; $w_c^*$ whose value depends on the viscosity ratio and the strength of heterogeneity. Moreover, it is shown that for small values of the effective Péclet number, the qualitative behavior and structure of the flows are virtually identical to those of the homogeneous case. These results and scaling obtained in the case of diffusive flows were found to be also valid when an anisotropic velocity-dependent dispersion is considered. The scaling of MZL was further extended to account for the effects of the mobility ratio and permeability variance and lead to a general master curve that can be used to characterize quantitatively any flow in layered heterogeneous media. Such master curves allow to superpose the MZL up to viscous fingering regime and allows to identify clearly the start of this last regime.

The flow was also characterized in terms of the breakthrough time; $t_{BT}$. It was found that the variation of $t_{BT}$ with the number of layers $q$ is non-monotonic and goes through a minimum for small values of the number of layers $q$ and a maximum for intermediate values. Media with large number of layers lead to the same $t_{BT}$ as the homogeneous medium. Two optimal values of the effective Péclet number; $w_{opt}^*$ that lead to a maximum and a minimum value of $t_{BT}$ were determined. Here too, these optimal values are expected to depend on the permeability variance and fluids viscosity ratios and the total length of the domain.

The present study has focused on the viscous fingering instability in isothermal miscible displacements. However, it is expected that similar characterizations can be extended to

other displacements such as in Rayleigh-Taylor (gravity driven) instability [141, 149], or thermo-viscous fingering [130] and would help to explain observed phenomena like resonance between the driving mechanisms of instability [149] or dominance of any of the mechanisms at different length scales [141, 130]. Furthermore, similarity in the behavior of the mixing zone for different heterogeneous media has been also reported for immiscible displacements [150] and it is presumable that the present scaling approach can be also adopted to characterize the flow behavior in immiscible flows.

# Chapter 5

# Heat and Mass Transfer in Melting Porous Media: Stable Miscible Displacements

---

[1] Changes in the porosity and permeability of a porous medium due to melting are modeled. A frozen phase, which initially fills a part of the porous medium, melts and gets dissolved in the injected hot solvent. The amount of melted material, the rate of melting as well as the profiles of temperature, porosity, and concentration are analyzed to understand the nature of this naturally and industrially important phenomenon. Four reference scenarios corresponding to instantaneous thermal equilibrium, no heat transfer to the frozen phase, no-melting, and instantaneous melting conditions are solved analytically and the effects of different parameters are discussed. Numerical simulation results show that the profiles of the fluid temperature, porosity of the medium, and solvent concentration, form three fronts moving at different rates. It is found that for heat transfer coefficients above a certain value, the rate of melting is independent of this parameter and the system can be considered to have reached instantaneous thermal equilibrium. Moreover, slow heat transfer in the medium is shown to increase the rate of melting at long time periods by involving larger areas in the melting process. Heterogeneous scenarios are also analyzed by introducing frozen blocks of different geometries. The ability of the flow to bypass the frozen region involves a new heat transfer mechanism identified as outer-boundary convection. The effects of the

[1]This chapter is the exact reproduction of the following journal article:
M. Sajjadi and J. Azaiez, "Heat and Mass Transfer in Melting Porous Media: Stable Miscible Displacements", *International Journal of Heat and Mass Transfer*, vol. 88, pp. 926-944, 2015.

geometry of the block along with the other parameters on the melting process are examined. Furthermore a generalizing scheme is proposed to predict the melt production for different block geometries and values of the saturation of the frozen phase.

## 5.1 Introduction

The structure of a porous medium may change dynamically by fluid flow, as a result of heat and mass transfer. In this study, miscible displacement processes in media with changing porosity due to melting are investigated. Such interactions can be encountered in a number of natural phenomena such as the flow of magma, melting of sea ice or frozen soil as well as in industrial processes such as secondary oil recovery or solute transport processes. In these processes the frozen region is porous and has some permeability to the heated fluid. Therefore the convection of heat through the frozen region is one of the main mechanisms of heat transfer in such systems. In this regard this model is different from the classical works studying the the melting of frozen porous media [91, 92, 93] or the melting cavities [151, 152] in which conduction and natural convection are responsible for the heat transfer to the boundaries of the frozen region.

As stated earlier, there are many fields in which melting in the porous medium is central to the flow. These include the flow of magma melting the rocks and the ensuing change in the permeability of the medium which has been the subject of numerous studies [98, 99, 100]. The porous medium in which the magma flows is considered to be deformable and heat and mass transfer occur through the melting of the rocks and chemical reactions between the components of the magma and the solid phase [99]. The heat transfer equations describing these models are the closest to our model since they include the effect of the convection of the hot fluid through the melting porous medium. The deformable porous medium of such systems is replaced in our model by a melting solid phase and a non-deformable rock phase.

Melting of ice due to the flow of water in partially frozen soil is another related application. Studies on such systems started in the 1920s with the attempts to model heat and fluid transport in frozen soil and to address frost related damage of roads in Scandinavia and North America [153, 154, 155, 156]. Uneven ground displacements due to heaving pressure, loss of mechanical strength of the soil due to thawing of the ice in the frozen regions, and changes in unfrozen water level beneath the permafrost are examples of problems investigated through such modelings. Despite some similarities between the present study and those discussing freezing and thawing of frozen ground, the models and the relevant concepts are different. The driving forces for the flow in frozen soils consist of gravity and the increase in the volume of water upon freezing which pushes the moisture towards the colder regions and causes the flow of heat and mass in the medium [153]. Furthermore, the models describing freezing and thawing of the ground are configured mostly in one dimension along the gravity direction [153, 154]. In the present study however, changes in the specific volume upon melting as well as the effects of gravity are neglected while the flow is induced by the injection of the solvent to the medium.

Changes in the medium porosity are also encountered in the field of oil recovery, which is the main motivation of the present study. This pertains in particular to the hot solvent flooding of preheated bitumen reservoirs where the inhabitant fluid is immobile and may be regarded as frozen at the initial temperature. In the recovery of bitumen or heavy oil, the co-injection of a solvent with a heating medium (mostly steam) has become popular and many studies have been devoted in recent years to processes like solvent aided SAGD, VAPEX and solvent assisted hot water flooding [157, 158, 128]. Melting of the bitumen occupying some of the pore space of the medium changes the porosity available to the fluids and in turn the dynamics of the flow. The formation of the melting zone through injection of hot solvent to the bitumen reservoirs has not been studied before.

Our objective of this work is to understand the effect of parameters such as the initial porosity, the rate of heat transfer and the melting potential of the flowing fluid on the melting rate and the development of the melting zone. Such a systematic study of the melting process is beneficial in describing and predicting the trends of natural phenomena such as melting of sea ice and thawing of soil. Also a better understanding of the trends of heat and solvent transfer to the bitumen at different conditions can help enhance the efficiency and reduce the environmental impacts of these industrial processes.

A detailed definition of the problem, along with the mathematical and numerical models are presented in the next section. In the Results section, at first four reference scenarios are defined for the melting process according to which different scenarios can be categorized. Then a quantitative study is presented which aims at predicting the melting rate as a function of the flow conditions and determining the conditions that lead to the maximum melting. At last the melting mechanisms in heterogeneous media are discussed and a quantitative analysis of the process is carried for different configurations of the frozen region.

## 5.2 Modeling

The problem is defined such that the porous medium is partially saturated with a frozen material. The rest of the porous medium is filled with a fluid (e.g. the melt) that is fully miscible with the melted form of the frozen phase. A hot fluid, fully miscible with the inhabitant one, is injected in the medium to displace the inhabitant fluid and the melt. Due to the heat of the injected fluid, the frozen material is melted and the pore space it initially occupied becomes available to the flow. To model this system, it is assumed that three phases are present in the medium, namely the rock or the porous medium, the frozen fluid or the solid phase and the fluid or the flowing phase. The rock in this model is the part of the solid matrix that remains unchanged during the whole displacement process and has a

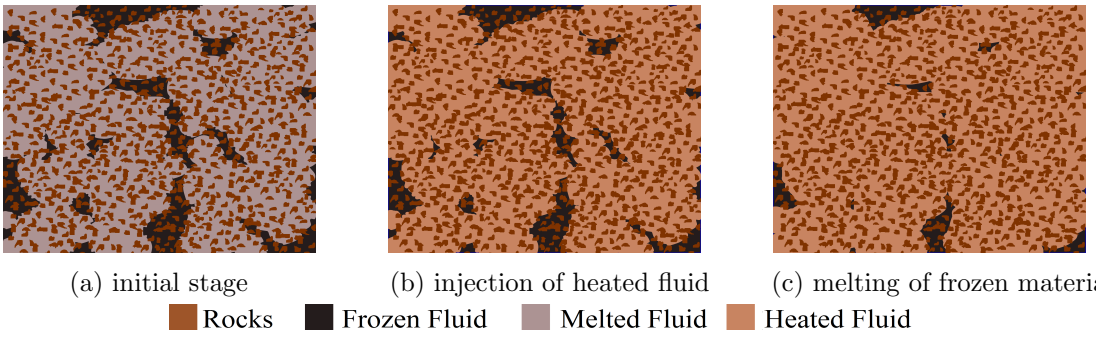


Figure 5.1: Schematic of the phases present in the domain and the melting process: a) initial stage with rock, frozen material, and melted fluid present; b) volume flooded by heated fluid; c) melting of the remainders of frozen material.

*homogeneous* porosity distribution of $\phi_R$. In other words, the void space per unit volume available to the flow if no frozen material is present is $\phi_R$. The porous medium is partially saturated with the frozen material, or what we refer to as the solid phase, of volume per unit volume of formation $(\phi_R - \phi)$ , where $\phi = \phi(x, y, t)$ is the porosity available to the fluid flow in the presence of the frozen phase. The porosity $\phi(x, y, t)$ changes dynamically with the variation of the saturation of the frozen material in the medium.

When the thermal front floods a region, it melts part of the frozen material in the area it comes in contact with and increases its porosity and permeability. Initially the saturation of the frozen material in the frozen medium is at its maximum value $S_0$ providing a minimum pore space for the flow, referred to as $\phi_{min}$. In any displacement scenario, the porosity can vary between the initial porosity $\phi_{min}$ and the rock porosity $\phi_R$. Figure 5.1 shows a schematic of the melting process. At the initial stage (Figure 5.1a) the medium has a porosity $\phi_{min}$ and all three phases are at thermal equilibrium at the melting temperature $T_m$. When the heated fluid is injected into the medium (Figure 5.1b) there is a difference between the temperatures of the frozen material and the flowing fluid which provides a source of heat for melting. As a result of the gradual melting of the remainders of the frozen material in the medium, the porosity increases and ultimately reaches that of the rock, $\phi_R$.

At the scale of the reservoir, the model is defined as a hot solvent with concentration $C_1$ and temperature $T_1$ being injected at a uniform rate $U$ into a rectangular porous domain of length $L_x$ and width $L_y$ and initial porosity $\phi_{min}$ (see Figure 5.2). The injected fluid displaces the inhabitant one, of concentration $C_2$ and temperature $T_m$ as well as the melted material, and heats the medium. The concentration, temperature and porosity form advancing fronts that will be referred to as the solutal, thermal, and melting fronts, respectively. The simplified profiles of these fronts are shown in Figure 5.2 at $t_0$ and a later time.

The heat transfer inside the fluid takes place through convection and diffusion while inside the rock heat is distributed through conduction. The heat transferred to the matrix (consisting of the rock and the frozen phase) causes the thermal front in the fluid to lag behind the solutal front. This lag depends on the share of heat capacity of the fluid compared to that of the matrix [25]. It will be assumed here that the rock is in instantaneous thermal equilibrium (ITE) with the fluid due to the large contact area between them [129], which implies that the temperature distributions in both of these phases are the same. During the melting process the frozen phase remains at the melting temperature. The ITE assumption between the melting phase and the fluid requires that at each point, the fluid remains at the melting temperature as long as the frozen material is present. Previous studies indicate that the ITE assumption between the frozen material and the flowing phase makes the problem inherently grid-size dependent. In this work, a transient thermal equilibrium between the flowing and the frozen phases is considered. Hence the energy equation is formulated for the temperature of the fluid-rock system separately from the saturation of the frozen phase in the medium. Such handling of the energy equation allows for adjustment of the heat transfer rate between ITE and transient thermal equilibrium at which the fluid can retain a temperature higher than that of the melting phase even in the presence of some saturation of the frozen material.

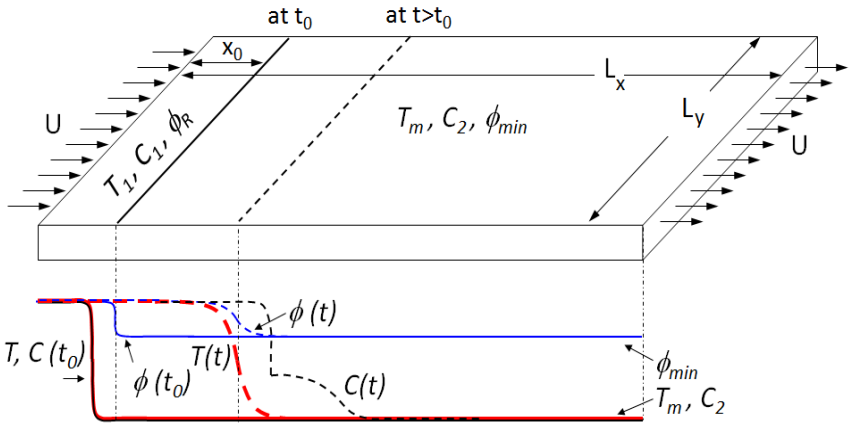


Figure 5.2: Diagram of the modeled domain with the solvent concentration, fluid temperature, and porosity distribution profiles at $t_0$ and $t > t_0$

### 5.2.1 Main Model Equations

In this study we are interested in determining the distribution of temperature, solvent concentration, and porosity of the medium during the displacement process. Hence the governing equations are mass and momentum conservation, advection-diffusion of concentration, and conservation of energy:

$$\nabla.\vec{u}_D = 0 \tag{5.1}$$

$$\nabla P = -\frac{\mu}{\kappa}\vec{u}_D \tag{5.2}$$

$$\frac{\partial(\phi C)}{\partial t} = -\nabla.(C\vec{u}_D) + D_C\nabla.(\phi\nabla C) \tag{5.3}$$

$$(\rho_f c_{pf}\phi + \rho_R c_R(1-\phi_R))\frac{\partial T}{\partial t} =$$

$$\nabla.[(k_f\phi + k_R(1-\phi_R))\nabla T] - \rho_f c_{pf}\nabla.(T\vec{u}_D)$$

$$-h(T-T_m) \tag{5.4}$$

$$(\rho_s\Delta h_f + \rho_f c_{pf}(T-T_m))\frac{\partial\phi}{\partial t} = h(T-T_m) \tag{5.5}$$

Equations 5.1 and 5.2 are the mass conservation and Darcy's law, respectively. Equation

5.3 describes the coupled variations of concentration and porosity with time, which includes the effects of melting on the dilution of the solution. The energy conservation equation (which reduces to heat conservation if no dissipation of kinetic energy is considered) is written in two separate equations for the fluid-rock phase and the solid phase. The first one (i.e. Equation 5.4) describes the changes in temperature of the fluid-rock system as heat is brought to the medium through conduction (the first term on the right) and convection (the second term on the right) after a part of the heat is shared with the frozen phase (the last term on the right hand side). The solid phase (i.e. the frozen fluid) is always at the melting temperature and when melted, it is assumed that its temperature reaches instantaneously that of the fluid ($T$). Therefore in Equation 5.5 the heat transferred to the solid phase is used to melt some parts of the frozen material and to raise the melted material's temperature to that of the flowing fluid.

In the above equations, $\vec{u}_D$ is the Darcy velocity and $\phi$ as defined before is the porosity of the medium available to fluid flow. The fluid pressure is denoted by $p$ while $\mu$ is the viscosity of the fluid which is a function of temperature and solvent concentration, and $\kappa$ is the permeability of the medium assumed to be a function of porosity. In Equation 5.3, $C$ is the volume concentration of the solvent varying between $C_1$ at the injection and $C_2$ at the downstream boundaries while $D_C$ is the mass diffusion coefficient. The thermal equilibrium assumption between the rock and the fluid phases requires one temperature $T$ representing both phases. In Equation 5.4, $\rho_f$ and $\rho_R$ are the densities of the fluid, and rock phases respectively while $c_{pf}$, $c_R$, $k_f$, and $k_R$ are the corresponding specific heat capacities and thermal heat conductivities respectively. The heat transfer coefficient $h$ and the difference between the fluid-rock temperature and the melting temperature $T - T_m$ determine the amount of heat that goes towards melting. Finally, $\rho_s$ in Equation 5.5 is the density of the frozen material while $\Delta h_f$ is the latent heat of melting.

Additional assumptions beside ITE between the fluid and the rock and the homogeneity of the rock, were made for adopting these equations. They include assumptions that the material and the medium are continuous at the scale under consideration, that the flows are laminar and incompressible and that the density of each phase is independent of temperature and concentration. Also in the mass conservation equation, it is assumed that the pore volume that the solid phase occupies is the same as the volume it fills after it melts which neglects any changes in the density between the solid and the fluid phases. Furthermore, the solvent concentration is assumed to affect neither the melting temperature nor the latent heat of melting. The inertia and boundary effects that are shown to be important in high permeability media and for small mobility ratios [159, 160, 19] are also neglected in this work.

### 5.2.2 Constitutive Correlations

In what follows, expressions and correlations of some of the physical parameters are discussed.

Heat Transfer Coefficient Determination of the value of the heat transfer coefficient $h$ is critical in this model. For a porous bed of particles, Dixon and Cresswell [161] proposed the following correlation:

$$h = \bar{s}h^* \tag{5.6}$$

where $\bar{s}$ is the surface area per unit volume of the porous medium (specific surface area) whose definition will be given shortly. For $h^*$, Alazmi and Vafai proposed the following expression [162]:

$$h^* = \frac{k_f}{d_p}\left[2 + \mathrm{Pr}^{1/3}\mathrm{Re}_p^{0.6}\right] \tag{5.7}$$

According to the data provided in Tables 5.1 and 5.2 which correspond to the displacement of bitumen in Cold Lake (Alberta) and to the melting of ice, the product in Equation 5.7, $\mathrm{Pr}^{1/3}\mathrm{Re}_p^{0.6} = 2e-5$ to $1e-2$ is negligible compared to the constant 2, and $h^*$ can be simplified to $h^* = 2\frac{k_f}{d_p}$.

Permeability For the variation of the permeability with the porosity $\kappa(\phi)$, different forms of Kozeny's empirical correlation have been used extensively in the literature. In particular, Emmanuel and Berkowitz [103] used the form:

$$\kappa = c_K \frac{\phi^3}{\bar{s}^2} \tag{5.8}$$

where $c_K = 0.5$ is Kozeny's constant. Assuming that the porous medium consists of spherical grains, the specific surface area is determined through:

$$\bar{s} = \bar{s}_0 \left( \frac{1-\phi}{1-\phi_0} \right)^{2/3} \tag{5.9}$$

where the reference specific surface area $\bar{s}_0$ is defined as $\bar{s}_0 = 6\frac{(1-\phi_0)}{d_p}$ [161]. Emmanuel and Berkowitz showed that although the value of the permeability defined by Equation 5.8 depends on the choice of $\bar{s}$ as a function of porosity, the trend of variation of the permeability with porosity remains the same regardless of this choice [103]. An alternative correlation for $\kappa(\phi)$ was proposed by Alazmi and Vafai [162] for media with variation of porosity near the impermeable boundaries:

$$\kappa = \frac{\phi^3 d_p^2}{150(1-\phi)} \tag{5.10}$$

Kozeney's correlation as shown in Equation 5.8 results in permeability values twice as much as those determined through Equation 5.10 in which the porosity is expected to decrease at the impermeable boundaries. However the trends for the variation of $\kappa$ with $\phi$ are similar for both methods, and actually the substitution of $\bar{s}$ in Equation 5.8 confirms the proportionality

Table 5.1: List of values for the thermal properties of the fluid, rock and solid phases, and the flow in formation corresponding to the displacement of bitumen in Cold Lake formation in northern Alberta, Canada.

| Parameter | Value | Units |
|---|---|---|
| **Fluid (Bitumen at** 100 deg **C )** [163] | | |
| Specific Heat Capacity | $c_{pf} = 2.15$ | $KJ/KgK$ |
| Thermal Conductivity | $k_f = 0.10$ | $W/mK$ |
| Density | $\rho_f = 960$ | $Kg/m^3$ |
| **Solid** (Bitumen at 15 deg C ) [163] | | |
| Specific Heat Capacity | $c_s = 1.8$ | $KJ/KgK$ |
| Density | $\rho_s = 1000$ | $Kg/m^3$ |
| Latent Heat of Melting | $\Delta h_f \approx 72$ | $KJ/Kg$ |
| **Rock** [163] | | |
| Specific Heat Capacity | $c_R = 0.7$ | $KJ/KgK$ |
| Thermal Conductivity | $k_R = 1 - 4$ | $W/mK$ |
| Density | $\rho_R = 2650$ | $Kg/m^3$ |
| Injection Velocity | $U = 2e - 6$ | $m/s$ |
| Grain Size [163] | $d_p = 2$ | $\mu m$ |
| Reference Porosity | $\phi_0 = 0.15$ | |
| Viscosity at Inlet (at 120 deg C) [164] | $\mu_1 = 0.02$ | Pa.$s$ |
| Viscosity at outlet (at 50 deg C) [164] | $\mu_2 = 1.0$ | Pa.$s$ |

Table 5.2: List of values for the the thermal properties of the fluid, rock, and solid phases corresponding to flow of water in frozen ground.

| Parameter | Value | Units |
|---|---|---|
| **Fluid** (Water at 0 deg C ) | | |
| Specific Heat Capacity | $c_{pf} = 4.2$ | $KJ/KgK$ |
| Thermal Conductivity [165] | $k_f = 0.56$ | $W/mK$ |
| Density [166] | $\rho_f = 998$ | $Kg/m^3$ |
| **Solid** (Ice at $-2$ deg C ) [163] | | |
| Latent Heat of Melting | $\Delta h_f = 330$ | $KJ/Kg$ |
| Density | $\rho_s = 920$ | $Kg/m^3$ |
| Viscosity at Inlet (at 20 deg C) | $\mu_1 = 1.0$ | $m$Pa.$s$ |
| Viscosity at outlet (at 0 deg C) | $\mu_2 = 1.8$ | $m$Pa.$s$ |

of the results. In the present study the domain of interest is assumed to be a section of a larger porous medium in which the displacement process is taking place. Therefore periodic boundary conditions are applied on the transverse boundaries and it is assumed that the flow is not affected by any impermeability close to the boundaries of the domain. Hence the permeability correlation in Equation5.8 is adopted.

Fluid-Frozen Phase Surface Area Equation 5.9 is for the specific surface area in a porous medium contacted by the fluid, which decreases to zero as the porosity reaches $\phi = 1$. To determine the heat transfer coefficient, we are interested in the contact area between the fluid and the frozen (solid) phase $\bar{s}_s$ which is expected to be zero when the porosity reaches $\phi_R$. Hence, to determine the specific surface area of the solid phase, some modifications are

made in equation 5.9:

$$\bar{s}_s = \bar{s}_{s,0} \left( \frac{\phi_R - \phi}{\phi_R - \phi_0} \right)^{2/3} \tag{5.11}$$

$$\bar{s}_{s,0} = 6 \frac{(\phi_R - \phi_0)}{d_p} \tag{5.12}$$

This modification is based on the assumption that the specific surface area of the frozen particles in contact with the fluid decreases with the melting of the frozen material. The maximum contact between the fluid and the frozen material occurs when the saturation of the frozen material is $\phi_R - \phi_{min}$ and it decays to zero as the porosity reaches that of the rock. Although this correlation can affect the rate of heat transfer to the frozen regions and the rate of melting, its effect is limited to slow melting scenarios. As will be shown later in the results section, the heat transfer coefficient in natural formations is so large that they meet the instantaneous thermal equilibrium condition. The rate of melting in such scenarios is independent of the heat transfer coefficient and of the correlation chosen for the specific surface area-porosity.

Viscosity For the dependence of the viscosity on temperature and solvent concentration, an exponential correlation is adopted [22]. This correlation describes closely the "quarter power mixing rule", that is widely used in the petroleum industry to describe the viscosity of aqueous and non associating mixtures [136, 137, 16]:

$$\mu = \mu_1 exp \left( \beta_C \left( \frac{C_1 - C}{C_1 - C_2} \right) + \beta_T \left( \frac{T_1 - T}{T_1 - T_m} \right) \right) \tag{5.13}$$

According to this correlation, the viscosity ratio, also regarded as the mobility ratio for miscible displacements, is defined as the viscosity of the inhabitant fluid over that of the injected fluid; *i.e.* $\mu_2/\mu_1 = exp(\beta_C + \beta_T)$. Therefore $\beta_C$ and $\beta_T$ are referred to as the solutal and thermal log-mobility ratios, respectively.

### 5.2.3 Initial and Boundary Conditions

As shown in Figure 5.2, the domain of interest is a rectangle of length $L_x$ and width $L_y$. Initially the system is considered to be at the melting temperature $T_m$ at a minimum porosity $\phi_{min}$ and solvent concentration $C_2$, except for a small band of thickness $x_0$ from the injection boundary where the domain is assumed to be flooded with the hot solvent and has a temperature $T_1$, a porosity $\phi_R$ and a solvent concentration $C_1$. The initial conditions are formulated as follows:

$$\vec{u}_D(x, y, t_0) = U\mathbf{i} \tag{5.14}$$

$$T(x, y, t_0) = \frac{(T_1 - T_m)}{2}\text{erfc}(\frac{x - x_0}{2\sqrt{D_T t_0}}) + T_m \tag{5.15}$$

$$C(x, y, t_0) = \frac{C_1 - C_2}{2}\text{erfc}(\frac{x - x_0}{2\sqrt{D_C t_0}}) + C_2 \tag{5.16}$$

$$\phi(x, y, t_0) = \frac{(1 - \phi_{min})}{2}\text{erfc}(\frac{x - x_0}{2\sqrt{D_T t_0}}) + \phi_{min} \tag{5.17}$$

In the above equations $D_T$ is the diffusion rate of heat which is defined by the effective thermal conductivity and specific heat capacity of the rock-fluid system (Equation 5.28).

During the displacement process, the hot solvent with uniform temperature and concentration $T_1$ and $C_1$ is injected at a uniform and constant Darcy velocity $U$ from the left side of the domain (upstream boundary) and the temperature and concentration at the downstream boundary remain as $T_m$ and $C_2$. The porosity at the injection boundary is $\phi_R$ while it is $\phi_{min}$ at the downstream boundary. Transverse to the flow direction, periodic boundary conditions

are adopted.

$$
\begin{aligned}
&(C,T)(0,y,t) = (C_1,T_1)\\
&(C,T)(L_x,y,t) = (C_2,T_m)\\
&\frac{\partial}{\partial x}(C,T)(0,y,t) = \frac{\partial}{\partial x}(C,T)(L_x,y,t) = (0,0)\\
&(C,T)(x,0,t) = (C,T)(x,L_y,t)\\
&\frac{\partial}{\partial y}(C,T)(x,0,t) = \frac{\partial}{\partial y}(C,T)(x,L_y,t)\\
&(\phi,\vec{u}_D)(0,y,t) = (\phi_R, U\mathbf{i})\\
&(\phi,\vec{u}_D)(x,0,t) = (\phi,\vec{u}_D)(x,L_y,t)
\end{aligned}
\tag{5.18}
$$

### 5.2.4 Dimensionless Equations

The equations are made dimensionless using a diffusive scaling:

$$
\begin{aligned}
&c^* = \frac{C-C_2}{C_1-C_2} \quad \theta^* = \frac{T-T_m}{T_1-T_m} \quad (u^*,v^*) = \frac{(u_D,v_D)/\phi}{U/\phi_R}\\
&(x^*,y^*) = \frac{x,y}{D_C\phi_R/U} \quad t^* = \frac{t}{D_C\phi_R^2/U^2} \quad \phi^* = \frac{\phi}{\phi_R}\\
&p^* = \frac{p}{\phi_R\mu_1 D_C/\kappa_R} \quad \mu^* = \frac{\mu}{\mu_1} \quad \kappa^* = \frac{\kappa}{\kappa_R}
\end{aligned}
\tag{5.19}
$$

The scaling for the porosity is used so that the model is independent of the rock porosity. The resulting dimensionless equations are:

$$\nabla.(\phi^*\mathbf{u}^*) = 0 \tag{5.20}$$

$$\nabla p^* = -\frac{\mu^*}{\kappa^*}\phi^*\mathbf{u}^* \tag{5.21}$$

$$\frac{\partial(\phi c^*)}{\partial t^*} = -\phi^*\mathbf{u}^*.\nabla c^* + \nabla.(\phi^*\nabla c^*) \tag{5.22}$$

$$\frac{\partial\theta^*}{\partial t^*} = \frac{1}{(1-\lambda(1-\phi^*))}[\mathrm{Le}\nabla.\left((1-(1-\phi^*)k_{rel}\right)\nabla\theta^*) - \lambda\phi^*\mathbf{u}^*\nabla.\theta^* - \frac{\mathrm{Le}k_{rel}}{\mathrm{Pe}_p^2}\left(12(1-\phi_0^*)^{1/3}(1-\phi^*)^{2/3}\right)\theta^*] \tag{5.23}$$

$$\frac{\partial\phi^*}{\partial t^*} = \frac{1}{\frac{\rho_{rel}}{\mathrm{Ste}'}+\theta^*}\left[\frac{\mathrm{Le}k_{rel}}{\lambda\mathrm{Pe}_p^2}\left(12(1-\phi_0^*)^{1/3}(1-\phi^*)^{2/3}\right)\theta^*\right] \tag{5.24}$$

where:

$$\lambda = \frac{\rho_f c_{pf}\phi_R}{(\rho_f c_{pf}\phi_R + \rho_R c_R(1-\phi_R)} \tag{5.25}$$

$$\rho_{rel} = \frac{\rho_s}{\rho_f} \tag{5.26}$$

$$\mathrm{Le} = \frac{D_T}{D_C} \tag{5.27}$$

$$D_T = \frac{k_f\phi_R + k_R(1-\phi_R)}{\rho_f c_{pf}\phi_R + \rho_R c_R(1-\phi_R))} \tag{5.28}$$

$$k_{rel} = \frac{k_f\phi_R}{k_R(1-\phi_R)+k_f\phi_R} \tag{5.29}$$

In the above equations, the Lewis number $\mathrm{Le} = \frac{D_T}{D_C}$ is the ratio of the diffusion rate of heat over that of the concentration, the Stefan number $\mathrm{Ste}' = \frac{c_{pf}(T_1-T_m)}{\Delta h_f}$ represents the relative internal energy of the fluid to that of melting (or melting potential of the fluid), while the pore scale Péclet number $\mathrm{Pe}_p = \frac{Ud_p}{D_C} = \mathrm{Pe}\frac{d_p}{L_x}$ defined and used in the calculation of the heat transfer coefficient, corresponds to the dimensionless grain diameter. Moreover, the Péclet number $\mathrm{Pe} = \frac{UL_x}{D_C}$ defining the relative importance of convection to diffusion appears as the dimensionless length of the domain, and the dimensionless width of the domain is defined as $L_y^* = Pe/A$ where $A = L_x/L_y$ is the aspect ratio. Finally, the rate of convective heat transfer

between the fluid and the solid phase in Equation 5.24 is defined as $H_T = \frac{12\text{Le}k_{rel}(1-\phi_0^*)^{1/3}}{\text{Pe}^2(d_P/L_x)^2}$ and in all that follows, we set $\text{Ste} = \text{Ste}'/\rho_{rel}$. The pore scale Péclet number is integrated in $H_T$ and when studying the effects of different parameters $H_T$ will be adjusted independently from the main Pe which is fixed throughout the chapter.

Using the newly defined dimensionless groups and dropping the asterisks from the dimensionless quantities Equations 5.20 to 5.24 simplify to:

$$\nabla.(\phi\mathbf{u}) = 0 \tag{5.30}$$

$$\nabla p = -\frac{\mu}{\kappa}\phi\mathbf{u} \tag{5.31}$$

$$\frac{\partial(\phi c)}{\partial t} = -\phi\mathbf{u}.\nabla c + \nabla.(\phi\nabla c) \tag{5.32}$$

$$\frac{\partial\theta}{\partial t} = \frac{1}{(1-\lambda(1-\phi))}[\text{Le}\nabla.\left((1-(1-\phi)k_{rel}\right)\nabla\theta)$$

$$-\lambda\phi\mathbf{u}\nabla.\theta - H_T(1-\phi)^{2/3}\theta] \tag{5.33}$$

$$\frac{\partial\phi}{\partial t} = \frac{1}{1+\text{Ste}\theta}\frac{\text{Ste}H_T}{\lambda}(1-\phi)^{2/3}\theta \tag{5.34}$$

The boundary and initial conditions are also formulated in dimensionless form. A stream function-vorticity formulation $\omega = -\nabla^2\psi$ is used to recast the momentum and mass conservation equations as follows:

$$\nabla\times\nabla p = -(\nabla\frac{\mu}{\kappa}\times\phi\mathbf{u} + \frac{\mu}{\kappa}\nabla\times\phi\mathbf{u})$$

$$0 = -\frac{\kappa}{\mu}\nabla\frac{\mu}{\kappa}\times\phi\mathbf{u} - \omega$$

$$\omega = -\nabla(ln(\mu) - ln(\kappa))\times\phi\mathbf{u}$$

Using the dimensionless form of Equation 5.13 which results in $\nabla ln(\mu) = -\beta_C\nabla c - \beta_T\nabla\theta$ and setting $f = ln(\kappa)$, the expression of vorticity becomes:

$$\omega = -(\beta_C\nabla c + \beta_T\nabla\theta + \nabla f).\nabla\psi \tag{5.35}$$

The velocity field can be obtained by extracting the stream function from the vorticity distribution. It should be noted that the vorticity is the curl of velocity, and therefore the stream function obtained from the vorticity through $\omega = -\nabla^2\psi$ only retrieves the fluctuations of the velocity and not the constant part. Therefore, the total velocity vector is obtained by adding the constant and uniform injection velocity to the one obtained from the stream function.

$$\mathbf{u} = (u, v) = \frac{1}{\phi}(\frac{\partial\psi}{\partial y} + 1, -\frac{\partial\psi}{\partial x})$$

## 5.3 Numerical Method

The problem of the melting medium formulated by Equations 5.30 to 5.34 is highly nonlinear and stiff. The main source of stiffness arises from the heat transfer to the frozen phase taking place at a much faster rate than the diffusion and convection phenomena. The fast heat transfer between the fluid and the melting medium leads to sudden changes in the porosity $\phi$ and the temperature $\theta$ and results in sharp gradients at the corresponding fronts. Therefore choosing the appropriate numerical method for solving Equations 5.30 to5.34 is of utmost importance.

Spatial Derivatives For the differentiation in space, spectral and finite difference methods have been considered. The highly accurate spectral methods are powerful and fast tools but require periodic boundary conditions. For the velocity, periodic boundary conditions in the $-y$ direction and zero fluctuations at the upstream and downstream boundaries allow to implement such conditions in both flow directions. Furthermore for the other variables, to implement periodic boundary conditions, the concentration, temperature, and porosity were split as the sum of the initial base state profiles (defined in Equations 5.14 - 5.17) and

the remaining terms that have non-zero values around the advancing fronts but decay to zero towards the boundaries. Unfortunately a number of limitations have been encountered with the implementation of the spectral methods. First, the fact that spectral methods are defined for uniform grid distributions had limited the accuracy for this problem with rapid variations over a small region of the domain. Moreover, this model involves many nonlinear terms whose calculations require numerous direct and inverse transformations that turned out to be very computationally costly. For these reasons, the finite difference method with non-uniform grid distribution which adapts itself with the melting front's profile has been adopted. Hence the grid clusters are refined when the melting front has a sharp gradient and are distributed widely if the melting front is spread over the domain. The grids in the $-y$ direction are distributed evenly across the flow domain and the derivatives are defined using second-order central difference formula. The derivatives in the $x$ direction are determined using a second-order accurate finite difference discretization on a non-uniform grid [167].

Temporal Discretization For time stepping, a number of algorithms have been explored and tested. In general, fully implicit schemes are very difficult to implement due to the high degree of nonlinearity of the equations. Therefore linear multi-step methods were adopted and in particular, a Runge-Kutta method as well as a semi implicit predictor-corrector method were tested and their efficiency compared in terms of the computational time, stability and accuracy. A fourth order Runge-Kutta (RK4) method and a second-order Adams-Bashforth - Adams-Moulton predictor-corrector method were used for this comparison. In the AB-AM predictor-corrector method the first step is based on the second order explicit Adams-Bashforth method (AB) with a small region of stability. The second step, which can be repeated for better convergence and stability, is the implicit Adams-Moulton (AM) algorithm. Due to its implicit nature, Adams-Moulton method has a larger region of numerical stability compared to the other schemes discussed here but its combination with

the predictor reduces the region of stability for the predictor-corrector scheme [168].

The Runge-Kutta methods of a given order might have different coefficients but all have the same stability properties [169]. Based on the A-stability graphs, RK4 has a larger stability region than the second order AB-AM method. However the number of evaluation steps in the predictor-corrector method has a significant effect on its stability and therefore it is difficult to say whether an iterative AB-AM method ($P(EC)^m E$) is less unstable than RK4 or not. In order to compare the efficiency of these numerical methods in solving the proposed model, a large number of numerical simulations were performed for different scenarios and the computational time and the results were compared. In one of the performed tests, for example, the parameters were set as $\phi_{min} = 0.95$, $\beta_C = 1$, $\beta_T = 1$, Pe $= 256$, $A = 2$, $\lambda = 0.8$ and Le $= 1$. The heat exchange rate and the melting potential were set to $H_T = 0.01$ and Ste $= 1.2$ respectively. A mesh of $512 \times 512$ with initial grid size of $dx = 0.11$ to 1.0 and $dy = 0.25$ and a time step size of $dt = 1e-4$ was used for this case. At a run time of 80 hours the RK4 method reached $t = 24$ while AB-AM method reached the end time of $t = 50$ at 31 hours run time. For all the compared scenarios the run time of the AB-AM method was smaller than the RK4 method. Comparisons of the results showed perfect agreement between the two methods and therefore the second order AB-AM method was chosen. In the next section, the validation and convergence of the numerical code are discussed.

### 5.3.1 Validation

Before proceeding with the discussion of the results, the validation and convergence of the numerical code are presented. First, the prediction of the code have been compared with those obtained from analytical solutions of limiting cases that will be discussed in further details in the next section. The results from the exact analytical and numerical solutions are shown in Figure 5.3 for cases of very slow heat transfer ($H_T \to 0, H_T = 1e-7$), instantaneous

melting ($\text{Ste} \to \infty, \text{Ste} = 100$) and no melting ($\text{Ste} \to 0, \text{Ste} = 1e-5$). There are clearly excellent agreements between the two solutions which indicate that the numerical code is accurate and has converged, at least in those limits.

Furthermore we have also attempted to validate the code for unstable scenarios, which constitutes a more stringent test. In the literature, modeling of instabilities in frozen media are limited and there are no similar studies analyzing the development of fingers at the melting front. Therefore, for validating the code, a non-melting scenario with $\phi_{min} = 1$ has been considered. The simulation results for $\beta_C = 2$, $\beta_T = 1$, $\lambda = 1$, $\text{Pe} = 2000$, $\text{Le} = 1$ and $L_x/L_y = 2$ that correspond to thermo-viscous fingering in homogeneous porous media have been matched with simulation results of [130]. It was found that there is very good agreement between the number, size and growth rate of the developed fingers in both methods.

Finally, the sensitivity of the results to the time step size and the grid size has been confirmed by changing the time step size from $dt = 1e-3$ to $1e-4$ and by comparing the results for stable scenarios with and without mesh refinement. The results do not show any dependence on $dt$ in the ranges that do not result in numerical instability. The mesh refinement was however found to affect the results for fast melting scenarios as sharp gradients were smoothed by large grid size of regular meshing. Therefore the melting front has a faster advancement (by around 1% for $H_T = 1$) when mesh refinement is applied.

## 5.4 Results and Discussion

The proposed model for the melting porous medium with forced convection through the medium involves a large number of parameters that are expected to affect the process, such as $\beta_C$, $\beta_T$, $\phi_{min}$, $\lambda$, Le, Pe, $k_{rel}$, $H_T$, and Ste. Due to the large number of possible values and combinations, it is impractical to analyze the effects of all these parameters. Therefore the analysis will be limited to some parameters that are expected to have a more significant

influence on the advancement and growth of the thermal, melting, and solutal fronts. In particular the study will deal only with stable scenarios and therefore $\beta_C = \beta_T = 0$. For stable flows with uniform distribution of the frozen material, the effect of changing the Péclet number Pe is limited to adjusting the dimensionless length of the medium. Therefore, unless stated otherwise the Péclet number is fixed as Pe = 1000. The thermal lag coefficient $\lambda$ is very important in systems involving the coupling between mass and heat transfer in porous media. This parameter defines the rate of advancement of the thermal front and determines the share of heat that is required to increase the temperature of the rocks to that of the fluid. The effect of $\lambda$ on thermo-viscous fingering has been extensively studied in previous studies [22, 130], and will be fixed here as $\lambda = 0.8$. The thermal conductivity of a fluid is in general smaller than that of a solid. As a result, the parameter $k_{rel}$ which represents the relative thermal conductivity of the fluid to that of the fluid-rock system has generally a very small value (between 0.01 to 0.2 for the range of parameters given in Tables 5.1 and 5.2). This implies that the term $(1 - \phi)k_{rel}$ in Equation 5.33 is negligible with respect to 1. Therefore variations of $k_{rel}$ are not expected to have significant impact on the results, and this parameter is fixed as $k_{rel} = 0.03$.

In the following sections, the effects of $H_T$, Ste, $\phi_{min}$, and Le, are investigated for stable scenarios with uniform distribution of the frozen material across the flow domain. In addition, the effect of non-uniformity in the initial porosity distribution is examined by defining the initial porosity such that the frozen region forms a block within the domain's boundaries. The flow is still kept viscously stable for these scenarios. In the first part of the study dealing with uniform porosity distribution transverse to the flow, all derivatives with respect to $y$ vanish and the model and consequently the results can be presented in a single spatial dimension $(-x)$. In this part, results are presented in 1D graphs starting from a maximum value of 1 at the injection boundary and decreasing to the minimum values of 0 for temperature and

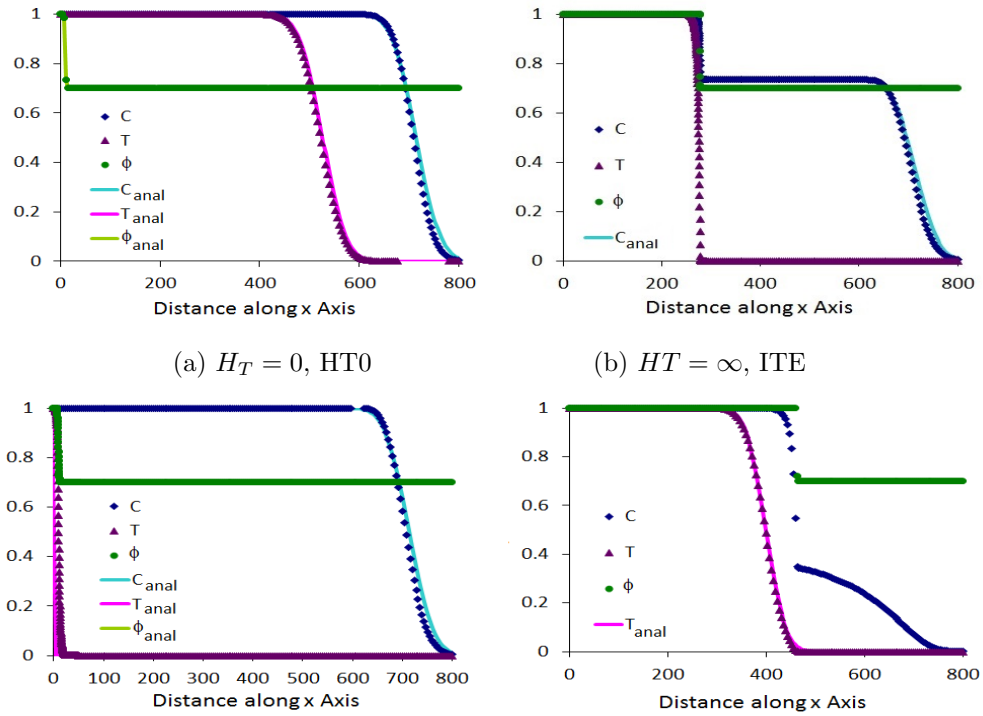


(a) $H_T = 0$, HT0 (b) $HT = \infty$, ITE

(c) Ste $= 0$, *Non-melting* (d) Ste $= \infty$, *Instantaneous Melting*

Figure 5.3: The average Concentration, Temperature, and porosity profiles for reference scenarios with $\phi_{min} = 0.7$ and Le $= 1$: a) no heat transfer to melting (HT0) scenario ($H_T = 1e-7$, Ste $= 0.54$), b) instantaneous thermal equilibrium scenario ($H_T = 100$, Ste $= 0.54$), c) non-melting scenario ($H_T = 10$, Ste $= 1e-5$) and d) instantaneous melting scenario ($H_T = 10$, Ste $= 100$) with numerical solutions and the corresponding approximations.

concentration and $\phi_{min}$ for porosity. In the second part of the results, where frozen blocks are defined, the results are presented in 2D contours of the dimensionless variables.

### 5.4.1 Reference Scenarios

Before analyzing the effects of the different parameters, some reference cases in which $H_T$ and Ste adopt asymptotically large or small values are examined first. These limiting cases will help categorize different scenarios of the flow, infer some of the physics of the system and formulate the general observed trends. In addition and more importantly, the equations for these reference scenarios can be simplified and in some cases be solved analytically. This

has helped validating the numerical code as well as predicting the location and profile of the three fronts evolving in the system.

The first reference scenario is the HT0 scenario in which the heat transfer coefficient between the fluid and the frozen phase is very small (i.e. $H_T \approx 0$). Such a situation can be expected in displacement processes with extremely large injection rates, or in porous media with small contact areas between the fluid and the frozen phase, that do not allow effective heat transfer to the frozen phase. Also if the thermal conductivity of the fluid is very small, not a lot of heat is transferred to the frozen phase and this can result in a HT0 situation. $H_T$ determines the priority of melting over the change of temperature at each point. As a result of a weak heat transfer, the frozen material does not melt and most of the heat brought to the medium is spent on changing the fluid-rock temperature. Thus, it is expected that the injected fluid will not affect the initial porosity distribution of the medium (i.e. $\frac{\partial \phi}{\partial t} = 0$) and the equations may be simplified to:

$$\nabla.(\phi \mathbf{u}) = 0$$
$$\vec{\nabla} p = -\frac{\mu}{\kappa}\mathbf{i}$$
$$\frac{\partial c}{\partial t} = -\frac{1}{\phi}\frac{\partial c}{\partial x} + \frac{\nabla \phi}{\phi}.\nabla c + \frac{\partial^2 c}{\partial x^2}$$
$$\frac{\partial \theta}{\partial t} = \frac{1}{(1-\lambda(1-\phi))}[\mathrm{Le}\nabla.\left((1-(1-\phi)k_{rel})\,\nabla\theta\right) - \lambda\frac{\partial \theta}{\partial x}]$$

where $\phi$ retains its initial profile defined in Equation 5.17. In that equation, the initial porosity varies from 1 to $\phi_{min}$ in a narrow region and remains unaffected outside this region. When both concentration and thermal fronts are well behind or ahead of the porosity drop region, the terms $\nabla\phi.\nabla c$ and $\nabla\phi.\nabla\theta$ vanish everywhere. Therefore, the concentration and temperature profiles can be expressed as:

$$c = \frac{1}{2}\text{erfc}\left(\frac{x - t/\phi}{2\sqrt{t}}\right) \tag{5.36}$$

$$\theta = \frac{1}{2}\text{erfc}\left(\frac{x - \lambda\hat{t}}{2\sqrt{\hat{\text{Le}}\hat{t}}}\right) \tag{5.37}$$

where

$$\hat{t} = \frac{t}{(1 - \lambda(1 - \phi))} \tag{5.38}$$

$$\hat{\text{Le}} = \text{Le}(1 - (1 - \phi)k_{rel}) \tag{5.39}$$

In the above equations, $\hat{t}$ and $\hat{\text{Le}}$ are the scaled time and the effective Le that depend on the porosity of the medium. If $\phi = 1$ then $\hat{t} = t$ and $\hat{\text{Le}} = \text{Le}$.

The results of the numerical simulations and the analytical solutions for HT0 scenario are shown in Figure 5.3a. As expected, the porosity does not change throughout the displacement process and the concentration and the temperature profiles adopt error-function forms described by Equations 5.36 and 5.37.

The second reference scenario corresponds to an asymptotically large heat transfer coefficient; $H_T \approx \infty$ which results in *instantaneous thermal equilibrium (ITE)* between the injected fluid and the frozen material. Opposite to the HT0 case, a very slow flow of hot fluid in the medium, a large contact area between the two phases or a considerably large thermal conductivity for the fluid result in an efficient transfer of heat to the frozen phase and lead to ITE. In this limit, melting is the dominant effect compared to temperature increase, and the fluid looses all its heat to the frozen phase and reaches the melting temperature when flowing through the frozen region. Therefore, as shown in Figure 5.3b, there is a sharp change in the temperature at the melting front. This indicates that in such limits, one must expect challenges related to numerical stability as a result of the sensitivity of the solution

to the grid and time-step sizes, and the simulations may have to be conducted for moderate $H_T$. However, although moderate values may not *a-priori* be physically justified, as we shall see next, the physics of the flow are not substantially changed once $H_T$ exceeds a critical value.

This reference scenario does not result in any simplification of the problem, and the fronts' profiles still need to be determined numerically. However, the general form of the temperature, porosity, and concentration profiles can actually be approximated. As mentioned before, the temperature and porosity fronts experience sharp gradients at the melting front. Aside from the sudden drop at the melting front and when the concentration front is well past the melting region, the change in concentration is governed by the usual convection-diffusion process with no changes in porosity on its way. Hence, a simplified model describing the concentration profile ahead of the melting front will have the form:

$$\bar{c}_{\phi_{min}} = \frac{1}{2}\alpha \times \text{erfc}\left(\frac{x - t/\phi_{min}}{\sqrt{t/\phi_{min}}}\right) \tag{5.40}$$

The coefficient $\alpha$ is expected to depend on the rate of melting and hence a general value cannot be *a-priori* determined. In the present study, $\alpha$ was determined from the results of the simulations using the value of the concentration right after the drop at the melting front. The agreement between the concentration profile in Figure 5.3b and the analytical description in Equation 5.40 confirms that the concentration profile past the melting front is not affected by the melting process and follows an error-function type profile.

The next two reference scenarios are defined based on extreme values of the Stefan number; the first being Ste = 0. As mentioned before Ste is the potential of the fluid to melt the frozen phase. In other words, for any given amount of heat, it determines how fast the frozen material gets melted. A very small sensible heat content of the injected fluid with respect to the latent heat of the frozen phase can result in a small Ste and a slow melting rate. An infinitely small Ste results in *non-melting* conditions, but unlike the HT0 scenario

for such a system depending on $H_T$ some share of heat is devoted to melting the frozen material. As illustrated in Figure 5.3c, a large heat transfer rate causes the thermal front to get stuck behind the melting (non-melting) front, and although the concentration and the porosity profiles are similar for HT0 and *non-melting* scenarios, their temperature profiles are different. Like in the HT0 scenario, the analytical description of the concentration profile matches very well the simulations' results.

In the last reference scenario of *instantaneous melting* with Ste $\approx \infty$, the frozen phase shows no resistance against the flow of heat in the medium and all the melting takes place immediately at the first contact of the hot fluid at the tip of the thermal front. Hence the temperature profile does not experience any changes in porosity as it hardly meets the frozen material. Therefore the profile of the thermal front follows a simple error-function form:

$$\theta = \frac{1}{2}\mathrm{erfc}\left(\frac{x-\lambda t}{2\sqrt{\mathrm{Le}.t}}\right) \tag{5.41}$$

The above expression is equal to Equation 5.37 for $\phi = 1$. Since the concentration distribution depends on the rate of melting and therefore is correlated with the temperature and porosity distributions, numerical solution of the equations is required to determine the concentration profile. For the porosity distribution, one can expect the melting front to lead to a sharp porosity drop at the end point of the thermal front. Ideally instantaneous melting should be independent of the value of $H_T$, nevertheless for this numerical analysis (see Figure 5.3d) since Ste adopts a large but finite value, the value of $H_T = 10$ is used to ensure instantaneous melting not being delayed by the heat transfer coefficient.

Although an extremely large heat transfer coefficient $H_T \approx \infty$ may be expected to result in instantaneous melting, as will be seen in the following section, for high $H_T$ values the melting rate is mainly controlled by the melting potential of the injected fluid (Ste). Hence, rapid heat transfer between the fluid and the frozen phase does not guarantee instantaneous

melting condition to be met.

In the following section the trends of changes in the profiles are discussed as the heat transfer coefficient is varied between the HT0 and the ITE scenarios.

### 5.4.2 Effect of $H_T$

The heat transfer coefficient represents the amount of heat that can be made available to melt the frozen phase. Figure 5.4 depicts the temperature, porosity, and concentration profiles at $t = 500$ for different values of the heat transfer coefficient, and for Ste $= 0.5$ and $\phi_{min} = 0.7$. The effects on the temperature, porosity, and concentration are discussed next.

**Temperature** In the case $H_T = 100$, melting starts shortly after the thermal front reaches the low porosity region, and most of the heat that comes to the melting front goes to the frozen material. As a result, the temperature decreases rapidly to the melting temperature ($\theta_m = 0$). There are no noticeable changes in the temperature profile as $H_T$ is reduced to 1. Further reduction of $H_T$ results in slower melting of the frozen material. As a consequence, some part of the heat is carried to regions further downstream of the melting front and melts some of the frozen material in those regions. This is well illustrated by the temperature profiles for $H_T = 0.01$ and 0.001 which extend further downstream than those corresponding to larger $H_T$. For $H_T = 1e-7$ (HT0) the temperature profile can be described by the error function presented in Equation 5.37.

**Porosity** Due to the sharp changes in the temperature at the melting front for $1 \leq H_T \leq 100$, the porosity shows a step-function like profile that was found to shift forward with time. Note that here too, the porosity for $H_T = 100$ and $H_T = 1$ are essentially indistinguishable. The diffusion of heat in the medium and the extended profile of temperature for intermediate values; $0.001 \leq H_T \leq 0.1$ result in the advancement of the end of the melting front along side the thermal front. However, the slow rate of melting due to a smaller share of heat

available for melting causes the beginning of the melting front to advance slowly. Hence, the melting front is extended in the medium for the small heat transfer coefficients. When $H_T = 1e-7$ the change in porosity from its initial configuration is negligible.

**Concentration** For the largest examined heat transfer coefficient ($H_T = 100$), as expected the concentration profile shows a sudden drop due to the melting and dilution of the solvent with the melted fluid. Beyond the melting front, the solvent enters a medium with a porosity $\phi_{min}$ smaller than that in the upstream regions with $\phi = 1$. Thus, the flow velocity increases and the concentration front advances much more rapidly. Since for this large $H_T$ all the melting takes place at a narrow region of the medium, there are no interactions between the flow and the medium ahead of the melting front and the concentration adopts an error-function like profile. Like what was observed in the temperature and porosity profiles, the reduction of $H_T$ from 100 to 1 leads to virtually no changes in the concentration profiles. A non-monotonic concentration profile that extends along the melting front is observed in the intermediate range; $0.001 \leq H_T \leq 0.01$. This non-monotonic behavior is attributed to the fact that the rate of melting increases with time, which we shall further discuss next when looking at the time trends of the process. So the melting starts with a slow rate that then ramps up in time. Hence, the concentration shows a small drop at the melting front at early times. As the solutal front advances faster than the thermal front, those leading parts of the fluid that experience a small drop in concentration move ahead and do not get affected by the melting front any more. Later in the process, the following fluid experiences more decrease in concentration at the melting front as more rapid melting takes place, leading to a non-monotonic concentration distribution. By further reducing $H_T$ to smaller values (i.e. $H_T = 1e-7$), the share of heat that can lead to melting becomes so small that the profiles follow those of a HT0 scenario, and the concentration profile can be adequately described by Equation 5.36.

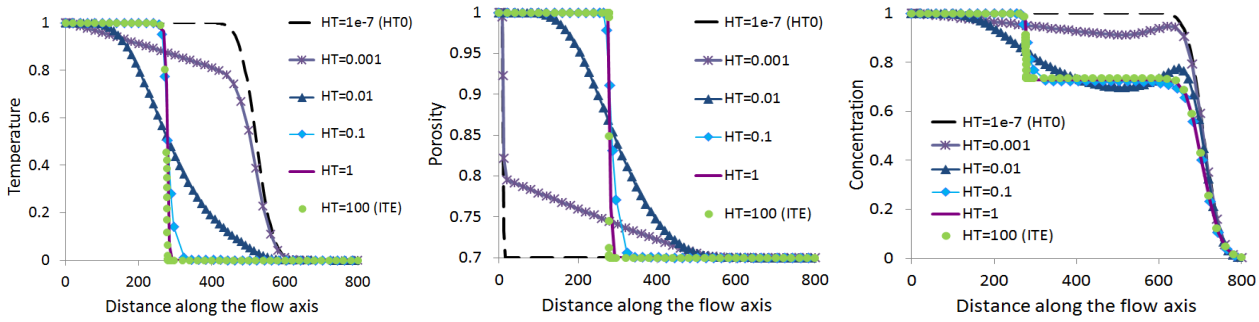


(a) Temperature (b) Porosity (c) Concentration

Figure 5.4: Effect of $H_T$ on temperature, porosity, and concentration profiles for Le $= 1$, $\phi_{min} = 0.7$, Ste $= 0.5$, and $H_T = 1e-7$ to 100 at $t = 500$.

One of the major conclusions that can be made based on the graphs of Figure 5.4 is that, for the adopted values of the parameters, the temperature, porosity, and concentration profiles do not show significant changes with an increase of the heat transfer coefficient beyond $H_T = 1$. This may be attributed to the fact that the heat brought to the medium by the injected fluid has a limited amount, and even though the heat transfer coefficient may be increased, no larger amount of heat can be provided by the fluid. In order for the fluid to provide more heat to the medium either the fluid's melting potential (i.e. Ste) or the diffusion rate of heat into the fluid-rock system (i.e. Le) has to increase. The effect of changing these parameters on the melting process will be presented and discussed in the following sections. Hence fixing all the other parameters, there is a critical heat exchange rate for each scenario above which any increase in the heat transfer coefficient does not increase the rate of melting or affect the flow. For the parameters' values of Figure 5.4 it is reasonable to expect that for even larger heat transfer coefficients (as large as required for ITE conditions) the results will be close to those for $H_T = 1$. Since in real applications the heat transfer coefficients between the fluid and the frozen medium is large, henceforth we only discuss the effect of the other parameters for a constant heat transfer coefficient $H_T = 10$ that corresponds to ITE condition for a wider range of parameters than $H_T = 1$.

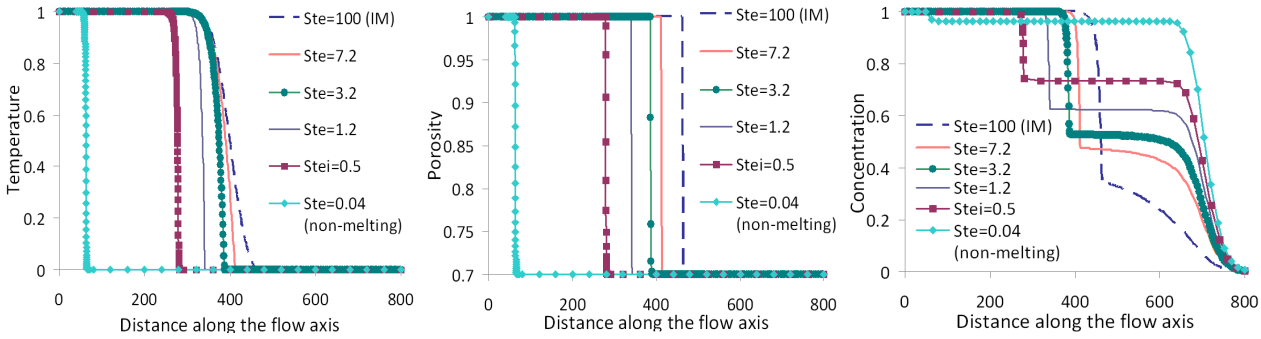


(a) Temperature (b) Porosity (c) Concentration

Figure 5.5: Effect of Ste on temperature, porosity, and concentration profiles for Le = 1, $H_T = 10$ and $\phi_{min} = 0.7$, and Ste = 0.04 to 100 at $t = 500$.

### 5.4.3 Effect of Ste

In Figure 5.5, results are presented for different Ste values varying between 0.04 and 100 which approximate the *non-melting* and *instantaneous melting* scenarios, respectively. The heat transfer coefficient is set to $H_T = 10$ with $\phi_{min} = 0.7$ and all the profiles are depicted at $t = 500$.

**Temperature** A larger melting potential of the injected fluid leads to a faster melting and a faster advancement of the thermal front. So the thermal front gets less hindered by the melting front and for large Ste values, the temperature profile has a smoother transition to the melting temperature. As discussed before, the *instantaneous melting* scenario describes the large limit of such an increase for which the temperature profile is described by Equation 5.41. The effect of Ste on the advancement rate of the thermal front is more important for smaller Ste values. This effect can be attributed to the error function profile of Equation 5.41 setting a limit on the advancement of the thermal front for large Ste. Thus the advancement of the melting front (and the thermal front) for small Ste values is controlled by the melting rate and for larger Ste is limited by the rate of convection-diffusion of heat in the medium.

**Porosity** The rate of melting depends on $H_\phi = \text{Ste}/\lambda \times H_T$, so for a constant $H_T$, increasing Ste implies a faster melting and faster advancement of the melting front. As mentioned before, for smaller values of Ste the rate of melting is mainly controlled by the fluid's melting potential. However, as Ste increases, the melting front has to wait for the thermal front to advance. Therefore in the porosity profiles in Figure 5.5, the effects of Ste on the advancement of the melting front are more significant for smaller values and become less important as the scenarios become closer to *instantaneous melting* reference scenario.

**Concentration** The effect of larger Ste on the concentration distribution is to decrease the concentration to a smaller value at the melting front by inducing faster melting. Although the extent of decrease in the concentration and its location are affected by the rate of melting as well as the position of the melting front, the end point of this front remains more or less the same (around $x = 800$) for different Ste values.

### 5.4.4 Effect of $\phi_{min}$

The next parameter to be analyzed is $\phi_{min}$ which defines the initial saturation of the frozen material in the medium ($S_s = 1 - \phi_{min}$). Figure 5.6 shows the profiles at $t = 500$ for different values of the initial porosity ($\phi_{min} = 0.6$ to $0.9$) and for Ste $= 0.5$, $H_T = 10$. It should be noted that when $\phi_{min} = 1$, there is no frozen material present in the medium and the temperature and concentration profiles can be simply described by Equations 5.36 and 5.41.

**Temperature and Porosity** Since in this figure the assigned $H_T$ represents ITE conditions and Ste is small, the advancement of the thermal front is hindered by the melting front. By decreasing $\phi_{min}$, there is more frozen material that should be melted before the melting front can move further. This consequently causes a slower movement of the melting front. The amount of heat devoted to melting as described in Equation 5.34 couples the effect of

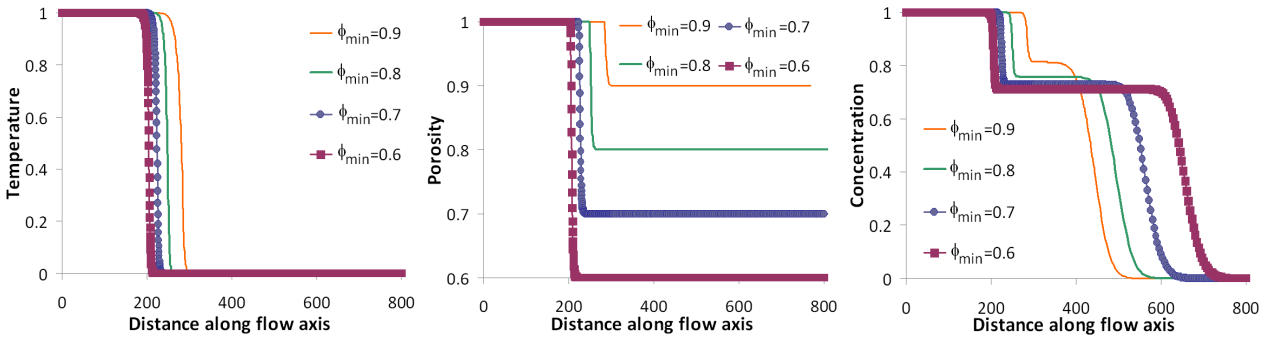


(a) Temperature (b) Porosity (c) Concentration

Figure 5.6: Effect of $\phi_{min}$ on temperature, porosity, and concentration profiles for stable scenarios with Le = 1, Ste = 0.5, $H_T = 10$ and $\phi_{min} = 0.6$, 0.7, 0.8, and 0.9 at $t = 500$

the initial saturate of the frozen material with the heat transfer coefficient $H_T$. Therefore although a smaller $\phi_{min}$ results in a larger heat transfer rate, as seen for $H_T$ when the process reaches ITE conditions, decreasing $\phi_{min}$ below a certain value may not affect the melting rate. This is the case as seen in Figure 5.6 when $\phi_{min} = 0.6$ and 0.7 .

**Concentration** Due to a smaller porosity of the medium at the frozen regions compared to the entrance area with $\phi = 1$, the interstitial velocity of the fluid is larger in the frozen area and it increases by further decreasing $\phi_{min}$. As a consequence, the concentration front has a faster movement in cases with smaller $\phi_{min}$. Moreover, since the melting front's advancement is slower for smaller $\phi_{min}$, the distance between the first concentration drop at the melting front and the leading edge of the concentration front increases by a decrease of $\phi_{min}$. The concentration profiles in Figure 5.6 show that the drop in the solvent concentration at the melting front is smaller when there is less frozen material to melt, although the difference is less significant for smaller values of $\phi_{min}$. This effect can be attributed to the melting rate mainly controlled by Ste. So for small $\phi_{min}$ values and small Ste, although there is more material to melt, the amount that actually melts is limited by Ste regardless of the saturation of the frozen material.

The porosity of the frozen regions $\phi_{min}$ is the only parameter that affects the position of

the end point of the concentration front and consequently the breakthrough time. Progress of the solvent concentration ahead of the melting front is important as it increases the contact between the solvent and the inhabitant fluid farther ahead of the thermal front. Therefore, although the diffusion rate of mass is much smaller than that of heat, convection of the solvent to farther points may increase the efficiency of miscible displacement processes over immiscible ones for cases where early breakthrough of the solvent is not an issue (like in SAGD and VAPEX chambers).

### 5.4.5 Effect of Le

Since heat diffuses in the medium much faster than mass does, the Lewis number, or the relative rate of diffusion of the heat to that of the concentration, is expected to be much larger than 1. The reason for choosing Le = 1 in the scenarios discussed so far is to be able to compare the growth of the mixing zone for temperature and concentration fronts. In Figure 5.7 scenarios with $H_T = 10$, $\phi_{min} = 0.7$, Ste = 0.5 and 3.2, are compared for Le = 1 and 10 at $t = 500$. The system's response to changes of Le for different values of the other parameters, may turn out to be complex. Equation 5.33 shows the interplay of three terms in the transfer of heat. The convection and diffusion terms result in a net motion of the thermal front in the downstream direction. The term corresponding to the heat transfer to the frozen phase however, favors melting over the advancement of the thermal front. A larger Le results in stronger diffusion of heat in the fluid and the rock phases and leads to a more diffused thermal front. The value of the heat transfer coefficient $H_T = 10$ used in this analysis, favors melting over temperature redistribution. Therefore, a slow melting process suppresses the thermal front while a fast melting scenario gives way to an enhanced advancement of the thermal front. Having these interpretations in mind, the graphs shown in Figure 5.7 are now discussed.

**Temperature** The stronger heat conduction due to larger Le results in a more diffused temperature profile. The resistance of the frozen region to melting and the diffusion of heat in the medium are clearly observed in Figure 5.7 for Ste = 0.5 which does not allow the thermal front to advance even though diffusion is enhanced. For Ste = 3.2 the fast melting allows the thermal front to develop a more diffused profile and a higher Le results in a faster melting.

**Porosity** The porosity distribution graphs show that faster diffusion of heat in the medium increases the melting by providing increased amount of heat that reaches the frozen regions. This effect is different from the effect of the heat transfer coefficient $H_T$ which changes the share of heat that is used for melting. Increasing Le, as stated before, increases the amount of heat that is provided to the low temperature regions. Thus the critical $H_T$ beyond which the system shows no improvement in terms of melting should be larger for systems with larger Le. As mentioned before, a slower melting of the frozen region for Ste = 0.5 limits the expansion of the thermal front. As a result, the effect of larger Le on the melting front is less significant for smaller Ste.

**Concentration** The rapid diffusion of heat in the medium results in a faster melting and a larger jump in concentration at the melting front. It also causes the drop in concentration to take place at farther points down the flow as the advancement of the melting front is enhanced. While such an effect is not clear for Ste = 0.5, the concentration profile of Ste = 3.2 and Le = 10 shows significantly larger drop at the melting front and then a smoother distribution at the frozen regions which results from the faster melting at the beginning of the process for Le = 10 than for Le = 1.

The previous results represent a snapshot in time of the system and therefore do not show the transient nature of the flow. In addition, although the profiles and positions of the

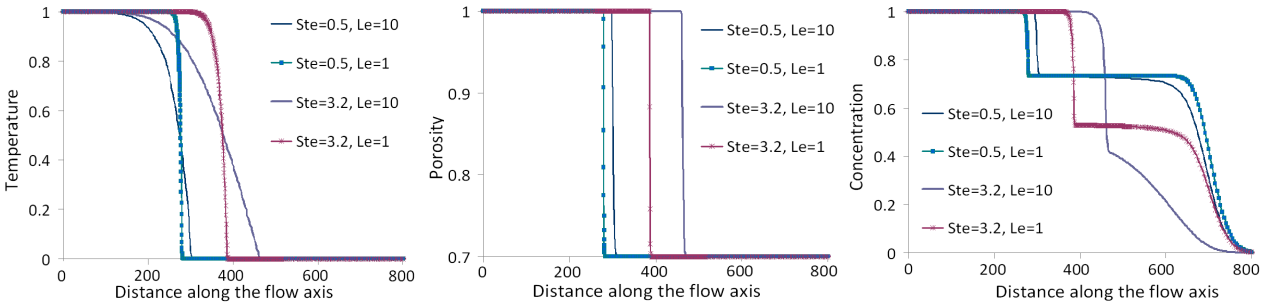


(a) Temperature (b) Porosity (c) Concentration

Figure 5.7: Effect of Le on temperature, porosity, and concentration profiles for stable scenarios with $\phi_{min} = 0.7$, $H_T = 10$ and Ste $= 0.5$ and 3.2 and Le $= 1$ and 10 at $t = 500$.

temperature, melting and the concentration fronts provide useful information, they may not be easily measured in real applications. One may therefore be interested in analyzing the transient behavior of measurable characteristic quantities. Depending on the purpose of the displacement process or the natural phenomenon being studied, different quantities can be defined to assess and categorize different scenarios. The efficiency of a process is one of the interesting criteria to be defined and measured. Since the extent of melting of the frozen phase is one of the main focuses of the present system, the cumulative produced melt is a good representative of the efficiency of the process and its time trends are analyzed next.

### 5.4.6 Time trends of melting

The amount of frozen material that has been melted up to a specific time is measured by subtracting the porosity of the medium from its initial value and integrating over the domain and dividing by the length of the domain Pe. Although for scenarios with sharp porosity gradients, the amount of melt produced is expected to be commensurate with the advancement of the melting front in time, for scenarios with extended melting fronts such a dependence is not *a-priori* trivial.

The time trends of melting for different scenarios are shown in Figure 5.8 where $H_T$ is varied between $1e-4$ and 100, for Ste $= 15$, $\phi_{min} = 0.7$ and Le $= 1$. As expected, the

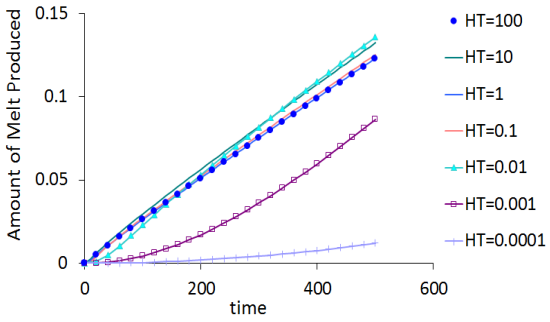


Figure 5.8: Effect of heat transfer coefficient on the amount of melt produced for different scenarios with Le $= 1$, $\phi_{min} = 0.7$, Ste $= 15$, and $H_T = 1e-4$ to 100.

scenarios close to ITE condition (i.e. with $H_T > 1$) have virtually the same amount of melt and rate of melting. For the slow heat transfer scenarios, expansion of the thermal front over the frozen domain covers more area with melting. Therefore, although a lower $H_T$ results initially in a slower melting rate, it does lead to more cumulative melt at later times. This is the case with the $H_T = 0.1$ scenario for which the melting curve surpasses those of the larger $H_T$ at $t \approx 200$ and ends up with the maximum amount of melt. Given enough time for the melting process to speed up, one expects the cases with $1e-4 \leq H_T \leq 0.001$ to also ultimately lead to larger melt production than the scenarios with large $H_T$.

When the melting front experiencing a fast heat transfer between the fluid and the frozen phase, it only shifts in space and does not show any growth or change in its form. This causes the melt product for ITE scenarios to have an almost perfect linear growth with time. Hence the slope of the melting curve (i.e. the rate of melting) for fast heat transfer scenarios can be used to fully characterize the whole melting process. This conclusion is however limited to moderate values of Ste. For large Ste values, as shown before, the rapid melting results in a diffused thermal front. The rate of melting is therefore affected by the diffusive growth of the heated zone as $\sqrt{\text{Le}t}$ for instantaneous melting conditions and the melting zone does not grow linearly with time any more.

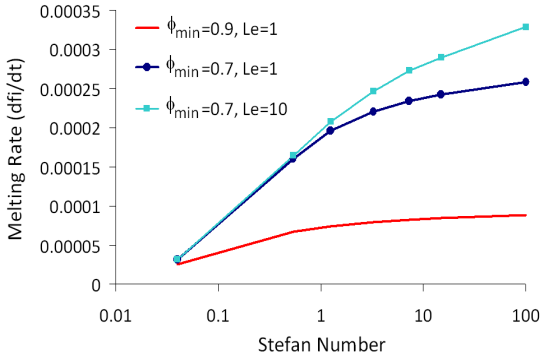


Figure 5.9: Effect of Ste, Le, and $\phi_{min}$ on melting rate at ITE conditions, for $H_T = 10$,Le $= 1$ and 10, $\phi_{min} = 0.7$ and 0.9, and Ste $= 0.04$ to 100.

The rate of melting for different scenarios at ITE depends on Ste, $\phi_{min}$ and Le. Figure 5.9 shows the slopes for different scenarios with a heat transfer coefficient of $H_T = 10$ versus Ste for $\phi_{min} = 0.7$ with Le $= 1$ and 10, and for $\phi_{min} = 0.9$ with Le $= 1$. As shown before, by increasing Ste the rate of melting increases and is expected to ultimately reach that of the corresponding instantaneous melting condition. That is why in all three curves the melting rate increases faster for smaller Ste values and then reaches a plateau as Ste $\to \infty$. A higher saturation of the frozen phase has a faster heat transfer rate and provides more material to be melted. Therefore the melting rate curve for $\phi_{min} = 0.7$ is above that of $\phi_{min} = 0.9$ for all Ste values. However as the melting potential of the fluid decreases, so does the effect of the initial porosity on the rate of melting. In fact for very small Ste the amount of heat devoted to melting is the same and results in similar melting rate for different values of $\phi_{min}$. Faster diffusion of the heat in the medium is expected to result in faster advancement of the leading edge of the thermal front in the medium. However the thermal front encountered in the melting is impeded by the melting front. Therefore as discussed in the previous section and is shown clearly in Figure 5.9, a larger Le does not have any significant effect on the melting rate when Ste is small. An enhancement of melting as a result of larger Le is however observed for Ste $> 1$.

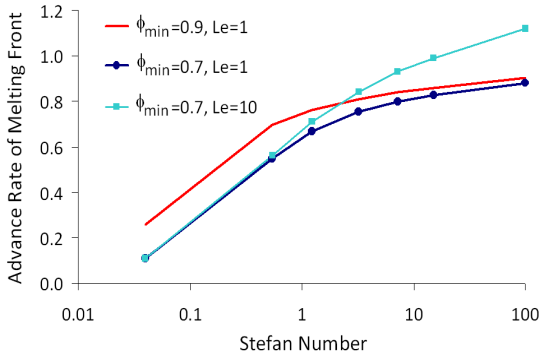


Figure 5.10: Effect of Ste, Le, and $\phi_{min}$ on the advance rate of the melting front at ITE conditions, for $H_T = 10$,Le $= 1$ and 10, $\phi_{min} = 0.7$ and 0.9, and Ste $= 0.04$ to 100.

The rate of advancement of the melting front is plotted in Figure 5.10 versus Ste for similar scenarios. This parameter can be determined by scaling the melting rate over $(1 - \phi_{min})$/Pe and has the dimension of length per unit time. It is more or less trivial that the melting front has a faster advancement when there is less material to melt. However when Ste is large, then the thermal front has enough potential to melt all the frozen material on its way and therefore the saturation of the frozen material does not affect the advancement of the melting front. Figure 5.9 showed that the melting rate is the same for different scenarios at very small Ste values while in Figure 5.10 the advancement of the melting front (which can be scaled back to the amount of melt) is found to be the same for different $\phi_{min}$ values at very large Ste. Therefore, using these data points, one can approximate the melting rate for different $\phi_{min}$ values at fast melting and non-melting conditions.

The analytical study of the rising rate of steam chamber in heavy oil reservoirs by Gotawala and Gates [119] revealed an inverse proportionality between the vertical advancement rate of the chamber and the oil content per unit reservoir rock volume (i.e. $S_0$). The melting rate is equivalent to the advance rate of the melting front times the saturation of the frozen material $(1 - \phi_{min})$. Then a inverse proportionality between the advancement rate and the saturation of the frozen material can be translated to a constant melting rate for

different $\phi_{min}$ values. The equivalent melting potential of steam at 100 deg $C$ for the melting of bitumen is around Ste = 0.02. We can therefore conclude that this observation agrees with Figure 5.9 in which, for small Ste, the melting rate is nearly constant for different $\phi_{min}$ values.

### 5.4.7 Frozen Blocks

In the displacement scenarios discussed so far, the changes in porosity occur only along the flow direction. Thus although the interstitial velocity increases as the fluid flows through the frozen regions, the velocity profiles transverse to the flow remain unchanged throughout the process and the system can be effectively treated as 1D. However if the frozen region is defined as a confined block within the flow domain, then the system will behave differently and the velocity field around the frozen block will have a non-uniform distribution. The ability of the fluid to avoid the frozen region is the main difference between the scenarios discussed so far and the heterogeneous scenarios consisting of frozen blocks. The velocity distributions in these heterogeneous media depend on $\nabla f$ (i.e. the range and the length scale of the of permeability variations [170]). The range of variation of the permeability in the domain, according to Equation 5.8, is determined by the porosity of the frozen region and the length scale of the variations depends on the geometry of the frozen block. The heterogeneity of the medium introduces some instabilities to the solutal and the thermal fronts. It should however be stressed that the system is still viscously stable with $\beta_C = \beta_T = 0$.

The frozen block in Figure 5.11a is defined as a square of size $L_x/3$ with $\phi_{min} = 0.2$. The flow takes place in a medium of length Pe = 128 with Le = 1, Ste = 1.2, and $\lambda = 0.8$. The change in porosity $(\phi - \phi_{t=t_0})$ showing the local cumulative melt and the differential velocity vectors $(\phi\mathbf{u} - \mathbf{i})$ at $t = 30$ are depicted in Figure 5.11b and the temperature iso-profiles are shown in Figure 5.11c. The melt contours show that the melting occurs mainly at the side

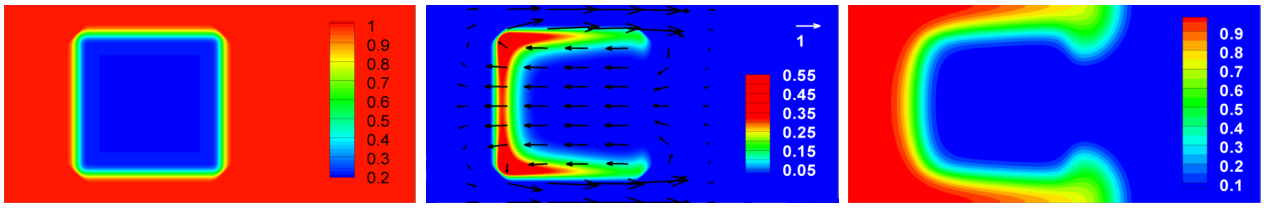


(a) (b) (c)

Figure 5.11: Melting of a square shaped frozen block of size $l = Pe/3$ for Pe $= 128$, Le $= 1$, $\lambda = 0.8$, Ste $= 1.2$. a) Initial porosity distribution for $\phi_{min} = 0.2$, b) Change in porosity and differential velocity contours at $t = 30$, and c) Temperature contours at $t = 30$.

of the frozen block facing the flow and partially on the transverse boundaries along the flow. These are the regions where the hot fluid comes into contact with the frozen block. The differential velocity vectors inside the frozen region point backwards which indicates that the velocity in this region is less than the injection rate $|\phi\mathbf{u}| < 1$. In the more permeable channels, between the frozen region and the transverse boundaries of the domain (i.e. $y = 0$ and $y = \text{Pe}/A$), the differential velocity vectors are larger (almost three times larger) than the injection velocity. The fast flow in these high permeable channels results in fast advancement of the thermal front and increases the contact length between the high temperature fluid and the frozen material at the boundaries of the frozen block. Ahead and behind the frozen block the velocity is virtually not affected by the introduced heterogeneity and the differential velocity is zero.

To analyze the effect of the initial porosity, the melting patterns, differential velocity vectors and the temperature contours for a frozen square block with a larger initial porosity of $\phi_{min} = 0.8$ are presented in Figures 5.12a and b. By increasing the porosity of the frozen region (and consequently its permeability), the velocity inside the frozen region increases to close to 1 and a larger fraction of the heat can flow through the frozen block. Although the velocity in the high permeable channels is larger than the one through the frozen region it is slightly larger than the injection velocity. Thus in Figure 5.12 the temperature profiles have slower advancement in the high permeable areas and provide smaller contact length

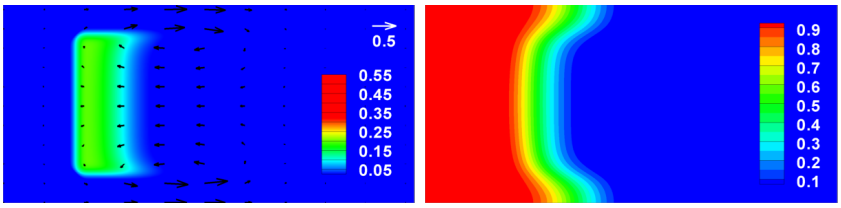


(a) (b)

Figure 5.12: Melting of a square frozen block with $\phi_{min} = 0.8$ at $t = 30$ a) Change in porosity and differential velocity and b) Temperature contours. The other parameters are similar to those in Figure 5.11.

between the hot fluid and the frozen block. In this case, the frozen block melts evenly in the $y$ direction as a result of the more even distribution of the velocity field in the medium. This is to be contrasted with the low porosity block (Figure 6.11) where the bulk of the hot fluid rushes around the frozen block extending the melting on the side walls where the frozen block contacts the hot fluid.

These observations lead to distinguishing two main mechanisms for the melting of the frozen block. The first mechanism is the internal heat transfer that melts the frozen material through the flow of heat inside the frozen block, similar to the one dimensional scenarios discussed earlier. The second mechanism melts the frozen material on the sides of the frozen block adjacent to the high permeable channels. In these regions the melting is due to the heat convection between the fluid and the frozen block and therefore the second melting mechanism is called *outer-boundary convection*. A larger velocity in the high permeable channels increases the melting through this mechanism. Any possible dominance of the involved melting mechanisms depends on the velocity distribution in the domain and hence the geometry and initial porosity of the frozen block. A strong flow through the frozen region as observed in Figure 5.12 improves melting inside the frozen region while a fast flow around the frozen block as observed in Figure 6.11 enhances melting through the outer-boundary convection.

Beside the initial porosity, the heterogeneity of the medium is also characterized by the

length scale of permeability variations which can be reflected by the width of the frozen block. Figures 5.13 and 5.14 depict the same contours as shown in Figure 6.11, for two rectangular blocks of size (Pe/12 $\times$ Pe/3) extended along and transverse to the main flow direction, respectively. These geometries will be referred to as the long and the wide rectangle blocks, respectively. The porosity of both blocks is $\phi_{min} = 0.2$. When the long rectangle block and the square one in Figure 6.11 are compared, one finds that a reduction of the block's width decreases the flow velocity inside the frozen block as it is easier for the flow to avoid the low permeable region. This reduces the rate of melting through the first melting mechanism. Also the flow of the fluid in the high permeable channels around the long rectangle block is slower since the width of these channels is larger for this block geometry. As mentioned before, a slower flow around the frozen block reduces the melting on its boundaries by reducing the equivalent convective heat transfer coefficient. Furthermore, the heat transfer due to outer-boundary convection depends strongly on the contact length between the thermal front and the frozen block. A slower flow, which means a slower progress of the thermal front as shown in Figure 5.13c, provides a smaller contact length between the high temperature fluid and the frozen block and hence a smaller contribution to melting through outer-boundary convection (compare Figures 5.11c and 5.13c).

The wide rectangle has a higher permeability to the flow than the square block as its length is smaller and therefore the velocity inside the wide rectangle block is slightly larger than that in the square one. For the same reason in the high permeable channels beside the frozen block, the velocity is smaller for the wide rectangle than the square block. The smaller velocity in the high permeable regions and the smaller length of the wide rectangle frozen block can result in smaller outer-boundary convection. In spite of this, the fast progress of the thermal front in the high permeable channels observed in Figure 5.14c allows the heat to encircle the frozen block over a short time and increases the outer-boundary convection

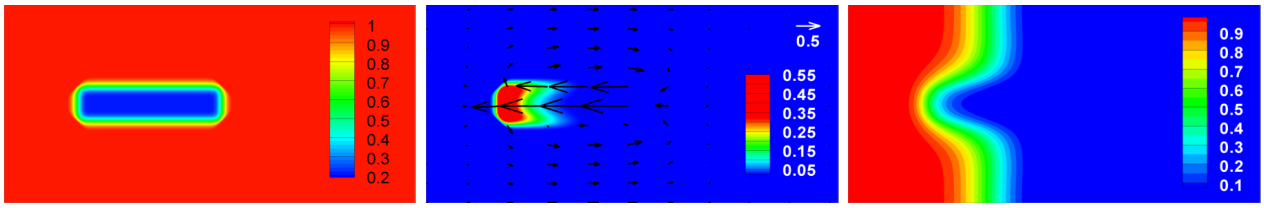


(a) (b) (c)

Figure 5.13: Melting of a long rectangle shaped frozen block of length $l = Pe/3$ and width $w = Pe/12$ for Pe $= 128$, Le $= 1$, $\lambda = 0.8$, Ste $= 1.2$. a) Initial porosity distribution for $\phi_{min} = 0.2$, b) Change in porosity and differential velocity contours at $t = 30$, and c) Temperature contours at $t = 30$.

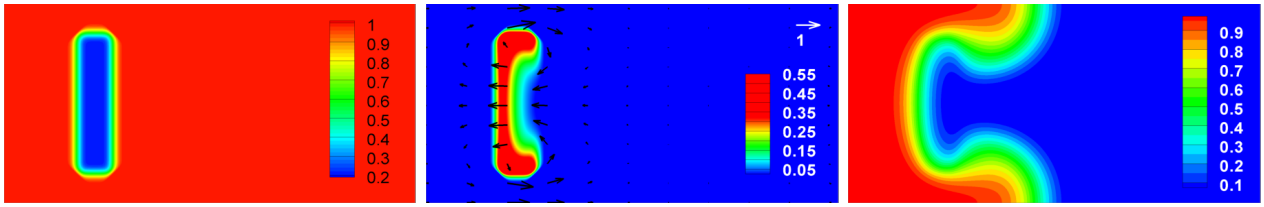


(a) (b) (c)

Figure 5.14: Melting of a wide rectangle shaped frozen block of length $l = Pe/12$ and width $w = Pe/3$ for Pe $= 128$, Le $= 1$, $\lambda = 0.8$, Ste $= 1.2$. a) Initial porosity distribution for $\phi_{min} = 0.2$, b) Change in porosity and differential velocity contours at $t = 30$, and c) Temperature contours at $t = 30$.

by increasing the contact length between the hot and the frozen phases.

The two dimensional contours are helpful in understanding some aspects of the melting process. However one cannot make definite conclusions about the contribution of any of the melting mechanisms based solely on these profiles. It is also hard to make comparative analyses between the different geometries and initial porosity values based on such contours. In the following sections a more quantitative analysis is presented.

Contribution of the Melting Mechanisms

To determine the importance of each of the melting mechanisms, the velocity fields are analyzed with a particular focus on the flow inside the frozen blocks. If the rate of melting due to the transport of heat inside the frozen region is assumed to be proportional to the flux of heat through this region, then an estimation of the heat flux through the frozen block

would be helpful in determining the contribution of this melting mechanism to the total melting.

For the condition of the discussed scenarios and based on the velocity profiles in Figures 6.11-5.14, that retain the uniform injection velocity profile closely before and after the frozen region, the length of influence of heterogeneity can be assumed to be equal to the block's length. Such an assumption may not be valid for large injection rates and an equivalent length for the block should be defined. Hence, the velocity $u_F$ inside the frozen region with relative permeability $\kappa_{min}$ and $u_O$ in the high permeable channels of relative permeability 1, can be approximated from the mass and momentum conservation equations:

$$\begin{aligned} u_F\nu + u_O(1-\nu) &= 1 \\ \frac{u_F}{u_O} &= \kappa_{min} \end{aligned} \tag{5.42}$$

Therefore

$$\begin{aligned} u_F &= \frac{\kappa_{min}}{\kappa_{min}\nu + (1-\nu)} \\ u_O &= \frac{1}{\kappa_{min}\nu + (1-\nu)} \end{aligned} \tag{5.43}$$

Here $\nu = w_{FB}/(\mathrm{Pe}/A)$ is the relative width of the block ($w_{FB}$) to that of the domain ($\mathrm{Pe}/A$). The permeability of the frozen region $\kappa_{min}$ is scaled with respect to the rock permeability as defined in Equation 5.19 and is always less than 1.

Equation 5.43 shows that both $u_F$ and $u_O$ decrease as the width of the block $\nu$ is decreased. The effect of the initial porosity can also be deduced from this equation. With an increase of $\kappa_{min}$, the velocity inside the frozen block increases while $u_O$ decreases. It should be noted that during the melting process, the geometry of the block and its porosity change and therefore the initial descriptions of the block only give rough estimates for the velocity at later times.

The total 2D heat flow through the domain and the share that enters the frozen block are:

$$\begin{aligned} Q_{total} &= \rho_f c_{pf}(\mathrm{Pe}/A)(u_F\nu + u_O(1-\nu)) \\ &= \rho_f c_{pf}\mathrm{Pe}/A \\ Q_{block} &= \rho_f c_{pf}(\mathrm{Pe}/A)u_F\nu \end{aligned} \tag{5.44}$$

Hence the fraction of the total heat flux that enters the frozen region is $u_F \times \nu$ and can be determined using Equation 5.43. The fractional heat flux for different block geometries and initial porosity values are plotted in Figure 5.15. For the one dimensional scenario, the fraction of heat that enters the frozen regions is trivially constant; 1. According to the graphs, the fractional heat flux is the same for the wide rectangle and the square blocks and is smaller for the long rectangle than the other two block geometries. In a homogeneous medium with $\phi_{min} = 1$, the share of heat that flows through the defined frozen block would be equal to the corresponding $\nu$ of the block which is $\nu = 0.67$ for the square and the wide rectangle blocks and $\nu = 0.17$ for the long rectangle one.

As mentioned earlier, we are assuming that the heat transfer inside a frozen block is proportional to the flux of heat passing through this region. Therefore, neglecting the melting at the outer-boundaries of the block, the ratio of the cumulative melt of a frozen block over that of the one dimensional case (relative cumulative melt) should be close to the fractional heat flux passing through the frozen block. A comparison between these two ratios (i.e. the relative cumulative melt and the fractional heat flux) can help determining the importance of each of the melting mechanisms. In Figure 5.15, two sets of scattered data points represent the relative cumulative melt of the frozen blocks at two different time steps $t = 5$ (the solid triangles) and $t = 30$ (the asterisks) for $\phi_{min} = 0.4$. At the early time steps ($t = 5$) when the effect of heat convection to the outer boundaries of the frozen block is negligible, the

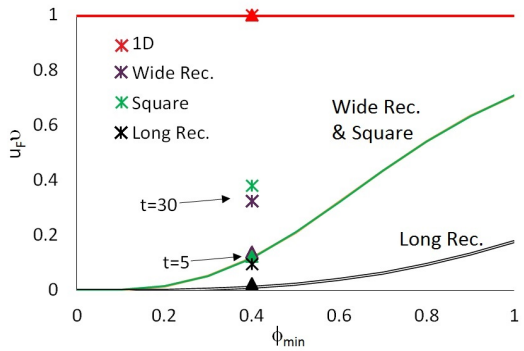


Figure 5.15: Fractional flux of heat entering the frozen region ($u_f\nu$) for different block geometries and the one dimensional scenario. The data points represent cumulative melt ratio (i.e. cumulative melt of the frozen block over the cumulative melt of the 1D scenario at each time step) for the corresponding frozen block geometry at $t = 5$ (triangles) and $t = 30$ (asterisks). Other parameters are set as $H_T = 0.1$, Pe $= 128$, Le $= 1$, $\lambda = 0.8$, Ste $= 1.2$.

data points are close to the curves for all block geometries. These data points confirm the validity of our premise about the proportionality of melting to the heat flux. At $t = 30$ the advancement of the thermal front in the high permeable channels increases the contribution of convection at the outer boundary to the cumulative melt, and the relative cumulative melt values become significantly larger than the fractional heat flux values. The difference between the relative cumulative melt and the fractional flux is due to the contribution of the outer-boundary convection to melting. The data points confirm that the contribution of this melting mechanism is larger in the square block geometry than in the rectangular blocks. Even the wide rectangle block shows a larger contribution of the outer boundary convection than the long rectangle block. As stated earlier, this is due to the larger contact length that forms between the thermal front and the frozen region for the wide rectangle block as the thermal front encircles the frozen region.

Comparative Analysis

In order to compare the different melting scenarios, like in the one dimensional case, the cumulative melt production is used as it has been shown to be helpful in defining the efficiency

of the melting processes and tracking the effect of different parameters. The ratio of the amount of melted material to that of the initial frozen material (Melt %) is also presented as this parameter scales the melt with respect to the initial saturation of the frozen material and the geometry of the frozen block.

As we shall see next, both of the cumulative melt and the Melt % have in general *S-shape* history profiles that result from the different regimes of melting. In the initial regime, the rate of melting is slow as the only melting mechanism is through the flow of heat into the frozen region. Later melting increases as a result of outer-boundary convection and finally forms a plateau once all the frozen block has melted. This *S-shape* profile has been observed in a wide variety of phenomena and is considered to be a characteristic of systems that follow the constructal law [171]. A succession of invasion and consolidation regimes characterizes these phenomena [171, 172]. The invasion regimes in this model are driven by the development of thermal fingers in the high permeability regions increasing the melting through outer-boundary convection which slows down as the fingers reach the end of the frozen block. Beyond this point, the melting process goes through the so called "consolidation" regime where in the absence of invasion, the rate of melting gradually decreases. Different parameters affect the rate of melting in each of these regimes. Here for brevity, we will only look at the effect of $\phi_{min}$ and the frozen block's geometry.

Effect of $\phi_{min}$ The effect of initial porosity on the cumulative melting is illustrated in Figure 5.16. In this figure only the cumulative melting curves of the wide rectangle block are shown as they show interesting non-monotonic trends. By reducing the initial porosity from $\phi_{min} = 0.8$ to $\phi_{min} = 0.4$, the cumulative melt increases significantly. This is expected as a smaller $\phi_{min}$ in the one dimensional scenarios was shown to increase the cumulative melt by allowing a larger amount of frozen material to melt as well as by increasing the share of heat that is devoted to melting. However the melting rate for $\phi_{min} = 0.4$ is larger

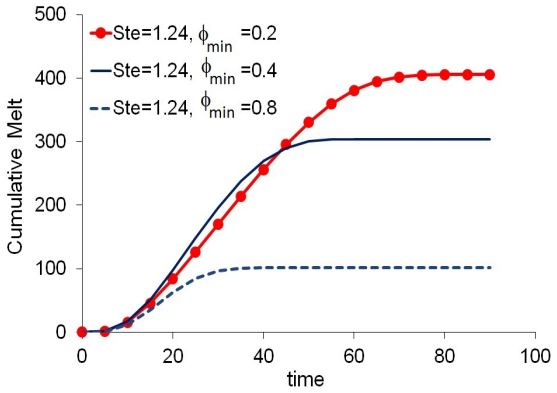


Figure 5.16: Cumulative melt production for the wide rectangle frozen block with dimensions similar to Figure 5.14an for Pe = 128, Le = 1, $\lambda = 0.8$, Ste = 1.2.

than for $\phi_{min} = 0.2$ when $t < 40$. This is attributed to the significant decrease in heat flux through the frozen region due to the decrease in the initial porosity. So the possibility for the flow to avoid the low permeable area decreases the melting rate through heat flux and this reduction prevails over the mentioned mechanism that leads to faster melting of the blocks with smaller porosity. For $t > 40$ all of the frozen material in the block with $\phi_{min} = 0.4$ gets melted and the cumulative melt for $\phi_{min} = 0.2$ scenario becomes larger. Such non-monotonic behavior was not observed for the other two geometries. For the square block more outer-boundary convection due to larger velocity in the high permeable channels overcomes the smaller heat flux through the frozen block and the cumulative melt increases with a decrease of $\phi_{min}$. Moreover, melting of the long rectangle block occurs mainly due to the outer-boundary convection. Therefore reducing $\phi_{min}$ increases the heterogeneity and enhances the melting by this mechanism.

Effect of the Block Geometry The cumulative melt curves for different block geometries are shown in Figure 5.17. The results from these curves, along with the previous discussions, reveal a faster melting for the square frozen block than the rectangular ones. Also the wide rectangle block melts faster than the long one. Since the heat fluxes through the wide

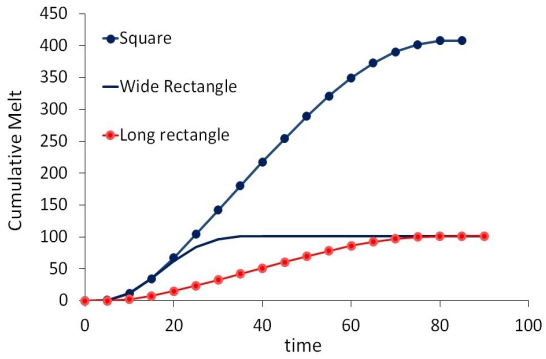


Figure 5.17: Effect of the block geometry on cumulative melt production; Parameters set as Pe = 128, Le = 1, $\lambda = 0.8$, Ste = 1.2 and $\phi_{min} = 0.8$.

rectangle and the square shaped blocks are similar, both geometries have the same melting rates in the early stages of the process. Later, the contact length between the thermal front and the frozen region increases, and the outer-boundary convection enhances the melting for the square block. As mentioned earlier, the long rectangle has a smaller heat flux and a smaller outer-boundary convection compared to the other blocks.

Melt % Graphs As can be seen in Figures 5.16 and 5.17, the ultimate values of the cumulative melt depend on the block geometry as well as the initial saturation of the frozen material. To factor in the effect of the amount of initial material, plots of the melt percentage defined as $Melt\% = cumulative\ melt/(w_{FB} l_{FB}(1 - \phi_{min}))$ are shown in Figure 5.18 for different geometries and initial porosity values. The wide rectangle, shows a larger Melt % than the other two geometries. This can be attributed to the fact that the long rectangle and square blocks extend along the flow direction and it takes longer for the flow to sweep the whole frozen region. Between the long rectangle and the square geometries, although the outer boundary convection in the square geometry is stronger, its area of influence compared to the total area of the frozen region is smaller. While in the long rectangle block the small width of the frozen block causes the outer boundary convection to reach the middle of frozen region and the melting grows evenly transverse to the frozen region. So the Melt % is larger

for the long rectangle geometry than the square one.

In Figure 5.18 the effect of $\phi_{min}$ on the Melt % is monotonic and frozen blocks of the same geometry but smaller porosities show a slower growth of Melt %. As described by Equation 5.34, when all other parameters are fixed, the rate of melting grows as $(1-\phi_{min})^{2/3}$ while the amount of material that can be melted grows as $(1-\phi_{min})$. As a result, the growth of Melt % decreases as $(1-\phi_{min})^{-1/3}$. So for the same geometry, a block of smaller $\phi_{min}$ has a smaller Melt % growth. This argument is obviously applicable only to 1D scenarios as it does not consider the redistribution of velocity field around the frozen block due to changes of initial porosity. In heterogeneous media, as the porosity of the frozen region decreases less heat flows through this region and this contributes to the reduction of melting rate. On the other hand decreasing $\phi_{min}$ increases the flow rate in the high permeability regions and consequently increases the rate of melting thorough outer-boundary convection. Hence, when the effect of the outer-boundary convection is dominant, as in the case of the long rectangle with small $\phi_{min}$, the effect of $\phi_{min}$ on decreasing Melt % is weaker (see the small difference between the curves corresponding to the long rectangle block with $\phi_{min} = 0.2$ and 0.4). However when the contribution of the outer-boundary convection to melting is smaller than the flow of heat inside the frozen region, the effect of $\phi_{min}$ on Melt % is more significant (e.g. for the wide rectangle block).

Unification of the Cumulative Melting Curves

The dependence of the cumulative melt on the amount of the frozen material in the medium and the geometry of the frozen block, makes it difficult to compare different scenarios. Hence, a scaling factor with respect to the amount of frozen material present in the frozen region and the shape of the frozen block, is required to compare the rate of melting for the discussed scenarios and may allow to extend the predictions to other block geometries and other initial porosity conditions. For the effect of $\phi_{min}$, as applied for Melt %, the cumulative melt can

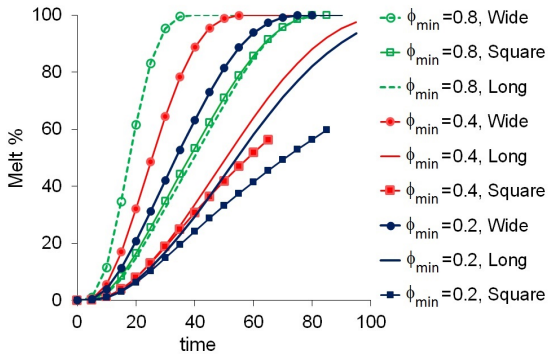


Figure 5.18: Effect of the block geometry and initial porosity of the frozen block on Melt % production for Pe = 128, Le = 1, $\lambda = 0.8$, Ste = 1.2.

be scaled by the initial amount of the frozen material per unit area of the block. This scaling transforms the cumulative melt to the equivalent area that has been melted. Throughout the melting process the melted area increases from 0 and reaches the total area of the block for all initial porosity values. As observed in the Melt % graphs in Figure 5.18 the scaling with respect to the area of the frozen block results in faster growth of the scaled parameter for blocks of smaller length. So in order to account for the geometry of the frozen block the width of the block facing the flow is used as a scaling factor which transforms the melted area to the melted length of the block (equivalent to the advancement of the melting front in the frozen block). Before scaling the curves based on the proposed factors, another scaling is applied to time which reveals interesting results. In Equation 5.34, assuming that the whole porosity varies from $\phi_{min}$ to 1 in a single time step at a constant $\theta$ results in a melting time scale proportional to $(1 - \phi_{min})^{1/3}$. This suggests that a block of larger $\phi_{min}$ takes less time to melt than a block with a smaller initial porosity, and the proportionality factor for their rate of melting is $(1 - \phi_{min})^{1/3}$. The cumulative melt curves for different $\phi_{min}$ values and geometries are scaled and plotted versus the scaled time in Figure 5.19. The results show good agreement between the curves corresponding to different block widths and initial porosity values.

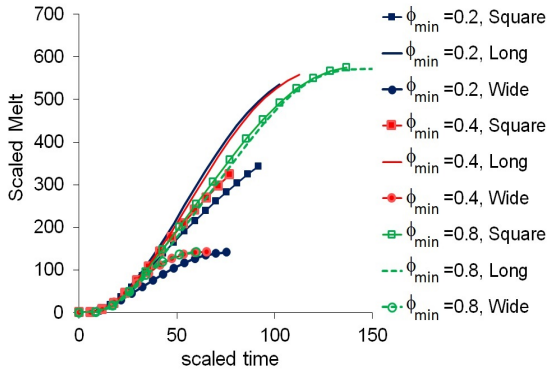


Figure 5.19: Unification of cumulative melt curves for different geometries and different initial porosity values for the scaled cumulative melt $melt/((1-\phi_{min}) \times w_{FB})$ versus scaled time as $t/(1-\phi_{min})^{1/3}$. Other parameters are Pe = 128, Le = 1, $\lambda = 0.8$, Ste = 1.2.

Although the width of the frozen block seems to be effectively scaling the melting curves for rectangular block shapes, its validity for other block geometries like a circular one needs further investigation. The flow through and around the frozen block (and therefore the rate of melting) depends on its width facing the flow. Intuitively, a block of streamlined shape melts more slowly than a rectangular block as it allows the flow to pass around it and a smaller share of the fluid flows through the frozen region. Such characteristics of the cumulative melt are similar to the drag force and therefore the drag coefficient can be adopted as a reference for finding the scaling factor of frozen blocks of different shapes. The drag factor for a two dimensional flow around a square obstacle is 2.05 whereas a circular obstacle with the same projected area normal to flow has a drag factor of 1.17. Using the width of the block as the scaling factor, the scaling factor for a circular block of diameter $D_{FB} = w_{FB}$ is $0.57 \times w$. The results of scaling depicted in Figure 5.20 show good agreement between the three initial porosity values of the round block and the curve corresponding to the long block with $\phi_{min} = 0.2$ which was chosen as a representative of the matched curves in Figure 5.19. Of course there are differences between the two phenomena compared together. Yet for the scaling of the cumulative melt even such a rough approximation of the shape

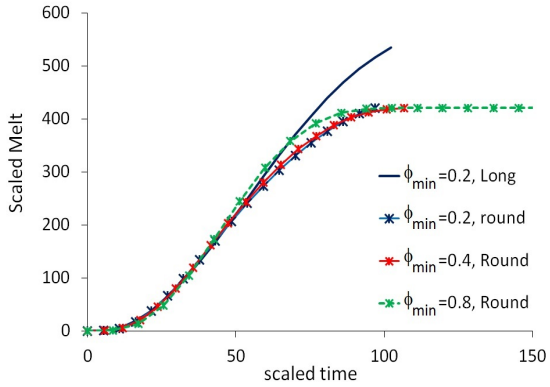


Figure 5.20: Scaling of cumulative melt production for circular obstacles with different initial porosity values matched with that of a long rectangle with $\phi_{min} = 0.2$. Other parameters are Pe = 128, Le = 1, $\lambda = 0.8$, Ste = 1.2.

factor gives satisfactory match between the graphs.

## 5.5 Conclusion

In this study we have developed a two dimensional model for non-isothermal displacements through melting porous media. Viscously stable scenarios in homogeneous and heterogeneous media have been defined and analyzed to understand these processes for possible improvement and optimization. A transient thermal equilibrium between the fluid-rock system and the frozen phase allowed us to examine the effect of the heat transfer coefficient on melting. It has been shown that large heat transfer coefficients that exceed a certain critical value do not result in significant changes in the process, and the temperature, porosity, and concentration profiles are those of instantaneous thermal equilibrium (ITE). In addition to ITE, three other limit cases including HT0, *non-melting* and *instantaneous melting* have been defined as reference scenarios. Analytical solutions for the distribution of the variables of interest have been provided where applicable, and the simulation results have been matched with the analytical solutions. A study of the effect of the different parameters on the melting process showed that a small heat transfer coefficient results in a diffused ther-

mal (and consequently melting) front. In contrast, a fast heat transfer between the fluid and the frozen phase increases the gradients at the melting front. A similar conclusion was reported by Harlan [153] in an analysis of flow in partially frozen soil where the soil-water redistribution area in finer textured soils (with large heat transfer rate) was reported to be more restricted to a proximity of the freezing front. In terms of the melting potential of the fluid, it was found that a large Ste results in faster melting. However for very large values, the advancement of the melting front is limited by the heat's diffusion and convection in the medium. By reducing the initial porosity in the frozen phase, the saturation of the frozen material increases. A smaller initial porosity therefore results in a slower advancement of the melting front. This parameter, $\phi_{min}$ is the only parameter that has a significant influence on the breakthrough time of the concentration front by increasing the interstitial velocity in the frozen regions. Increasing the rate of diffusion of heat, Le, increases the advancement of the melting front, however its influence was found to be not significant for small Ste. The cumulative melt production and the rate of melting that has been scaled to determine the advancement rate of the melting front have been used to compare different scenarios. According to the time trend profiles of melting, a small heat transfer coefficient can result in more melt production in a sufficiently long time period than the thermal equilibrium conditions. Moreover the results showed that for small Ste values the effects of the initial porosity and Le (as mentioned before) on the rate of melting are negligible while for large Ste values, the rate of melting is proportional to the initial saturation of the frozen material $(1 - \phi_{min})$. The effect of heterogeneity has been also examined by considering frozen blocks of different shapes. The mechanisms of melting of the frozen blocks have been shown to be internal heat transfer and outer-boundary convection. Reducing the initial porosity and increasing the width of the frozen block have been shown to increase the velocity around the block and hence the melting through outer-boundary convection. Premising the internal heat trans-

fer to be proportional to the heat flux through the frozen block allowed us to estimate the contribution of each of the involved melting mechanisms at different time steps. Finally by scaling the cumulative melt and time, a generalized curve independent of the geometry and initial porosity of the frozen block, has been obtained.

# Chapter 6

# Hydrodynamic Instabilities of Flows Involving Melting in Under-Saturated Porous Media

---

[1] The process of melting in partially saturated porous media is modeled for flow displacements prone to instability due to adverse mobility ratios. The effects of the development of instabilities on the melting process are investigated through numerical simulations and analytical solution of simplified models. The effects of melting parameters namely the melting potential of the fluid, the rate of heat transfer to the frozen phase, and the saturation of the frozen material along with the parameters defining the viscous forces, i.e. the thermal and solutal log mobility ratios are examined. Nonlinear simulation results are presented for different scenarios and the enhancement or attenuation of instabilities are discussed based on the the dominant physical mechanisms. Beside an extensive qualitative analysis, the performance of different displacement scenarios are compared with respect to the melt production and the contribution of instability to the enhancement of melting. It is found that the development of instabilities in general enhances melting but the rate of enhancement depends on how the melting front covers the instabilities at the thermal front. A larger melting potential and a smaller saturation of the frozen material increase the contribution of instability to melting.

[1]This chapter is the exact reproduction of the article submitted to *Physics of Fluids* journal with the same title.

## 6.1 Introduction

In this chapter the dynamics of non-isothermal miscible displacements through under-saturated frozen media are studied. The fundamental aspects of the problem have been investigated in an article on modeling of the viscously stable scenarios [173]. In this study we would like to examine the instabilities driven by viscous forces in the described displacement processes and evaluate their effects on the melt production. The instability that happens due to viscosity contrast between the injected and the inhabitant fluids is called viscous fingering. Due to causing early breakthrough of the displacing agent and reduction of the sweep efficiency of the displacement process, this form of instability has been studied extensively through lab experiments [34, 174, 4] and numerical simulations [8, 35, 175, 139]. In non-isothermal displacements, due to the involvement of temperature in defining the viscosity of the fluid the instability is known as thermo-viscous fingering. Nonlinear simulations and linear stability analyses of thermo-viscous fingering along with the related experiments have been the subject of numerous studies including but not limited to [25, 52, 176, 22, 27, 24, 130, 23]. These studies reveal the details of the developing fingers and the rate of growth of the instabilities for different thermal/solutal mobility ratios and thermal properties of the fluid/porous medium.

In a melting porous medium, the development of fingering instabilities is coupled with the changes in the permeability of the medium due to the melting of the frozen phase. The heterogeneity of the medium resulting from the melting introduces another source of instability in the flow, namely channeling or heterogeneity induced instability which closely interacts with the viscous forces through the melting process. The effect of heterogeneity on miscible displacement processes has been extensively discussed in a number of previous studies. Some of these studies were devoted to defining the parameters that characterize

the strength of heterogeneity of the medium [58, 76, 131] while others investigated the interactions between viscous fingering and heterogeneity induced instabilities [64, 72, 73, 69, 66, 177] and led to characterization of the unstable flow regimes [178, 170]. There are however no studies that have examined flow displacements where the heterogeneity is a result of the melting of one phase and hence is dynamically evolving throughout the displacement process. This is despite the fact that flows through melting porous media are inherently unstable and even the viscously stable scenarios are prone to the development of instabilities in the presence of irregularities in the media's porosity distribution. In particular, in the modeling of large scale phenomena involving the melting of the porous medium such as permafrost melting, flow of magma, or sea ice melting, consideration of the effect of instabilities at the melting front is important. Most particularly the effect of instability on melting has been recognized in heavy oil recovery processes. In steam assisted gravity drainage (SAGD) recovery processes the rising of the steam chambers in bitumen reservoirs has been shown to be due to the development and growth of steam fingers [116, 115]. The systematic analysis of the effect of the instabilities on the rate of melting and advancement of the melting front, and examination of the coupling between the created heterogeneity and growth of instabilities are beneficial for the named applications.

## 6.2 Modeling

The problem consists of the injection of a hot solvent in a porous medium of size $L_x \times L_y$ (with aspect ratio of $A = L_x/L_y$) at a uniform and constant injection velocity $U$. The solvent concentration and temperature of the injected fluid and the inhabitant one are $C_1$ and $T_1$, and $C_2$ and $T_2$, respectively. Due to the higher temperature of the injected solvent and the higher solvent concentration, this fluid has larger mobility than the inhabitant one and therefore their interface is prone to hydrodynamic instability. Initially the medium

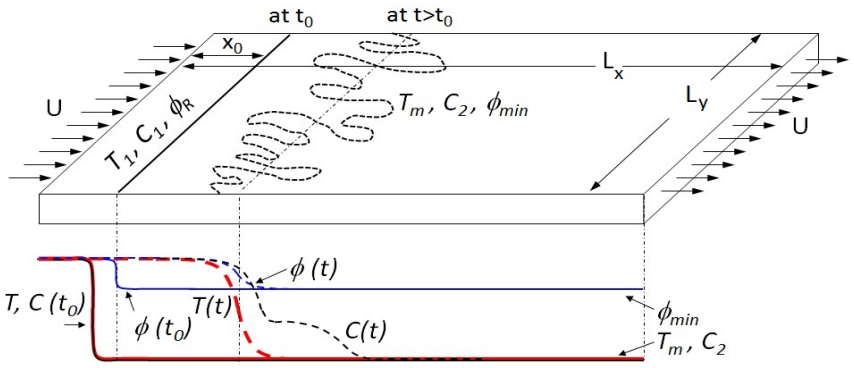


Figure 6.1: Diagram of the modeled domain at $t_0$ and $t > t_0$

is partially saturated with a frozen material that, when melted, is fully miscible with the injected solvent. The objective is to displace the inhabitant fluid and the melted material and produce them at the other end of the domain. The matrix (here called the rock) has a constant and homogeneous porosity $\phi_R$ and permeability $\kappa_R$ available to the fluid when all the frozen material is melted. The porosity of the medium $\phi$, initially assigned as $\phi_{min}$, defines the saturation of the frozen material $S_s = \phi_R - \phi$ that varies with time and location during the melting process. As the injected fluid enters the frozen region, melting starts and the injected heat serves to melting the frozen material and increasing the porosity as well as to increasing the temperature of the fluid and the matrix. Unlike the heat, the solvent concentration is contained within the fluid during the displacement process as no deposition or chemical reaction between the fluid and the matrix is considered. The only change in concentration, other than the regular convection-diffusion, takes place at the melting region as the melted fluid dilutes the solution. Figure 6.1 is a schematic of the process.

The physical system consists of three phases, namely the rock, the frozen (solid) and the fluid phases. The conservation of mass and momentum and a convection-diffusion equation for solvent concentration are adopted for the fluid phase. In terms of the heat transfer, the fluid and the rock are assumed to reach thermal equilibrium instantaneously but the frozen phase melts and reaches the temperature of the rock-fluid phase through a transient process.

Therefore, the conservation of energy is formulated in two parts. The first one describes the convection and diffusion of heat in the rock-fluid phase including the share of heat that goes towards melting. The second equation describes the amount of the frozen material that gets melted by the heat transferred to the frozen phase.

$$\nabla.\vec{u}_D = 0 \tag{6.1}$$

$$\nabla P = -\frac{\mu}{\kappa}\vec{u}_D \tag{6.2}$$

$$\frac{\partial(\phi C)}{\partial t} = -\nabla.(C\vec{u}_D) + D_C\nabla.(\phi\nabla C) \tag{6.3}$$

$$(\rho_f c_{pf}\phi + \rho_R c_R(1-\phi_R))\frac{\partial T}{\partial t} =$$

$$\nabla.[(k_f\phi + k_R(1-\phi_R))\nabla T] - \rho_f c_{pf}\nabla.(T\vec{u}_D) - h(T-T_m) \tag{6.4}$$

$$(\rho_s\Delta h_f + \rho_f c_{pf}(T-T_m))\frac{\partial\phi}{\partial t} = h(T-T_m) \tag{6.5}$$

In the above equations $\vec{u}_D(x,y,t) = (u_D, v_D)$ is the Darcy velocity vector, $P(x,y,t)$ is the pressure, and $\mu(x,y,t)$ and $\kappa(x,y,t)$ are the fluid viscosity and the medium's permeability, respectively. As mentioned before $\phi(x,y,t)$ is the porosity and $C(x,y,t)$ is the solvent concentration while $D_C$ is the mass diffusion coefficient. The rock-fluid temperature is denoted by $T$ and $T_m$ refers to the melting temperature of the frozen phase. The density, specific heat capacity, and thermal conductivity of different phases are referred to as $\rho$, $c$, and $k$ corresponding to different phases depending on the assigned subscripts as $_f$ for the fluid, $_s$ for the solid or the frozen phase, and $_R$ for the rock. The latent heat of melting is denoted by $\Delta h_f$. The equations are made dimensionless using the following diffusive scaling:

$$\begin{aligned} c^* &= \frac{C-C_2}{C_1-C_2} \quad \theta^* = \frac{T-T_m}{T_1-T_m} \quad (u^*,v^*) = \frac{(u_D,v_D)/\phi}{U/\phi_R}(x^*,y^*) = \frac{x,y}{D_C\phi_R/U} \\ t^* &= \frac{t}{D_C\phi_R^2/U^2} \quad p^* = \frac{P}{\phi_R\mu_1 D_C/\kappa_R} \quad \mu^* = \frac{\mu}{\mu_1} \quad \kappa^* = \frac{\kappa}{\kappa_R} \quad \phi^* = \frac{\phi}{\phi_R} \end{aligned} \tag{6.6}$$

The subscripts $_1$ and $_2$ correspond to the properties assigned to the injected and the

inhabitant fluids, respectively. The resulting dimensionless equations are:

$$\nabla.(\phi^*\mathbf{u}^*) = 0 \tag{6.7}$$

$$\nabla p^* = -\frac{\mu^*}{\kappa^*}\phi^*\mathbf{u}^* \tag{6.8}$$

$$\frac{\partial(\phi c^*)}{\partial t^*} = -\phi^*\mathbf{u}^*.\nabla c^* + \nabla.(\phi^*\nabla c^*) \tag{6.9}$$

$$\frac{\partial\theta^*}{\partial t^*} = \frac{1}{(1-\lambda(1-\phi^*))}\times$$
$$[\mathrm{Le}\nabla.\left((1-(1-\phi^*)k_{rel})\,\nabla\theta^*\right) - \lambda\phi^*\mathbf{u}^*.\nabla\theta^* - \frac{12\mathrm{Le}k_{rel}}{\mathrm{Pe}^2(d_P/L_x)^2}(1-\phi_0^*)^{1/3}(1-\phi^*)^{2/3}\theta^*] \tag{6.10}$$

$$\frac{\partial\phi^*}{\partial t^*} = \frac{1}{\frac{\rho_{rel}}{\mathrm{Ste}'}+\theta^*}\left[\frac{12\mathrm{Le}k_{rel}}{\lambda\mathrm{Pe}^2(d_P/L_x)^2}(1-\phi_0^*)^{1/3}(1-\phi^*)^{2/3}\theta^*\right] \tag{6.11}$$

where:

$$\lambda = \frac{\rho_f c_{pf}\phi_R}{(\rho_f c_{pf}\phi_R + \rho_R c_R(1-\phi_R)}, \qquad \rho_{rel} = \frac{\rho_s}{\rho_f}, \quad k_{rel} = \frac{k_f\phi_R}{k_R(1-\phi_R)+k_f\phi_R} \tag{6.12}$$

$$D_T = \frac{k_f\phi_R + k_R(1-\phi_R)}{\rho_f c_{pf}\phi_R + \rho_R c_R(1-\phi_R))}, \quad \mathrm{Le} = \frac{D_T}{D_C}, \quad \mathrm{Ste}' = \frac{c_{pf}(T_1-T_m)}{\Delta h_f} \tag{6.13}$$

In these equations $\lambda$ denotes the thermal lag coefficient, Le and Ste$'$ are the Lewis and Stefan numbers, and $D_T$ is the diffusion rate of heat in the rock-fluid phase. Finally $k_{rel}$ is the relative thermal conductivity of the fluid to that of the fluid-rock phase. The constitutive correlations used for the derivation of the model include: The *heat transfer coefficient* adopted from [162] and modified by [173]:

$$h = h^*\bar{s}_s \approx 12\phi_R\frac{k_f}{d_p^2}(1-\phi_0^*)^{1/3}(1-\phi^*)^{2/3} \tag{6.14}$$

where $d_p$ is the porous medium's pore dimension and $\phi_0$ is a reference porosity with a known specific surface area. For the *permeability-porosity correlation* a form of Kozeny's empirical correlation is used [103]:

$$\kappa^* = \frac{\kappa}{\kappa_R} = \phi^{*3}\left(\frac{1/\phi_R - 1}{1/\phi_R - \phi^*}\right)^{4/3} \tag{6.15}$$

The *Viscosity* of the fluid is defined as an exponential function of the fluid temperature and the solvent concentration adopted from [25, 22] extensively used to determine the viscosity of aqueous and non associating mixtures [136, 137, 16].:

$$\mu^* = exp\left(\beta_C(1-c^*) + \beta_T(1-\theta^*)\right) \tag{6.16}$$

Thus the viscosity ratio (i.e. the mobility ratio for miscible displacements) is $\mu_2^* = exp(\beta_C + \beta_T)$ and $\beta_C$ and $\beta_T$ are referred to as the solutal and thermal log-mobility ratios, respectively.

The group $H_T = \frac{12\text{Le}k_{rel}}{\text{Pe}^2(d_P/L_x)^2}(1-\phi_0^*)^{1/3}$ is regarded as the heat transfer coefficient in the new dimensionless system. Although $H_T$ is dealt with as an independent factor, when examining the effect of Pe and Le on the system, the changes in these parameters are reflected in the value of $H_T$ as well. Also $\text{Ste} = \text{Ste}'/\rho_{rel}$ is used to describe the melting potential of the injected fluid.

Equations 6.7 and 6.8 are recast to obtain the velocity field using the vorticity ($\omega$) and the stream function ($\psi$):

$$\begin{aligned}
\nabla \times \nabla p^* &= -(\nabla \frac{\mu^*}{\kappa^*} \times \phi^* \vec{v^*} + \frac{\mu^*}{\kappa^*} \nabla \times \phi^* \vec{v^*}) \\
\omega &= -\nabla(ln(\mu^*) - ln(\kappa^*)) \times \phi^* \vec{v^*} \\
&= -(\beta_C \nabla c^* + \beta_T \nabla \theta^* + \nabla f).\nabla \psi
\end{aligned}$$

Dropping the asterisks for brevity, the final form of the dimensionless equations is:

$$\omega = -(\beta_C \nabla c + \beta_T \nabla \theta + \nabla f).\nabla \psi \tag{6.17}$$

$$\omega = -\nabla^2 \psi \tag{6.18}$$

$$\frac{\partial(\phi c)}{\partial t} = -\phi \mathbf{u}.\nabla c + \nabla.(\phi \nabla c) \tag{6.19}$$

$$\frac{\partial \theta}{\partial t} = \frac{1}{(1-\lambda(1-\phi))}[\text{Le}\nabla.\left((1-(1-\phi)k_{rel})\nabla\theta\right) - \lambda\phi\mathbf{u}.\nabla\theta - H_T(1-\phi)^{2/3}\theta] \tag{6.20}$$

$$\frac{\partial \phi}{\partial t} = \frac{1}{1+\text{Ste}\theta}\frac{\text{Ste}}{\lambda} H_T(1-\phi)^{2/3}\theta \tag{6.21}$$

### 6.2.1 Initial and Boundary Conditions

Except for a small band of thickness $x_0$ from the injection boundary where the hot solvent has melted all the frozen material and the temperature of the fluid-rock has reached that of the injection boundary, the rest of the domain is initially filled with the inhabitant fluid at the melting temperature. The initial conditions are formulated as:

$$\theta(x, y, 0) = \frac{1}{2}\text{erfc}(\frac{x - x_0}{2\sqrt{t_0}}) \tag{6.22}$$

$$c(x, y, 0) = \frac{1}{2}\text{erfc}(\frac{x - x_0}{2\sqrt{t_0}}) \tag{6.23}$$

$$\phi(x, y, 0) = \frac{(1 - \phi_{min})}{2}\text{erfc}(\frac{x - x_0}{2\sqrt{t_0}}) + \phi_{min} \tag{6.24}$$

During the displacement process, the hot solvent is injected from the left side of the domain (upstream boundary) and the temperature and concentration at the downstream and upstream boundaries remain constant. Transverse to the flow direction, periodic boundary conditions are adopted. The following equations describe the dimensionless boundary conditions:

$$\begin{aligned}
&(c, \theta)(0, y, t) = (1, 1) \\
&(c, \theta)(\text{Pe}, y, t) = (0, 0) \\
&\frac{\partial}{\partial x}(c, \theta)(0, y, t) = \frac{\partial}{\partial x}(c, \theta)(\text{Pe}, y, t) = (0, 0) \\
&(\phi, \mathbf{u})(0, y, t) = (1, \mathbf{i}) \\
&(c, \theta, \frac{\partial c}{\partial y}, \frac{\partial \theta}{\partial y}, \phi, \mathbf{u})(x, 0, t) = (c, \theta, \frac{\partial c}{\partial y}, \frac{\partial \theta}{\partial y}, \phi, \mathbf{u})(x, \text{Pe}/A, t)
\end{aligned} \tag{6.25}$$

## 6.3 Numerical Method

A finite difference method with non-uniform grid distribution which adapts itself with the melting front's profile has been adopted. The grids in the $y$ direction are distributed evenly

transverse to the flow and the derivatives are determined using second-order central difference formula. A weighted derivation method with second order accuracy has been used to obtain the first and second derivatives in the $x$ direction [167]. For the temporal discretization a second order iterative AB-AM predictor corrector scheme was adopted.

The predictions of the code for stable scenarios were verified through comparisons with analytical solutions of limiting cases including very slow heat transfer ($H_T \to 0$), instantaneous melting (Ste $\to \infty$) and no melting (Ste $\to 0$) scenarios [173]. The results of the numerical simulations agreed perfectly with the analytical solutions indicating the convergence of the numerical method. To validate the code for scenarios with hydrodynamic instability, due to the absence of relevant results in the literature on instabilities in frozen media, a non-melting scenario has been considered. The results for $\phi_{min} = 1$, $\beta_C = 2$, $\beta_T = 1$, $\lambda = 1$, Pe $= 2000$, Le $= 1$ and $L_x/L_y = 2$ that correspond to thermo-viscous fingering in homogeneous porous media have been matched with those reported in [130]. It was found that there is very good agreement in terms of the number, size, and growth rate of the fingers. Finally, the convergence with the temporal and spatial resolution has been ascertained.

## 6.4 Results and Discussions

The effects of different parameters on the enhancement or weakening of the instability are examined under different scenarios. The main parameters to be analyzed in unstable scenarios are the solutal and thermal log mobility ratios ($\beta_C, \beta_T$) that define the strength of viscous instabilities and those that affect the melting process; namely $H_T$, Ste, and $\phi_{min}$.

In the first part of this section, the development and growth of melting instabilities due to the coupling between thermo-viscous forces and the medium heterogeneity induced by the instabilities are examined. The results are mostly qualitative and are presented in the form of 2D temperature, porosity and concentration iso-profiles. The reasons behind the observed

trends and how the system behaves for a wider range of parameters will be presented in the following part analyzing the physical mechanisms responsible for the instabilities. In a subsequent part, a quantitative analysis of the performance of the melting process and the contribution of instabilities to melting for different scenarios are presented and a unified trend for the enhancement of melting is proposed. Finally the effect of Pe, Le, and $\lambda$ on the development of instabilities and increase of melting are discussed briefly. Throughout the chapter unless stated otherwise, the values of the parameters are fixed as: $H_T = 1$, $\mathrm{Pe} = 1000$, $A = 2$, $\mathrm{Le} = 1$, $\lambda = 0.8$, $(\beta_C, \beta_T) = (2, 2)$, and $\phi_{min} = 0.7$.

### 6.4.1 Simulation Results for Unstable Scenarios

In pure thermo-viscous fingering (i.e. non-melting) scenarios, the instabilities on the thermal and solutal fronts depend on the values of the corresponding log mobility ratios as well as the rates of advancement of those fronts. In such scenarios the concentration front moves ahead of the thermal front with the gap between them increasing with $1 - \lambda$ and time. Depending on the gap and the assigned mobility ratios, the interaction between the fronts can enhance or attenuate the instabilities [25, 27, 130]. In the case where melting takes place, the advancement rates of the thermal and the melting fronts are closely interdependent. Furthermore due to melting, the concentration also exhibits a sharp drop at the melting front which moves at the pace of that front. Therefore in melting scenarios, thermal, solutal, and melting fronts are strongly interconnected. Ahead of the melting front, the concentration travels at a faster rate than in the melted region (due to the smaller porosity of the domain) and forms an advanced solutal front. The nature of the instabilities that develop on these fronts are examined next.

Effect of $\beta_C$ and $\beta_T$

In Figure 6.2 the role of the thermal log mobility ratio ($\beta_T$) is examined. To isolate the effects of the concentration gradient, the solutal log mobility ratio is set to $\beta_C = 0$ and as a result the solutal front is intrinsically stable. The adverse mobility ratio at the thermal front forms melted fingers in the frozen region. The growth rate of these fingers depends on the strength of the viscous forces, and as expected instabilities are stronger for larger values of $\beta_T$. It is worth noting that the solutal front remains stable for $\beta_T = 2$ as the rate of growth of melting fingers is not strong enough to affect this front. For $\beta_T = 4$ however, the growth rate of the thermal fingers increases such that the thermal instabilities reach the advancing solutal front and affect its profile.

The effects of the melting process on the instabilities can be better understood when the results for $\beta_T = 4$ are compared with those of an analogue scenario with no melting (see Figure 6.3a). The heat transfer coefficient and the melting potential of the fluid for non melting scenarios have been chosen small enough ($H_T = 1e-7$ and Ste $= 0.04$) to ensure that there are no changes in the medium due to melting. The flow structures are substantially different in this case, with weaker less developed fingers at the thermal front and virtually none at the solutal one. Moreover, the thermal front has moved further downstream compared to the melting case. These different behaviors can be explained by the fact that in the melting case, the change in the porosity and the ensuing heterogeneity add to the instability of the thermal front and are the origin of the finger structures observed on the solutal front. On the other hand when no heat is transferred to melt the frozen part, the thermal front is able to proceed further downstream. Due to the weaker instability on the thermal front and the homogeneous permeability in the non-melting case, the solutal front is not affected by the thermal one and remains stable. The results of a counterpart scenario with $(\beta_C, \beta_T) = (4, 0)$ in which the concentration gradient is driving the instability are

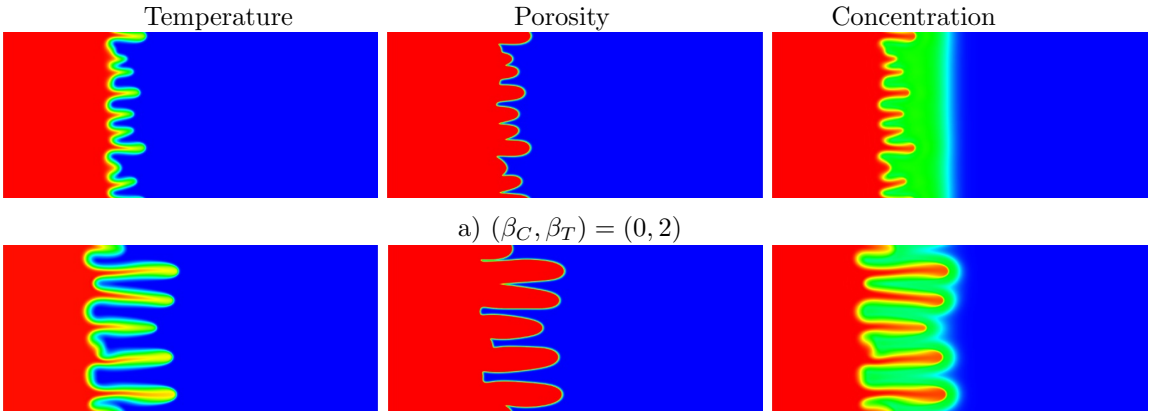


a) $(\beta_C, \beta_T) = (0, 2)$

b) $(\beta_C, \beta_T) = (0, 4)$

Figure 6.2: The effect of the thermal log mobility ratio ($\beta_T$) on development of instabilities; Ste $= 3.2$, $t = 250$.

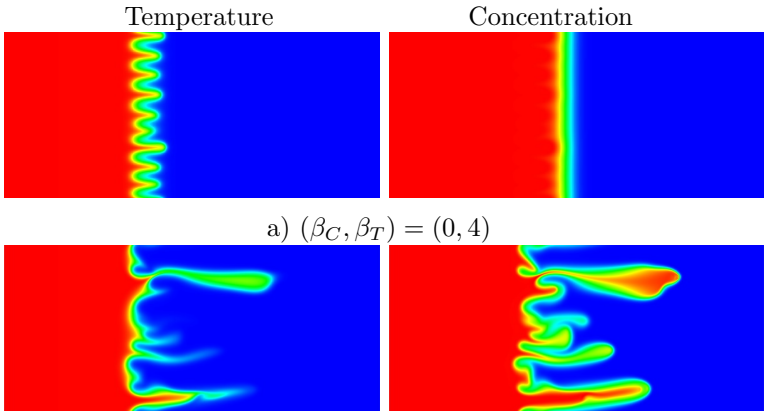


a) $(\beta_C, \beta_T) = (0, 4)$

b) $(\beta_C, \beta_T) = (4, 0)$

Figure 6.3: The effect of $\beta_C$ and $\beta_T$ on instabilities of non-melting scenarios; $H_T = 1e-7$, Ste $= 0.04$, $\phi_{min} = 0.7$, $t = 250$.

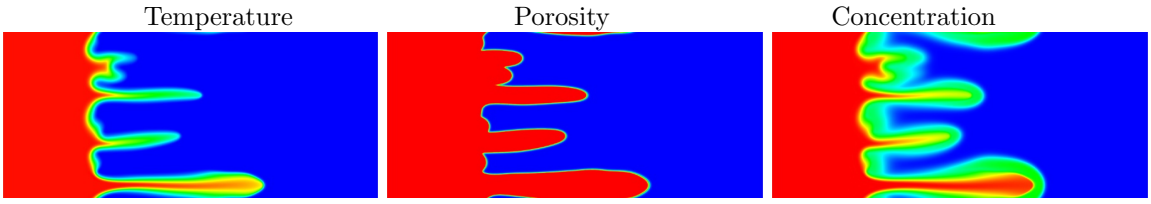


$(\beta_C, \beta_T) = (4, 0)$

Figure 6.4: The effect of the solutal log mobility ratio ($\beta_C$) on development of instabilities; Ste $= 3.2$, $t = 250$.

depicted in Figure 6.4. As mentioned earlier, the concentration has two fronts in melting scenarios both of which are susceptible to instability for $\beta_C > 0$. At the melting region, the instability of the solutal front develops in the direction of the flow with little or no interactions between the fingers. Moreover, the solutal, thermal and porosity fronts bear great resemblance, which as we shall see later, is a result of the close interactions between them. Again the role of melting can be assessed by comparing the iso-profiles in Figure 6.4 with those of the analogue non-melting scenario shown in Figure 6.3b. Compared to the concentration iso-profile in Figure 6.4 the concentration front in the non-melting scenario has a faster advancement rate and the solutal fingers are more complex with closer interactions. The fingers are however longer in the melting case. These differences can be attributed to the fact that in the non-melting case, the instabilities at the thermal front develop only as a result of those on the solutal one. In the melting case however, the instabilities at the solutal front give rise to thermal front instabilities which in turn result in melting and changes in the medium porosity. The induced heterogeneity in the form of channels guides and enhances the growth of the instabilities at the solutal front and results in long non-interacting fingers.

By comparing the effects of the solutal log mobility ratio with those of the thermal log mobility ratio, it can be concluded that the former plays a more important role in the subsequent development of instabilities. This behavior turns out to be dependent on the melting parameters and will be discussed in more details when examining the mechanisms driving the instability and the effect of the melting parameters on these mechanisms.

Effect of $H_T$

The heat transfer coefficient $H_T$ determines the share of melting over the distribution of heat in its sensible form in the medium. A small $H_T$ implies that only a small portion of heat is dedicated to melting and most of the heat is convected further downstream. A large $H_T$ on the other hand results in most of the heat being used towards melting and therefore past

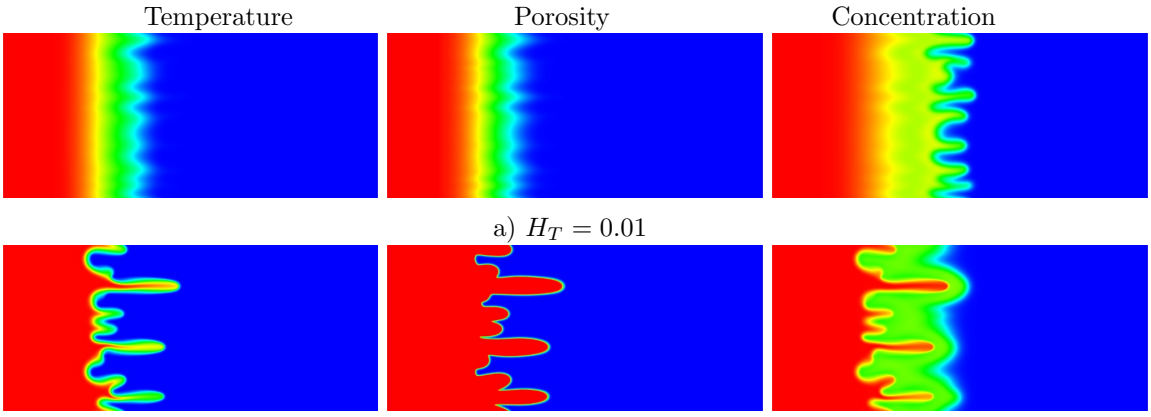


Figure 6.5: The effect of the heat transfer coefficient ($H_T$) on development of instabilities; Ste = 1.2, $t = 250$.

the melting front, there is not enough sensible heat to raise the temperature of the fluid. The described effect causes the thermal front to be more diffused into the frozen regions for small $H_T$ and to have sharp gradients at the melting front for large $H_T$.

The temperature, porosity, and concentration iso-profiles shown in Figure 6.5 illustrate the effect of $H_T$ on the development of instabilities in the domain. The temperature and porosity fronts are clearly less unstable for $H_T = 0.01$ and only advancing waves are formed on these fronts. The small $H_T$ that extends the melting region and reduces the concentration and temperature gradients attenuates the instabilities at the melting front. Due to this attenuation and the gap between this front and the advanced solutal front, the instabilities on the latter arise solely as a result of viscous forces. For $H_T = 1$ on the other hand, the sharp gradients lead to the development and growth of well separated fingers on both temperature and porosity fronts. The melted fingers reach the advanced solutal front and through the induced heterogeneity, dictate and guide the instabilities on this front.

Effect of Ste

The next parameter to look at is the melting potential of the fluid (Ste). This parameter defines the rate of melting for a given heat transfer coefficient. A small Ste results in a

slow melting process which inhibits the thermal and melting fronts from advancing in the frozen region. It also reduces the dilution of solvent concentration at the melting front. The effects of Ste on the instabilities are illustrated in Figure 6.6, where the scenario of Figure 6.5b is examined for two different melting potential values as Ste = 0.2 and Ste = 20. A smaller potential of the fluid to melt down the frozen region reduces the ability of the melted fingers to grow. Therefore for Ste = 0.2 the melted fingers are smaller than the other two compared scenarios. The extended gap between the melting and the advanced solutal fronts results in the development of instabilities on the advanced solutal front independent of the melted fingers. Although by increasing the melting potential the growth of fingers in the frozen region is facilitated, the melted fingers in Figure 6.6b with Ste = 20 do not show any significant progress compared to those in the Ste = 1.2 case. The reason lies again in the effect of the melting parameters on the mechanisms of instabilities. These mechanisms are the advancement of the melting fingers, viscosity gradient, and heterogeneity of the medium. By increasing Ste, the rate of advancement of fingers in the frozen region is enhanced, but the other two mechanisms show non-monotonic responses to changes of this parameter and therefore can reduce the growth rate of the fingers. These mechanisms and the effect of the melting parameters on them will be discussed further in a corresponding section. The faster melting resulting from the larger Ste in Figure 6.6b reduces the gap between the melting and the advanced solutal front such that the latter forms around the melted fingers and is indistinguishable from the concentration front formed at the melting front.

Effect of $\phi_{min}$

The initial porosity of the medium in the frozen region is defined by $\phi_{min}$. A smaller $\phi_{min}$ results in a larger permeability variation between the frozen region and the melted zone and a stronger heterogeneity in the medium. This parameter meanwhile defines the saturation of the frozen material in the un-melted regions ($S_s = 1-\phi_{min}$) with a smaller $\phi_{min}$ corresponding

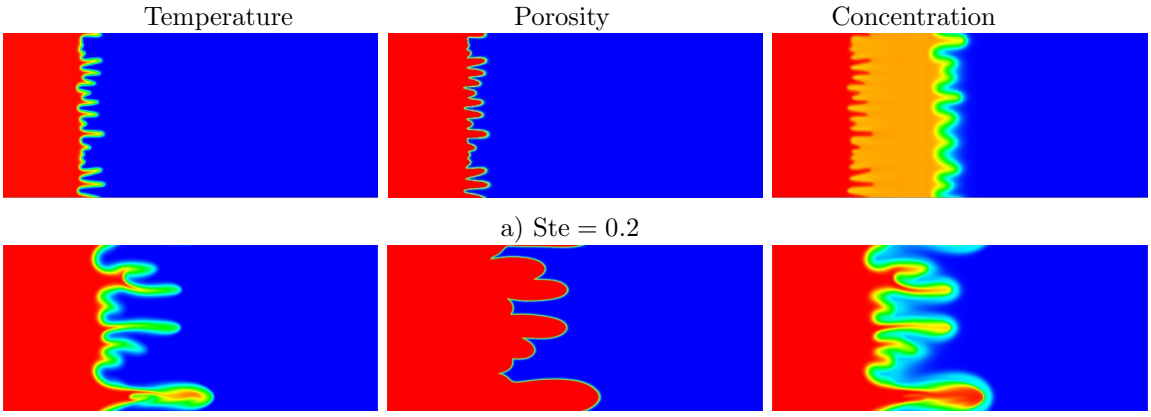


Figure 6.6: The effect of the melting potential of the fluid (Ste) on development of instabilities; $t = 250$.

to a larger saturation of frozen material to be melted. Figure 6.7 shows the concentration isoprofiles for three scenarios with different values of initial porosity. Due to the small melting potential of the fluid adopted in these scenarios (Ste = 0.2) and the well separated melting and advanced solutal fronts, the concentration contours in this figure adequately reflect the shapes of the melting fronts as well. Thus only the concentration profiles are presented.

A smaller porosity in the frozen region leads to a larger interstitial velocity ahead of the melting front that increases the gap between the fronts as well as the instability on the advanced solutal front. On the melting fronts, as illustrated in Figure 6.7, increasing the initial porosity from 0.7 to 0.9 does not result in any significant changes in the lengths of the melted fingers. However the widths of the fingers increase with increasing $\phi_{min}$. The enhancement of the lateral growth of fingers in media with larger $\phi_{min}$ can be attributed to the smaller saturation of the frozen material that needs to be melted for the advancement of the melting front. A similar effect is however not observed for the longitudinal growth of instabilities. The reason again can be sought in the counteracting effects of the mechanisms in favor and against the growth of fingers in media with larger initial porosity. While the advancement of fingers in such media is facilitated by the reduction of the saturation of

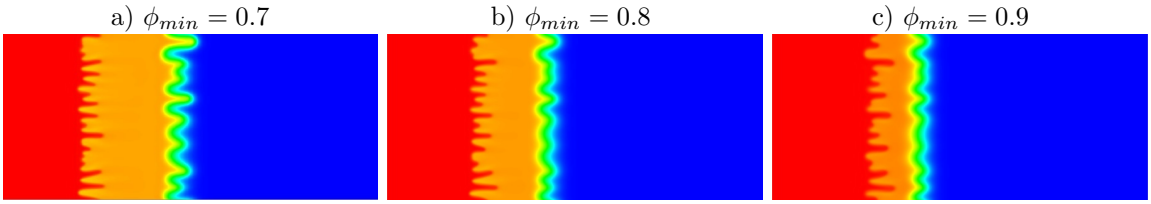


Figure 6.7: The effect of the initial saturation of the frozen material ($\phi_{min}$) on development of the instabilities; Ste = 0.2, $t = 250$.

the frozen material, the reduced heterogeneity attenuates the instabilities. The changes in concentration and temperature gradients at the melting front as a result of the reduction of $\phi_{min}$ require a closer analysis that will be presented in the following section.

### 6.4.2 Mechanisms Affecting the Development and Growth of Instabilities

As mentioned previously, the development of the instability is closely connected to the advancement rate of the melting front (determining the growth rate of the melting fingers), the viscosity gradient (defining the strength of the viscous forces), and finally the heterogeneity of the medium. In order to explain the results reported earlier, the effect of melting parameters on the strengthening or weakening of these mechanisms are examined. In unstable flows, the growth rate of the melting fingers or the gradients of temperature and concentration at the melting front vary from point to point and are affected by viscous instability and heterogeneity mechanisms. Therefore it is not possible to isolate the effect of the parameters on each mechanism. Hence, except for the heterogeneity which can only be seen in two dimensional models, the other two mechanisms will be analyzed next considering one-dimensional stable cases to gain more insight into the physics of the flow.

#### Advancement Rate of the Melting Front

We will propose here a semi-analytical model for the rate of advancement of the melting front in stable scenarios. To this end we will recognize that the heat injected in the domain is equal to the increase in the sensible and latent heat of the medium. For better clarity,

the formulation will be initially obtained using dimensional variables. The total energy injected by time $t$ is $(\rho_f c_{pf} L_y U t(T_1 - T_m))$. To determine the increased heat content of the domain, it will be assumed that the heat transfer coefficient is very large such that the melting and thermal fronts have sharp gradients over a narrow melting region. Hence, both temperature and porosity drop from $T_1$ and $\phi_R$ to $T_m$ and $\phi_{min}$ at the same location $x_\phi(t)$ which is an estimate of the distance traveled by the melting front. As discussed in Appendix A, this assumption is actually not restrictive and a proposed unification scaling suggests that the prediction of this analysis is applicable to any process with any rate of heat transfer. At any time $t$, the sensible energy of the fluid and the rock is increased by $(\rho_f c_{pf}\phi_{min} + \rho_R c_R(1-\phi_R))L_y x_\phi(T_1 - T_m)$. The frozen material in the swept region is melted and its temperature is increased to that of the injected fluid $(T_1)$. As a result its energy is increased by $(\rho_f c_{pf}(T_1 - T_m) + \rho_s \Delta h_f)(\phi_R - \phi_{min})L_y x_\phi$. The balance of heat implies that:

$$\begin{aligned}&\left[\left(\rho_f c_{pf}\phi_{min} + \rho_R c_R(1-\phi_R)\right)(T_1 - T_m) + (\rho_f c_{pf}(T_1 - T_m) + \rho_s \Delta h_f)(\phi_R - \phi_{min})\right] x_\phi \\ &= \rho_f c_{pf} U t (T_1 - T_m) \end{aligned} \tag{6.26}$$

Assuming a constant rate of advancement of the melting front, $\frac{dx_\phi}{dt} \approx \frac{x_\phi}{t}$, the following expression is derived from Equation 6.26 for the rate of advancement of the melting front in dimensionless form:

$$\frac{dx^*_\phi}{dt*} = \frac{\lambda}{1 + (\lambda/\mathrm{Ste})(1 - \phi^*_{min})} \tag{6.27}$$

It should be noted that for moderate Ste values, the assumption of constant rate of advancement is reasonable and is confirmed from earlier results for stable scenarios [173]. Using this equation, it can be easily shown that the rate of advancement increases monotonically with $\lambda$, Ste and $\phi_{min}$ and that it is bounded by an upper limit value $\lambda$ corresponding to the rate of advancement of the thermal front. This upper limit is reached at large enough values of Ste or when the initial porosity of the frozen region is close to that of the rock. Here forth we

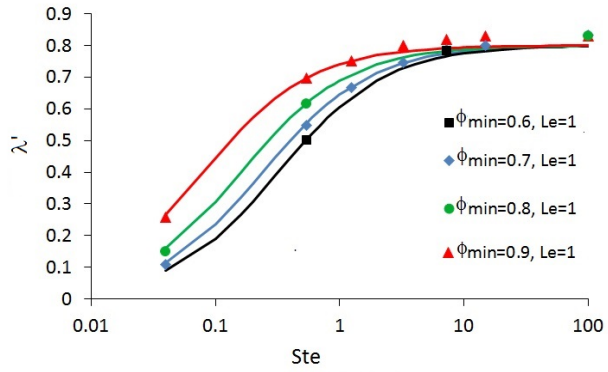


Figure 6.8: Approximation of $\lambda'$ in stable scenarios; solid lines correspond to analytical approximations and the scattered data points present the obtained values from non-linear numerical simulations.

are going to call the advancement rate of the melting front described by Equation 6.27 as $\lambda'$. The predictions of this model are compared to those obtained from the numerical solutions for different values of Ste and $\phi_{min}$ (Figure 6.8). It is clear that there is a very good agreement between the model predictions and the numerical simulation results. As predicted, beyond a critical value of the Stefan number ($\text{Ste}_c \approx 10$ for the chosen parameters), the rate of advancement levels off to the value of the thermal lag coefficient; $\lambda = 0.8$.

Viscosity Gradient at the Melting Front

The strengths of viscous forces driving the instability depend on the concentration and temperature gradients as well as the corresponding log mobility ratios. In this part we will examine how the melting parameters affect these gradients by looking at the stable cases; $\beta_C = \beta_T = 0$. The semi-analytical model for the advancement rate of the melting front will be used to determine the variation of the concentration at the melting front. For large $H_T$, the concentration drops from 1 to $\alpha$ at the melting front and past the melting front it adopts a convective diffusive profile described as [173]:

$$\bar{c}_{\phi_{min}} = \frac{1}{2}\alpha \times \text{erfc}\left(\frac{x - t/\phi_{min}}{2\sqrt{t/\phi_{min}}}\right) \tag{6.28}$$

The conservation of mass of the solvent leads to the following balance equation in dimensional form:

$$((C_1 - C_2)\phi_R - (C_{drop} - C_2)\phi_{min})x_\phi + (C_{drop} - C_2)\phi_{min}U\frac{t}{\phi_{min}/\phi_R} = (C_1 - C_2)Ut \quad (6.29)$$

Here $C_{drop}$ is the solvent concentration right after being diluted at the melting front and $\alpha = \frac{C_{drop}-C_2}{C_1-C_2}$. The first term on the left hand side corresponds to the increase in solvent concentration in the melted region with the advancement of the melting front while the second one represents the convection of solvent in the frozen region. The right hand side term is simply the mass of the solvent injected by time $t$. The equation reduces in dimensionless form to:

$$(1 - \alpha\phi_{min})\frac{dx^*_\phi}{dt^*} + \alpha = 1 \quad (6.30)$$

Thus $\alpha$ is obtained as:

$$\alpha = \frac{1 - \lambda'}{1 - \phi_{min}\lambda'} = \frac{1 + \frac{\lambda}{\mathrm{Ste}}(1 - \phi_{min}) - \lambda}{1 + \frac{\lambda}{\mathrm{Ste}}(1 - \phi_{min}) - \lambda\phi_{min}} \quad (6.31)$$

or

$$1 - \alpha = \frac{\lambda'(1 - \phi_{min})}{1 - \phi_{min}\lambda'} = \frac{\lambda(1 - \phi_{min})}{1 + \frac{\lambda}{\mathrm{Ste}}(1 - \phi_{min}) - \lambda\phi_{min}} \quad (6.32)$$

According to Equation 6.32 the drop in concentration increases monotonically with Ste and $(1 - \phi_{min})$. For large Ste, the drop in concentration becomes insensitive to variations of the melting potential and levels off at a maximum of $\frac{\lambda(1-\phi_{min})}{1-\lambda\phi_{min}}$. For small Ste the drop in concentration becomes independent of $\phi_{min}$ as $1 - \alpha$ approaches Ste. The predictions of the model are compared with the maximum values of concentration gradient behind the melting front obtained from the numerical simulations of stable flows for different values of Ste and $\phi_{min}$ (Figure 6.9a). Since the magnitude of the negative concentration gradient defines the strength of this term, absolute values of $\nabla c$ are considered. It is clear that there

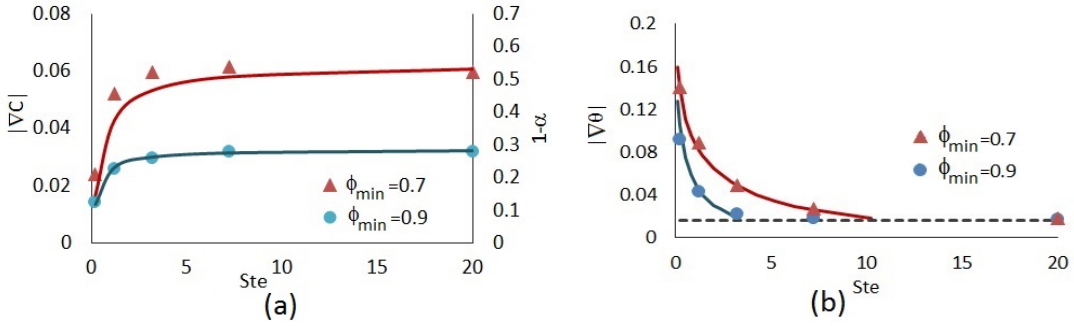


Figure 6.9: The effect of Ste and $\phi_{min}$ on the gradient magnitudes for stable scenarios; $(\beta_C, \beta_T) = (0, 0)$, $t = 250$. a) Concentration gradient, b) Temperature gradient

is a very good agreement between the results of the numerical simulations (data points) and the predictions of the model (solid lines). This indicates that the drop in concentration at the melting front can be assumed to represent the concentration gradient at that point. However given the assumption that the drop in concentration occurs at a certain point ($x_\phi$) that was used in deriving the analytical model, the value of $\alpha$ cannot be strictly interpreted in terms of $\nabla c$. Still, the analytical model can be useful in explaining the effect of different parameters on the concentration gradient at the melting front.

The other parameter that plays an important role in defining the viscosity distribution is the temperature. An analytical model for $\nabla\theta$ is developed based on an estimation of the temperature distribution behind the melting front. According to Equation 6.20, in the region with $\phi = 1$ (behind the melting front) the temperature distribution obeys the following equation:

$$\frac{\partial\theta}{\partial t} = \mathrm{Le}\nabla^2\theta - \lambda\nabla\theta \tag{6.33}$$

Assuming that in melting scenarios the temperature profile only shifts forward with an advancement rate of $\lambda'$, then the temperature and its gradients would be functions of $\zeta = x - \lambda' t$ and thus Equation 6.33 can be recast as:

$$-\frac{\partial\theta}{\partial\zeta}\lambda' = \mathrm{Le}\frac{\partial^2\theta}{\partial\zeta^2} - \lambda\frac{\partial\theta}{\partial\zeta} \tag{6.34}$$

If the maximum of the temperature gradient happens at point $\zeta_\nabla$ with the corresponding temperature of $\theta_\nabla$ then an integration of Equation 6.34 from $\zeta = -\lambda' t$ (where $\theta = 1$ and $\frac{\partial\theta}{\partial\zeta} = 0$) to $\zeta = \zeta_\nabla$ results in:

$$\left.\frac{\partial\theta}{\partial\zeta}\right|_{\zeta_\nabla} = \frac{(\lambda - \lambda')}{\mathrm{Le}}(\theta_\nabla - 1) \tag{6.35}$$

The temperature $\theta_\nabla$ depends on the melting parameters and is obtained based on the results of the numerical simulations for stable scenarios with different Ste and $\phi_{min}$ values following the correlation:

$$\theta_\nabla = 0.76 exp\left(\frac{-0.17}{1-\phi_{min}}\mathrm{Ste}\right) \tag{6.36}$$

The maximum temperature gradient can be obtained by substituting $\theta_\nabla$ from Equation 6.36 into Equation 6.35. The derivation of Equation 6.35 is based on the assumption that the thermal front keeps its profile and does not experience any diffusion. But as shown in [173] for large Ste values the thermal front that encounters minimal resistance from the frozen phase, has an error-function-like profile and thus the temperature gradient is more closely described by:

$$\frac{\partial\theta}{\partial\zeta} = \frac{-1}{2\sqrt{\mathrm{Le}\pi t}} exp\left[-\frac{\zeta^2}{4\mathrm{Le}t}\right] \tag{6.37}$$

The local minimum of this equation occurs at $\zeta = 0$ and has a value of $\frac{1}{2\sqrt{\mathrm{Le}\pi t}}$ that is independent of Ste or $\phi_{min}$ but is a function of time. The two temperature gradient criteria of Equations 6.35 and 6.37 form the solid and the dashed lines in Figure 6.9b. The magnitude of temperature gradients obtained through nonlinear simulations are depicted as scattered data points in Figure 6.9b as well. As illustrated in this figure the analytical estimations match perfectly the numerical simulation results. These data points and the matched curves show that $\nabla\theta$ has an exponential decrease with increase of $\frac{\mathrm{Ste}}{1-\phi_{min}}$ that merges to a plateau of $\frac{1}{2\sqrt{\mathrm{Le}\pi t}}$. The descending trend of $\nabla\theta$ with Ste is due to the slower advancement of the melting

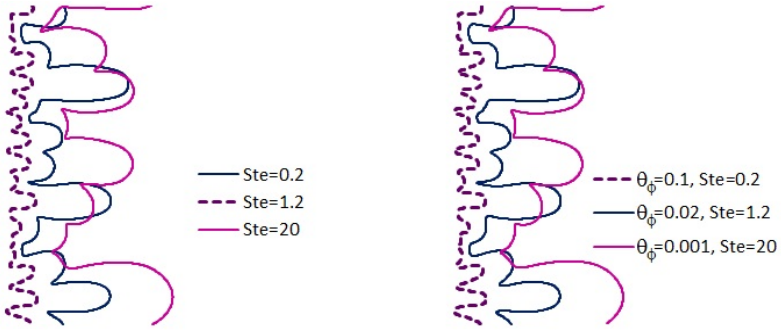


(a) $\phi = 0.85$ contours (b) Temperature contours

Figure 6.10: The contour lines of constant porosity $\phi_{min} = 0.85$ and the matching contours of constant temperature for different Ste values; $t = 250$

front for smaller Ste and the build up of heat behind this front. The same reasoning applies to larger saturation of frozen material that increases the temperature gradient behind the melting front.

The diffused profile of the temperature for large Ste values may be captured for unstable scenarios by comparing the temperature isoprofiles of Figures 6.5b and 6.6. Figure 6.10 illustrates the melting profiles of these scenarios and the corresponding temperature contours that match these profiles. These graphs indicate that the melting front forms on a constant temperature contour line ($\theta_\phi$) whose value decreases with increasing Ste. Therefore for larger melting potential values, the melting front forms on an outer boundary of the temperature profile and like in stable scenarios, this decreases the temperature gradients at the melting front.

Medium Heterogeneity

The heterogeneity of the medium in this model is induced by the developed fingers. Therefore, in addition to the range of variation of the permeability (defined by $\phi_{min}$), the structures of the fingers that define the length scale of these variations are important in determining the instability. Both the fact that the formation of fingers is the source of the heterogeneity, and that the heterogeneity is one of the driving mechanisms for the development of fingers,

make it difficult to analyze how changes in each parameter may affect this mechanism. In general the pressure drop inside a finger has a direct relation with the finger's length and longer fingers are more favorable to fluid flow and the enhancement of the instability. On the other hand and for a given flow rate through a finger, an increase in the width of the finger reduces the local velocity and the contribution of heterogeneity to instability. Therefore longer and thinner fingers enhance the instability due to heterogeneity while the opposite is expected for wider or shorter ones. Moreover the number of long fingers affects the growth rate of the fingers. An even transverse distribution of the instabilities results in a more even distribution of the flow velocity in the medium. Therefore one expects that a single isolated finger will induce a stronger heterogeneity in the medium than many fingers of the same size developed close to each other.

The effect of Ste on the structure of the fingers can be inferred by comparing the porosity contours in Figure 6.10a. Small fingers are observed for Ste = 0.2 while for Ste = 1.2 the fingers are larger in length and width. The enhancement of the instability works towards increasing the heterogeneity by increasing the length of the fingers. However for Ste = 20, the stronger melting potential of the fluid prevents the persistence of thin regions of the frozen phase in between the developed fingers and the base of the fingers gets melted. This effect inhibits the growth of fingers' length and thus reduces the heterogeneity. The effect of Ste on the rate of growth of the melting fingers is better observed in Figure 6.11 where the variation of the melting zone length ($\mathrm{MZL}_\phi$) with Ste is depicted at $t = 250$. The melting zone length is defined as the length of the region with average porosity of $\phi_{min} < \phi_{ave} < 1$. It is observed that as the melting potential of the fluid is increased, $\mathrm{MZL}_\phi$ first increases and then for Ste $> 3.2$ it decreases. Clearly heterogeneity is enhanced by increasing the melting potential of the fluid for the range of $0.2 \leq \mathrm{Ste} \leq 3.2$. However further increase of Ste that results in the reduction of the melting zone length (i.e. the length of the fingers) attenuates

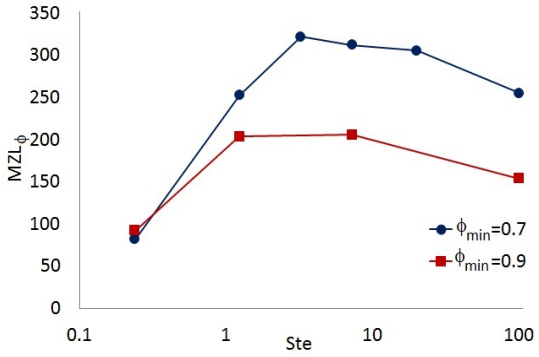


Figure 6.11: The effect of Ste and $\phi_{min}$ on the Melting Zone Length (MZL$_\phi$); $t = 250$.

the effect of this mechanism. The effect of $\phi_{min}$ on MZL$_\phi$ is also illustrated in Figure 6.11 for $\phi_{min} = 0.7$ and $\phi_{min} = 0.9$. A small melting potential of the fluid results in a slower advancement of the fingers. Thus a smaller saturation of the frozen material can help the growth of instabilities for such scenarios. Therefore for Ste $= 0.2$, $\phi_{min} = 0.9$ leads to a larger MZL$_\phi$ than $\phi_{min} = 0.7$. However for moderate and large Ste, easier melting of the base of the fingers due to the smaller saturation of the frozen material for $\phi_{min} = 0.9$ results in smaller finger lengths. Despite its positive effect on the length of the fingers in the lower range of Ste, increasing $\phi_{min}$ reduces the variance of permeability and therefore it weakens the heterogeneity regardless of the value of Ste.

Based on the previous discussions it is possible to explain some of the observed trends in the 2D contours. For example when comparing the importance of the log mobility ratios in Figures 6.2b and 6.4 it was noted that the solutal log mobility ratio has a stronger effect in the destabilization of the front than the thermal log mobility ratio. Looking at Figure 6.9 it can be seen that for the parameter values in these scenarios (Ste $= 3.2$ and $\phi_{min} = 0.7$) $|\nabla c|$ is larger than $|\nabla \theta|$, hence the stronger contribution from $\beta_C$ is not surprising. It can be said that for Ste $\geq 3.2$, the larger concentration gradient results in a stronger contribution from the solutal log mobility ratio. For smaller Ste however, $\beta_T$ will have the leading role

and will affect the instability more strongly.

Also in Figures 6.5b and 6.6, where the effects of Ste on the development of instabilities were examined, a non-monotonic trend was observed . It is now clear that an initial increase of Ste from 0.2 to 1.2 leads to a significant enhancement in the rate of melting and $|\nabla c|$ and the length of the fingers also show considerable increase. So despite the reduction of $|\nabla\theta|$, the fingers show faster development at the melting front. Increasing the melting potential to Ste = 20 does not result in significant changes in $\lambda'$ or $|\nabla c|$ and $|\nabla\theta|$. Yet it decreases $\mathrm{MZL}_\phi$ and thus reduces the contribution of heterogeneity and attenuates the instability.

Finally the negligible effects of $\phi_{min}$ on the instability in Figure 6.7 is now better understood considering the small melting potential used in this figure (Ste = 0.2). With the decrease of $\phi_{min}$ while $\lambda'$ decreases significantly, the temperature gradient at the melting front shows a relatively significant increase. These mechanisms and the reduced heterogeneity as a result of the increased $\phi_{min}$ balance each other and lead to virtually constant lengths of the melting fingers for different $\phi_{min}$. For larger values of Ste the effects of $\phi_{min}$ on the temperature gradient and $\lambda'$ wear off and the synergetic decrease of concentration gradient and the heterogeneity which increasing $\phi_{min}$ reduces the instability in media with smaller saturation of the frozen material.

Although the qualitative analysis of the development of instabilities is beneficial in understanding the reasons behind the different observed trends, it does not provide an overall image of the performance of the melting process. Hence in the following section a quantitative study of the melt production for different scenarios and the effect of the instability on the enhancement of the process are presented.

### 6.4.3 Melting Trends in Unstable Scenarios

In this section the effects of the instabilities on the melt production compared with the corresponding stable scenarios are analyzed. The difference between the porosity of the medium and the initial porosity gives a measure of the amount of melt produced during the displacement. The melt production is scaled with respect to the amount of frozen material initially present in the domain to give the relative amount of melted material.

$$Melt\% = 100 \times \frac{\int_0^{\mathrm{Pe}} (\phi - \phi_{t_0}) dx}{\mathrm{Pe}(1 - \phi_{min})} \tag{6.38}$$

Effect of $\beta_C$ and $\beta_T$ for different Ste and $H_T$

Figure 6.12a illustrates the effects of the solutal and thermal log mobility ratios on the $Melt\%$ for Ste = 0.2 and 3.2. The corresponding stable scenarios are also presented for comparison. For the larger value of the Stefan number, Ste = 3.2, the melting curves for $(\beta_C, \beta_T) = (4, 0)$ and $(0, 4)$ superpose and show significant increase in melting compared to the stable case. For Ste = 0.2 however the instabilities are significantly attenuated and the difference between the stable scenario and the unstable one is relatively small. In fact the melting curve for $(\beta_C, \beta_T) = (4, 0)$ follows closely that of the corresponding stable scenario. As discussed before the effect of the solutal log mobility ratio on the instabilities and thus on the enhancement of melt production, is more pronounced at large Ste. By decreasing the melting potential, the gradient of the concentration and thus the instability at the melting front are attenuated, therefore decreasing the difference with the stable case.

For small heat transfer coefficients, the instabilities on the melting front are found to be attenuated due to the reduction of the temperature gradient. In Figure 6.12b the effects of the thermal instability $(\beta_C, \beta_T) = (0, 4)$ are illustrated for two different heat transfer coefficients. For $H_T = 0.01$ the slight appearance of instabilities on the thermal front results in some increase in the relative melt production but the differences between the unstable

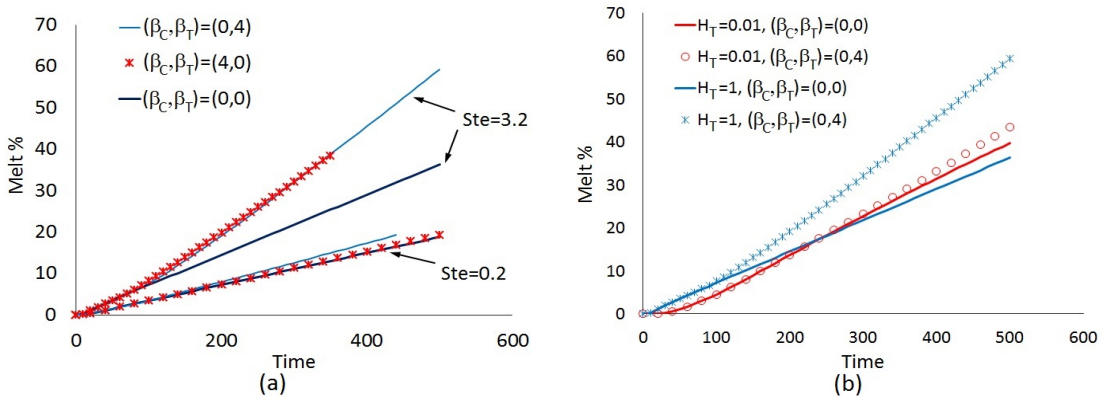


Figure 6.12: The effects of $\beta_C$ and $\beta_T$ on the melt production for a) Ste = 0.2 and 3.2 and $H_T = 1$, and b) $H_T = 0.01$ and 1 and Ste = 3.2.

and the stable cases are not significant. For the larger heat transfer coefficient $H_T = 1$, the increase in melting rate as a result of the developed instability is more significant. These results are to be contrasted with those of the stable cases for which the smaller heat transfer coefficient leads to slightly more melting than the larger one [173].

Effect of $\phi_{min}$ and Ste

Figure 6.13a depicts the effects of $\phi_{min}$ on the melt production for two values of the Stefan number. For Ste = 0.2 the melting rate increases as $\phi_{min}$ is increased. This trend is however reversed for large Stefan number; Ste = 20. This result can be explained based on the discussion in the previous section, where it was found that while a larger saturation of frozen material attenuates the instability for small Ste, for large Ste, as the resistance of the frozen region against the development of instabilities becomes weaker, it results in enhanced development of fingers.

The effects of Ste on melt production are shown in Figure 6.13b for $\phi_{min} = 0.7$. As discussed earlier, for large Ste all the instability mechanisms and even $\lambda'$ that defines the rate of melting for stable scenarios become insensitive to variations of the the melting potential of the fluid. So while increasing Ste tends to increase the $Melt\%$ in the lower ranges of Ste,

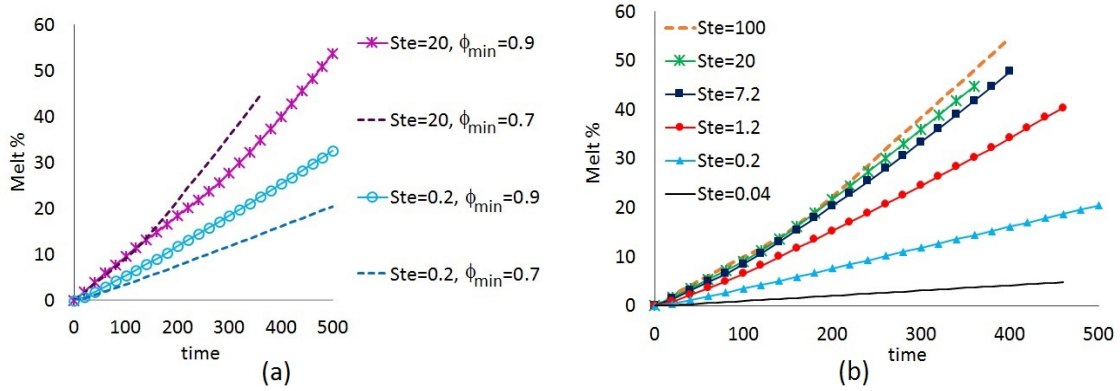


Figure 6.13: The Effects of $\phi_{min}$ and Ste on melt production a) $\phi_{min} = 0.7$ and 0.9, and Ste $= 0.2$ and 20 , and b) $\phi_{min} = 0.7$ and Ste $= 0.04 - 100$.

this effect becomes less important at large values of the melting potential.

The previous results show that the instability enhances the melting rate but the comparison between the melt production of different processes does not provide a measure of the exact contribution of the instability to the increase of melt production. In the following section the instability and its contribution to melt production are examined quantitatively.

### 6.4.4 Quantitative Study of Enhancement of Melting due to Instabilities

In order to determine the extent of the contribution of the instability to melting one should first quantify the *increase in melt* and the *instability*. The increase in melt is quantified using the Relative Melt Increase (RMI) as the scaled difference between the melt production in an unstable scenario and that of the corresponding stable scenario:

$$RMI = \frac{Melt_{Unstable} - Melt_{Stable}}{Melt_{Stable}} \tag{6.39}$$

In Figure 6.14a the time trends of RMI are presented for different scenarios with $\phi_{min} = 0.7$ (solid lines) and $\phi_{min} = 0.9$ (dashed lines) and for Ste $= 0.2 - 20$. The RMI does not show a monotonic variation with the melting parameters Ste or $\phi_{min}$. For both examined values of initial porosity, an increase in Ste up to Ste $= 7.2$ is accompanied by a strong enhancement

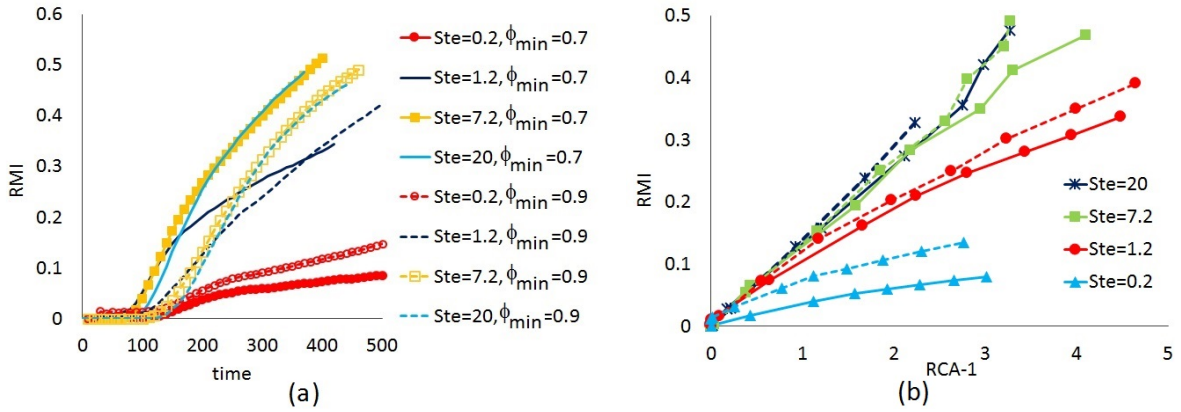


Figure 6.14: Relative Increase of Melting (RMI) in unstable scenarios for different Ste values and $\phi_{min} = 0.7$ (solid lines) and $\phi_{min} = 0.9$ (dashed lines) a) versus time, b) versus the increase in relative contact area RCA$-1$.

of melt production due to instability. Further increase of the melting potential to Ste $\geq 20$ however, puts an end to this trend. The cases with $\phi_{min} = 0.7$ show larger RMI than those with $\phi_{min} = 0.9$ except for Ste $= 0.2$ where the trend is reversed. These non-monotonic trends can be explained in terms of the flow instability if one can show that RMI is directly correlated with the instability of the process. The instability of a displacement process can be measured through different parameters such as $\text{MZL}_\phi$ (representing the length of the fingers) or the Relative Contact Area (RCA) defined as the length of a contour line representing the front's profile over the width of the domain. For a stable scenario RCA remains constant equal to 1 throughout the process. For unstable scenarios a larger RCA corresponds to larger fingers or more complexity of the front's profile, and therefore RCA can be used as a measure of the strength of the instability. In this work the RCA of the thermal front measured at $\theta = 0.5$ will be adopted to quantify the instability.

In Figure 6.14b the RMI is plotted versus $RCA - 1$ (i.e. the increase in RCA due to the instability). Clearly the increase of the relative contact area correlates well with the RMI. Yet the same level of instability (as measured by RCA) results in a larger RMI when Ste or $\phi_{min}$ are larger. For large Ste as shown in Figure 6.10 the melted region covers the

tip of the thermal fingers. This behavior, which will be elaborated on shortly magnifies the effect of instabilities on the melt production and results in larger RMI for faster melting scenarios. Considering the fact that for small melting potential values a medium with larger $\phi_{min}$ affords faster melting of the base and lateral growth of the melting fingers, the effect of larger $\phi_{min}$ on the increase of the RMI can be expected. Hence, the sharper the temperature gradient at the melting front and the larger the saturation of the frozen material in the medium, the more closely the melting front moves with the thermal front and the smaller is the contribution of instability (however strong it may be) to the enhancement of melting.

The effect of the diffused temperature profile on the increase of the melted area is illustrated in Figure 6.15. Here it is assumed that two scenarios with different melting potentials have matching $\theta = 0.5$ contour lines (the solid line). For a small Ste scenario, the melting front forms on the same contour line as (or very close to) the $\theta_\phi \approx 0.5$ line. However for larger Ste when the temperature is allowed to diffuse in the medium the melting front forms on an outer temperature contour line (the dashed line) with $\theta_\phi = 1e-3$. The difference between the swept areas by the two lines shows the difference in the contribution of instability to the melt production for the two different Ste values.

In fact what makes the unstable cases more efficient in terms of melting compared to the stable ones is the enhanced diffusion of heat in the medium due to instability and the formation of the melting front ahead of the thermal fingers. If for an unstable scenario the melting and the thermal fronts have sharp gradients and form the same profiles, then the area swept by these fronts ($A_\phi$) times the changes in the sensible and the latent heat is equal to the heat injected into the medium. Since in both unstable and stable scenarios the injected heat is the same, the swept area for the unstable scenario is equal to the stable one. Based on this, for the same profile of the thermal front (the same level of instability), in order to enhance the melt production one needs to shift the melting front on the temperature contour

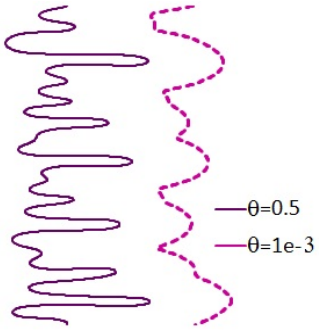


Figure 6.15: Temperature contour lines $\theta_\phi = 0.5$ and $\theta_\phi = 1e-3$ representing the melting front's profiles for different scenarios with small and large melting potentials.

lines. As mentioned earlier (and shown in Figure 6.10) such a shift is inversely proportional to the increase in Ste. Therefore for larger Ste the shift becomes less sensitive to the fluid's melting potential and the RMI curves for different Ste superpose.

### 6.4.5 Effect of Le, Pe, and $\lambda$ on Melting

The main focus of this study has been on the parameters that distinguish the melting processes from the non-melting ones. But there are other parameters involved in the model such as Le, $\lambda$, or Pe that can affect the instabilities and the melt production. The roles of these parameters are briefly discussed in this last section of results.

**Effect of Le** A larger Le corresponds to a faster diffusion rate of heat in the fluid-rock phase and consequently a smaller temperature gradient at the melting front. Thus a larger Le results in a more even distribution of melting in the domain and attenuates the instability. Therefore, even though increasing Le for stable scenarios enhances the melting rate, for unstable scenarios the attenuation of instability results in reduction of melt production.

**Effect of Pe** The ratio of the convection rate over the diffusion rate is reflected in the model by Pe, with larger Pe corresponding to weaker mass and heat diffusion in the medium. On the other hand, according to the definition of the heat transfer coefficient, $H_T \propto \frac{1}{\mathrm{Pe}^2}$,

larger Pe values result in more diffused temperature profiles. As shown in the appendix, the diffusion of the melting front scales like $D_C/H_T \propto$ Pe. hence by increasing Pe, the overall result would be a stronger diffusion of the melting front and an attenuation of instabilities at this front. In the range of the Pe values we studied ($500 \leq \text{Pe} \leq 2000$) which corresponds to varying $H_T$ between 0.25 and 4, variation of Pe was not found to result in any significant changes in the melt production.

**Effect of $\lambda$** In non-melting media, the thermal lag coefficient defines the rate of advancement of the thermal front relative to that of the solutal one. In melting media, according to Equations 6.27 and 6.32, increasing $\lambda$ increases the advancement rate of the melting front and the concentration gradient behind this front. Yet these mechanisms are less sensitive to variations of $\lambda$ in scenarios with small Ste. The results of the numerical simulations show that the effect of $\lambda$ on $\nabla\theta$ is negligible. So overall, increasing $\lambda$ enhances the instability and the rate of melting.

## 6.5 Summary and Conclusion

The effects of hydrodynamic instabilities on melting in under-saturated porous media has been investigated. The model describing the non-isothermal displacement processes, considers a transient thermal equilibrium between the fluid-rock and the melting phases and thus allows the diffusion of the thermal front in the frozen region. In the first part of this study a qualitative observation of the effects of the melting parameters on the development of fingers has been presented based on the results of nonlinear simulations. In the second part, the mechanisms enhancing or attenuating the instabilities namely the advancement rate of the melting front, the viscosity gradient, and the heterogeneity of the medium are discussed. Analytical descriptions for the first two mechanisms are obtained and the observed phenomena

in the first part are explained accordingly. Finally the effect of different parameters on the melting trends have been discussed in the last part of the study and the correlation between the instability and the increase in the melting rate is examined.

It was found that in general the unstable scenarios have larger melting rates than the corresponding stable one and a stronger instability, as quantified by the relative contact area (RCA) of the thermal front leads to more melting. In regards to the effect of different parameters on the instability and consequently the melting, the instability of the melting front is enhanced by an increase of the thermal and solutal log mobility ratios. In the lower range of Ste values, the contribution of the solutal log mobility ratio is less significant while the thermal log mobility ratio shows a stronger effect. A smaller heat transfer coefficient attenuates the instability by decreasing the temperature and concentration gradients. The effects of Ste and $\phi_{min}$ on melting have been shown to be non-monotonic. In the lower range of Ste, increasing the melting potential increases the instability and has positive influence on enhancement of melting. Yet further increase of Ste attenuates the contribution of heterogeneity by melting the base of the fingers. Moreover, for small Ste, a larger saturation of the frozen material attenuates the instability while for larger Ste it enhances the heterogeneity and thus results in faster developing fingers.

Based on the results of this study, the contribution of the instabilities to the melting process is limited for smaller Ste values as the sharp thermal profile does not allow for any increase in the swept area by the melting front. This behavior is improved by decreasing the initial saturation of the frozen material in the medium.

# Chapter 7

# Summary and Conclusion

---

This dissertation consists of four manuscripts investigating the flow instabilities in porous media with and without the effect of heterogeneity. In order to gain the prerequisite knowledge for modeling non-isothermal displacements in melting media where heterogeneity grows with the advancement of the instabilities and melting (the problem defined in Chapters 6 and 5) non-isothermal displacements in homogeneous media and isothermal displacements in heterogeneous media have been thoroughly investigated. The original numerical simulations of these problems have been based on a pseudo-spectral method that transforms the nonlinear equations in space and results in initial value problems with ordinary differential equations. The spectral method could not however be used for the melting media as the sharp gradients at the melting front required non-uniform grid distributions which did not comply with transformation algorithms. Therefore, in the melting models a second order non-uniform finite difference scheme has been used to obtain spatial derivatives. The second order Adams-Bashforth - Adams-Moulton predictor-corrector time stepping algorithm modified with a correction-evaluation sequence has been employed in all of the models to secure the stability and accuracy of the solutions.

The stability of non-isothermal flows has been examined in Chapter 3 and the simulation results in the form of 2D contours have been analyzed to recognize the physical behavior of the flow at different conditions. Different combinations of adverse and favorable mobility ratios on the thermal and the solutal fronts have been examined for different thermal lag

coefficients ($\lambda$) and diffusion rates of heat in the medium. In each scenario one of the thermal or the solutal fronts had a favorable mobility ratio while the other one was viscously unstable. The results showed that the rate of heat exchange with the medium that defined the thermal lag coefficient is an important parameter to indicate the stability of the process. The average concentration and temperature curves have been used to study the interactions between the thermal and fluid fronts. For small thermal lag coefficients and small diffusion rates the gap between the two fronts did not allow for efficient interactions between them and the fluid front determined the stability conditions. For the scenarios where the instability grew on the thermal front, the development of instability showed a non-monotonic trend with variations of the thermal lag coefficient. Larger heat losses to the porous medium resulted in slower advancement rates of the thermal front and smaller effective Peclet numbers that reduced the instability on this front. So increasing $\lambda$ (reducing the heat loss) resulted in enhancement of the instability on the thermal front. Yet because the solutal front had a favorable mobility ratio, it resisted the development of instabilities. So a large $\lambda$ that led to a small gap and improved interaction between the two fronts, inhibited the thermal fingers to develop into the fluid front and thus attenuated the instability on the thermal front. For the scenario with favorable thermal mobility ratio and unfavorable solutal mobility ratio the instability of the process was mainly defined by the fluid front and the thermal front became less and less influential as $\lambda$ was decreased. A larger diffusion rate of heat was shown to weaken the role of the thermal front in stabilizing or destabilizing the fluid front. Also the sensitivity of stability to $\lambda$ decreased as $Le$ was increased. As a quantitative measure of instability, breakthrough time of the mixing zone at the production boundary and the thermal and solutal sweep efficiency have been determined for different scenarios. The conclusions from these quantitative analyses and those of the 2D contours were in agreement. New scenarios with both fronts having unfavorable mobility ratios were examined quantitatively. The

efficiency analyses revealed that an unstable thermal front enhanced the instability at the solutal front and lowered the sweep efficiency and breakthrough time of the process. This effect was weakened by higher diffusion rate of heat and faster heat exchange with the porous medium.

Chapter 4 has been dedicated to the study of the coupling between viscous fingering and heterogeneity induced instability. Qualitative analysis of concentration contours as well as quantitative characterizations through the mixing zone length (MZL) and the breakthrough time (BT) have been performed for a wide range of flow parameters and heterogeneity scales. The qualitative studies showed that reducing the width of the high permeable layers (by increasing the number of the layers or increasing the aspect ratio of the medium) results in a non-monotonic trend of the growth of instabilities. At first, by reducing the width of the layers the growth rate of fingers increased and reached a maximum value that then decreased by further reduction of the layers' widths. This trend, that was attributed to a resonance between the length scale of heterogeneity and the intrinsic length scale of viscous instabilities in the previous works [69, 72, 73] has been shown in this study to be time dependent and a result of each case going through a different flow regime at the time of interest. Further quantitative analyses revealed that in essence, all the examined scenarios went through similar flow regimes, namely an initial diffusive regime followed by a channeling regime then lateral dispersion and finally viscous fingering, though not necessarily at the same extent and with the same intensity. In fact in media with very small heterogeneity layers or in scenarios with high diffusion rates, the flow regime dominated by heterogeneity was bypassed to viscous fingering. These flow regimes that had been recognized in previous studies [67] have been characterized in this study by scaling time and MZL for different combinations of the mobility ratios and variances of permeability distribution. Such characterization of the flow regimes helped explain the dominance of viscous fingering or channeling regimes reported

in earlier studies for different flow conditions and heterogeneous media. Furthermore, by finding the critical effective Péclet number (the scaling factor) this scaling allowed identifying the scenarios in which heterogeneity could be neglected and the flow could be treated as homogeneous. Interestingly, for very small effective Péclet values, the qualitative behavior and structure of the flows were virtually identical to those of the homogeneous case. These results and scaling obtained in the case of diffusive flows, were found to be also valid when an anisotropic velocity-dependent dispersion was considered. The effects of the mobility ratio and variance of permeability were accounted for in the unification factor and allowed to superpose the MZL of any flow in layered heterogeneous media on a master curve that characterized the flow regimes up to the start of viscous fingering. In the quantitative studies the scaling was shown to efficiently describe the variations of breakthrough time and sweep efficiency of different processes. Two optimal values of the effective Péclet number that led to a maximum and a minimum value of break through time were determined. In Appendix A the application of the proposed scaling in industry has been illustrated by looking at different examples of industrial scenarios. By scaling the location of the front's end point (EP) and MZL in the lab experiment the optimum flow conditions were obtained by choosing the breakthrough time in the lateral dispersion regime. Back scaling the EP position to field dimensions could be used to find the optimum injection velocity or well spacing, depending on the fixed parameters.

In Chapter 5, a two dimensional model for non-isothermal displacements through melting porous media has been developed. The fundamentals of melting phenomenon in under-saturated porous media for viscously stable scenarios have been analyzed. The effects of the melting parameters (i.e. the melting potential of the fluid, the heat transfer coefficient, and the saturation of the frozen material) on the profiles of the involved variables including the medium's porosity, and fluid's temperature and concentration have been investigated.

The heat transfer coefficient was observed to define the extent of heat penetration into the frozen region with smaller $H_T$ resulting in more extended thermal and melting fronts. In the higher range of $H_T$ values, it was found that beyond a certain value, large heat transfer coefficients did not result in significant changes in the process, and the temperature, porosity, and concentration profiles were those of instantaneous thermal equilibrium ($ITE$). This conclusion had a significant influence on relaxing the numerical stiffness of the problem and also has important practical implications that led to the unification scheme presented in Appendix B. The melting potential of the fluid was shown to define the rate of melting and to have a significant role in defining the location of the melting front. While for small Ste values the thermal front was stuck behind the melting front, for very large Ste, the advancement of the thermal front was no longer inhibited by melting and rather limited by the heat's diffusion and convection in the medium. A larger saturation of the frozen phase in the medium was shown to result in a slower advancement of the melting front if the melting potential of the fluid was small. For larger melting potential values, the effect of this parameter was observed to be negligible. A quantitative analysis of different melting scenarios using the cumulative melt production were essential in finding the insensitivity of the melting process to the heat transfer coefficient for large values of this parameter. The melt production curves corresponding to the ITE conditions revealed a linear trend with time. So the melting rate was assigned as a characteristic of each melting scenario for large $H_T$ values and its variations with respect to the melting parameters were examined. Further analysis of the stable scenarios discussed in Chapter 6 led to analytical description of the melting rate as a function of the melting parameters and a perfect agreement was found between the analytical results and the rates obtained from numerical simulations. Moreover, it has been shown in Appendix B that regardless of the value of the heat transfer coefficient, the melting rate of all melting scenarios asymptotically merges to the analytically derived

rate. The short term simulations of Chapter 5, however showed that at each time step there was a heat transfer coefficient smaller than the critical one that resulted in more melt production than the other scenarios. The effects of diffusion rate of heat in the medium (Le) has also been investigated and a larger Le is shown to enhance the melting process. Yet based on the studies on the effect of $H_T$ and the asymptotic trends of melting for scenarios with larger Le it can be premised that a larger diffusion rate has the same effect as a smaller heat transfer coefficient and the melting rate of such scenarios merge to the analytical solution as well. The observed insignificant effect of large Le for small Ste values also agrees with this premise.

In the final section of Chapter 5 the effects of heterogeneity on the melting trends have been examined by considering frozen blocks of different shapes in the porous medium. In addition to the internal heat transfer mechanism (similar to the one acting in the previously discussed homogeneous scenarios), outer-boundary convection between the bypassing fluid and the boundaries of the frozen region promoted melting. The new melting mechanism was observed to be enhanced by a reduction in the initial porosity of the frozen block and an increase in its width as both increased the velocity around the frozen block. An estimate of the contribution of each melting mechanism was obtained by premising the internal heat transfer to be proportional to the heat flux through the frozen block. Finally the melting trend of different frozen blocks were unified by scaling the melt production based on the initial saturation of the frozen material and the shape factor (similar to the one used for drag force calculation) of the block.

The effects of hydrodynamic instabilities on melting in under-saturated porous media have been investigated in Chapter 6. The qualitative observation of the effects of the melting parameters on the instabilities have been followed by introduction of the mechanisms enhancing or attenuating the instabilities. Due to the complex interactions between different

instability mechanisms (namely viscous fingering and heterogeneity induced channeling) and the feedback from the melting process, general conclusions could not be derived by studying individual scenarios. Thus characterization of the mechanisms that contributed to viscous fingering or channeling was found to be of utmost importance. Analytical description of these mechanisms, namely the advancement rate of the melting front, the viscosity gradient, and the heterogeneity of the medium, allowed the identification of the role of the melting parameters in enhancing or attenuating the instability. According to these analyses, the unstable scenarios had larger melting rates than the corresponding stable ones and a stronger instability led to more melting. Thus any parameter that promoted an enhancement of instability (e.g. larger log mobility ratios) increased the melting rate although the extent of the contribution of these parameters varied in different scenarios. For example the solutal log mobility ratio only affected the instability if the assigned Ste was large enough while the opposite was true for the thermal log mobility ratio. The effects of the melting parameters on instability was in general non-monotonic except for the heat transfer coefficient that attenuated the instability by producing smaller gradients at the melting front. A larger melting potential in the lower range of Ste, increased the instability but a further increase of Ste resulted in weakening of the contribution of heterogeneity. A larger saturation of the frozen material attenuated the instability in scenarios with limited melting potential while for larger Ste the heterogeneity was enhanced by an increase of the saturation and faster developing fingers were observed. Overall, the contribution of instabilities to the enhancement of melting was found to depend on the increase in the melted area as a result of the development of fingers. Therefore for smaller Ste values corresponding to the temperature and porosity profiles forming close to each other, insignificant improvement in melting was observed while the same level of instability resulted in improved melting for larger melting potentials or smaller saturations of frozen material.

In the analyses conducted in this research work, for non-isothermal displacements, it has been assumed that the medium is homogeneous and the heterogeneity is studied for isothermal displacements. The coupling between these two phenomena is not as simple as including the heat conservation equation in the heterogeneous model. The reason is that the thermal properties of the medium are highly dependent on the porosity and the correlation between variations of permeability and porosity in the medium should be considered. Thus many of the parameters deemed constant in the equations (such as heat diffusion rate and thermal lag coefficient) are to be redefined. This would be an interesting subject for further investigation due to its extensive application in different displacement processes. Another limitation of this work is the model of permeability employed to study the effect of heterogeneity on instabilities. Although the simple model turned out to simplify the characterization of the flow regimes and the development of a unification scheme, its application in real field is limited. Finding the parameters, resembling the ones defined for the layered heterogeneity, for random permeability distributions would extend the application of the proposed scaling to industrial displacements. Also the similarity between the flow patterns in other forms of hydrodynamic instability, such as gravity driven instability or immiscible viscous fingering, coupled with heterogeneity of the medium, suggests that the present scaling approach can be also adopted to characterize the flow behavior in these phenomena. Therefore a systematic study could facilitate unification of these types of flow instabilities as well. The flow instability in melting media with all the employed simplifying assumptions is a stiff numerical problem. Yet inclusion of some other mechanisms such as gravity forces and the change in density during melting could expand the applicability of the results to more natural and industrial applications. The problem as described in this work can also benefit from more investigation towards analytical solution of the equations for 1D stable scenarios especially for moderate melting potential cases. Although parts of this research work have been con-

ducted on the extensively studied topics such as non-isothermal displacements or flow in heterogeneous media, its contributions to the knowledge about these phenomena are novel and recognized by well ranked scientific journals. To the author's knowledge there has been no previous study that looked at the dynamic heterogeneity discussed in this dissertation and the model, the numerical simulations and the analytical solutions have been originally developed by the author.

# Appendix A

# Improvement of Sweep Efficiency of Miscible Displacement Processes in Heterogeneous Porous Media

---

In this appendix the application of the proposed scheme in Chapter 4 is discussed for optimization of miscible displacements in heterogeneous porous media through studying five different miscible displacement scenarios defined in Table A.1 in dimensional form. In the first four cases the injection velocity, diffusion rate and well spacing parameters are changed but all the displacements happen in a medium with layered heterogeneity of width 25.6 m. The last scenario resembles the conditions for a lab experiment and shows how experimental results can be applied to field scale projects. For measurement of the success of the displacement scenarios their sweep efficiencies are plotted against time and the optimum flow conditions are sought based on these graphs. For comparing different scenarios the position of the tip of the front (EP) is used in addition to the previously defined mixing zone length for its convenience of measurement and its direct relation with the distance between the injection and production wells at breakthrough time. The same scaling scheme used for generalization of MZL graphs can be applied for scaling the position of the tip of the mixing zone ($x_{EP}$) in time.

In the first three cases defined in Table A.1, the only varying parameter is the injection velocity which has been increased from $5e{-}6\ m/s \equiv 0.43 m/day$ to $20e{-}6\ m/s \equiv 1.73 m/day$.

The previous definition of the characteristic time and length in dimensional form ($t_c = w^2/D$ and $x_c = Uw^2/(D\phi)$) which has been used for scaling implies that the injection velocity does not affect the transition time between the channeling and lateral dispersion regimes in dimensional form. Dimensional plots of mixing zone length, endpoint position and sweep efficiency of these three scenarios plotted versus time in Figure A.1 agree with this conclusion. Increase of injection velocity from cases 1 to 3 results in faster growth of instabilities in each regime and increases the advance rate of the EP position. The breakthrough time values for each of the injection velocities for a fixed spacing between the injection and the production wells ($l = 550$ m) are given in Table 1. The fact that higher injection rate results in earlier breakthrough of the solvent, if not trivial, is expected but it does not mean that a lower injection rate necessarily results in a higher efficiency of the process. In fact the calculated values of the sweep efficiency of these processes show a better performance for case 2 with the injection rate of $U = 10e-6$ m/s than the other two scenarios. The sweep efficiency of a displacement process is significantly affected by the instabilities and therefore is correlated with the flow regime in heterogeneous media. Due to the growth of fingers in the channeling regime the flow has lower sweep efficiency in this regime and the efficiency improves as lateral dispersion develops. By the start of viscous fingering the sweep efficiency drops again. Figure A.1c shows the variations of the sweep efficiency of the discussed scenarios with time and the breakthrough time of each of the processes are marked on them as well as on the MZL and EP position curves in Figures A.1 a and b. It is apparent that because the breakthrough of case 1 with $U = 5e-6$ m/s occurs during the viscous fingering period, its efficiency is lower than the other two cases whose breakthrough times are during the lateral dispersion period. So, slower injection of the solvent in this case reduces both the rate of production and the recovery.

In what follows we discuss how the scaling scheme proposed in this chapter helps to find

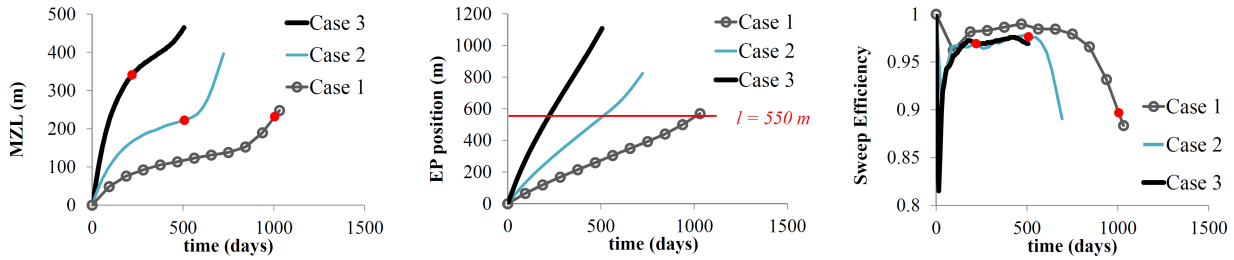


(a) (b)

Figure A.1: Quantitative description of the displacement front behavior through analysis of time variation of a) MZL, b) EP position, c) Sweep Efficiency; breakthrough of each case is marked as a solid circle on its curve

the optimum injection velocity or in general the optimum conditions that would result in higher sweep efficiencies while maintaining high production rates.

As mentioned before the data used to plot the curves in Figures A.1a and b can be scaled using the proposed dimensional scaling and the result would be a unified curve that can be scaled back to the dimensional curve based on the parameter values of use. Figure A.2 shows that scaled graphs. To examine the application of scaling for various diffusion coefficients and widths of the layers cases 4 and 5 are also presented in these figures. Case 4 has a higher diffusion rate of $1e-5\ m^2/s$ compared to that of the previous three cases ($5e-6\ m^2/s$) but otherwise is similar to case 3. Case 5 has smaller dimensions which could correspond to an experimental setup. The width of the layers in this case is 2.56 $cm$ and the diffusion rate and injection velocity are larger than the ones in cases 1 to 3. Despite the vast difference in size between the different scenarios, the scaling of MZL and EP position matches all the scenarios together. It is also interesting to note that cases 2 and 4 have the same $w^2U/D_C$ which means that the fronts in these two cases look similar at the same position. This explains why they show the same sweep efficiency at the breakthrough time while reaching it at different times as case 4 has an injection velocity double that of case 2. These unified curves can be obtained from test results or experimental data of different sizes and can be scaled back to the units of interest for any scenario as long as the mobility ratio is kept

the same. In this practical approach the variance of permeability has been kept constant and the generalization is performed based on Equation 4.14 but according to our previous discussions the effect of this parameter can be included in the scaling as well by using the proper scaling. Another limitation is that since the dynamics of the flow in viscous fingering regime is dominated by advection rather than diffusion, unification of the curves is only valid up to the start of viscous fingering in the process. So it is not possible to predict the time at which viscous fingering starts. Breakthrough time can be calculated from the generalized curves by setting $x_{\tilde{EP}} = l/(w^2U/D_C)$ and adjusting the parameters that could be changed like injection rate or the distance between the production and injection wells such that the breakthrough happens in lateral dispersion regime. Since the scaling of different scenarios in time synchronizes their flow regimes, plotting the sweep efficiency curves of these scenarios with respect to the scaled time makes them to fall together as the flows go through the channeling regime and rise again as the flows go through the lateral dispersion regime. Such curves are useful for a direct determination of the optimum injection rate or well spacing for a displacement process design based on the highest sweep efficiency. For example if only production data of case 5 are available through lab experiments and the objective is to find optimum well spacing for the scenario defined as case 1. The sweep efficiency of this scenario versus scaled time (as in Figure A.2c) shows that if breakthrough happens between scaled times of 0.2 and 0.5 then the process will have higher sweep efficiency. The scaled time values on scaled EP plot in Figure A.2b refer to $x_{\tilde{EP}}$ of 0.3 to 0.6 which can be scaled back to dimensional values through $l = x_{\tilde{EP}} \times (25.6^2 \times 5e-6/5e-6)$ and give the optimum well spacing of 100 to 450 meters with the corresponding breakthrough time values of 300 to 750 days. These predictions agree well with the plots corresponding to case 1 in Figure A.2. The optimum well spacing values for other scenarios are calculated similarly and are given in Table A.1. The same procedure can be employed for optimization of the injection velocity

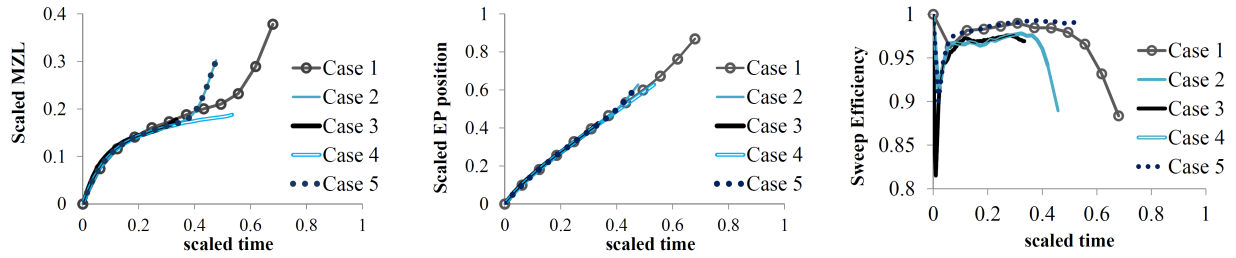


(a) (b)

Figure A.2: Unified curves after scaling the length and time using the diffusive scaling for a) MZL, b) EP position and c) sweep efficiency with respect to scaled time.

for a fixed well spacing.

Table A.1: Flow conditions for the described displacement scenarios and the corresponding breakthrough time, weep efficiency at breakthrough and optimum well spacing for each scenario.

| Case | U (m/s) | w (m) | $D_C$ $(m^2/s)$ | SE at BT | $t_{BT}$ (Days) | $l_{opt}$ (m) |
|---|---|---|---|---|---|---|
| 1 | 5e-6 | 25.6 | 5e-6 | 0.897 | 1005.1 | 65 to 450 |
| 2 | 10e-6 | 25.6 | 5e-6 | 0.976 | 508.0 | 120 to 650 |
| 3 | 20e-6 | 25.6 | 5e-6 | 0.969 | 219.7 | 250 to 1100 |
| 4 | 20e-6 | 25.6 | 1e-5 | 0.976 | 253.99 | 120 to 650 |
| 5 | 5e-3 | 0.0256 | 1e-6 | - | - | 0.25 to 1.65 |

# Appendix B

## Generalization of the Melting Curves for Different $H_T$

A slow heat transfer between the fluid and the frozen material allows the heat to be spent on melting more gradually and results in the melting region to extend more along the flow direction. Therefore the temperature and porosity fronts will have more diffused profiles for smaller $H_T$. So the effect of smaller $H_T$ on the melting process translates into a faster diffusion of heat in the domain. Considering this premise, to generalize the analysis of the effect of $H_T$ we revisit the original equations and re-formulate the dimensionless groups where $D_C$ is scaled with respect to $H_T$:

$$(x^*, y^*) = \frac{x, y}{\frac{D_C}{H_T}\frac{\phi_R}{U}} \quad t^* = \frac{t}{\frac{D_C}{H_T}\frac{\phi_R^2}{U^2}} \quad p^* = \frac{p\kappa_R}{\phi_R\mu_1\frac{D_C}{H_T}} \quad \mu^* = \frac{\mu}{\mu_1} \quad \kappa^* = \frac{\kappa}{\kappa_R} \tag{B.1}$$

The resulting dimensionless equations are:

$$\nabla.(\phi\vec{v}) = 0 \tag{B.2}$$

$$\nabla p = -\frac{\mu}{\kappa}\phi\vec{v} \tag{B.3}$$

$$\frac{\partial(\phi C)}{\partial t} = -\phi\vec{v}.\nabla C + H_T\nabla.(\phi\nabla C) \tag{B.4}$$

$$\frac{\partial\theta}{\partial t} = \frac{1}{(1-\lambda(1-\phi))}[H_T\mathrm{Le}\nabla.\left((1-(1-\phi)k_{rel})\,\nabla\theta\right) - \lambda\phi\vec{v}\nabla.\theta - (1-\phi)^{2/3}\theta] \tag{B.5}$$

$$\frac{\partial\phi}{\partial t} = \frac{1}{1+\mathrm{Ste}\theta}\frac{\mathrm{Ste}}{\lambda}(1-\phi)^{2/3}\theta \tag{B.6}$$

With this scaling, the dimensionless equation for melting is independent of $H_T$ and the heat transfer coefficient appears only in the diffusion terms in the concentration and heat equations. Hence the melting rate and the amount of heat devoted to melting do not depend

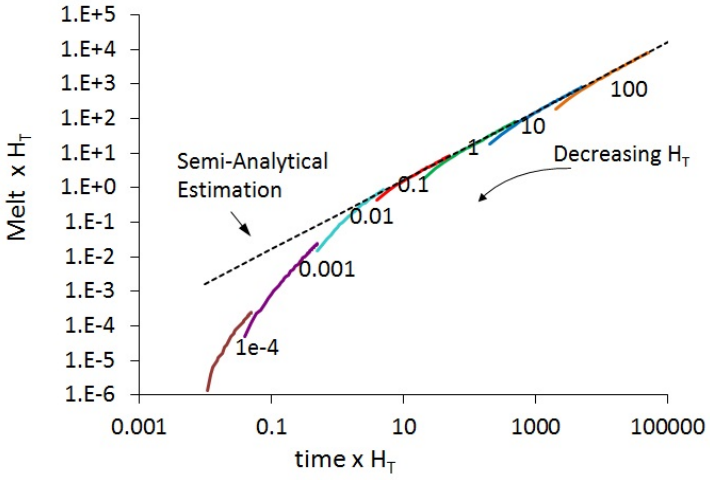


Figure B.1: Melt % in the new dimensionless system scaling the diffusion rate with respect to $H_T$.

on $H_T$. Figure B.1 shows the cumulative melt curves for stable scenarios with different values of $H_T$ based on the new dimensionless groups. The melting curves for different $H_T$ correspond to different parts of a unified curve and indicate that different heat transfer coefficients result in the same melting trends only at different time scales.

# Bibliography


[1] G. Homsy, "Viscous fingering in porous media," *Annual Review on Fluid Mechanics*, vol. 19, pp. 271 – 311, 1987.

[2] K. McCloud and J. Maher, "Experimental perturbations to saffman-taylor flow," *Physics Reports*, vol. 260, no. 3, pp. 139 – 185, Sept. 1995.

[3] E. Koval, "A method for predicting the performance of unstable miscible displacement in heterogeneous media," *SPE Journal*, vol. 3, no. 2, pp. 145–154, 1963.

[4] M. Saghir, O. Chaalal, and M. Islam, "Numerical and experimental modeling of viscous fingering during liquid-liquid miscible displacement," *Journal of Petroleum Science and Engineering*, vol. 26, no. 1-4, pp. 253 – 262, 2000.

[5] S. Hill, "Channelling in packed columns," *Chemical Engineering Science*, vol. 1, pp. 247 – 253, 1952.

[6] P. G. Saffman and G. Taylor, "The penetration of a fluid into a porous medium or hele-shaw cell containing a more viscous liquid," *Proceedings of the Royal Society of London. Series A. Mathematical and Physical Sciences*, vol. 245, no. 1242, pp. 312–329, 1958.

[7] C. Tan and G. Homsy, "Stability of miscible displacements in porous media: rectilinear flow," *Physics of Fluids*, vol. 29, no. 11, pp. 3549 – 3556, 1986.

[8] C. Tan and G. Homsy, "Simulation of nonlinear viscous fingering in miscible displacement," *Physics of Fluids*, vol. 31, no. 6, pp. 1330 – 1338, 1988.

[9] Y. Yortos and M. Zeybek, "Dispersion driven instability in miscible displacement in porous media," *Physics of Fluids*, vol. 31, no. 12, pp. 3511–3518, 1988.

[10] M. Christie, A. Muggeridge, and J. Barley, "3d simulation of viscous fingering and wag schemes," *SPE Reservoir Engineering (Society of Petroleum Engineers)*, vol. 8, no. 1, pp. 19 – 26, 1993.

[11] W. Zimmerman and G. Homsy, "Nonlinear viscous fingering in miscible displacement with anisotropic dispersion," *Physics of Fluids A (Fluid Dynamics)*, vol. 3, no. 8, pp. 1859 – 1872, 1991.

[12] J. Azaiez and B. Singh, "Stability of miscible displacements of shear thinning fluids in a hele-shaw cell," *Physics of Fluids*, vol. 14, no. 5, pp. 1557 – 1571, 2002.

[13] K. Ghesmat and J. Azaiez, "Viscous fingering instability in porous media: Effect of anisotropic velocity-dependent dispersion tensor," *Transport in Porous Media*, vol. 73, no. 3, pp. 297 – 318, 2008.

[14] A. De Wit, "Viscous fingering in reaction-diffusion systems," *Journal of Chemical Physics*, vol. 110, no. 17, pp. 8663 – 8675, 1999.

[15] S. Hejazi, P. Trevelyan, J. Azaiez, and A. De Wit, "Viscous fingering of a miscible reactive a + b = c interface: A linear stability analysis," *Journal of Fluid Mechanics*, vol. 652, pp. 501 – 528, 2010.

[16] S. Hejazi and Azaiez, "Non-linear interactions of dynamic reactive interfaces in porous media," *Chemical Engineering Science*, vol. 65, pp. 938 –949, 2010.

[17] Q. Yuan and J. Azaiez, "Cyclic time-dependent reactive flow displacements in porous media," *Chemical Engineering Science*, vol. 109, pp. 136 – 146, 2014.

[18] Q. Yuan and J. Azaiez, "Miscible displacements in porous media with time-dependent injection velocities," *Transport in Porous Media*, vol. 104, no. 1, pp. 136 – 146, 2014.

[19] Q. Yuan and J. Azaiez, "Inertial effects of miscible viscous fingering in a hele-shaw cell," *Fluid Dynamics Research*, vol. 47, no. 1, p. 015506 (21 pp.), 2015.

[20] Q. Yuan and J. Azaiez, "Inertial effects in cyclic time-dependent displacement flows in homogeneous porous media," *Canadian Journal of Chemical Engineering*, vol. 93, no. 8, pp. 1490 – 1499, 2015.

[21] A. Woods and S. Fitzgerald, "The vaporization of a liquid front moving through a hot porous rock," *Journal of Fluid Mechanics*, vol. 251, pp. 563 – 579, 1993.

[22] M. Islam and J. Azaiez, "Miscible thermo-viscous fingering instability in porous media. part 1: Linear stability analysis," *Transport in Porous Media*, vol. 84, no. 3, pp. 821 – 844, 2010.

[23] M. Mishra, P. Trevelyan, C. Almarcha, and A. De Wit, "Influence of double diffusive effects on miscible viscous fingering," *Physical Review Letters*, vol. 105, no. 20, p. 204501 (4 pp.), 2010.

[24] J. Azaiez and M. Sajjadi, "Stability of double-diffusive double-convective miscible displacements in porous media," *Physical Review E (Statistical, Nonlinear, and Soft Matter Physics)*, vol. 85, no. 2, p. 026306 (12 pp.), 2012.

[25] D. Pritchard, "The instability of thermal and fluid fronts during radial injection in a porous medium," *Journal of Fluid Mechanics*, vol. 508, pp. 133 – 163, 2004.

[26] M. Islam and J. Azaiez, "New viscous fingering mechanisms at high viscosity ratioand peclet number miscible displacements," *Journal of Porous Media*, vol. 10, no. 4, pp. 357 – 376, 2007.

[27] M. Islam and J. Azaiez, "Miscible thermo-viscous fingering instability in porous media.

part 2: Numerical simulations," *Transport in Porous Media*, vol. 84, no. 3, pp. 845 – 861, 2010.

[28] R. Slobod and B. Caudle, "X-ray shadowgraph studies of areal sweepout efficiencies," *American Institute of Mining and Metallurgical Engineers – Journal of Petroleum Technology*, vol. 4, no. 11, pp. 265 – 270, 1952.

[29] P. Saffman, "Theory of dispersion in porous medium," *Journal of Fluid Mechanics*, vol. 6, no. Part 3, pp. 321 – 349, 1959.

[30] R. Chuoke, P. van Meurs, and C. van der Poel, "Instability of slow, immiscible, viscous liquid-liquid displacements in permeable media," *Petroleum Transactions, AIME*, vol. 216, pp. 188 – 194, 1959.

[31] D. Peaceman and H. Rachford, Jr., "Numerical calculation of multidimensional miscible displacement," *Society of Petroleum Engineers – Journal*, vol. 2, no. 4, pp. 327 – 339, 1962.

[32] R. Wooding, "Growth of fingers at an unstable diffusing interface in a porous medium of hele-shaw cell," *Journal of Fluid Mechanics*, vol. 39, pp. 477 – 495, 1969.

[33] R. Slobod and R. Thomas, "Effect of transverse diffusion on fingering in miscible-phase displacement," *Society of Petroleum Engineers – Journal*, vol. 3, no. 1, pp. 9 – 13, 1963.

[34] R. Wooding and H. Morel-Seytoux, *Multiphase fluid flow through porous media*, vol. 8, pp. 233 – 274. 1976.

[35] W. Zimmerman and G. Homsy, "Three-dimensional viscous fingering: a numerical study," *Physics of Fluids A (Fluid Dynamics)*, vol. 4, no. 9, pp. 1901 – 1914, 1992.

[36] C. Tan and G. Homsy, "Stability of miscible displacements in porous media: Radial source flow," *Physics of Fluids*, vol. 30, no. 5, pp. 1239–1245, 1987.

[37] Y. Ben, E. A. Demekhin, and H.-C. Chang, "A spectral theory for small-amplitude miscible fingering," *Physics of Fluids*, vol. 14, no. 3, pp. 999 – 1010, 2002.

[38] M. C. Kim and C. K. Choi, "The stability of miscible displacement in porous media: Nonmonotonic viscosity profiles," *Physics of Fluids*, vol. 23, no. 8, p. 084105 (8 pp.), 2011.

[39] M. Kim and C. Choi, "Linear stability analysis on the onset of buoyancy-driven convection in liquid-saturated porous medium," *Physics of Fluids*, vol. 24, no. 4, 2012.

[40] O. Manickam and G. Homsy, "Simulation of viscous fingering in miscible displacements with nonmonotonic viscosity profiles," *Physics of Fluids*, vol. 6, no. 1, pp. 95 – 95, 1994.

[41] M. Islam, J. Azaiez, and B. Maini, "Numerical simulations of thermo-viscous fingering instability in porous media," *Computational Thermal Sciences*, vol. 2, no. 2, pp. 183 – 201, 2010.

[42] X. Kong, M. Haghighi, and Y. Yortsos, "Visualization of steam displacement of heavy oils in a hele-shaw cell," *Fuel*, vol. 71, no. 12, pp. 1465 – 1471, 1992.

[43] S. Farouq Ali and S. Snyder, "Miscible thermal methods applied to a two-dimensional, vertical tar sand pack, with restricted fluid entry.," *Journal of Canadian Petroleum Technology*, vol. 12, no. 4, pp. 20 – 26, 1973.

[44] S. Farouq Ali and J. Ferrer, "State-of-the-art of thermal recovery models.," *Journal of Energy Resources Technology, Transactions of the ASME*, vol. 103, no. 4, pp. 296 – 300, 1981.

[45] M. Tamim, J. Abou-Kassem, and S. Farouq Ali, "Recent developments in numerical simulation techniques of thermal recovery processes," *Journal of Petroleum Science and Engineering*, vol. 26, no. 1-4, pp. 283 – 289, 2000.

[46] K. Helfrich, "Thermo-viscous fingering of flow in a thin gap: a model of magma flow in dikes and fissures," *Journal of Fluid Mechanics*, vol. 305, pp. 219 – 238, 1995.

[47] J. Kuang and T. Maxworthy, "The effects of thermal diffusion on miscible, viscous displacement in a capillary tube," *Physics of Fluids*, vol. 15, no. 5, pp. 1340 – 1343, 2003.

[48] K. E. Holloway and J. R. de Bruyn, "Viscous fingering with a single fluid," *Canadian Journal of Physics*, vol. 83, no. 5, pp. 551–564, 2005.

[49] K. E. Holloway and J. R. de Bruyn, "Numerical simulations of a viscous-fingering instability in a fluid with a temperature-dependent viscosity," *Canadian Journal of Physics*, vol. 84, no. 4, pp. 273–287, 2006.

[50] T. Sheorey, K. Muralidhar, and P. P. Mukherjee, "Numerical experiments in the simulation of enhanced oil recovery from a porous formation," *International Journal of Thermal Sciences*, vol. 40, no. 7, pp. 981 – 997, 2001.

[51] T. Sheorey and K. Muralidhar, "Isothermal and non-isothermal oilwater flow and viscous fingering in a porous medium," *International Journal of Thermal Sciences*, vol. 42, no. 7, pp. 665 – 676, 2003.

[52] D. Pritchard, "The linear stability of double-diffusive miscible rectilinear displacements in a hele-shaw cell," *European Journal of Mechanics, B/Fluids*, vol. 28, no. 4, pp. 564 – 577, 2009.

[53] M. Islam and J. Azaiez, "Thermo-viscous fingering in quarter five-spot miscible displacements," *European Journal of Mechanics, B/Fluids*, vol. 30, no. 1, pp. 107 – 119, 2011.

[54] R. Blackwell, J. Rayne, and W. Terry, "Factors influencing the efficiency of miscible displacement," *Petroleum Transactions, AIME*, vol. 217, pp. 1 – 8, 1959.

[55] M. Lorenz, "Methods of measuring the concentration of wealth," *American Statistical Association*, vol. 9, no. 70, pp. 209–219, 1905.

[56] J. Schmalz and H. Rahme, "The variation of waterflood performance with variation in permeability profile," tech. rep., Production Monthly 14:9, 1950.

[57] J. Warren and H. Price, "Flow in heterogeneous porous media," *SPE Journal*, vol. 1, no. 3, pp. 153 – 169, 1961.

[58] J. L. Jensen and L. W. Lake, "The influence of sample size and permeability distribution on heterogeneity measures," *SPE Reservoir Engineering (Society of Petroleum Engineers)*, vol. 3, no. 2, pp. 629 – 637, 1988.

[59] D. Tiab and M. Osman, "Extension of the dykstra-parsons method to layered-composite reservoirs," 1986.

[60] N. A. F. El-Khatib, "The modification of the dykstra-parsons method for inclined stratified reservoirs," *SPE Journal*, vol. 17, no. 4, pp. 1029 – 1040, 2012.

[61] M. Todd and W. Longstaff, "The development, testing, and application of a numerical simulator for predicting miscible flood performance," *Journal of Petroleum Technology*, vol. 24, pp. 874–882, 1972.

[62] F. Fayers, "An approximate model with physically interpretable parameters for representing miscible viscous fingering," *SPE Reservoir Engineering*, vol. 3, no. 2, pp. 551–558, 1988.

[63] M. Christie and D. Bond, "Detailed simulation of unstable processes in miscible flooding.," *SPE Reservoir Engineering (Society of Petroleum Engineers)*, vol. 2, no. 4, pp. 514 – 522, 1987.

[64] U. G. Araktingi and F. M. Orr Jr., "Viscous fingering in heterogeneous porous media," *SPE Advanced Technology Series*, vol. 1, no. 1, pp. 71 – 80, 1993.

[65] L. W. Gelhar and C. L. Axness, "Three-dimensional stochastic analysis of macrodispersion in aquifers.," *Water Resources Research*, vol. 19, no. 1, pp. 161 – 180, 1983.

[66] C.-Y. Chen and E. Meiburg, "Miscible porous media displacements in the quarter five-spot configuration. part 2. effect of heterogeneities," *Journal of Fluid Mechanics*, vol. 371, pp. 269 – 299, 1998.

[67] J. Waggoner, J. Castillo, and L. Lake, "Simulation of eor processes in stochastically generated permeable media," *SPE Formation Evaluation*, vol. 7, no. 2, pp. 173–180, 1992.

[68] H. Tchelepi, J. Orr, F.M., N. Rakotomalala, D. Salin, and R. Woumeni, "Dispersion, permeability heterogeneity, and viscous fingering: acoustic experimental observations and particle-tracking simulations," *Physics of Fluids A (Fluid Dynamics)*, vol. 5, no. 7, pp. 1558 – 1574, 1993.

[69] C. Tan and G. Homsy, "Viscous fingering with permeability heterogeneity," *Physics of Fluids A (Fluid Dynamics)*, vol. 4, no. 6, pp. 1099 – 1101, 1992.

[70] M. Shinozuka and C.-M. Jan, "Digital simulation of random processes and its applications," *Journal of Sound and Vibration*, vol. 25, no. 1, pp. 111 – 128, 1972.

[71] E. Fernandez, C. Grotegut, G. Braun, K. Kirschner, J. Staudaher, M. Dickson, and V. Fernandez, "The effects of permeability heterogeneity on miscible viscous fingering: a three-dimensional magnetic resonance imaging analysis," *Physics of Fluids*, vol. 7, no. 3, pp. 468 – 477, 1995.

[72] A. De Wit and G. Homsy, "Viscous fingering in periodically heterogeneous porous media. i. formulation and linear instability," *Journal of Chemical Physics*, vol. 107, no. 22, pp. 9609 – 9618, 1997.

[73] A. De Wit and G. Homsy, "Viscous fingering in periodically heterogeneous porous media. ii. numerical simulations," *Journal of Chemical Physics*, vol. 107, no. 22, pp. 9619 – 9628, 1997.

[74] M. Ferer, W. Sams, R. Geisbrecht, and D. Smith, "Crossover from fractal to compact flow from simulations of two-phase flow with finite viscosity ratio in two-dimensional porous media," *Physical Review E (Statistical Physics, Plasmas, Fluids, and Related Interdisciplinary Topics)*, vol. 47, no. 4, pp. 2713 – 2723, 1993.

[75] M. Ferer, W. Sams, R. Geisbrecht, and D. H. Smith, "Fractal nature of viscous fingering in two-dimensional pore level models," *AIChE Journal*, vol. 41, no. 4, pp. 749 – 763, 1995.

[76] M. Ferer, K. Stevenson, G. Bromhal, J. Gump, J. Wilder, and D. Smith, "2-d network model simulations of miscible two-phase flow displacements in porous media: Effects of heterogeneity and viscosity," *Physica A*, vol. 367, pp. 7 – 24, 2006.

[77] N. Eriksson and G. Destouni, "Combined effects of dissolution kinetics, secondary mineral precipitation, and preferential flow on copper leaching from mining waste rock," *Water Resources Research*, vol. 33, no. 3, pp. 471–483, 1997.

[78] S. D. Rege and H. Fogler, "Competition among flow, dissolution, and precipitation in porous media," *AIChE Journal*, vol. 35, no. 7, pp. 1177 – 1185, 1989.

[79] C. Petrich, J. Karlsson, and H. Eicken, "Porosity of growing sea ice and potential for oil entrainment," *Cold Regions Science and Technology*, vol. 87, pp. 27 – 32, 2013.

[80] P. Wadhams, "Ocean freshening, sea level rising, sea ice melting," *Geophysical Research Letters*, vol. 31, no. 11, p. L11311 (4 pp.), 2004.

[81] K. I. Ohshima, K. Yoshida, H. Shimoda, M. Wakatsuchi, T. Endoh, and M. Fakuchi, "Relationship between the upper ocean and sea ice during the antarctic melting season," *Journal of Geophysical Research: Oceans*, vol. 103, no. C4, pp. 7601–7615, 1998.

[82] S. Nihashi, K. I. Ohshima, M. O. Jeffries, and T. Kawamura, "Sea-ice melting processes inferred from iceupper ocean relationships in the ross sea, antarctica," *Journal of Geophysical Research: Oceans*, vol. 110, no. C2, p. C02002 (12 pp.), 2005.

[83] C. Krembs, H. Eicken, and J. Deming, "Exopolymer alteration of physical properties of sea ice and implications for ice habitability and biogeochemistry in a warmer arctic," *Proceedings of the National Academy of Sciences of the United States of America*, vol. 108, no. 9, pp. 3653–3658, 2010.

[84] O. Andersland and B. Ladanyi, *Frozen Ground Engineering*. New York: Wiley, 2003.

[85] G. Johnston and R. Brown, "Some observations on permafrost distribution at a lake in the mackenzie delta, n.w.t., canada," *ARCTIC*, vol. 17, no. 3, pp. 163 – 175, 1964.

[86] W. Kemper, "Water and ion movement in thin films as influenced by the electrostatic charge and diffuse layer of cations associated with clay mineral surfaces," *Soil Science Society of America Journal*, vol. 24, no. 1, pp. 10 – 16, 1960.

[87] A. Jumikis, "Some concepts pertaining to the freezing soil systems," *Highway Research Board Special Report*, no. 40, pp. 178–190, 1958.

[88] P. Hoekstra and E. Chemberlain, "Electro-osmosis in frozen soil," *Nature*, vol. 203, pp. 1406–1407, 1964.

[89] A. Fic, "Fem solution of heat transfer problem in the ground with change of phase and groundwater flow," 2000.

[90] M. Goldstein and R. Reid, "Effect of fluid flow on freezing and thawing of saturated porous media," *Proceedings of the Royal Society of London, Series A (Mathematical and Physical Sciences)*, vol. 364, no. 1716, pp. 45 – 73, 1978.

[91] P. Jany and A. Bejan, "Scales of melting in the presence of natural convection in a rectangular cavity filled with porous medium.," *Journal of Heat Transfer*, vol. 110, no. 2, pp. 526 – 529, 1988.

[92] A. Bejan, "Theory of melting with natural convection in an enclosed porous medium," *Journal of Heat Transfer*, vol. 111, no. 2, pp. 407 – 415, 1989.

[93] S. Chellaiah and R. Viskanta, "Natural convection melting of a frozen porous medium," *International Journal of Heat and Mass Transfer*, vol. 33, no. 5, pp. 887 – 899, 1990.

[94] M. Kazmierczak, D. Poulikakos, and I. Pop, "Melting from a flat plate embedded in a porous medium in the presence of steady natural convection," *Numerical Heat Transfer*, vol. 10, no. 6, pp. 571–581, 1986.

[95] P. Jany and A. Bejan, "Scaling theory of melting with natural convection in an enclosure," *International Journal of Heat and Mass Transfer*, vol. 31, no. 6, pp. 1221 – 1235, 1988.

[96] C. Beckermann and R. Viskanta, "Natural convection solid/liquid phase change in porous media," *International Journal of Heat and Mass Transfer*, vol. 31, no. 1, pp. 35 – 46, 1988.

[97] R. Koeller and A. Zebib, "A non-equilibrium thermodynamic theory of flow through deformable porous media," *Acta Mechanica*, vol. 30, no. 3-4, pp. 259 – 274, 1978.

[98] D. McKenzie, "The generation and compaction of partially molten rock," *Journal of Petrology*, vol. 25, no. 3, pp. 713 – 765, 1984.

[99] H. Iwamori, "A model for disequilibrium mantle melting incorporating melt transport by porous and channel flows," *Nature*, vol. 366, no. 6457, pp. 734 – 741, 1993.

[100] M. Spiegelman, "Flow in deformable porous media. I. simple analysis," *Journal of Fluid Mechanics*, vol. 247, pp. 17 – 38, 1993.

[101] D. Perugini and G. Poli, "Viscous fingering during replenishment of felsic magma chambers by continuous inputs of mafic magmas: Field evidence and fluid-mechanics experiments," *Geology*, vol. 33, no. 1, pp. 5 – 8, 2005.

[102] M. Hayek, G. Kosakowski, and S. Churakov, "Exact analytical solutions for a diffusion problem coupled with a precipitation-dissolution reaction and feedback of porosity change," *Water Resources Research*, vol. 47, no. 7, p. W07545 (13 pp.), 2011.

[103] S. Emmanuel and B. Berkowitz, "Mixing-induced precipitation and porosity evolution in porous media," *Advances in Water Resources*, vol. 28, no. 4, pp. 337 – 344, 2005.

[104] P. Dijk and B. Berkowitz, "Precipitation and dissolution of reactive solutes in fractures," *Water Resources Research*, vol. 34, no. 3, pp. 457–470, 1998.

[105] C. Noiriel, P. Gouze, and D. Bernard, "Investigation of porosity and permeability effects from microstructure changes during limestone dissolution," *Geophysical Research Letters*, vol. 31, no. 24, p. 4 pp., 2004.

[106] B. Kieffer, C. F. Jové, E. H. Oelkers, and J. Schott, "An experimental study of the reactive surface area of the fontainebleau sandstone as a function of porosity, permeability, and fluid flow rate," *Geochimica et Cosmochimica Acta*, vol. 63, no. 21, pp. 3525 – 3534, 1999.

[107] M. Canals and J. Meunier, "A model for porosity reduction in quartzite reservoirs by quartz cementation," *Geochimica et Cosmochimica Acta*, vol. 59, no. 4, pp. 699 – 709, 1995.

[108] C. Jové Coón, E. Oelkers, and J. Schott, "Experimental investigation of the effect of dissolution on sandstone permeability, porosity, and reactive surface area1," *Geochimica et Cosmochimica Acta*, vol. 68, no. 4, pp. 805 – 817, 2004.

[109] C. Steefel, D. DePaolo, and P. Lichtner, "Reactive transport modeling: An essential tool and a new research approach for the earth sciences," *Earth and Planetary Science Letters*, vol. 240, no. 34, pp. 539 – 558, 2005.

[110] S. Olivella, J. Carrera, A. Gens, and E. Alonso, "Porosity variations in saline media caused by temperature gradients coupled to multiphase flow and dissolution/precipitation," *Transport in Porous Media*, vol. 25, no. 1, pp. 1–25, 1996.

[111] Y.-J. Lee and J. Morse, "Calcite precipitation in synthetic veins: implications for the time and fluid volume necessary for vein filling," *Chemical Geology*, vol. 156, no. 14,

pp. 151 – 170, 1999.

[112] H. C. and J. Urai, "Experimental study of syntaxial vein growth during lateral fluid flow in transmitted light: first results," *Journal of Structural Geology*, vol. 24, no. 67, pp. 1029 – 1043, 2002.

[113] P. Lichtner, "The quasi-stationary state approximation to fluid/rock reaction: Local equilibrium revisited," in *Diffusion, Atomic Ordering, and Mass Transport* (J. Ganguly, ed.), vol. 8 of *Advances in Physical Geochemistry*, pp. 452–560, Springer US, 1991.

[114] V. Lagneau and J. van der Lee, "Operator-splitting-based reactive transport models in strong feedback of porosity change: The contribution of analytical solutions for accuracy validation and estimator improvement," *Journal of Contaminant Hydrology*, vol. 112, no. 1-4, pp. 118 – 129, 2010.

[115] Y. Ito and G. Ipek, "Steam fingering phenomenon during sagd process," 2005.

[116] R. Butler, "Rise of interfering steam chambers," *Journal of Canadian Petroleum Technology*, vol. 26, no. 3, pp. 70 – 75, 1987.

[117] Y. Ito and T. Hirata, "Numerical simulation study of a well in the jacos hangingstone steam pilot project near fort mcmurray," *Journal of Canadian Petroleum Technology*, vol. 38, no. 13, 1999.

[118] Y. Ito, T. Hirata, and M. Ichikawa, "The effect of operating pressure on the growth of the steam chamber detected at the hangingstone sagd project," *Journal of Canadian Petroleum Technology*, vol. 43, no. 01, pp. 47–53, 2004.

[119] D. R. Gotawala and I. D. Gates, "Steam fingering at the edge of a steam chamber

in a heavy oil reservoir," *Canadian Journal of Chemical Engineering*, vol. 86, no. 6, pp. 1011 – 1022, 2008.

[120] K. Sasaki, A. Satoshi, N. Yazawa, and F. Kaneko, "Microscopic visualization with high resolution optical-fiber scope at steam chamber interface on initial stage of sagd process," 2002.

[121] J. Daniel, *Numerical Methods That Work*. Society for Industrial and Applied Mathematics, 1990.

[122] R. Butler, "The behavior of non-condensible gas in sagd - a rationalization," *Journal of Canadian Petroleum Technology*, vol. 43, no. 01, pp. 28 – 34, 2004.

[123] Q. Jiang, R. Butler, and C. Yee, "The steam and gas push (sagp)-2:mechanism analysis and physical model testing," *Journal of Canadian Petroleum Technology*, vol. 39, no. 04, pp. 52 – 61, 2000.

[124] R. Butler and I. Mokrys, "A new process (vapex) for recovering heavy oils using hot water and hydrocarbon vapour," *Journal of Canadian Petroleum Technology*, vol. 30, no. 01, pp. 97 – 106, 1991.

[125] T. Nasr and E. Isaacs, "Process for enhancing hydrocarbon mobility using a steam additive," May 15 2001. US Patent 6,230,814.

[126] O. Mohammadzadeh, N. Rezaei, and I. Chatzis, "Pore-scale performance evaluation and mechanistic studies of the solvent-aided sagd (sa-sagd) process using visualization experiments," *Transport in Porous Media*, vol. 108, no. 2, pp. 437–480, 2015.

[127] O. Mohammadzadeh, N. Rezaei, and I. Chatzis, "Pore-level investigation of heavy oil and bitumen recovery using solvent -aided steam assisted gravity drainage (sa-sagd) process," *Energy and Fuels*, vol. 24, no. 12, pp. 6327 – 6345, 2010.

[128] O. Mohammadzadeh and I. Chatzis, "Pore-level investigation of heavy oil recovery using steam assisted gravity drainage (sagd)," *Oil and Gas Science and Technology*, vol. 65, no. 6, pp. 839 – 857, 2010.

[129] A. Bejan and D. Nield, *Convection in Porous Media*. New York: Springer, third ed., 2006.

[130] M. Sajjadi and J. Azaiez, "Dynamics of fluid flow and heat transfer in homogeneous porous media," *Canadian Journal of Chemical Engineering*, vol. 91, no. 4, pp. 687 – 697, 2013.

[131] H. Siddiqui and M. Sahimi, "Computer simulations of miscible displacement processes in disordered porous media," *Chemical Engineering Science*, vol. 45, no. 1, pp. 163 – 182, 1990.

[132] K. Sorbie, F. Feghi, G. Pickup, P. Ringrose, and J. Jensen, "Flow regimes in miscible displacements in heterogeneous correlated random fields," *SPE Advanced Technology Series*, vol. 2, no. 2, pp. 78 – 87, 1994.

[133] Z. Yang, Y. Yortsos, and D. Salin, "Asymptotic regimes in unstable miscible displacements in random porous media," *Advances in Water Resources*, vol. 25, no. 8-12, pp. 885 – 898, 2002.

[134] A. Riaz and E. Meiburg, "Vorticity interaction mechanisms in variable-viscosity heterogeneous miscible displacements with and without density contrast," *Journal of Fluid Mechanics*, vol. 517, pp. 1 – 25, 2004.

[135] M. Mishra, M. Martin, and A. De Wit, "Differences in miscible viscous fingering of finite width slices with positive or negative log-mobility ratio," *Physical Review E*

*(Statistical, Nonlinear, and Soft Matter Physics)*, vol. 78, no. 6, p. 066306 (11 pp.), 2008.

[136] L. Snyder and J. Kirkland, *Introduction to Modern Liquid Chromatography.* New York: Wiley, 1979.

[137] M. Martin and G. Guiochon, "Theoretical study of the gradient elution profiles obtained with syringe-type pumps in liquid chromatography," *Journal of Chromatography A*, vol. 151, no. 3, pp. 267 – 289, 1978.

[138] A. Watson and A. Poirson, "Separable two-dimensional discrete hartley transform," *Journal of the Optical Society of America A (Optics and Image Science)*, vol. 3, no. 12, pp. 2001 – 2004, 1986.

[139] M. Islam and J. Azaiez, "Fully implicit finite difference pseudo-spectral method for simulating high mobility-ratio miscible displacements," *International Journal for Numerical Methods in Fluids*, vol. 47, no. 2, pp. 161 – 183, 2005.

[140] M. N. Islamt, "Simulation of viscous fingering in high mobility ratio miscible displacements," Master's thesis, University of Calgary, Calgary, 2003.

[141] A. Tartakovsky, "Lagrangian simulations of unstable gravity-driven flow of fluids with variable density in randomly heterogeneous porous media," *Stochastic Environmental Research and Risk Assessment*, vol. 24, no. 7, pp. 993 – 1002, 2010.

[142] A. Arya, T. Hewett, R. Larson, and L. Lake, "Dispersion and reservoir heterogeneity," *SPE Reservoir Engineering*, vol. 3, no. 1, pp. 139 – 148, 1988.

[143] W. Shu, "A viscosity correlation for mixtures of heavy oil, bitumen, and petroleum fractions.," *Society of Petroleum Engineers journal*, vol. 24, no. 3, pp. 277 – 282, 1984.

[144] R. Gharbi, E. Peters, and A. Elkamel, "Scaling miscible fluid displacements in porous media," *Energy and Fuels*, vol. 12, no. 4, pp. 801– 811, 1998.

[145] U. Araktingi and F. Orr Jr., "Viscous fingering, gravity segregation, and reservoir heterogeneity in miscible displacements in vertical cross sections," in *Proc. SPE/DOE Enhanced Oil Recovery Symposium*, pp. 39 – 46, 1990.

[146] A. Coutinho and J. Alves, "Finite element simulation of nonlinear viscous fingering in miscible displacements with anisotropic dispersion and nonmonotonic viscosity profiles," *Computational Mechanics*, vol. 23, no. 2, pp. 108 – 116, 1999.

[147] M. A. Cala and R. A. Greenkorn, "Velocity effects on dispersion in porous media with a single heterogeneity.," *Water Resources Research*, vol. 22, no. 6, pp. 919 – 926, 1986.

[148] J. Bear and Y. Bachmat, *Introduction to modeling of transport phenomena in porous media*, vol. 4 of *Theory and applications of transport in porous media*. Kluwer Academic, 1990.

[149] D. Horváth, S. Tóth, and Á. Tóth, "Periodic heterogeneity-driven resonance amplification in density fingering," *Physical Review Letters*, vol. 97, no. 19, p. 194501 (4 pp.), 2006.

[150] F. Furtado and F. Pereira, "Scaling analysis for two-phase immiscible flow in heterogeneous porous media," *Computational and Applied Mathematics*, vol. 17, no. 3, pp. 237 – 263, 1998.

[151] C. Desai and K. Vafai, "A unified examination of the melting process within a two-dimensional rectangular cavity," *Transactions of the ASME. Journal of Heat Transfer*, vol. 115, no. 4, pp. 1072 – 1075, 1993.

[152] Y. Wang, A. Amiri, and K. Vafai, "An experimental investigation of the melting process in rectangular enclosure," *International Journal of Heat and Mass Transfer*, vol. 42, no. 19, pp. 3659 – 3672, 1999.

[153] R. Harlan, "Analysis of coupled heat-fluid transport in partially frozen soil," *Water Resources Research*, vol. 9, no. 5, pp. 1314 – 1323, 1973.

[154] N. Morgenstern and J. Nixon, "One-dimensional consolidation of thawing soils," *Canada Geotechnical Journal*, vol. 8, pp. 558 – 565, 1971.

[155] F. Ling and T. Zhang, "Numerical simulation of permafrost thermal regime and talik development under shallow thaw lakes on the Alaskan Arctic Coastal Plain," *Journal of Geophysical Research D: Atmospheres*, vol. 108, no. 16, p. ACL 8 (11 pp.), 2003.

[156] K. Hansson, J. Simunek, M. Mizoguchi, L. Lundin, and M. T. van Genuchten, "Water flow and heat transport in frozen soil: Numerical solution and freeze-thaw applications," *Vadose Zone Journal*, vol. 3, no. 2, pp. 693 – 704, 2004.

[157] D. Zhao, J. Wang, and I. Gates, "Thermal recovery strategies for thin heavy oil reservoirs," *Fuel*, vol. 117, pp. 431 – 441, 2014.

[158] V. Pathak, T. Babadagli, and N. Edmunds, "Heavy oil and bitumen recovery by hot solvent injection," *Journal of Petroleum Science and Engineering*, vol. 78, no. 3-4, pp. 637 – 645, 2011.

[159] V. Srinivasan and K. Vafai, "Analysis of linear encroachment in two-immiscible fluid systems in a porous medium," *Journal of Fluids Engineering, Transactions of the ASME*, vol. 116, no. 1, pp. 135 – 139, 1994.

[160] K. Vafai and B. Alazmi, "On the linear encroachment in two-immiscible fluid systems in

a porous medium," *Journal of Fluids Engineering, Transactions of the ASME*, vol. 125, no. 4, pp. 738 – 739, 2003.

[161] A. Dixon and D. Cresswell, "Theoretical prediction of effective heat transfer parameters in packed beds," *AIChE Journal*, vol. 25, no. 4, pp. 663 – 676, 1979.

[162] B. Alazmi and K. Vafai *Journal of Heat Transfer*, vol. 126, no. 3, pp. 389 – 399, 2004.

[163] D. Prowse, E. Wallace, R. Lott, L. Daingneault, and N. Shelly, "Some physical properties of bitumen and oil sand," industry access report, Alberta Oil Sands Technology and Research Authority (AOSTRA)/Alberta Research Council (ARC), Edmonton, Alberta, September 1983.

[164] R. Buckles, "Steam stimulation heavy oil recovery at cold lake, alberta," in *Proc. SPE California Regional Meeting*, (Ventura, California), pp. 1–12, Society of Petroleum Engineers, April 1979.

[165] M. Ramires, C. Nieto de Castro, Y. Nagasaka, A. Nagashima, M. Assael, and W. Wakeham, "Standard reference data for the thermal conductivity of water," *Journal of Physical and Chemical Reference Data*, vol. 24, no. 3, pp. 1377 – 1381, 1995.

[166] R. Weast, M. Astle, and W. Beyer, *CRC Handbook of Chemistry and Physics (75th anniversary edition)*. Boca Raton, Florida: CRC Press, 69 ed., 1988-1989.

[167] A. E. P. Veldman and K. Rinzema, "Playing with nonuniform grids," *Journal of Engineering Mathematics*, vol. 26, no. 1, pp. 119–130, 1992.

[168] J. Sand and O. Osterby, *Regions of absolute stability*, vol. 102 of *DAIMIPB Report Series*. 1979.

[169] C. Canuto, M. Y. Hussaini, A. Quarteroni, and T. A. Zang Jr., *Spectral Methods in Fluid Dynamics*. Springer Berlin Heidelberg, 1988.

[170] M. Sajjadi and J. Azaiez, "Scaling and unified characterization of flow instabilities in layered heterogeneous porous media," *Physical Review E (Statistical, Nonlinear, and Soft Matter Physics)*, vol. 88, no. 3, p. 033017 (12 pp.), 2013.

[171] A. Bejan and S. Lorente, "The constructal law origin of the logistics s curve," *Journal of Applied Physics*, vol. 110, no. 2, p. 024901 (5 pp.), 2011.

[172] A. Bejan, S. Ziaei, and S. Lorente, "The s curve of energy storage by melting," *Journal of Applied Physics*, vol. 116, no. 11, p. 114902 (7 pp.), 2014.

[173] M. Sajjadi and J. Azaiez, "Heat and mass transfer in melting porous media: Stable miscible displacements," *International Journal of Heat and Mass Transfer*, vol. 88, pp. 926–944, 2015.

[174] P. Petitjeans, C.-Y. Chen, E. Meiburg, and T. Maxworthy, "Miscible quarter five-spot displacements in a hele-shaw cell and the role of flow-induced dispersion," *Physics of Fluids*, vol. 11, no. 7, pp. 1705 – 1716, 1999.

[175] C. Chen and E. Meiburg, "Miscible porous media displacements in the quarter five-spot configuration. part 1. the homogeneous case," *Journal of Fluid Mechanics*, vol. 371, pp. 233 – 268, 1998.

[176] Y. Nagatsu, N. Fujita, Y. Kato, and Y. Tada, "An experimental study of non-isothermal miscible displacements in a hele-shaw cell," *Experimental Thermal and Fluid Science*, vol. 33, no. 4, pp. 695 – 705, 2009.

[177] C. Chen, L. Wang, and Y. Kurosaki, "Numerical simulations of heat transfer in porous

media with effect of heterogeneities," *JSME International Journal, Series B (Fluids and Thermal Engineering)*, vol. 45, no. 2, pp. 315 – 321, 2002.

[178] F. Furtado and F. Pereira, "Crossover from nonlinearity controlled to hetogeneity controlled mixing in two-phase porous media flows," *Computational Geosciences*, vol. 7, no. 2, pp. 115–135, 2003.